Computational Formulation of Material Laws for Intervertebral Discs

Geza T. Nagy

A thesis submitted in partial fulfilment of the requirements of the
Nottingham Trent University for the degree of
Doctor of Philosophy

This research programme was carried out in the
School of Engineering
Faculty of Computing and Technology
The Nottingham Trent University, Burton Street, Nottingham, NG1 4BU, UK

March 2002

ABSTRACT

The lack of a good understanding of the detailed mechanical behaviour of all the parts of the spine is a major obstacle to improving the safety and health of people in a wide variety of situations, ranging from simple lifting operations to passenger vehicle crashes. Early computational modelling of soft tissues as non-linear springs had some success, particularly with ligaments in situations where they only deform axially. Similar treatment of the discs, however, was recognised as having many shortcomings. Although the overall static load/deflection properties of the disc could be reproduced accurately, a detailed representation of the pressure, shear and torsion in the individual components did not fit the available *in vitro* data. It is therefore necessary to attempt a complete characterisation of the material properties of the annulus fibrosus, even though this is an almost insurmountable task due to lack of engineering data.

In the presented study a novel approach to implementing a fully non-linear, anisotropic material into the LS-Dyna3D dynamic finite element solver was developed, implemented, and tested. An experimental study was carried out on a large-scale model of the L2-L3 motion segment establishing the role of the main components of the disc and their influence on the overall disc behaviour. An analytical study was also completed on the disc bulge. Finally a detailed FEM of the full ligamentous L1-S1 lumbar spine was built and tested showing the future direction. Throughout the simulations, the features of the disc which are governed by the individual properties were of special interest. A material property sensitivity study was undertaken on all models establishing important information on the intervertebral disc mechanics. Using the novel approach modelling the annulus fibrosus a greater accuracy was proven. Validation of the model by comparison of its response with literature data shows excellent matching in terms of vertical displacement for complex loading situations. The validation results of the disc confirm that the presented way of implementing non-linear materials into FEM solvers is a promising approach to full computational simulation of non-linear anisotropic materials such as the annulus of the intervertebral disc.

ACKNOWLEDGEMENTS

The author wishes to thank the following for their respective contributions in preparing this thesis.

Firstly, I would like to express my gratitude to **Prof. C. R. Gentle**, director of studies, for his invaluable support and guidance throughout the work; without him this could not have been attempted.

Special thanks to **Prof. J. B. Hull** and **Prof. R. Bedzinski**, for providing the opportunity of carrying out this investigation.

A big thank you to **my parents** for their generous support, and for giving me the opportunity to undertake all that I have achieved.

I also thank the many fellow students who were involved with the Biomechanics Research Group during this project. I would like to express my particular thanks to Dr. Frank Heitplatz and Dr. Waldemar Z. Golinski, for help and advice during our collaboration.

Many thanks are extended to my friends and colleagues, for their help and support throughout this PhD.

LIST OF PUBLICATIONS

Nagy, G. T., Golinski, W. Z., Heitplatz, F. Gentle, C. R.,
Investigation into the Range of Motion of the Cervical Spine Based on a Non-linear Finite Element Model,
Journal of Proceedings in Osteology, 7(1), 27-30, 1999

Nagy, G. T., Golinski, W. Z., Gentle, C. R.,
Three-dimensional Non-linear Finite Element Analysis of the Human Lumbar Intervertebral Disc,
Proceedings of BUDAMED '99 Conference on Biomedical and Clinical Engineering, 12-14 September, Budapest, Hungary, 1999

Nagy, G. T., Golinski, W. Z., Gentle, C. R.,
Analysis of the Human Lumbar Intervertebral Disc Based on a Three-dimensional Non-linear Finite Element Model,
Journal of Technology in Engineering and Medicine, 38(1), 5-11, 2000

Nagy, G. T., Gentle, C. R.,

Soft Tissue Modelling in Intervertebral Discs,

Proc. 10th International Conference on BioMedical Engineering,

Singapore, 6-9 December 2000

Nagy, G. T., Gentle, C. R.,

Significance of the Annulus Properties to Finite Element Modeling of Intervertebral Discs,

Journal of Musculoskeletal Research, 5(3), 159-171, 2001

Nagy, G. T., Gentle, C. R.,

Experimental Stress Analysis of Intervertebral Discs Based on a Large Scale Model,

International Society of Biomechanics XVIIIth Congress, Zurich, Switzerland, July 8-13, 2001

TABLE OF CONTENTS

LIST OF TABLES AND FIGURES

Tables

Figures

CHAPTER 1. - INTRODUCTION

1.1 History

Car manufacturers spend enormous sums in crashing their vehicles and observing the effect on crash test dummies; they then simulate these collisions on sophisticated and complex finite element computer models, which include a dynamic consideration of dummies and the damage they incur. As a result, society is in the strange position of designing its vehicles so that they are safe to dummies!

What car manufacturers can not begin to do at present is estimate the response of real passengers or the injuries they suffer. The reason for this is that current finite element techniques, although excellent for normal engineering materials such as metals and polymers, can become quite inaccurate when applied to biological materials. In some cases it is simply a matter of adapting existing material laws and computer coding, as in the modelling of the large, rigid bones, such as the femur, and this has been successfully used to analyse hip joints. In the case of soft tissues such as ligaments, tendons and muscles, the problem is more difficult and nowhere is this difficulty greater than in the intervertebral discs of the spine, since they are crucial in the transmission and distribution of large loads, and in providing flexibility, but have such a complex structure that they are difficult to analyse. Nevertheless it is essential that computational models of all the discs in the spine are developed so that full biomechanical analysis may be carried out of dynamic trauma situations in order to predict the mode of injury; that is the aim of the work reported here.

The Biomechanics Research Group of the Nottingham Trent University has developed a dynamic finite element model of the cervical spine shown on Fig. 1. which has been used successfully to demonstrate the likelihood of whiplash injuries in rear-end collisions. This model includes a treatment of the vertebrae and the skull as conventional rigid engineering materials. It also has successful original treatments of ligaments as non-linear springs but a similar treatment of

the disc was recognised as having many shortcomings and remains a major drawback to the more general use of the model and its extension to the full spine.

Nevertheless the NTU spinal model is recognised as a considerable advance, thanks in part to the earlier contribution of the candidate which has recently been published, and has been adopted by the Transport Research Laboratory (TRL) for grafting onto their standard finite element model of a crash test dummy to produce a hybrid which should lead to improved safety specifications for vehicles. Eventually the UK government, through TRL, wishes to produce car safety guidelines based on a full biomechanical model of the human body and the biggest obstacle to this at present is the lack of a general material law for the body's soft tissues, notable for the intervertebral disc. A neck structure [1] of the recently used crash test dummy can be seen on Fig. 2.

1.2 Programme of Study

The programme of study here is to produce a better material description of a general intervertebral disc in a form suitable for implementation in a finite element model. For the first investigation the lumbar L2-L3 complex shown on Fig. 3. was chosen not only because this has one of the biggest intervertebral discs in size, but also because it bears the largest loads during daily life. The research concentrated on two main areas comprising experimental and computational studies. There was an experimental research project to reproduce a disc as an engineering assembly, which simulates all the individual components shown on Fig. 4. the nucleus pulposus, the annulus fibrosus and the surrounding Sharpy's fibres. This oversized model includes a thick annulus of a cellular material such as Neoprene, wrapped around with strings to simulate the fibres, and a watery gel contained in an elastic rubber sac representing the nucleus, all sandwiched between steel endplates. Pressure tappings were built in to change and measure the pressure within the nucleus sac during testing. Mechanical testing of this

model in compression, tension, bending and shear serve to relate the overall behaviour to the properties of the components.

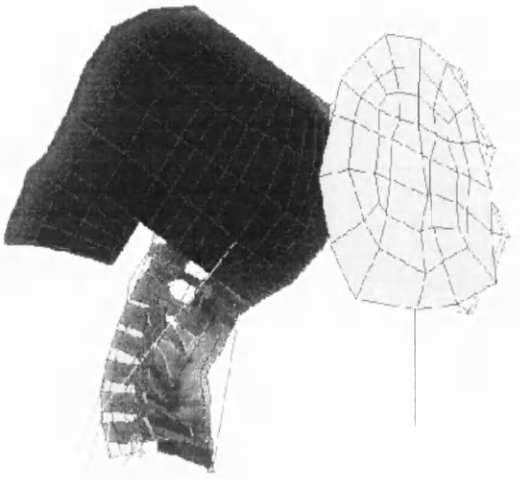

Fig. 1. The NTU head-neck model to investigate whiplash

Fig. 2. Neck of a rear-impact dummy

In parallel with this experimentation a study was done on the computational requirements for incorporating a material law into a finite element simulation model. This involved a study of dynamic viscoelastic behaviour of the disc acting in the role of dampers between adjacent vertebrae. Throughout the work important information was gained on the sensitivity of the material property values and the role of the individual disc components. Based on these findings, a novel form of material implementation was formulated for finite element solvers. The material law was tested and the results were compared against different experimental and FEM results. The project was carried out using the latest dynamic finite element solver software, LS-Dyna3D®, [2] which is the standard for the vehicle industry but is only available in three UK universities including NTU.

In the following chapter a brief history of the lumbar spine research can be found. In Chapter 3 a biomechanical overview of the lumbar spine, and the anatomy of the vertebra and the disc is discussed. Furthermore, a section about the functional biomechanics of the intervertebral disc summarises the disc structure and

behaviour, the different possible load conditions and the physical properties of the disc components. In Chapter 4 the project itself is discussed. Here the main aims and objectives are pointed out, and also there are some words about the results achieved. The background of the finite element analysis and the experimental work is introduced here, listing the resources used throughout the project. Chapter 5 gives a brief overview on finite element solvers and commonly used techniques at modelling non-linear materials with large deformation. In Chapter 6 the analytical studies done and the recent theory of soft tissues are briefly introduced. This chapter presents the possible ways of implementing various properties. Chapter 7 is looking for a relation between the vertical displacement of the top vertebra of a motion segment and the disc bulge. It draws important findings in connection to the internal stress-state of the annulus, and predicts the effect of fluid loss. The characterisation and validation of the nucleus and the annulus material can be found in Chapter 8. A novel approach is presented to implement the annulus properties into finite element solvers. In this chapter three different FE models are compared to each other and to the literature. A material property sensitivity study is also presented. Chapter 9 describes the work done on a large-scale experimental model of the lumbar motion segment. This project gave essential information about the interaction and importance of the different individual mechanical components and their material property. Finally in Chapter 10 a creation of a full lumbar spine model is explained in detail, together with a preliminary finite element study. This model evaluates the feasibility of extending the usage of the material formulation from Chapter 8 in larger models through a simple simulation. In Chapter 11 discussion of the results and conclusions of the entire project can be found.

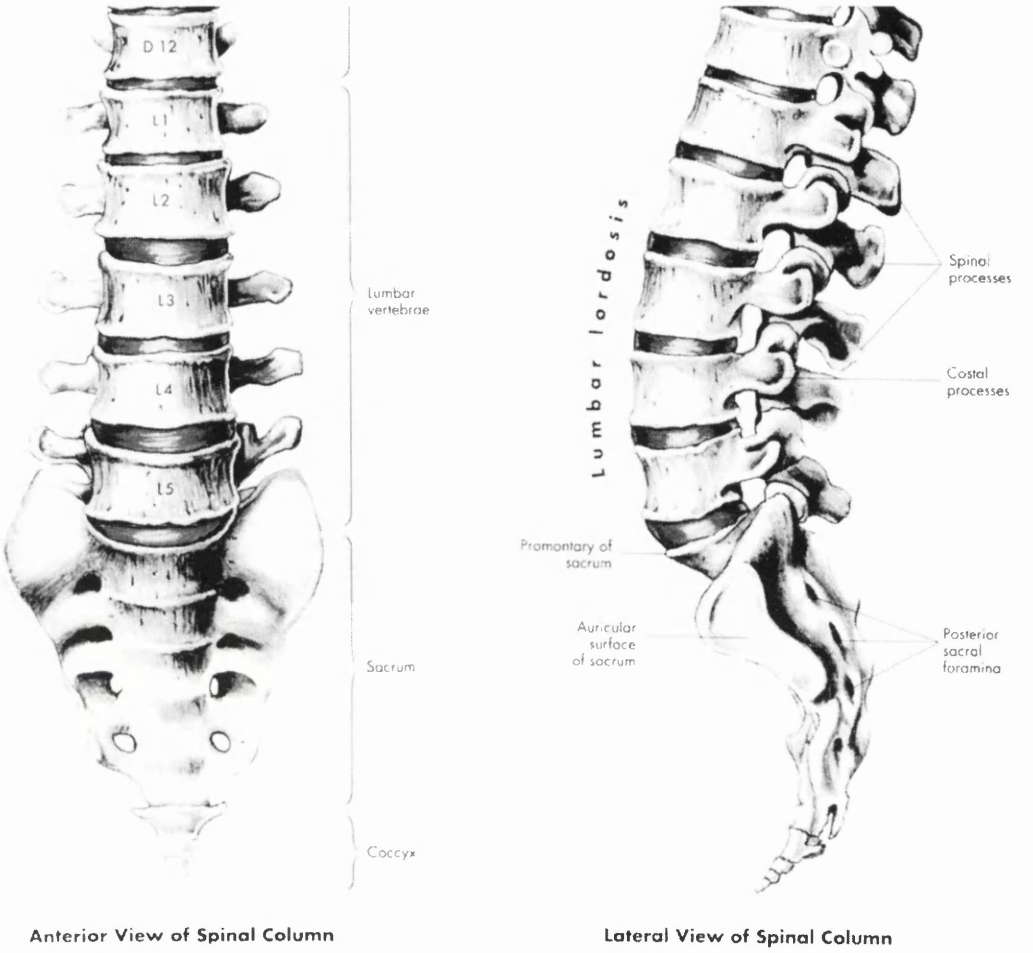

Fig. 3. The lumbar spine

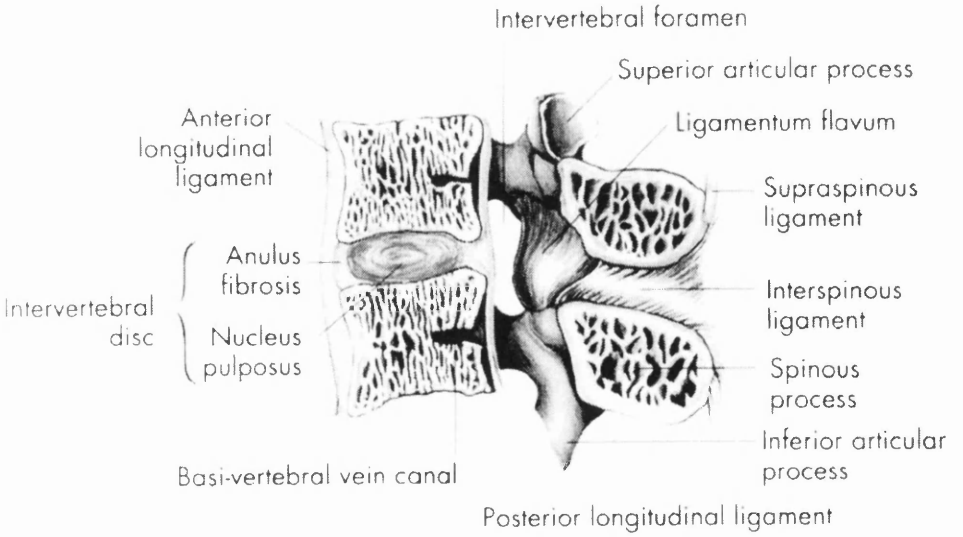

Fig. 4. The lumbar spine motion segment and its components

CHAPTER 2. - LITERATURE REVIEW

2.1 History of Research on the Lumbar Spine Motion Segment

Low back syndrome has a long history and has always been present causing acute pain, or even partial immobility, in patients. The first biomechanical stretching devices and orthopaedic benches made to ease back pain are known to have existed in the time of the ancient Greeks. Even before that era massage was widely used to treat patients with back problems. However society has concentrated on understanding the cause of back pain only from the late XIX-th century. Frequent studies on the spine and the intervertebral discs started in the 1920's. Researchers have been especially interested in the significance of the intervertebral disc in low back syndrome, its pathology and biochemistry, its physical quantities and the frequency of the structural changes with regard to the different ages and professions. They recognised that the overall incidence of backache is around 60% in society and this figure is currently on the rise [3].

Disabilities initiated by low back pain cause enormous losses for society, both economically and socially. In the 1930's and 1940's, it was learned that a multitude of structural changes may be found in lumbar intervertebral discs. On the basis of these and other observations, there has been a growing tendency to accept disc degeneration as the pathological anatomical explanation of low back pain. Some results from clinical studies on degeneration and changes in the intradiscal pressure of the disc were taken as a sign of the importance of mechanical factors. Also the most commonly held view on the cause of pain is that the disc is mechanically irritating the surrounding sensitive tissue elements. One of the first studies on the reaction of intervertebral discs to compression forces was done in 1955 by Hirsch [4] *in vitro*. Lumbar motion segments with the surrounding muscles cut were tested for compression. The overall characteristics of the disc response were recorded. Response to vibration and to initial shock compression by falling weights was also evaluated. In 1957 Brown *et. al.* [5] launched a wide range of mechanical tests. The disc was subjected to axial compression, tension and combined axial compression and bending. They

investigated fatigue, which produced no failure in axial compression. However, the sample failed very quickly when bending was also involved. One of the major results of this study is a tensile strength map of the intervertebral disc material, which shows the material inhomogeneity of the disc. Horton [6] investigated the arrangement of the annulus fibres using a polarising microscope and X-rays confirming earlier studies with the help of the latest technology available.

The first exhausting study on the tensile properties of the annulus material was done in 1967 by Galante [7]. In this investigation the tensile properties of the lumbar annulus fibrosus were studied in human post mortem specimens. There was an attempt to fully control the variables introduced by the methods of preparation and testing. Changes induced in the water content of the samples were also studied thoroughly. The methodology was further completed in regard to the sectioning and testing of the samples. After defining the *in vitro* laboratory conditions a study of tensile properties of the lumbar annulus fibrosus was made in relation to the orientation of the fibres, to the location of samples in different areas, to the time dependent effects, to tensile strength, and to the influence of age and degeneration. To evaluate these effects, morphological and biochemical correlations were also used. The findings were discussed in the general context of the mechanics of the intervertebral disc. Based on these studies, Sonnerup [8] investigated the stress distribution within the annulus fibrosus based on a large-scale experimental model. In summary, the problem set out was to study the influence of material inhomogenity and boundary conditions on the stress distribution through the annulus fibrosus in compression. The approach was to base an idealised, theoretical analysis of tangential and radial stress on previous experimental findings, and on a complementary experimental investigation on the lateral pressure distribution through the middle plane of the disc. The result was an analytical description of the stress distribution in a central slice of the annulus.

The first finite element studies were initiated by Belytschko *et. al.* [9]. Their novel inviscid incompressible contained fluid model was evaluated [10] on a finite element analysis of an intervertebral disc. This model replaced the inappropriate elastic formulation of the nucleus fluid, and researchers could

concentrate on the annulus material. This material model then was implemented into various solvers, and even nowdays it appears in the majority of the models built in the well-known ABAQUS package. In the same year of 1974 Markolf *et. al.* [11] published some tests on the lumbar motion segments involving the viscoelastic properties of the disc. Creep and relaxation tests were done. The effect of saline injection was also investigated. Lesions in the annulus and the response of the denucleated disc to compression were studied. Injections of saline caused axial distensions, but no increase in bulge. When defects of 2-4mm in diameter were made through the annular wall, significant decrease in compressive stiffness, and increase in creep and relaxation rates were recorded. Extrusion of nucleus material through the lesion accompanied by loud, popping sounds was observed. After discectomy the stiffness was reduced, while creep and relaxation were increased. In 1976 Wu *et. al.* [12] created an analytical description for an incompressible material with two families of extension fibres based on tensile tests on the annulus fibrosus. The material parameters stay very challenging to obtain and often the cause is a lack of accurate description to assist engineering analysis.

In 1978 a significant range of measurements were done by Lin *et. al.* [13]. These measurements are very well documented; both the sample geometry and other properties like age and degeneration are appropriately described. The measurement methods and techniques, the boundary conditions and the setup are also recorded in details. Axial and eccentric compression, flexion, extension and lateral bending, combined compression and shear tests are evaluated. A simple FE model was also done. [14] Part of the top and bottom vertebrae was removed to ensure parallel, horizontal faces to mount the specimen. Axial and off-centre loading were carried out. After a 22N preload, the load was applied in three steps. It was increased serially to 445N, 899N, and finally 1334N. Direct shear tests were done with total shear loads of up to 133N. The deformations of both the lower and upper vertebrae were small, and therefore a combined compression and shear test was developed using compressive loads of 223N and 445N. Combined compression and bending tests were carried out on a similar way to off-centre loading. There, a wedge-shape load head was pressed against the top vertebra 5

and 10mm away from the centroidal axis. Bulge was recorded on the anterior, left and right lateral, anterio-lateral, and postero-lateral sides of the disc. The above work is exceptionally useful for evaluating finite element simulations based on its results. In 1979 Schultz et. al [15] and Berkson *et. al.* [16] parallel published further tests on compression, flexion, extension, lateral bending, shear and torsion, refining the experimental methods and confirming previous studies.

Despite the various pathoanatomical studies already available, the biomechanical architecture of the disc at the ultrastructural level has not been very well demonstrated. Inoue [17] investigated the collagenous interconnections within the disc concentrating especially on the boundaries of the various structural components. Three-dimensional observation of the collagen framework of lumbar intervertebral discs by scanning electron microscopy confirmed that the fibrillar framework of the annulus and the cartilaginous end plate encircles the nucleus as a closed pack system. The cartilaginous end plate was made of a dense collagen framework aligned horizontally. There was no interconnection between the cartilaginous end plate and the lamellar subchondral collagen. In places, the vascular channels ran directly on the end plate. In the inner one-third of the annulus, obliquely oriented fibrillar lamellae interconnected with the cartilaginous end plate. In the outer two-thirds, the fibrillar lamellae were formed from fibrillar bundles and were firmly anchored into the vertebral bodies. By the end of the 1980's more and more FEA [18, 19, 20, 21, 22, 23, 24, 25, 26, 27] and refined experimental test results [28] emerged, starting to focus on the role of the ligaments and the facets. Also motion analysis of the spine took place by Adams *et. al.* [29] to investigate the effect of posture on stability [30] of the spine and to predict the mode of failure. [31]

In 1992 McNally *et. al.* [32] introduced and validated [33] stress profilometry, measuring the intradiscal pressure with a needle including a pressure transducer. Results from these investigations of direct interest for the magnitude and pressure distribution of stress in normal or moderately degenerated lumbar discs could be summarised as follows. The state of stress in the nucleus pulposus is hydrostatic. The relation between applied load as pressure, p and

measured pressure in the nucleus, p_n is linear, $p_n=cp$. The constant c is found to be independent of disc position in the lumbar spine, degree of disc degeneration, and age. Further, c also seems to be insensitive to differences in disc geometry. The mean values of c falls close to 1.5. Under normal physiological conditions, *in vivo* measurements show compressive loads in the range of 1000-3000N. Under more extreme circumstances, even higher values have been recorded. Adams *et. al.* [34] later used the technique to establish connection between posture and compressive strength of the lumbar spine. In the early 1990's there were some repeated tensile tests on the annulus, models of fluid loss, and hysteresis measurements. Some analytical studies were also launched looking for a novel analytical method, as the need for a material law of soft tissues became widely recognised. In 1997 Tadano *et. al.* [35] measured stress and strain directly in some tests on discs.

In the late 1990's data collection continued [36] [37] with special technologies available like elastography [38]. Muscle forces, spine kinematics [39, 40] and dynamics [41, 42] were investigated. The internal displacements of the disc were investigated by Seroussi *et. al.* [43] placing a matrix of metal beads inside. [44] Three rows of six evenly placed metal beads were implanted midsagittally into the discs of ten L4-5 human lumbar motion segments. The bead displacements in response to compression, flexion, and extension loads were obtained by digitising the bead positions from sagittal plane radiographs. The loading process was repeated on denucleated discs. For the intact discs, the intradiscal bead displacements were predominantly anterior. In flexion, the beads in the centre of the disc moved to the posterior direction whereas the beads closer to the periphery of the disc moved anteriorly. In extension, the central beads moved anteriorly and the beads closer to the periphery moved posterior. After denucleation, the bead displacements for compression and flexion implied an inward bulging of the inner wall of the annulus, despite outward bulging of the disc surface. A hypothesis was formed that the inward bulging causes radial tensile stresses within the disc, leading to disruption of adjacent layers of annulus. Separation of the adjacent annulus layers was also observed for repetitive loading of sheep spine specimens. The International Society of Biomechanics initiates [45] standardisation of data collection. There is a growing need for *in vivo* data.

Biphasic, viscoelastic [46, 47] or non-linear [48] material models have been published.

In 1999 Wilke *et. al.* [49] measured the intradiscal pressure for the first time *in vivo* on two human volunteers during general daily activities using stress profilometry. After the volunteer had been premedicated with antibiotics, a flexible pressure transducer was implanted into the L4-L5 disc. Measurements were made of the intradiscal pressure with the subject in various lying positions, then during sneezing and laughing, then for a series of activities, including various sitting positions in a chair, while standing, walking, jogging, stair climbing, load lifting, and finally during sleeping to monitor the biomechanical effect of dehydration. Some of the sitting positions, like slouching in a chair, resulted in much lower intradiscal pressure than suggested earlier.

Although there is a wide range of experimental measurement results available on the overall behaviour and the structure of the lumbar spine motion segments in the literature, there is still a lack of reliable data on some properties of the disc and the surrounding structures. This is often due to improper documentation or large scatter in measured values. Also, *in vivo* data is almost completely missing. There are still no appropriate material descriptions existing to model the anisotropic, non-linear, and inhomogeneous structure of the disc annulus. The aim of this study is to investigate the possibilities of implementing these properties into finite element solvers with respect to the intervertebral disc.

CHAPTER 3. - BIOMECHANICAL OVERVIEW

3.1 The Anatomy Of The Spine

The human spine consists of thirty-three vertebrae, separated by inter-vertebral discs, and stiffened by muscles and ligaments. A picture of the spine can be seen in Appendix 1. The spine is divided into five logical subsections, numbered from the top to the bottom as,

Cervical Spine - seven vertebrae from the skull to the top of the thoracic spine (**C1-C7**)

Thoracic Spine - twelve vertebrae to which the ribs are attached (**T1-T12**)

Lumbar Spine - five vertebrae (**L1-L5**)

Sacral Spine - five fused vertebrae

Coccygeal Spine - three to four fused segments

In the frontal plane the healthy spine is generally straight and symmetrical. In the lateral plane there are four normal anatomic curves, which are convex anteriorly in the cervical and lumbar regions (lordosis) and convex posteriorly in the thoracic and sacral regions (kyphosis).

3.2 The Lumbar Spine Motion Segment

3.2.1 The Lumbar Vertebra

The lumbar motion segment [50] consists of an intervertebral disc between two adjacent vertebrae. The vertebrae are very different in the cervical, thoracic and lumbar region. The work discussed here is related only to the lumbar region. The lumbar vertebra consists of an anterior block of bone, the vertebral body, and a posterior bony ring, known as the neural arch, containing articular, transverse and spinous processes. The vertebral body is roughly elliptical mass of cancellous bone contained in a thin shell of cortical bone. In the lumbar region there are 5 vertebrae of the 33 building the entire spinal column, usually denoted as L1 to L5 from the top to the bottom respectively. The lumbar vertebrae interlock along the facets.

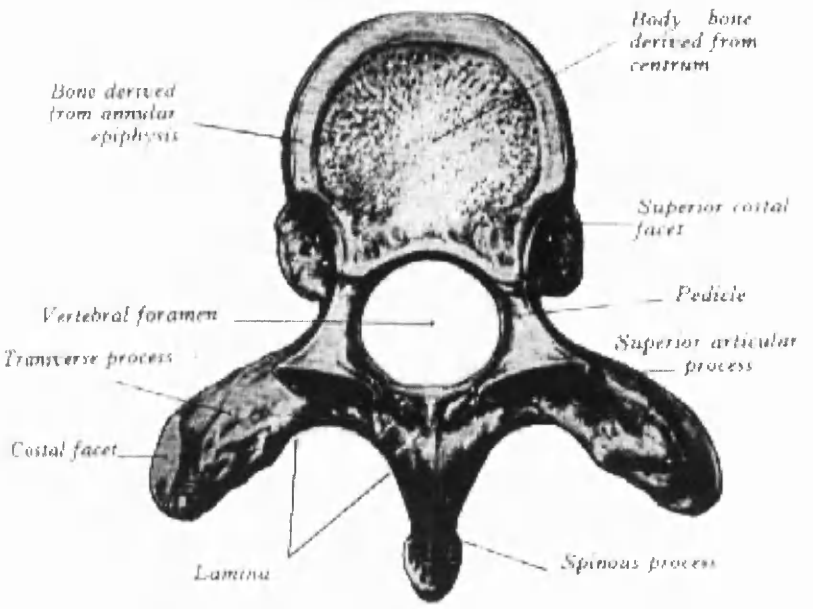

Fig. 5. The anatomy of the lumbar vertebra

3.2.2 Intervertebral Disc:

The intervertebral disc has probably received as much attention as any anatomic structure in the entire spine complex, [51] with the exception of the spinal cord. It constitutes 20-30% of the entire height of the spinal column. The intervertebral disc is comprised of three distinct parts: the nucleus pulposus, the annulus fibrosus and the cartilaginous end plates.

Nucleus Pulposus: The nucleus pulposus is a centrally located area composed of a very loose and translucent network of fine fibrous strands that lie in a mucoprotein gel containing various mucopolysacharides. The water content ranges from 70-90%. It is highest at birth and tends to decrease with age. With the help of MRI [52] it can be measured *in vivo*. The lumbar nucleus fills 30-50% of the total disc area in cross-section. In the low back, the nucleus is usually more posterior than central and lies at about the juncture of the middle and posterior thirds of the sagittal diameter. This non-central alignment can result in meshing difficulties at finite element analysis. The size of the nucleus and its capacity to swell are greater in the cervical and lumbar regions.

Annulus Fibrosus: The annulus fibrosus is a portion of the intervertebral disc that gradually becomes differentiated from the periphery of the nucleus and forms the outer boundary of the disc. This structure is composed of fibrous tissue of concentric laminated bands. [17] The fibres are arranged in a helicoid manner. They run in about the same direction in a given band but in opposite directions in any two adjacent bands. They are oriented at 30° to the disc plane and therefore at 120° to each other in the adjacent bands. The annulus fibres are attached to the cartilaginous end plates in the inner zone, while in the more peripherial zone they attach directly into the osseous tissue of the vertebral body and are called Sharpey's fibres. This attachment to the vertebra is a good deal stronger than the other more central attachments, which is a useful characteristic in the clinical evaluation of spine trauma, clinical stability, and surgical constructs. Three-dimensional architecture of the collagen framework has been studied, and morphological changes with aging have also been investigated.

3.2.3 Cartilaginous End-plate:

The end plates are composed of hyaline cartilage. They separate the other two components of the disc from the vertebral body. An excellent histological study of the lumbar vertebral end plate and its changes with age from 0 to 37 years has been provided by the literature. Starting with an active growth cartilage, the age changes result in irregularly arranged growth cartilage, which disappears with time and is replaced by bone.

3.3 *Functional Biomechanics of the Intervertebral Disc*

3.3.1 Structure and Behaviour

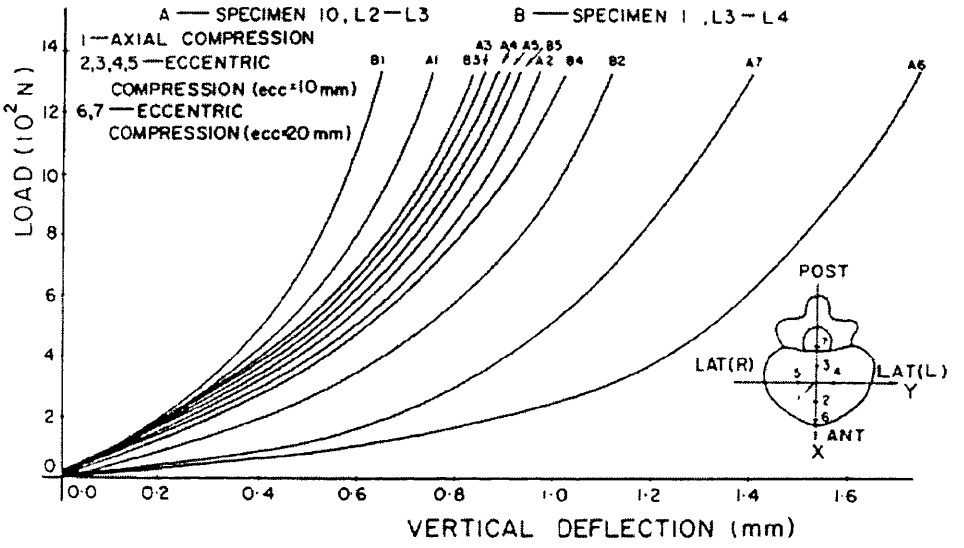

Fig. 6. Overall response of the intervertebral disc to compression

The overall response to compressive loading [13] can be seen on Fig. 6. The curves belong to two different specimens. It can be seen that the curves are different for different points on the disc. This is caused by the highly non-linear and anisotropic properties of the disc material. The other important aspect can be noticed on this diagram is that specimen A is slightly degenerated which results in the weaker characteristics.

The annulus fibrosus shown in Fig. 7. has a fibrous tissue in concentric laminated bands. The fibres are oriented at 30° to the disc plane. This can be seen on Fig. 8.

As the load is applied, pressure develops within the nucleus, which pushes the surrounding structures in all directions away from the centre. The compressive loads produce complex stresses within the annular ring. The schematics of the process can be seen on Fig. 9.

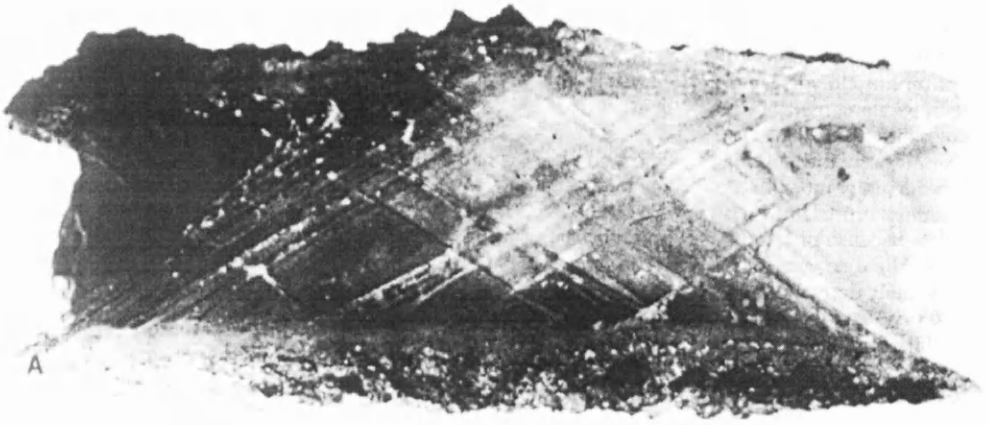

Fig. 7. Structure of the disc annulus

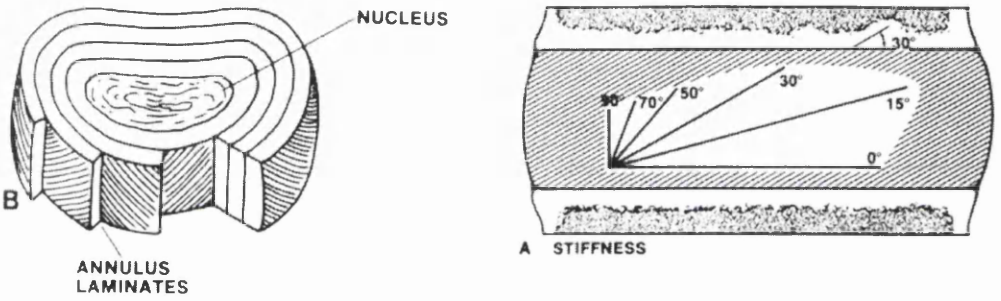

Fig. 8. Fibre direction within the laminates of the disc annulus

On Fig. 10. the pressure inside the disc can be seen during compression. [33] One can see the nucleus with relatively high pressure and the annulus where the pressure and stresses fall towards the edge. Note that there are no stresses at the outer rim of 1mm can be seen on the diagram. According to the recent theory [32] there are small tensile stresses existing there in the annulus caused by the disc bulge.

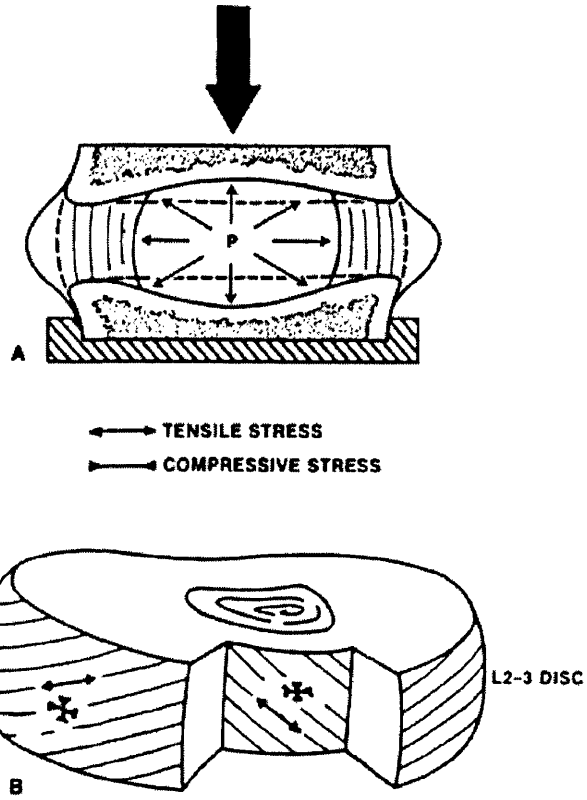

Fig. 9. Simplified theory of the disc behaviour under compression

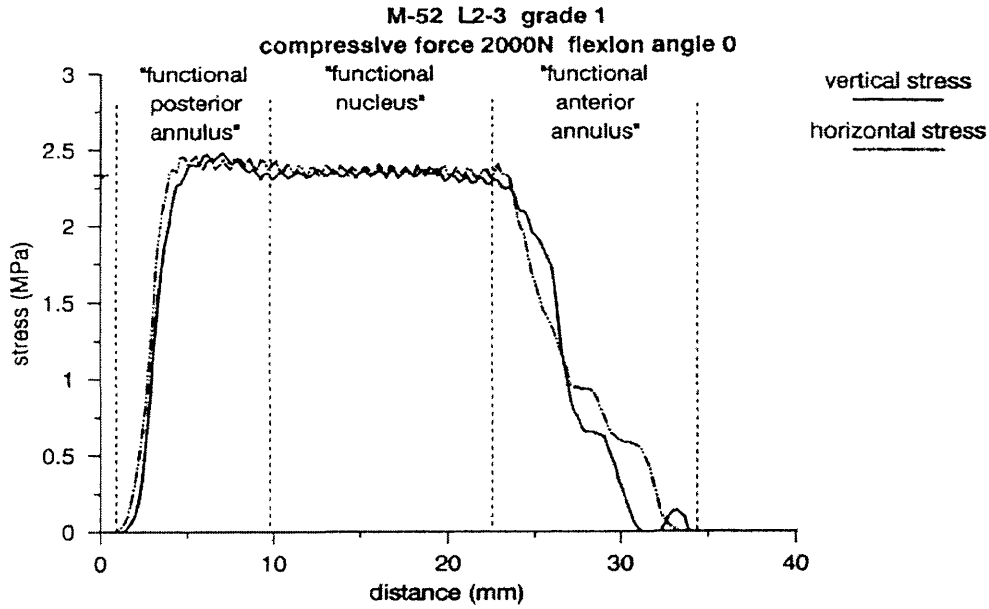

Fig. 10. Variation of pressure inside the disc along the sagittal plane

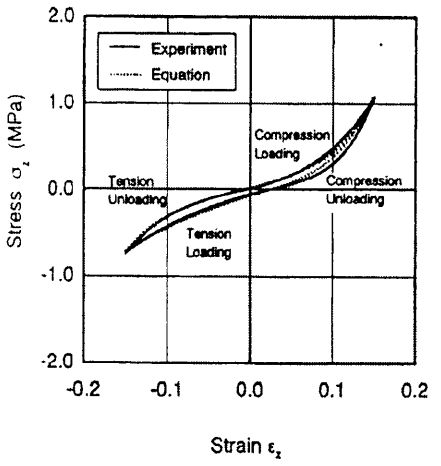

Fig. 11. Response of an intact disc to cyclic tension-compression

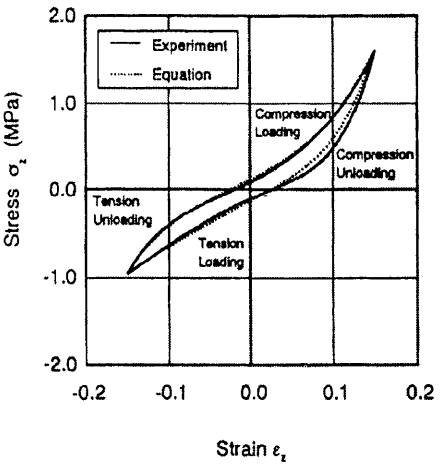

Fig. 12. Response of a denucleated disc to cyclic tension-compression

Here on Fig. 11. the overall tensile-compressive properties of the disc with and without the nucleus are presented. [35] The characteristics without the nucleus are on Fig.12. The nonlinearity and the hysteresis [53] can be seen nicely. But as was mentioned before, the properties of the annulus are different at any point on the disc. The intervertebral disc annulus has a radial nonlinearity as well, which will be explained later.

Understanding the failure of this complex material should lead to a better explanation of mechanical disc degeneration and other symptomatic disc disorders, as well as increased understanding of the spine as a whole.

3.3.2 Load Conditions

The intervertebral disc, which has many functions, is subjected to a considerable variety of forces and moments. Table 1. shows a summary of the load cases documented in the literature. These may be relatively simple (flexion) or complex (combined flexion, bending and torsion). Along with the facet joints, the disc is responsible for carrying all the compressive loading to which the trunk is subjected. When a person is standing erect, the forces on the discs are much greater than the weight of the portion of the body above it. Nachemson *et. al.* [15, 16] have determined that the force on a lumbar disc in a sitting position is more

than three times the weight of the trunk. Mathematical models have also predicted such large loads. [54] In addition with any activity where dynamic loads are involved like jumping, lifting, walking, the actual loads on the intervertebral disc are much higher. These are mainly compressive loads. The disc is also subjected to other types of loads and stresses. Tensile stresses are produced in certain portions of the disc during physiologic motions of flexion, extension and lateral bending. Axial rotation of the torso with respect to the pelvis causes torsional loads that result in shear stresses in a lumbar disc. Combined rotation and bending results in a combination of tensile, compressive and shear stresses.

It is important to distinguish between the load applied to the disc as a structure and the stresses produced within the disc material. For example, when we stand erect in neutral posture, the disc is subjected to a compression load, while its nucleus experiences compressive stresses and its annular fibres experience tensile stresses. Stress at point in a tissue is defined as the force per unit area. In order to understand the failure mechanisms of the disc, it is necessary to know the orientation and magnitude of stresses generated in response to the various loads applied to the disc. The stresses may be tensile, compressive or shear. In general, stresses are difficult to measure, especially on the inside of a structure. Therefore mathematical models are often used for this purpose.

The loads to which the disc is subjected may be divided into two categories according to the duration: short duration high amplitude loads (eg. lifting) and long duration low magnitude loads due to normal physical activities. This division is important, because the disc exhibits time-dependent properties such as viscoelasticity characterized by load-rate sensitivity, hysteresis, creep, and relaxation.

Table 1. Measurements on the lumbar spine, motion segment or on their components

References	Year	In Vivo	Specimen / Property	Denucl.	Tension	Comp.	Flex.	Ext.	Bend.	Shear	Torsion
Hirsch	*1955*		Motion segment			√					
Brown et. al.	*1957*		Motion segment		√	√	√	√	√		
Galante	*1967*		Annulus material		√						
Markolf et. al.	*1974*		Motion segment	√		√					
Lin et. al.	*1978*		Motion segment			√	√	√	√	√	
Berkson et. al.	*1979*		Motion segment			√				√	
Schultz et. al.	*1979*		Motion segment			√	√	√	√		√
Tencer et. al.	*1982*		Motion segment			√	√	√	√	√	√
Adams et. al.	*1986*	√	Range of motion				√				
Adams et. al.	*1988*		Motion segment					√			
Ohshima et. al.	*1989*		Water diffusion pathway			√					
Seroussi et. al.	*1989*		Internal deformations	√		√	√	√			
Mc Nally	*1991*		Intradiscal pressure			√	√	√			
Adams et. al.	*1993*		Annulus material		√						
Adams et. al.	*1993*		Intradiscal pressure				√	√			
Holmes et. al.	*1993*		Motion segment			√					
Adams et. al.	*1994*		Motion segment				√				
Chiu et. al.	*1995*		Internal deformations			√					
Fennel et. al.	*1996*		Nucleus migration				√	√			
Krismer et. al.	*1996*		Motion segment								√
Mc Millan et. al.	*1996*		Intradiscal pressure			√	√				
Kaigle et. al.	*1997*	√	Porcine spine cyclic			√					
Tadano et. al.	*1997*		Motion segment	√	√	√	√	√			√
Iartridis et. al.	*1998*		Annulus material			√					
Malko et. al.	*1999*	√	Fluid content (MRI)			√					
Patwardhan et. al.	*1999*		Full lumbar spine			√					
Wilke et. al.	*1999*	√	Intradiscal pressure			√	√				
Meakin et. al.	*2000*		Motion segment	√		√					

The human spine and the intervertebral discs are subjected, according to another categorisation, to physiological and traumatic loads. Short duration high-level loads may cause irreparable structural damage or trauma of the intervertebral disc when a stress of higher value than the ultimate failure stress is generated at a given point. The mechanism of failure during long duration low level repetitive loading is due to fatigue failure. A tear develops at a point where the nominal stress is relatively high, and it eventually enlarges and results in a complete disc failure.

Biomechanical behaviour of the disc is dependent upon its state of degeneration, which in turn is age dependent.

Compression

This is the most common stress state of the intervertebral disc. The compressive load is transferred from one vertebral end plate to the other by way of the nucleus pulposus and the annulus fibrosus. In the early years of life the nucleus has sufficient water content to act like a gelatinous mass. As the load is applied, a pressure develops within the nucleus, which pushes the surrounding structures in all directions away from the nucleus centre. The compression load produces complex stresses within the annular ring. The compression test has been the most popular mechanical test for the study of the disc, probably because the disc is the major compression-carrying component of the spine. Many experiments have been done to determine the compressive properties of the disc.

The disc provides very little resistance at low loads. But as the load is increased, the disc becomes stiffer. Thus, it provides flexibility at low loads and stability at high loads. The first component to fail in a pair of adjacent vertebrae and a disc being subjected to high compressive loads is the vertebra, because of the fracture of the end plates. No failure of the disc ever took place. The mode of failure was solely dependent on the condition of the vertebral body. Osteoporotic vertebrae showed extensive collapse of the end plate and the underlying bone at relatively low loads. It was observed, that there were no differences between the vertebra with normal disc and the one with degenerated disc. [5] Experiments were conducted on lumbar spine specimens using discography [55] to demonstrate

the movements of the nucleus pulposus under compressive loading. With central compressive loading, the disc was observed to bulge in the horizontal plane, but not in any particular direction.

Tension

The disc is hardly ever subjected to tensile loads under normal physiological activities. Even under the application of traction to the spine, like as in weight bath traction therapy, the discs are under compression load due to muscle activities. However, the disc annulus is subject to tensile stresses in various physiologic conditions. In flexion, the instantaneous axes of rotation lie in the frontal and transverse plane and pass through the middle of the disc. [56] Thus, in flexion, the posterior part of the disc is subjected to tensile stresses. The opposite is true in extension. In lateral bending, the tensile stresses are produced on the convex side of the bend. A detailed computer simulation of the disc under tensile loading has not been carried out. Tensile tests are used to determine local material properties [7, 57, 58] like the annulus characteristics to positive strains. Finally compressive loading also produces tensile stresses within the annulus, however they are small in amplitude.

Bending

Bending and torsional loads are of particular interest, because experimental findings [59] suggest that pure compression load does not damage the disc. Bending of 6-8° in the sagittal, frontal, and other vertical planes did not result in failure of the lumbar disc. However, after removal of the posterior elements and load it by 15° of anterior flexion, failure did occur. [60] Other interesting findings concerned the bulging of the disc during normal physiologic motions. The disc bulged anteriorly during flexion, posterior during extension and toward the concativity of the spinal curve during lateral bending. [61, 62] According to the experimental data denucleation increases the bulging.

Shear, Torsion

Experiments on torsion of the disc provide important information regarding the torsional strength of the disc as an intact structure. Although the disc is

subjected to shear stresses during torsional loading, the stresses are not uniformly distributed. They are high along the periphery and low in the centre. [63] Therefore the torsional experiments do not provide precise information about the horizontal shear characteristics of the disc. When the disc is subjected to an axial torque, the stress distribution in the disc is dependent upon the degree of degeneration, and whether the posterior elements are intact. Some findings suggest, that the annulus fibres play a significant role reducing the torsional movements of the disc. [64]

3.3.3 Physical Properties of the Disc

Elastic Characteristics

The intervertebral disc has a viscoelastic structure. To determine its elastic properties, the mechanical tests must be done at slow loading rate so that the viscoelastic effects are minimized. The viscoelastic behaviour acts like a damper in the system causing longer calculation time at dynamic computer simulation increasing the time reaching the steady state. A proper description of the test should include information concerning the loading rate. Older studies unfortunately do not provide such data.

Viscoelastic Characteristics

The physical properties of a structure that document its time dependent behaviour are its viscoelastic characteristics. If we repeat the same experiment at faster loading speed, the load-displacement curves would be different. In fact, they would exhibit stiffer behaviour with increasing loading speed. Some work has been done on applying the finite deformation biphasic theory. This continuum theory assumes that the tissue is a mixture of an intrinsically incompressible and elastic solid phase and an inviscid fluid phase. [65]

Creep and Relaxation

The higher loads produced greater deformation and faster rates of creep. Creep characteristics [11] and disc grades of degeneration are related.

Nondegenerated discs creep slowly and reach their final deformation value after a considerable time, as compared with the degenerated discs. The process of degeneration makes the disc less viscoelastic. This implies that as the disc degenerates it loses the capability to attenuate shocks and to distribute the load uniformly over the entire end plate.

Hysteresis

All viscoelastic structures, including the disc, exhibit hysteresis. In this phenomenon there is a loss of energy when a structure is subjected to repetitive load [35] and unload cycles. Hysteresis varies with the load applied and the age of the disc as well as its level of degeneration. The larger the load, the greater the hysteresis. It is largest in very young people and smallest in the middle-aged. The lower thoracic and the upper lumbar discs showed less hysteresis than the lower lumbar discs. The hysteresis decreased when the same disc is loaded a second time. This may mean that we are less protected against repetitive loads. Epidemologic studies show that people who drove motor vehicles have a higher incidence of herniated discs. The repetitive axial vibration may be the factor.

Fatigue Tolerance

Fatigue tests [4, 66] of the discs are important for establishing the number of load cycles can be tolerated before radial and circumferential tears develop. Since the biologic capacity for repair and regeneration of the disc is thought to be low, its fatigue properties are important. Unfortunately very little is known about this subject. The disc showed signs of failure after only 200 cycles of bending, and it completely failed after 1000 cycles. This indicates that the fatigue life is low under such experimental conditions *in vitro*. The fatigue tolerance of the disc *in vivo* is not known.

Intradiscal Pressure

There are very few precise studies of the spine components *in vivo*. Most of the work is done on cadavre materials. Although these studies have provided large amounts of valuable information, the magnitude of the loads applied to the disc could not be measured *in vivo*. Nachemson *et. al.* [15, 16] determined for the first

time the actual loads to which a disc is subjected *in vitro*. They used the concept of nucleus pulposus as a load transducer. By means of *in vitro* experiments on vertebra-disc-vertebra preparations, they found that the fluid pressure within the nucleus is directly related to the axial compression applied to the disc.

The pressure was measured by a transducer in the form of a special needle carrying a miniature electronic pressure gauge at the tip. By measuring the pressure within the nucleus the load on the disc can be computed. The reported average intradiscal pressures related to different postures are 154 kPa in prone, 550 kPa in standing, and 700 kPa in sitting.

Wilke *et. al.* [49] recently measured the intradiscal pressure *in vivo* during standard daily activities with an improved pressure transducer. Some of the results have disputed Nachemson's assumptions. They measured pressures in some relaxed sitting position close to the values obtained at standing.

Disc Degeneration

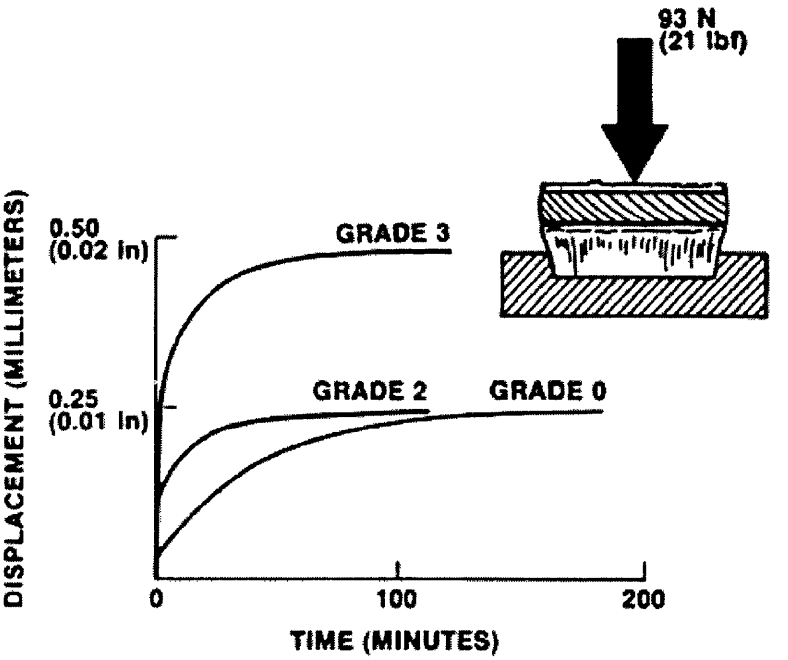

Fig. 13. Classification of discs based on their degeneration

Discography is used clinically to provide a qualitative description of disc degeneration. Nachemson suggested a classification method for disc degeneration

grading the disc between 0 and 3, where 0 is the non-degenerated disc and 3 is a disc with severe degeneration. [65]

Fluid Content

The fluid content of the disc material affects the mechanical properties of the intervertebral disc. [67] Using fresh cadaveric lumbar spine specimens investigators studied the mechanical properties of the disc before and after injection of fluid. [11] The discs of all the fluid retaining specimens became stiffer, while those that could not retain fluid showed, on average, no significant change in stiffness. Several studies were launched on understanding the water diffusion pathways. According to the latest theory water diffusion can occur through the endplates and through the annulus wall. Fig. 14. shows the simplified block diagram [68] of water diffusion pathways. Values of flow rate are in ml/h.

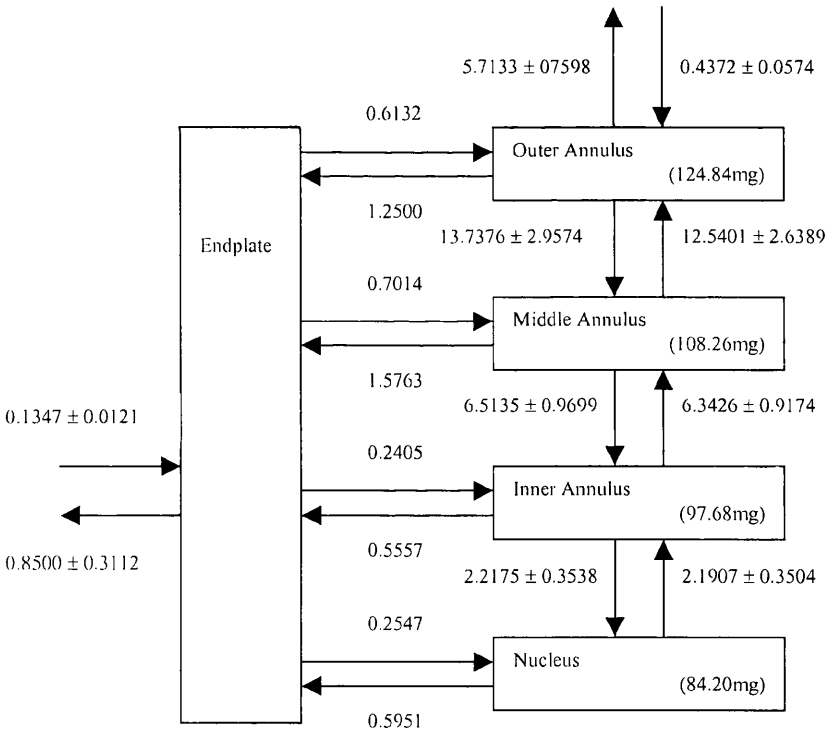

Fig. 14. Water diffusion pathways of the disc

One possible model for water diffusion in discs can be poroelasticity, which is widely used for modelling stems. [69] Only two-dimensional models are known, where the fluid flow is unidirectional. Currently LS-Dyna has no such material.

Disc Bulge

One of the mechanisms of nerve root irritation is thought to be the root impingement by disc bulge. This clinical interest has led to several *in vitro* studies that have carefully measured the disc bulge. In early studies, only compression load was applied, but in later studies, the effect of various other loads have also been measured along several directions. In most of these studies a fresh lumbar vertebra-disc-vertebra preparation with posterior elements removed [70] for observation was used. The specimen was subjected to one of the load cases and the bulge was observed by any of several methods: dial gauges, special transducers, and photographic methods. The largest disc bulge occurred in the mid-disc plane at compression. This value increased by up to more then two times in the case of degenerated discs. Considering that the space surrounding the intervertebral foramen is rather limited, especially in the degenerated spines with decreased disc height, the disc bulges may very well irritate the nerve root.

Internal Deformation of the Disc

Several attempts has been made to measure the internal deformations within the intervertebral disc. The most successful experimental work has been evaluated by placing metal beads [43] into the disc material. Radiographs were taken in different loading situations and the pictures were then digitalised for further analysis.

Mechanisms of Disc Prolapse

By using fresh cadaveric lumbar spine segments many attempts have been made to produce a disc prolapse [71] that is similar to that seen clinically. Compressive loading of the disc, at slow speed or at high speed, is known to result in fractures of the end plates and not in failure of the disc. This is true irrespective of the status of disc degeneration. Torsional loading of the disc beyond its

physiologic limits does result in circumferential tears in the annulus but does not result in disc prolapse. Simple flexion of the specimen generally result in tearing of the posterior ligaments or fractures of the laminae. Therefore, the experiments done are of significant clinical importance. For the first time disc prolapse was produced in a laboratory setting with the use of fresh cadaveric specimens. The disc prolapse was attempted by sudden load applications as well as by gradual loading.

Gradual Disc Prolapse

Since the majority of the low back pain patients with disc prolapse seen clinically do not report a traumatic event, an attempt was made to produce disc prolapse in the laboratory using slowly varying loads. One may conclude that the gradual disc prolapse is most likely not caused by the hyperflexion loading. It may be the result of combination of factors, such as weakened posterior disc annulus, relatively nondegenerated nucleus combined with relatively degenerated annulus with fissures, and another kind of loading.

Sudden Disc Prolapse

This form of disc prolapse is more likely occur at the lower lumbar levels. Sudden disc prolapse seems to be connected to the level of disc degeneration. According to the hypothesis the first stage of degeneration may result in some spinal dysfunction, but not instability. In the third stage, the spine is restabilised, probably because of ligament calcification and osteophytes. However in the second stage, which occurs between age 40 and 50 years, the disc degeneration has progressed to a point where the nucleus is still mobile. This is the instability stage. At this stage there is an increased risk of disc prolapse because of the traumatic overload of the spine.

Disc Function After Injury

After injury the compressive behaviour of the spine is not significantly altered by the injured disc, however most of the other three-dimensional properties are.

CHAPTER 4. – PROJECT DISCUSSION

4.1 The Work Done

The work to be presented is a 3-dimensional non-linear dynamic finite element (FE) analysis of the L2-L3 human lumbar intervertebral disc later denoted as Model 3 in Chapter 8. The FE-model includes characterisation of anisotropic material properties of the biomechanically relevant individual components of the disc. The novelty lay in modelling the disc microstructure with solid elements rather than as one-dimensional springs. Hence the components can interact with each other as well as exhibit responses to shear, torsion and bending.

The result is a model, which gives a much improved representation of all aspects of disc anisotropy and non-linearity. Therefore this model allows an accurate depiction of the mechanical response of an intervertebral disc under eccentric loading in addition to the simpler axial loading.

Furthermore an experimental stress analysis of intervertebral discs based on a large-scale model is also presented in Chapter 9. Construction and testing of a large-scale mechanical model of a typical intervertebral disc was carried out in order to predict and show the quantitative contribution of each component under a variety of loads and indicate the precise mode of failure.

Based on the above works analytical representation of some disc property and behaviour is also presented in Chapters 7 and 8, together with a novel approach to annulus characterisation in finite element solvers.

4.1.1 Milestones of the Work Done

- Installation and setup of the computer system/software.
- Literature research and data collection to obtain a detailed view about the structure, mechanical properties and mechanical response of the human lumbar intervertebral disc.
- Transfer and improvement of current intervertebral disc model of the research group from Ansys® to LS-Dyna3D®.

- FE model of L2-disc-L3 complex was created using LS-Dyna built-in materials.
- Research in methodology and know-how of implementing User Defined Material (UMAT) into LS-Dyna.
- DEC FORTRAN 77 programming language was studied as essential for UNIX programming.
- Test UMAT Hooke's law was written and tested.
- Numerical evaluation of some of the disc properties was undertaken.
- Improvements were made to the current mathematical description of the annulus.
- Highly non-linear, isotropic UMAT was coded and tested as disc annulus.
- User Defined Material (UMAT) was coded based on the developed material law above, it was tested and continuously improved.
- Large-scale experimental model of a vertebra-disc-vertebra joint was built and tested in the universal test machine to obtain a more detailed view of the significance of material property values on intervertebral disc behaviour.
- Non-linear, anisotropic UMAT was successfully implemented into the existing FE model of L2-L3 spine segment.
- FE model was remeshed using the latest capabilities of Altair Hypermesh® to reduce calculation time.
- CAD model of the lumbar spine was built including the L1-L6 five joint segments. Ligaments are added to the complex. The aim is to evaluate the final UMAT in a larger model.

4.1.2 Finite Element Analysis

Successful finite element analysis of complex structures with free surfaces requires powerful computational tools collaborating with each other. Throughout the project, the following software packages were essential:

Pro/Engineer®

AutoCAD®

Altair Hypermesh®

PC LS-Dyna3D®

Ls-Dyna for Digital Tru64 Unix

Oasys® for Digital Tru64 Unix with Primera, THIS, D3PLOT

Ansys®

MathCAD®

Fortran77 compiler for DEC Unix

C++ compiler for DEC Unix

Windows NT with MS Office

DEC Tru64 Unix 4.0F

C++

Zeus text editor

At the start of the project, not all of the above packages were available. The pre-processor and post-processor of LS-Dyna is currently under development. This means that parts of the necessary code can not be implemented by using the built-in options. These parts must be added to the file manually. To save time, this requires a specialised text-editor. Also, not all parts of the result file could be analysed with the post-processor. Especially at the beginning of the work, frequent C programming was needed to extract the necessary data. Luckily, by the end of 1999 the Oasys THIS postprocessor became powerful enough. However even the currently used Oasys8.1 has missing options in the Primera pre-processor.

The initial disc model of the Biomechanics Research Group in Ansys® includes the nucleus and annulus not separated, and assigned to one generalised non-linear material property obtained from the overall response of the disc to compression. The outside layer was modelled using linear spring elements. Vertebrae were modelled as rigid bodies.

The first LS-Dyna3D® model was improved by separating the annulus and nucleus. The model contains the nucleus as a fluid described by its Bulk modulus, and the annulus as a 3-dimensional non-linear orthotropic material. The bones are modelled as an elastic material. The outside shell consists of 2-dimensional non-linear orthotropic shell elements. The cortical and cancellous part of the vertebrae were separated, and different material properties were assigned.

The result was a working finite element model of an intervertebral disc which was evaluated successfully in terms of vertical displacement for axial and eccentric compression, to disc bulge for axial compression and lateral bending, to combined compression and shear test and intradiscal pressure for axial compression in the range of compressive forces 0-2000N and shear forces up to 440N. [72] This model already achieves the overall regressive disc response from the interaction of the individual disc structure and properties, such as the nucleus fluid contained by the annulus shell with progressive material characteristics, and the three-dimensional disc geometry.

These results were useful in evaluating the limits and weaknesses of the commonly used material laws. The novelty of the model lay in using solid and shell elements only, excluding the widely used non-linear springs.

4.1.3 Experimental Work

Parallel with this study an experimental model of the disc was built and tested [73] in the universal test machine, later described in Chapter 9. The basic idea was to construct a large-scale disc model recreating the major structural components. The objective was to have a better understanding of the behaviour of the intervertebral disc in compression. The materials used were tested and carefully selected based on their measured characteristics. The model has a rubber outside shell. The annulus is modelled by EPDM closed cell Neoprene (Ethylene Propylene Diene Terpolymer, Polychloroprene). EPDM Neoprene is widely used by the car industry for noise-absorption. Fluid with similar density and viscosity can represent the nucleus. The model has a pressure tapping to allow variation and measurement of the pressure inside the "nucleus". Several tests were done to investigate the significance of the individual properties on the behaviour of the disc under different conditions. Results of stress and strain have been obtained for axial and eccentric compression, which show excellent quantitative and qualitative agreement for the model as a whole with the latest data on human discs. More importantly, however, tests on incomplete versions illustrate the

contribution of each component and a failure test led to a physiologically accurate herniated disc. Images of the setup and assembly can be seen in Appendix 2.

From the results of the two models, and additional research on the possible analytical solutions for describing the disc annulus, several recommendations were made for improvements. From these, the final form of the annulus description was created, coded and tested as a UMAT. This description represents a non-linear, anisotropic material law. [74] According to the author's best knowledge this level of non-linearity is not available in any of the finite element solvers on the market. Furthermore, the unique form of description makes it possible to implement slightly different characteristics for tension and extension within a range. The material description and results of its implementation will be discussed later in Chapter 8. All models were evaluated against literature data, and the overall improvement on accuracy was proven based on modelling selected, well documented load cases of a sample with known geometry.

4.1.4 Resources and Model Generation

Generating an accurate CAD model of the human spine is a hard, time consuming task. Each vertebra is different, and the spinous processes interlock along complicated, free surfaces. Although the resolution of the model later highly depends on the mesh, the CAD model has to represent the geometric non-linearities as accurately as possible. Several methods exist to obtain the necessary geometric data, each has advantages and disadvantages. The most commonly used imaging techniques are X-Ray, Computer Tomography (CT), Magnetic Resonance Imaging (MRI) and Ultrasound. Unfortunately the image quality of these techniques is not very good when we are looking into both bones and soft-tissues. However, there is one existing male and female *in vitro* dataset called the Visible Human Project (VHP). The VHP database [75] provides actual size scans of one average male and female dataset. The Visible Human Project started in the United States several years ago. There was a 39 year old male criminal sentenced to death by lethal injection. He donated his body to the science. After death his body was filled with special liquid, was frozen and sliced to 1mm sections. Each

slice was scanned and the full-scale, true colour images are available on the internet.

The visible human dataset contains detailed sections about even the smallest parts of the human body. However, investigating the lumbar spine has brought up some new problems. The body was frozen in the lying position so all the muscles and ligaments are relaxed. The overall spine can be found in a different shape for a sitting or even a standing position, which are the most common postures in daily life. [76, 77, 78, 79, 80] This means that after obtaining the geometry of the elements of the spine, one has to modify the layout slightly based on other sources of *in vivo* imaging. The differences from the real life situation might be only some degrees of rotation or even less than a millimetres of displacement, but according to the computational tests done, this can affect the results by causing a significant difference. In Fig. 15. one example can be seen. Two load cases were studied. The disc was pressed by a force at the points shown. The difference in the stresses in Fig. 16. shows that the correspondent principal strain ε_z is significantly less when the disc is pressed at point 2 rather than at point 1. Point 2 is the geometrical centre point of the disc plane, but the actual centre point of stiffness is not here; it is somewhere close to point 1. Unfortunately the exact location of this centre point highly depends on the disc geometry, and as such is not easy to find.

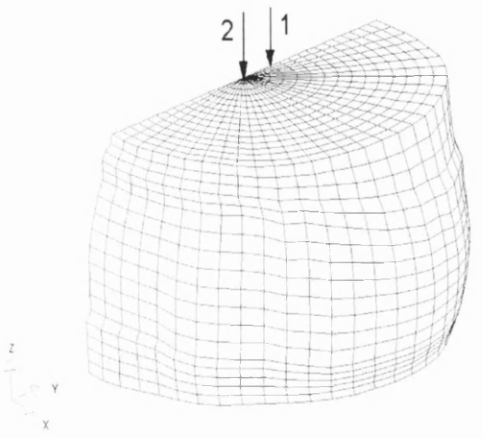

Fig. 15. Looking for the centre of the stiffness

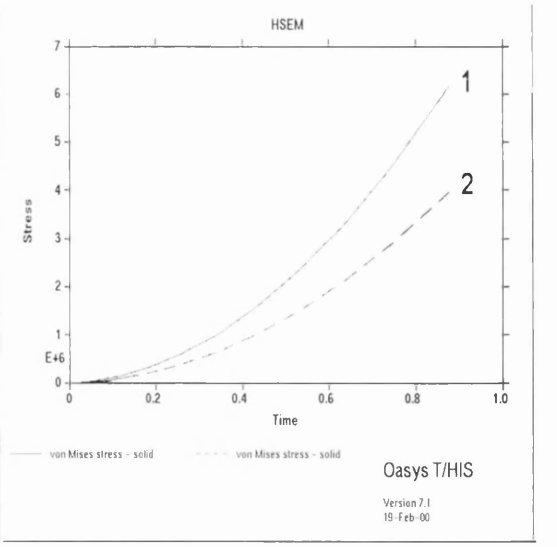

Fig. 16. Significance of the location of the loads

It is impossible to perform a numerical analysis of biomechanical motions without a knowledge of the materials used by nature. However up to the present date it remains very difficult to obtain accurate data describing the strength of biological materials. There are several difficulties in data collection, some are technical and others are moral. One of the biggest challenge in modelling the human spine is the intervertebral disc.

4.1.5 Aims of the Model Generation

Before the start of the model generation aims were set to determine the focus of the model development and ensure the quality which leads to the best possible solutions. These were,

- Reduce the number of elements
- Reduce the calculation time
- Increase accuracy on all levels
- Increase the complexity of the geometry
- Include all relevant anatomical parts

All of the points were successfully fulfilled.

CHAPTER 5. – FEA FOR NON-LINEAR, LARGE DEFORMATION PROBLEMS

5.1 Selection of solver and solution method, common techniques and their restrictions

Finite element analysis is an approximate analysis method, which is only as accurate as,

- the quality of the model
- the material properties used and their assumptions
- representation of the loads and boundary conditions
- the solution algorithm

5.1.1 Linear or non-linear load-extension behaviour

The origins of mechanics go back to early scientists such as Isaac Newton and Robert Hooke. Hooke discovered a simple linear relationship between force and deflection. This law is valid as long as the material remains linear elastic. Non-linearity appears in the cases, where the stress is no longer proportional to the strain.

In a uniaxial test involving pulling a rod of non-linear material in the longitudinal direction, the stretch ratio λ, is defined as the ratio of the deformed gauge length L, divided by the initial gauge length L_0.

$$\lambda = \frac{L}{L_0}$$

In large deformation analysis of elastomers, most non-linear FEA codes use a strain measure called the Green-Lagrangian strain E, which for uniaxial behaviour is defined as,

$$\mathrm{E} = \frac{1}{2}\left(\lambda^2 - 1\right)$$

and a corresponding work conjugate stress called the 2nd Piola-Kirchoff stress S_2,

$$S_2 = \frac{F}{A}\left(\frac{L_0}{L}\right)^2$$

Although the 2nd Piola-Kirchoff stress is useful for the mathematical material model, it has little physical significance and is difficult to use for the interpretation of results.

Therefore engineer resorts to either the Cauchy (true) stress σ,

$$\sigma = \frac{F}{A}$$

with energetically conjugate strain measure the logarithmic (true) strain ε,

$$\varepsilon = \ln \frac{L}{L_0}$$

or the familiar engineering (Biot) stress S_1,

$$S_1 = \frac{F}{A_0}$$

with energetically conjugate strain measure being engineering strain e, or deformation gradient f, in large deformation theory,

$$e = \frac{\Delta L}{L_0}$$

$$f = \frac{\partial x}{\partial X}$$

where x and X refer to the deformed and original coordinates of the body. For small strains, the differences between various measurements of stresses and strains are negligible.

5.1.2 Strain Energy Density

In the FEA of elastomers, material models are often characterised by different forms of their strain energy density functions. Such a material is also called hyperelastic. Implicit in the use of these functions, usually denoted by W, is the assumption that the material is isotropic and elastic. If we take the derivative of W with respect to the strain, we obtain the stress.

The commonly available strain energy functions have been represented either in terms of the strain invariants, which are functions of the stretch ratios or directly in terms of the stretch ratios themselves. Some of these functions are listed in Chapter 6. The three strain invariants can be expressed as,

$$I_1 = \lambda_1^2 + \lambda_2^2 + \lambda_3^2$$
$$I_2 = \lambda_1^2\lambda_2^2 + \lambda_2^2\lambda_3^2 + \lambda_3^2\lambda_1^2$$
$$I_3 = \lambda_1^2\lambda_2^2\lambda_3^2$$

In case of incompressible material, $I_3=1$.

5.1.3 Incompressible behaviour

Exact or total incompressibility literally means the material exhibits zero volumetric change (isochoric) under hydrostatic pressure. The third strain invariant is identically equal to one. The pressure in the material is not related to the strain in the material. It is an indeterminate quantity as far as the stress-strain relationship is concerned. Poisson's ratio is exactly 0.5, while the bulk modulus is infinite.

Analytical difficulties arise when incompressibility is combined with non-linearities such as large displacements, large strains, and contact. Near incompressibility means that Poisson's ratio is not exactly 0.5, but 0.49+. Perfect incompressibility is an idealisation to make modelling more amenable for obtaining closed form solutions. In the real world, natural materials are slightly compressible, thereby facilitating development of algorithms with greater numerical stability. Many materials are nearly incompressible in the non-linear range. In addition to rubber, the engineer may also encounter aspects of incompressibility in metal plasticity and fluid mechanics.

Incompressibility is one of the most troublesome areas in finite element analysis. Modern computational mechanics practice in the analysis of incompressible materials is to suppress the volumetric component of the strain field by appropriately selected variational principles.

A simple example shows below why incompressibility results in numerical problems. From the familiar elasticity relationship,

$$\frac{K}{G} = \frac{2(1+\upsilon)}{3(1-2\upsilon)}$$

where K is the bulk modulus, G is the shear modulus, ν is the Poisson's ratio.

For nearly incompressible materials, the Poisson's ratio approaches 0.5, and the bulk modulus becomes large relative to the shear modulus. In the limit, when the material is completely incompressible, ($\nu=0.5$), all hydrostatic deformation is precluded. In this limiting case, it is, therefore, not possible to determine the complete state of stress from strain only. This indeterminancy difficulty applies not only to isotropic materials, but also to orthotropic and anisotropic materials. Most materials are not completely incompressible, typical values of Poisson's ratio are in the range of 0.49 to 0.49999. It is important to note that the use of these values in finite element codes that have not been tailored for incompressibility analysis will lead to very serious numerical errors, caused by the ill-conditioning resulting from the division by a value which is nearly zero. More importantly, mesh locking may occur.

Whether a particular finite element code is suitable for analysing incompressible problems depends on the type of elements used and their formulation. For example, the standard low order quadrilateral isoparametric elements found in many FEA codes exhibit extremely poor performance in analysing incompressible problems and exhibit a pathological behaviour called mesh locking. Mesh locking refers to the inability of an element to perform accurately in an incompressible analysis, regardless of how refined the mesh is, due to an over-constrained condition and insufficient active degrees of freedom. Specifically, if a standard element is distorted into an hourglass mode, it will lock as the bulk modulus becomes infinite. The element will lock despite the fact that its area remains constant, resulting in the prediction of too small a displacement and too large a stress.

5.1.4 Viscoelasticity

Soft-tissue exhibits a rate-dependent behaviour and can be modelled as a viscoelastic material, with its properties depending on both temperature and time. When unloaded, it eventually returns to the original, undeformed state. When subjected to a constant stress, it creeps. When given a prescribed strain, the stress decreases with time; this phenomenon is called stress-relaxation. Hysteresis refers

to the different stress-strain relationship during unloading in such materials when the material is subjected to cyclic loading.

Linear viscoelasticity refers to a theory, which follows the linear superposition principle, where the relaxation rate is proportional to the instantaneous stress. Mechanical models are often used to discuss the viscoelastic behaviour of materials. The first is the Maxwell model, which consists of a spring and a viscous damper in series. The sudden application of a load induces an immediate deflection of the elastic spring, which is followed by a creep of the damper. On the other hand, sudden deformation produces an immediate reaction by the spring, which is followed by stress relaxation according to an exponential law. The second is the Kelvin-Voigt model, which consists of a spring and a damper in parallel. A sudden application of force produces no immediate deflection, because the damper will not move instantaneously. Instead, a deformation builds up gradually, while the spring assumes an increasing share of load. The damper displacement relaxes exponentially. A third model is the standard linear solid, which is a combination of a spring connected to a serial spring-damper in parallel. Its behaviour is a combination of the Maxwell and the Kelvin-Voigt models.

Non-linear viscoelastic behaviour may result when the strain is large. A finite strain viscoelastic model may be derived by generalising linear viscoelasticity in the sense that the 2nd Piola-Kirchoff stress is substituted for engineering stress, and the Green-Lagrange strain is used instead of engineering strain. The viscoelasticity can be both isotropic and anisotropic.

5.1.5 Linear or non-linear solution control

There are three major types of non-linearities,

- material non-linearity (plasticity, creep, viscoelasticity)
- geometric non-linearity (large deformations, large strains, buckling)
- boundary non-linearity (opening-closing gaps, contact, follower force)

The analysis is non- linear when,

The strain is no longer small

Most metallic materials are no longer useful when the strain exceeds one or two percent. However, some materials, notably rubbers, elastomers, and plastics, together with soft tissues, can be strained to hundreds of percent and will therefore require finite (large) strain analysis.

The strain-displacement relationship is no longer linear

This is true, if the rotations become large even though the strains are still small. The changes in the deformed shape can no longer be ignored. The physics of buckling, rubber analysis, metal forming, among others, requires that either a quadratic relationship exists between the strain and displacement (Green-Lagrange strain) or a logarithmic relationship exists (true strain). Engineering stress is no longer appropriate because of the geometric changes and the true stress (Cauchy-stress) should be used.

The stress-strain law may become non-linear

This behaviour is typical of soft-tissues, rubbers, elastomers, and certain composite materials whose properties are unequal in tension and compression.

The original equilibrium equations relating stress to loads may have to be updated

This can happen due to the geometrical changes in the shape of the structure. These relations mean that, in non-linear FEA, the load is no longer directly proportional to the displacement.

5.1.6 Implicit or Explicit

Implicit

An implicit operator solves a matrix system, one or more times per step, to advance the solution. It is appealing for a linear transient problem, because it allows a larger time step and has almost no numerical stability problems. Treatment of boundary non-linearities must occur within a step, and this fact along with the solution of large systems of equations make the coding more complicated than the explicit one. Some of the implicit operators have been shown to exhibit numerical damping problems, sensitivity to time step size, or stability problems, and the user must be extremely careful in their use.

Explicit

An explicit operator advances a solution without forming a stiffness matrix, a fact that makes the coding much simpler. For a given time step size, an explicit formulation requires fewer computations per time step than the implicit one. Complicated boundary conditions are handled easily, because non-linearities are handled after a step has been taken. The disadvantage of an explicit method is the existence of a definite stability limit, which means very small time steps are required and often, higher computer costs are incurred.

5.1.7 Solver and element type selection

The nature of the analysis of soft tissues, modelling highly non-linear, anisotropic, nearly incompressible materials exhibiting large deformation, requires a robust solver. In the analysis of intervertebral discs, all type of non-linearities are present. Therefore, an explicit solver was selected for the analysis. Due to the nearly incompressible properties, element types with hourglass control were chosen. 8-node solid elements with 1-point integration and hourglass control were used. Use of fully integrated solids was avoided because of the higher processing cost and their likelihood to suffer mesh locking. In the full spine model global viscous damping was introduced reducing hourglassing. Shell elements were

chosen with the Belytschko-Tsay formulation. Hughes-Liu beam elements with cross-section integration were used to model ligaments, with the cable option enabled.

The use of explicit solver technology has advantages for the calculation of large models with complex boundary conditions and large deformation theory. However, on the other hand, compromises have to be made on evaluating the results. Since no equilibrium criteria are satisfied the result can only be evaluated against a physical experiment. Therefore, the incorporation of experimental research is necessary for the success.

CHAPTER 6. – ANALYTICAL STUDIES AND THEORY

6.1 Non-linear Elasticity of Soft Tissues

Soft tissues are not elastic, because the stress depends on the strain and the strain history. However the hysteresis loop is only weakly dependent on strain rate. Therefore elasticity may be a suitable description for soft tissues if we use a different stress-strain relation for loading and unloading. This concept is called pseudoelasticity. Unlike in bone, linear elasticity [81, 82] is inappropriate for soft tissues. We need non-linear finite elasticity.

Conservation Energy

The rate of change of kinetic and internal energy in the region equals the rate at which mechanical work is done by the body forces and surface tractions acting on the region plus the rate at which heat enters the region across the surface.

Work done by external forces

Under isothermal conditions there are two types of forces acting on a continuous body, surface tractions acting on the boundary and body forces acting at every interior point of the body. During an incremental displacement Δu of the body, the incremental work ΔU done by external forces is given by

$$\Delta U = \int_{\Gamma} f_i \Delta u_i d\Gamma + \int_{\Omega} (\rho g)_i \Delta u_i d\Omega$$

Here f is the surface traction (force/area) acting at a point on the boundary Γ of the body Ω, g is the gravitational constant, and ρ is the material density.

Strain Energy

For an elastic body the work done by external forces equals the strain energy of the body.

$$U = \int_{\Omega} \tfrac{1}{2} C_{ijkl} \varepsilon_{ij} \varepsilon_{kl} d\Omega = \int_{\Omega} W d\Omega$$

U equals the total energy stored in the body. W is the strain energy density (strain energy/volume). The rate of work done by the stresses in the conservation

energy is given by the strain energy function. Its derivative with respect to the Cauchy strain is the stress. More detailed explanation of the formula can be seen in Appendix 3.

Principle of minimum potential energy

The potential energy V is defined by

$$V = \int_{\Omega} W d\Omega - \int_{\Gamma} f_i u_i d\Gamma - \int_{\Omega} (\rho g)_i u_i d\Omega$$

Of all displacements satisfying the given boundary conditions those which satisfy the equilibrium equations make the potential energy an absolute minimum and $dV=0$.

Hyperelasticity

For linear elastic, Hookean material there are two equivalent definitions:

$$T_{ij} = C_{ijkl}\varepsilon_{kl}$$

or

$$W = \tfrac{1}{2} C_{ijkl}\varepsilon_{ij}\varepsilon_{kl}$$

An elastic material has a stress-free natural state and a 1-to-1 relation between the stress tensor and the strain tensor. In a hyperelastic material the stress tensor is the derivative of the strain energy with respect to the strain tensor (measured with reference to the natural stress-free state). Hence, the stress is independent from the history of deformation.

$$\varepsilon_{ij} = \frac{\partial W}{\partial T_{ij}}$$

First Law of Thermodynamics

Rate of change of internal energy = Rate of change of heat absorbed + Rate of change of work done

Per unit mass:

$$dI = dQ + \tfrac{1}{\rho} dT_{ij} d\varepsilon_{ij}$$

Second Law of Thermodynamics

Rate of change of entropy = Rate of change of external energy + Rate of change of internal energy

$$ds = dS_e + dS_i$$

Elastic stress arises from an increase in internal energy I or a decrease in specific entropy S with respect to strain. The strain energy is either or both of these

$$T_{ij} = \rho\left[\frac{\partial I}{\partial \varepsilon_{ij}} - \frac{\theta \cdot \partial S}{\partial \varepsilon_{ij}}\right]_0$$

For an Isentropic, Isothermal Process

$dS=0$ and $d\Theta=0$

$$T_{ij} = \rho \frac{\partial I}{\partial \varepsilon_{ij}}|_{S,\theta}$$

In a perfect material the strain energy is equivalent to ρ times the internal energy.

Examples

Without full explanation there are some examples [83, 2] below for commonly used strain-energy functions:

2D-3D Orthotropic Exponential (on residual stress in arteries)

$$W = \tfrac{1}{2} C e^{Q}$$

2D Orthotropic Logarithmic (uniform strain hypothesis for arterial mechanics)

$$W = -C \ln(1 - Q)$$

Isotropic

$W = W(I_1, I_2, I_3)$ where I_1, I_2, I_3 are the principal invariants of C

like Hooke's law

$$W = \tfrac{1}{2}\left[\lambda(\delta_{ij}\delta_{kl}) + 2\mu(\delta_{ik}\delta_{jl} + \delta_{il}\delta_{jk})\right]\varepsilon_{ij}\varepsilon_{kl}$$

Mooney-Rivlin rubber

$$W = C_1(I_1 - 3) + C_2(I_2 - 3)$$

For skin and myocardium

$$W = C_1(e^{\alpha(I_1-3)} - 1) + C_2(I_2 - 3)$$

Ogden's Power Law for muscles, synthetic biomer and latex rubber

$$W = C\sum_{i=1}^{3}(\lambda_i^{\alpha} - 1)$$

Blatz-Ko rubber

$$W = C\sum_{i=1}^{3}(e^{\lambda_i^{\alpha}-1} - 1)$$

Anisotropic laws are used in 2D to model skin, blood vessels or pericardium. Transversely isotropic laws are used for the myocardium. Polynomial representation forms are also known for modelling stretched fibres.

Soft tissue has non-linear material properties. Because the strain rate effects are modest soft tissues can be approximated as elastic. For isotropic materials the strain energy is a function of the principal invariants, transverse isotropy or orthotropy introduce additional invariants. For incompressible materials an additional pressure enters. Usually biological soft tissues are considered to possess the properties of an incompressible and hyperelastic material.

6.2 Fluids

Fluids are shapeless. [84] In more technical terms we say that fluids do not resist being sheared. When a force is applied to a fluid, the pressure increases, but whereas the force is directional, the pressure is omnidirectional. The

omnidirectionality of pressure is equivalent to conservation of energy, the energy density (pressure) is constant throughout the fluid. Fluids are usually viscous. While they do not resist shear, they do resist changes in the rate of change of shear. The more viscous a fluid, the greater its resistance to changes in the rate of shear. Fluids flowing past a solid surface obey the no slip condition. That is the velocity of the fluid at the solid surface is zero. Since the velocity of the fluid is non-zero elsewhere, the no slip condition implies that a velocity gradient exists in the flowing fluid. In a pipe or blood vessel, the velocity profile across the diameter is essentially parabolic.

$$v = \frac{dP(r^2 - z^2)}{4lh}$$

where dP is the pressure difference between the head (upstream) and the tail (downstream) ends of the pipe, r is the radius of the pipe, z is the position along the diameter from the centre, l is the length of the pipe and h is the viscosity of the fluid. For a cross section of the pipe the velocity gradient has a circular symmetry. Fluids are often subject to turbulence. Smooth flow is called laminar. The flow is turbulent when eddies and vortices occur. Fluids lose energy through dissipation at both types of flow.

6.3 Soft Tissues as Structural Components

In contrast to engineering materials, biological tissues are not very well behaved, in the sense of being easily described in closed form mathematical expressions, because they are time and moisture dependent. When living, they are metabolically active and exhibit certain mechanical properties, which change soon after death. Moreover these mechanical properties may be age, strain rate and strain range dependent. To simplify the characterization of tissue when the loading is short enough in duration the viscous nature of the material can be ignored and the tissue can be assumed to behave elastically. This means that the state of the tissue only depends on the current loading, there is no effect from the previous loading. By idealizing the tissue as an elastic material, the task of

describing its behaviour is reduced to a matrix of 81 stiffness constants that must be specified. Since obtaining these constants is a very challenging task, additional assumptions are often made to reduce the complexity of describing the tissue behaviour. It is important to recognise the assumptions that are often used to create a simple mathematical model of a tissue system. Tissue has a hierarchical structure and by choosing the scale or size of the tissue samples being studied it is often possible to assume that the tissue is orthotropic, so the number of constants is reduced to 27. Then, by further restricting the scale of the sample so that the small structures in the system are randomly and uniformly distributed in the sample, the assumption of homogeneity is usefully employed so that only 12 constants are needed to describe the tissue. Again, if the scale of the tissue is picked with care, it may be appropriate to approximate the tissue as an isotropic material so that only two constants are needed to describe the tissue's response to mechanical loads. These two constants are the Lamé constants, or their technical derivatives, the Young's modulus and the Poisson's ratio. The elastic properties of soft tissues depend on their molecular building blocks, and on the microscopic and macroscopic structural organisation of these blocks. The standard medical practice of the soft-tissue palpation is based on qualitative assessment of the low-frequency stiffness of tissue. Pathological changes are generally known to be correlated with changes in tissue stiffness as well.

Over the past 20 years there have been numerous investigations conducted to characterize the mechanical properties of biological tissue systems, which have been idealized often as homogenous, isotropic, elastic materials. Much of the work has focused on bone, dental materials and vascular tissue. There are articles [51] that discuss methods used to characterize these tissues and there is large volume of experimental data about the mechanical response of these tissues to various types of loading. However there is a void in the retrievable literature regarding the mechanical properties of tissue systems tested *in vivo*. In fact, there is very limited information about the mechanical properties of most of the tissue systems that make up the body's organs. In measurement of tissues the majority of the information is related to uniaxial tensile tests of the tissue. [85, 86] The stiffness parameter can not be measured directly. Tissue elasticity measurement

methods fall into two categories, methods where a quasi-static compression is applied to the tissue and the resulting components of the strain tensor are eliminated and methods where vibration is applied to the tissue and the resulting tissue behaviour is inspected.

Another limitation of the present study is the large variation in the available experimental data for the annulus.

6.4 Assumptions about Fibrous Tissues

Incorrect assumptions, which are incorporated into mathematical models, have the potential to influence the model output. Given that output from spinal models is often used to assess ergonomic issues such as safe loads, validation of the assumptions is essential. However, a mathematical model is only as good as the data and assumptions used within it. In most of the engineering cases we assume that the body is homogenous with no differences in material properties between any two points. Characteristics dependent on time such as viscosity, creep and relaxation were neglected because they become significant only if the tissue undergoes accelerations greater than those in a quasi-static state.

6.4.1 Theory of Fibres

In a fibrous tissue most of the fibres are aligned in parallel with each other while a small amount of fibres are intermeshed. The stress can be written [87] as

$$\sigma = k_s \varepsilon , \qquad 0 \le \varepsilon \le \varepsilon_s$$

$$\sigma = k_e (\varepsilon - \varepsilon_s) + k_s \varepsilon_s , \qquad \varepsilon_s \le \varepsilon$$

where k_s is the modulus while a fibril is crimped, k_e is the modulus after the fibril becomes straight and ε_s is the strain at which the fibril becomes straight.

Based on the theory, we suppose that these fibres can be grouped to n groups by fibre length and each group of fibres becomes straight at a different strain level. In this case the theoretical stress-strain curve can be approached by a

multilinear characteristics shown in Fig. 17. If $n=3$, and $\gamma_1, \gamma_2, \gamma_3$ are the fibril lengths ($\gamma_1 + \gamma_2 + \gamma_3 = 1$) which become straight at the strain levels $\varepsilon_1, \varepsilon_2, \varepsilon_3$ ($\varepsilon_1 \le \varepsilon_2 \le \varepsilon_3$) then

$$\sigma_0 = k_s\varepsilon$$

$$\sigma_1 = k_s\varepsilon_1 + k_e(\varepsilon - \varepsilon_1)$$

$$\sigma_2 = k_s\varepsilon_2 + k_e(\varepsilon - \varepsilon_2)$$

$$\sigma_3 = k_s\varepsilon_3 + k_e(\varepsilon - \varepsilon_3)$$

therefore

$$\sigma = k_s\varepsilon \qquad 0 \le \varepsilon \le \varepsilon_1$$

$$= [k_s + \gamma_1(k_e - k_s)]\varepsilon - (k_e - k_s)\gamma_1\varepsilon_1 \qquad \varepsilon_1 \le \varepsilon \le \varepsilon_2$$

$$= [k_s + (\gamma_1 + \gamma_2)(k_e - k_s)]\varepsilon - (k_e - k_s)(\gamma_1\varepsilon_1 + \gamma_2\varepsilon_2) \qquad \varepsilon_2 \le \varepsilon \le \varepsilon_3$$

$$= k_e\varepsilon - (k_e - k_s)(\gamma_1\varepsilon_1 + \gamma_2\varepsilon_2 + \gamma_3\varepsilon_3) \qquad \varepsilon_3 \le \varepsilon$$

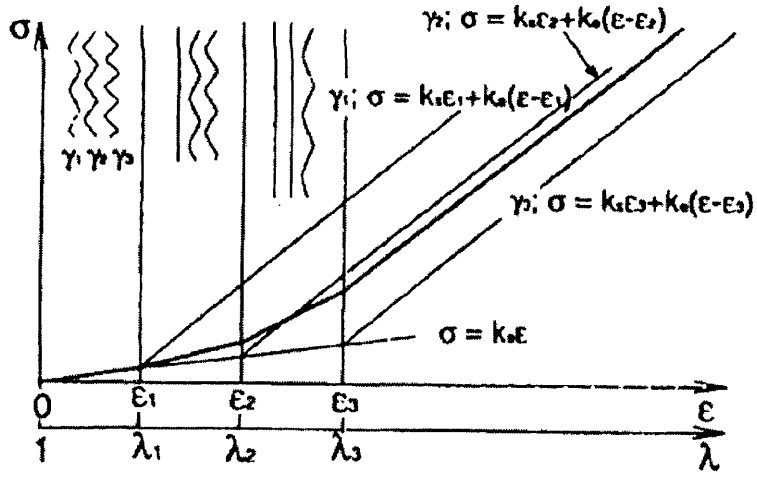

Fig. 17. Multilinear approach of fibrils with three fibre groups

The main disadvantages of the method described above are that the function is not continuous and at high values of n the approach becomes extremely difficult to work with.

6.4.2 Radial Inhomogeneity of the Annulus

According to the relation of Sonnerup [8] obtained on the basis of Galante's [7] experimental results, the annulus inhomogenity is taken into account by varying the Young's modulus in the radial direction $E_l(r)$,

$$E_l(r) = \frac{0.3E_l(r_0)}{1 - 0.7\frac{r}{r_0}}$$

where r is the radial coordinate and r_0 is the outer radius of the disc.

6.4.3 Nucleus-Annulus Volume Ratio

It is quite difficult to determine the exact area ratio occupied by the annulus fibrosus and the nucleus pulposus since they have an ill-defined mixed boundary. Belytschko *et. al.* [10] recommended to set the outer radius of the nucleus pulposus to be 0.707 times the outer radius of the disc based on previous studies.

6.4.4 Green's Theory on Fibre Density

The mean length of reinforcing fibres can be calculated for the simplified case of a planar sheet [58] in which all the fibres are orientated at α to the horizontal plane shown in Fig. 18.

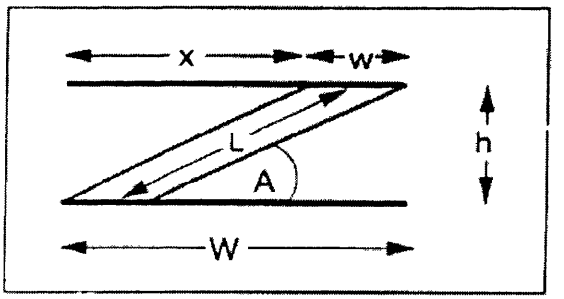

Fig. 18. Planar representation of fibre orientation

$$L = h / \sin\alpha$$

$$x = h / \tan\alpha$$

The proportion of intact fibres P is given by

$$P = w/(W+x) = (W-x)(W+x) = (W\tan\alpha - h)/(W\tan\alpha + h)$$

The proportion of non-intact fibres is *(1-P)*. Their average length is *L/2* because their length decreases from L to zero at either end of the specimen. Therefore the main fibre length is given by

$$L_m = PL + (1-P)L/2 = (P+1)L/2 = Wh/(W\sin\alpha + h\cos\alpha)$$

6.4.5 Material with Two-family Extensive Fibres

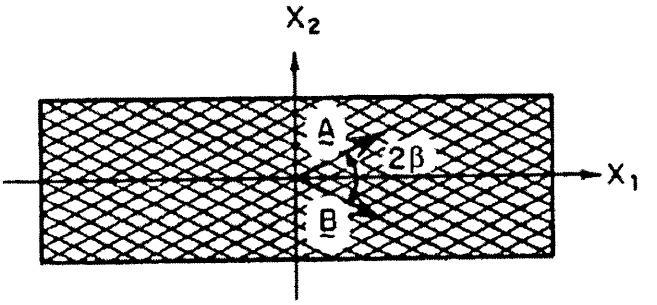

Fig. 19. Orthotropic material with two-family extensive fibres

The annulus fibrosus now, is considered to be a block of incompressible material [12], which is reinforced by two families of straight, parallel, extensive fibres and in which the fibres are densely distributed. Fig. 19. shows the fibre alignment. The fibres in the two families are inclined at an angle of 2β to each other. The x_1 and x_2 axes are chosen to be in the plane of the two families and to bisect the angles between the fibres of different families. The x_3 axis is normal to the x_1-x_2 plane. It is assumed that the plane of the fibres remains plane during the deformation. The two unit vectors defining the initial fibre orientations are given in the present case by,

$$A = (\cos\beta, \sin\beta, 0)$$

$$B = (\cos\beta, -\sin\beta, 0)$$

For simple tension the deformation is described by,

$$x_1 = \lambda_1 x_1$$

$$x_2 = \lambda_2 x_2$$

$$x_3 = \lambda_3 x_3$$

where λ_1, λ_2, λ_3 are extension ratios. Since fibres are extensible,

$$\lambda^2 = \lambda_1^2 \cos^2 \beta + \lambda_2^2 \sin^2 \beta$$

where λ is the extension ratio in the direction of the fibre. Since the deformation is homogenous, the fibres in either family remain parallel and straight after deformation. Assuming incompressibility, $\lambda_1 + \lambda_2 + \lambda_3 = 1$. The cauchy stress is,

$$\sigma = \frac{F}{A} = \frac{F}{A_0}\frac{1}{\lambda_2\lambda_3} = \lambda_1 \frac{F}{A_0} = \lambda_1 \sigma_0$$

Here F is the applied load, A_0 and A are respectively the initial and current cross-sectional areas of the specimen, and σ_0 is the nominal stress. The ratio of current volume V to the initial volume V_0 is given by,

$$\frac{V}{V_0} = \lambda_1\lambda_2\lambda_3$$

6.4.6 Hukins' Theory of the Annulus Internal Stress State

The annulus is modelled as thick cylindrical shell [88] of internal radius of r_i and external radius of r_e. It is considered to enclose the nucleus, which exerts an isotropic, constant pressure P. The stress distribution then has axial symmetry with a radial component, $s_r(r)$, which is compressive and a tangential component, $s_t(r)$, which is tensile. If these components are in balance with the internal pressure, their values are,

$$s_r(r) = \frac{r_i^2 P\left[1 - \left(\frac{r_e}{r}\right)^2\right]}{r_e^2 - r_i^2}$$

$$s_t(r) = \frac{r_i^2 P\left[1 + \left(\frac{r_e}{r}\right)^2\right]}{r_e^2 - r_i^2}$$

where r is the cylindrical polar radius and $r_i \leq r \leq r_e$

6.4.7 Brinckmann's Theory of Disc Bulge

A simple mechanical model was constructed [89] as shown on Fig. 20. to describe the relation between the disc bulge and intradiscal pressure on the mass of excised tissue. A disc of cross-section A, circumference B, and height H is loaded by a force F. Due to the pressure p, the membrane with a wall thickness of d bulges outward, its shape is approximated by a circle of radius R. The membrane inserts with an angle θ at the end plate of the vertebral body. The average fibre length is L. Tensile stress σ is present in the membrane only in the longitudinal direction. Hoop stress and bending stiffness of the membrane are neglected in this model.

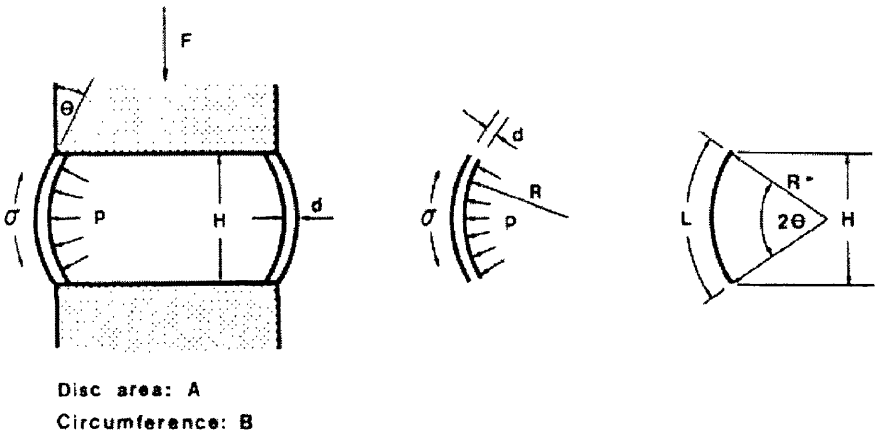

Fig. 20. Schematics of the model

Equilibrium forces in the plane of the vertebral body yields,

$$F = Ap - Bd\sigma\cos\theta$$

where

$$p = \sigma\frac{d}{R}$$

and

$$L = R2\theta$$

therefore

$$p = \frac{\frac{F}{A}}{(1-\frac{B}{A})\frac{L}{2\theta}\cos\theta}$$

CHAPTER 7. – STRESS STATE OF THE DISC ANNULUS, AN ANALYTICAL STUDY

7.1 *Analytical Study of the Relation Between the Disc Bulge and Vertical Displacement, the Stress-state of the Outside Annulus Rim, and the Effect of Volume (Fluid Content) Change*

From a clinical point of view the disc bulge is a very important measure of the disc state since the herniated disc bulging outwards can cause acute low back pain or even paralyse the patient by pressing on the sensitive nerves running in the spinal canal. Although the intervertebral disc has been studied thoroughly, there is still very little known about the internal stress-state of the annulus fibrosus containing the nucleus, even though any localised weakness of the annulus material or excessive stress concentration could result in failure of the disc material.

Despite many measurements having been carried out on the changing circumference of the disc under a variety of loading conditions, the available data on the clinical background of the disc hernia is limited. It is widely accepted that inappropriate lifting of heavy objects increases the risk of a herniated disc. Statistics show that occurrence of disc bulge increases with age and also in osteoporotic, injured or degenerated vertebrae. Acute disc hernia mainly occurs in the lumbar spine but has also been observed in the cervical region. The connection between the amplitude of loading and the displacement of the top vertebra in any pair of vertebrae has been studied thoroughly and so it is relatively easy to obtain Here, an analytical study [90, 91, 92] of the disc bulge is evaluated to gain more knowledge on the interaction between the top vertebra displacement and the magnitude of the disc bulge. From the results some suggestions also could be obtained on the stress state of the outside layer of the annulus and on the effect of fluid loss.

Five different simplified models denoted as Model A, B, C, D, E are presented in Fig. 21, 22, 23, 24, 25 respectively and the results have been compared with literature data.

Model A: The disc is represented as a simple cylinder. After compression its shape stays as a cylinder with reduced height and increased diameter.

Model B: The disc is represented as an ellipsoid. Throughout compression its shape stays as an ellipsoid with the small axis getting shorter and the other axis longer assuming volume constancy.

Model C: The disc is represented initially as a part of a sphere. The sagittal cross-section of the outer annulus boundary stays as an arc of a circle with changing radius during compression. The arc length of the boundary is considered to be constant.

Model D: The disc is represented initially as a part of a sphere. The sagittal cross-section of the outer annulus boundary stays as an arc of a circle with changing radius during compression. The disc volume is considered to be constant.

Model E: The disc is represented initially as a part of a sphere. When compressed, the disc boundary becomes part of a parabola. The disc volume and the arc length of the sagittal cross-section of the outer annulus boundary are assumed to be constant.

All models are symmetric and the direction of the top plate displacement is along the x-axis. The bulge magnitude is measured on the y-axis. The schematics show the sagittal cross-section rotated by 90°.

Nomenclature:

V_0	initial volume of the disc model
V_1	volume of the disc model after deformation
i_0	initial arc length of the sagittal cross-section of the outer annulus boundary
i_1	arc length of the sagittal cross-section after deformation
R	initial radius of the sagittal cross-section of the outer disc annulus (where the representation is an ellipse, R is the major axis)
r	radius of the small circle representing the sagittal cross-section of the outer disc annulus after deformation
m	half disc height
Δh	half of the top vertebra displacement
B	displacement of the outer disc boundary on the y-axis

Δh	magnitude of the bulge
α, β, α', α''	angles as represented in the figures
s, w, c, a	as represented in the figures

$$V_0 = V_1$$

$$V_0 = \pi(R^2 \cos^2 \alpha)\Delta h$$

$$V_1 = \pi \int_{-m+\frac{\Delta h}{2}}^{m-\frac{\Delta h}{2}} B^2 dx - \pi \int_{-m+\frac{\Delta h}{2}}^{m-\frac{\Delta h}{2}} R^2 \cos^2 x dx$$

where

$$\sin\alpha = \frac{m}{R}$$

$$\Delta h = B - R\cos\alpha$$

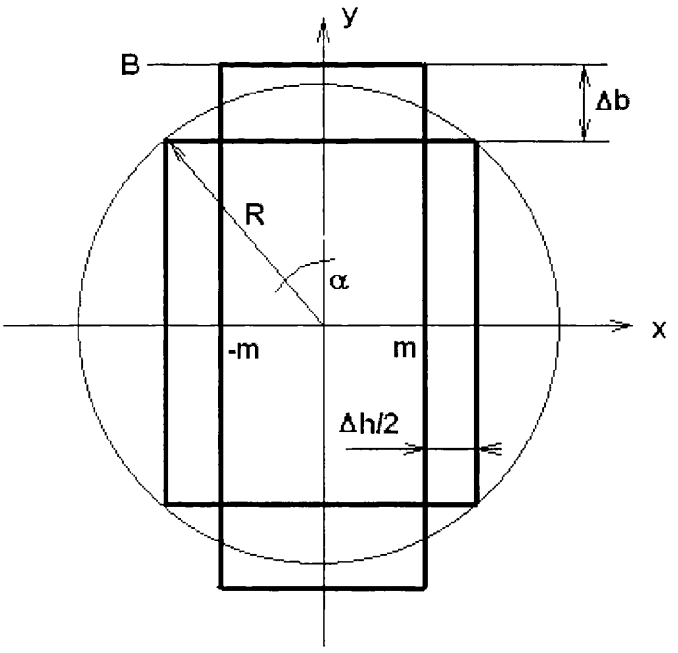

Fig. 21. Model A – Simplified model on disc bulge, volume constancy

$$V_0 = V_1$$

$$V_0 = \pi R^2 \int_{-m}^{m} dx - \pi \frac{R^2}{m^2} \int_{-m}^{m} x^2 dx$$

$$V_1 = \pi B^2 \int_{-m+\frac{\Delta h}{2}}^{m-\frac{\Delta h}{2}} dx - \pi \frac{B^2}{(m-\frac{\Delta h}{2})^2} \int_{-m+\frac{\Delta h}{2}}^{m-\frac{\Delta h}{2}} x^2 dx$$

where

$$\frac{x^2}{m^2} + \frac{y^2}{R^2} = 1 \rightarrow y^2$$

$$\Delta b = B - R$$

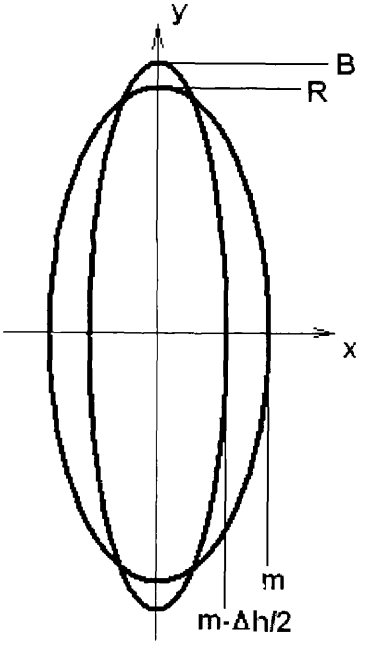

Fig. 22. Model B – Simplified model on disc bulge, representation with ellipsoids

$$i_0 = i_1 = 2r\beta = 2R\alpha = 2R\arcsin\frac{m}{R}$$

$$\sin\beta = \frac{m - \frac{\Delta h}{2}}{r} \Rightarrow \beta\frac{m - \frac{\Delta h}{2}}{\sin\beta} = R\alpha$$

where

$$x^2 + y^2 = R^2$$

$$\sin\alpha = \frac{m}{R}$$

$$s = r\cos\beta$$

$$w = R\cos\alpha - s$$

$$B = w + r$$

$$\Delta b = B - R$$

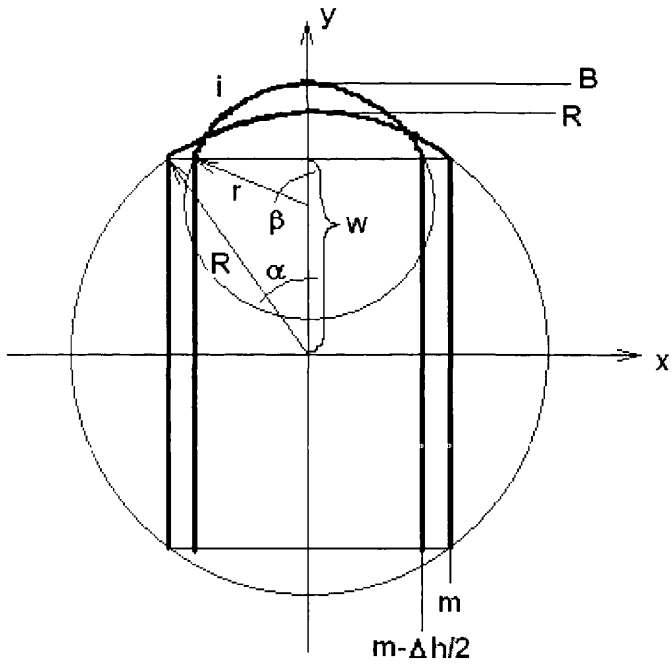

Fig. 23. Model C – Simplified model on disc bulge, arc length constancy

$$V_0 = V_1$$

$$V_0 = \pi \int_0^m \left(R^2 - x^2\right) dx$$

$$y^2 = r^2 - x^2$$

$$y = f(x) = \sqrt{r^2 - x^2} + B - r$$

$$V_1 = \pi \int_0^{m-\frac{\Delta h}{2}} f^2(x) dx$$

cosine rule

$$r^2 = (B-r)^2 + c^2 - 2(B-r)c\cos\alpha'$$

$$\left(\frac{h}{2}\right)^2 = R^2 + c^2 - 2Rc\cos\alpha''$$

iterating with given B and obtaining c, r then Δb.

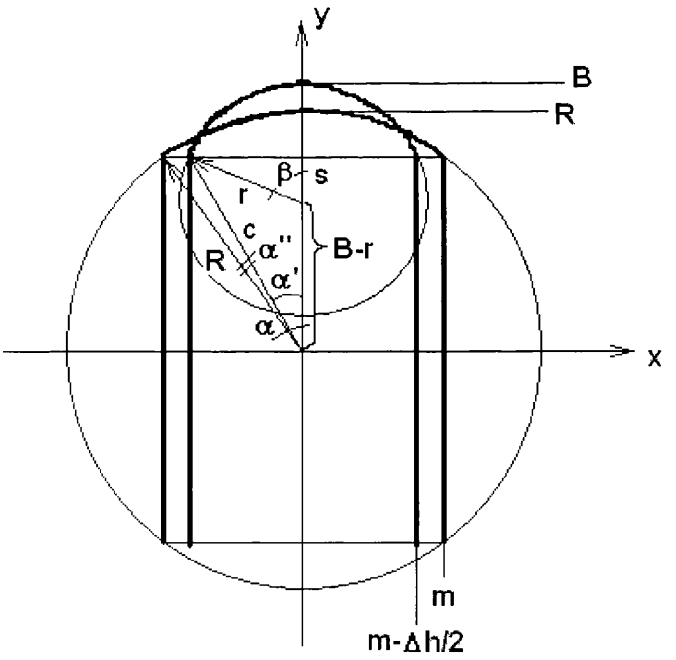

Fig. 24. Model D – Simplified model on disc bulge, representation with spheres

$$V_0 = V_1$$

$$i_0 = i_1$$

$$V_0 = 2\pi \int_0^m (R^2 - x^2)dx$$

$$V_1 = 2\pi \int_0^{m-\frac{\Delta h}{2}} (B - ax^2)^2 dx$$

$$i_0 = 2R\alpha$$

$$i_1 = \int_0^{m-\frac{\Delta h}{2}} \sqrt{1 + 4a^2x^2}\, dx$$

where

$$y = f(x) = B - ax^2$$

iterating with given B and obtaining a then Δb.

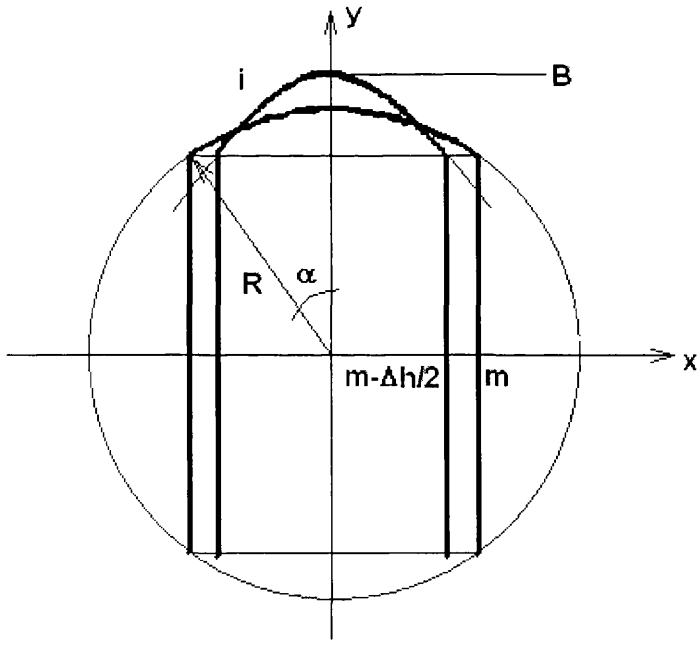

Fig. 25. Model E – Simplified model on disc bulge, volume and arc length constancy

Results and Discussion

Model A

$$\Delta b = R\cos\alpha\left[\sqrt{\frac{2m}{2m-\Delta h}}-1\right]$$

Model B

$$\Delta b = R\left[\sqrt{\frac{2m}{2m-\Delta h}}-1\right]$$

Model C

$$\Delta b = R\left[\alpha\frac{1-\cos\beta}{\beta}+\cos\alpha-1\right]$$

where

$$\frac{\sin\beta}{\beta}=\frac{m-\frac{\Delta h}{2}}{\alpha-R}$$

$$\alpha = \arcsin\frac{m}{R} \qquad (rad)$$

Model D

For model D no closed form solution was found. The result is obtained with iterative calculations.

Model E

For model E no closed form solution was found. The result is obtained with iterative calculations.

The magnitude of the bulge was calculated for a disc with dimensions R=20mm, m=6mm. The results of the calculations are shown in Fig. 26 and are compared with the experimental data of Lin *et al* [13] and Shah *et al* [93].

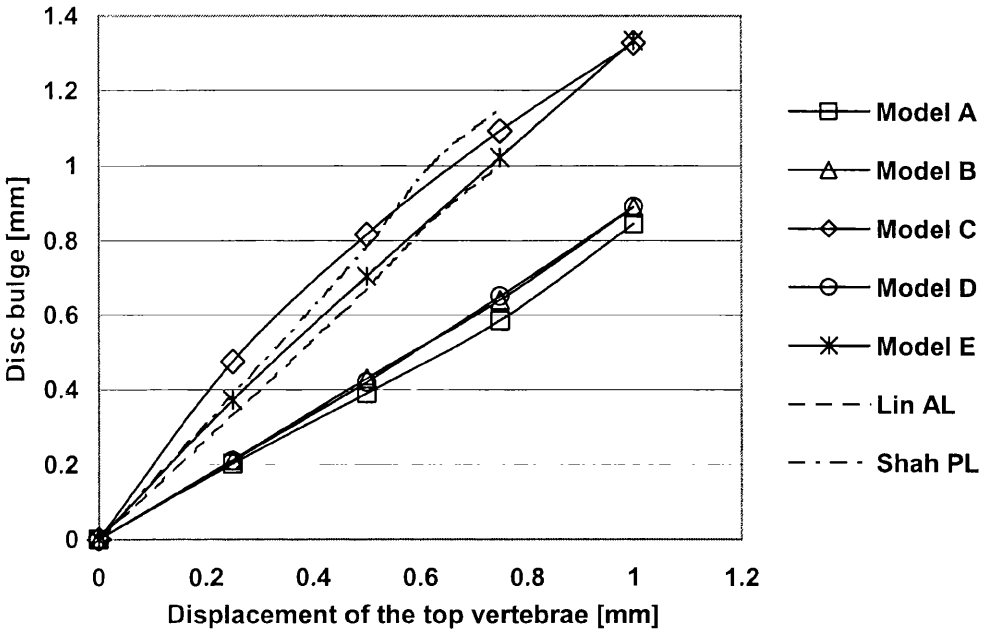

Fig. 26. Analytical approach to prediction of disc bulge magnitude in compression

Values of disc bulge in compression vary quite significantly in the literature. This makes the evaluation of any studies very difficult. The data differ with the location where the bulge was measured on the disc boundary, and also with the loading conditions, the presence of disc degeneration and the individual geometry. Here two sets of experimental data are included for comparison, one from Lin *et. al.* [13] where measurements were taken at the anterior and lateral side of the disc, then averaged, and one from Shah *et. al.* [93] measured at the posterolateral location where the disc bulge is reported to be the maximum. It can be seen that the calculated values of Model E, where both the volume and the arc length constancy were taken into consideration, give the best agreement with the experimental values. Calculation with volume constancy resulted in smaller values than the experiments, while arc length constancy gave larger values. The experimental curves show a slightly regressive characteristic at higher loads. The characteristic of the model based on volume constancy is progressive while the characteristic of the model based on arc length constancy is regressive. Model C shows that calculations based on arc length constancy agree fairly well with

experiment at low loads. The regressive curve of Model C and the experimental data intersect when the top vertebra displacement is 0.6mm. This displacement occurs if the healthy disc is subjected to a compressive force equivalent to around 880N, suggesting that the outside boundary of the annulus is under small compression if the load is below this level. Exceeding the 880N value will result in the annulus material being subjected to small tensile forces. Unfortunately there are limited amount of data existing in the literature [32] concerning the above issue. Tests were done at 500N and 2000N compressive loads only. The intradiscal pressure characteristics at 500N load, revealed by stress profilometry show small positive pressure on the outside disc boundary. The characteristics at 2000N load record no positive pressure at the outside 1 mm of the disc annulus. Surprisingly, the results for the analytical model that assumes volume constancy stay far below the measured data. This shows that the disc volume, together with the fluid content, plays a secondary role in directly governing the disc bulge.

The results correspond to measurements of the pressure inside the disc, where the pressure diagram shows no stresses at the outside disc boundary. Assuming very small stresses at the annulus rim, and taken together with the finite element findings described later in the next chapter which suggest that the annulus does not take part actively in the vertical load bearing of the disc, the results show that the role of the annulus structure is to fully damp the effects of a changing pressure within the nucleus and thereby safely contain its fluid. Disc hernia can develop where the annulus material locally fails to satisfy this condition due to excessive stress concentration or weakened material properties in one point causing gradual or sudden disc prolapse. Finite element results suggest that the non-linear disc geometry can be one of the causes of local stress concentration within the disc annulus. This study gives an analytical estimation of the expected disc bulge for compressed discs and this can be used for direct comparison to evaluate the level of disc hernia.

It is relatively hard to draw a parallelism between the above models and previous studies. Similar work, according to the author's best knowledge has never been done before and represents a very novel point of view.

CHAPTER 8. – FINITE ELEMENT MODELS OF THE L2-L3 MOTION SEGMENT

In this chapter, after some discussion on the FEM relevant properties of the disc nucleus and the annulus, four geometrically identical FE models of the L2-L3 lumbar motion segment denoted as Model 0, 1, 2, and 3 are presented. The results are compared to each other and also to one selected set of experimental data to which the model geometry complies. Model 3 contains the material law, which forms the base of the PhD study together with the experimental model and other findings already presented and to be presented in this thesis. The model generation process is described in details later in Chapter 10. Further information about the model can be found in Appendix 6.

8.1 The Nucleus Pulposus

The work was started with the nucleus, as the most well defined structure. Some early studies described the nucleus as standard, nearly incompressible elastic material, choosing a Poisson's ratio close to 0.5. Several recent works using ABAQUS as solver have used its inviscid incompressible fluid material. [9, 20] LS-Dyna has a very good material definition of contained fluid [2] for two-dimensional problems, but this material has severe boundary condition problems at three-dimensional models. The nucleus material behaves as a pressurized fluid inside the annulus shell, and thus it is like a water-filled balloon. Finally, the nucleus was modelled as a Newtonian fluid, described by its Bulk modulus, K, where p is the pressure rate, and ε is the strain.

$$K = \frac{E}{3(1-2\nu)}$$

$$p = -K\varepsilon_{ii}$$

8.2 The Annulus Fibrosus

The second stage was to identify the material properties of the annulus. The most important component of the intervertebral disc, from a structural perspective, is the annulus fibrosus since it bears most of the loads. As well as simple weight bearing, it also deforms in response to the differential compressive, tensile and shear forces generated during spinal movement. Its composition is that of a fibrous collagen matrix embedded within an aqueous gel of proteoglycans and other proteins. The highly oriented and layered structure of the annulus suggests that its material behaviour will be significantly non-linear and anisotropic.

8.2.1 Characterisation of the Disc Annulus

Based on previous measurements of the disc it is possible to determine the Young's modulus in each point of the annulus fibrosus. Sonnerup [8] investigated the radial nonlinearity in the material properties of the annulus, which resulted in the following function

$$E_L(r) = \frac{0.3 \cdot E_L(r_0)}{1 - 0.7 \cdot \frac{r}{r_0}}$$

where

r	radial coordinate
r_0	outer disc radius
E_L	Young's modulus

The intervertebral disc also has fluctuation in strength circumferentially. Studies of Brown *et. al.* [5] on two samples show that the anterior and posterior strength of the annulus is much higher than the lateral side of the disc as shown in Fig. 27. This inhomogenity of the disc annulus can be easily modelled by simply applying a cosine function.

Let's assume a 100% healthy disc with symmetrical layout of strength. At this point it is also useful to switch to a cylindrical coordinate system. Adding the two functions together,

$$E_L(r,\varphi) = \frac{0.3 \cdot E_L(r_0)}{1 - 0.7 \cdot \frac{r}{r_0}} \cdot |\cos\varphi|$$

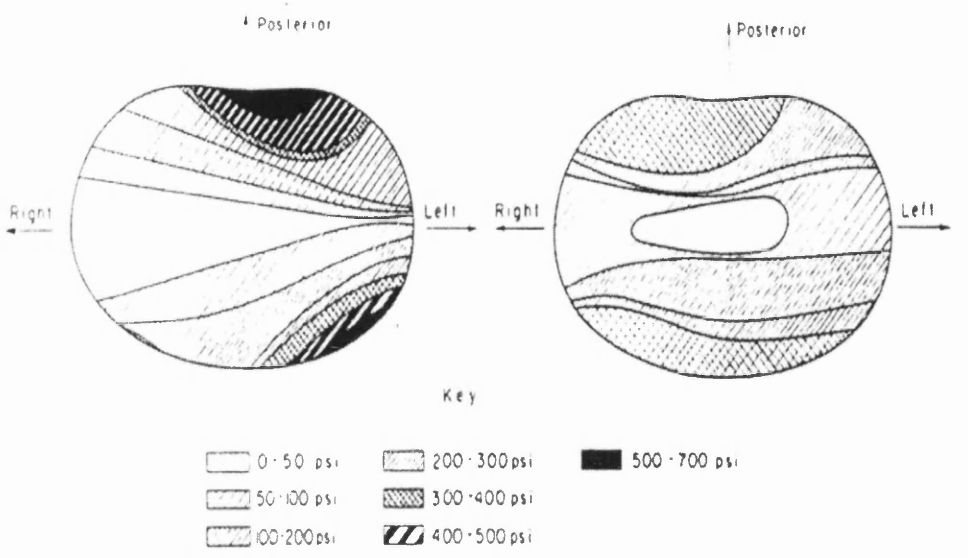

Fig. 27. Map of the average strength of the disc material

Fig.28. shows the above function in an orthogonal coordinate system. The MathCAD source code can be seen in Appendix 4. Please note, that the exact location of the origin of the coordinate system is still under investigation due to none of the previously used methods in the literature giving a satisfactory solution. The A-P direction is along the two highest values of the function.

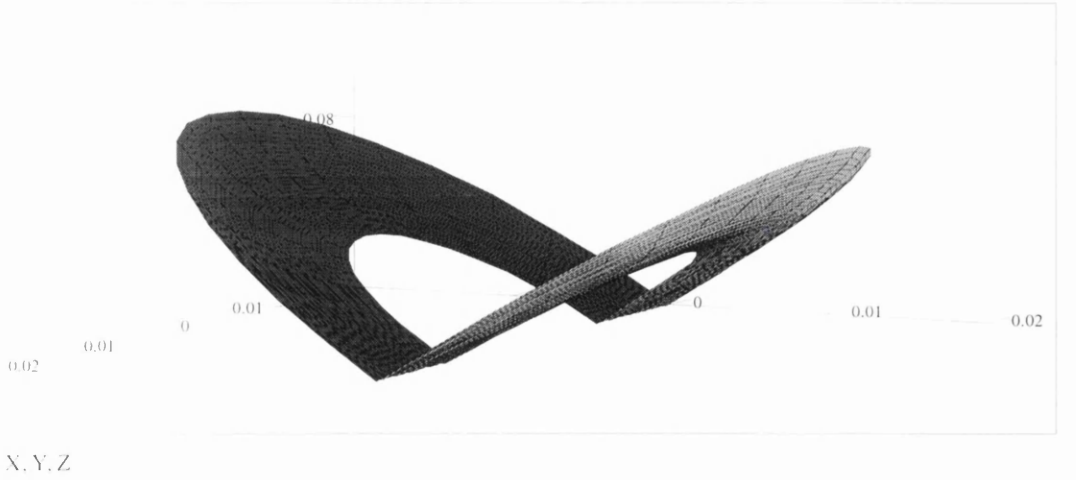

Fig. 28. Variation of the vertical Young's modulus in the annulus

However, it is known that it should be close to the centre of the nucleus pulposus. Most of the studies select the point where if the disc is pressed it responds with the maximum overall resistance against compression. [13]

The static material properties and the characteristics of the annulus fibrosus were also investigated. Although fatigue, failure and ageing of the disc were not considered in this study. The aim here was to determine the time history of the annulus characteristics in one point of the disc if we know the maximum possible Young's modulus $E_{\max} = E_L(r,\varphi)$ in that place.

A calculation method is presented below to obtain the fitting curve [90] from known coordinate points of one characteristic. A best fitting approach in a form of a third-order equation can be obtained by:

$$F(a,b,c) = a \cdot x^3 + b \cdot x^2 + c \cdot x$$

$$F(a,b,c) = \sum_{k=0}^{N} \left[y_k - x_k \cdot \left(a \cdot x_k^2 + b \cdot x_k + c \right) \right]$$

$$\frac{\partial F}{\partial a} = 0$$

$$\frac{\partial F}{\partial b} = 0$$

$$\frac{\partial F}{\partial c} = 0 \cdots\cdots \rightarrow a,b,c$$

Approaching Adams *et. al.* [57] and Galante's [7] measurements with the smoothest fitting curve,

$$E(\varepsilon) = -783.846\varepsilon^3 + 88.665\varepsilon^2 - 55.626\varepsilon$$

The objective is to implement this function into the finite element software. The detailed solution of the above function with the original coordinates can be seen in a form of MathCAD source based on the data of *Adams et. al.* [57] in Appendix 5. Further implementation of the above rules, which is the objective of this study, is described later as Model 3.

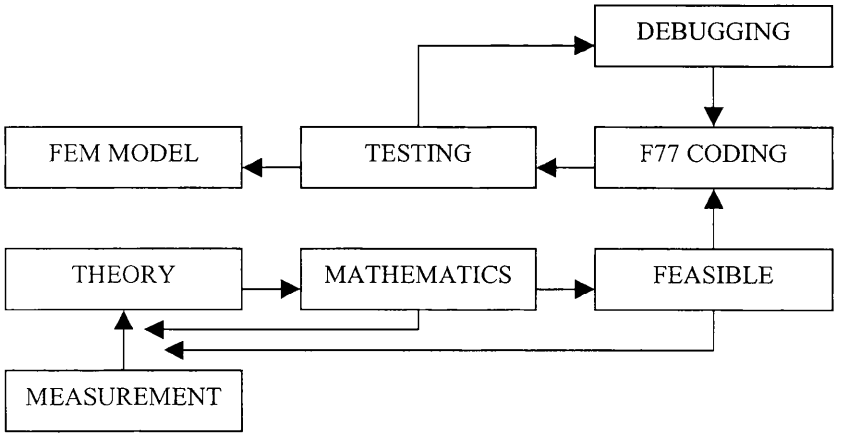

Fig. 29. Implementation process of material laws to FEM solver

Fig. 29. shows a block diagram of the process for implementing material laws specifically to LS-Dyna3D®. The aim to describe non-linear, anisotropic, and inhomogeneous materials in finite element solvers initiated a chain of problems that make the task very hard to solve. First of all, finite element software packages are unable to receive coordinate system dependent material properties. To do this, one has to define manually as many different materials as element groups the model has with different material properties. For a big model it is impossible to assign all these properties, not only because it is not time-effective, but also there are restrictions in the software. The only choice is simplification. However with simplification, as a side effect of making the end-user's job easier the task has to be broken into smaller pieces. This will again produce a major obstacle to programming and result in longer, time consuming preparation and calculation.

8.3 Model 0 – Non-linear Orthotropic Elastic-Plastic FEM

This model was the initial model. It is denoted as Model 0, because no novel approaches have been introduced in this model. However important information was gained on the behaviour of the FEM solver. Throughout the model generation, built in material properties from LS-Dyna3D [2] were used to represent the material properties. The aim was to build a model, which contains brick and shell elements only, thus reducing the total calculation time despite the more sophisticated material laws, because of the relatively low number of elements. The model contains the nucleus pulposus in the middle represented as fluid described by its bulk modulus and the annulus fibrosus as an orthotropic third order non-linear elastic material. Furthermore, the cancellous and the cortical bone are both represented as linear elastic with different Young's modulus and Poisson's ratio [93] as can be seen on Fig. 30. Table 2. contains further information about the materials used. The non-linear function of the annulus input curve given in Table 2. for certain components was approached by eight line segments. The initial value was taken from the slope of the stress-strain relation at $\varepsilon=0$. The shear modulus was calculated as: $G = \frac{E}{2(1+\nu)}$.

The model does not contain the posterior elements of the vertebrae. Experimental data of Lin *et. al.* [13] on a motion segment subjected to compression with and without the posterior elements suggests that the role played by the posterior elements in compression are not important compared to other loading modes, like torsion, where a second load path exists at the facets.

The model also does not contain the cartilaginous end plates as individual structural element. However, preliminary test results on the FE model revealed, that simulating the bone as rigid body increases the pressure within the elements significantly under the same loading conditions. Several studies reported the bulging of the bony end plates as the result of the high nucleus pressure. This process seems to be important on eliminating stress concentrations with the help

of a small volume change. In the model this process is allowed with giving a different, much weaker material property to the cancellous core.

Table 2. Material properties of the components of Model 0

Material	Elastic coefficients	Constitutive relation	Nomenclature
Cortical bone	E=12000MPa υ=0.3	elastic	E, Young's modulus υ, Poisson's ratio
Cancellous bone	E=100MPa υ=0.2	elastic	σ, Stress ε, Strain
Annulus solid	$\sigma(\varepsilon)=5.081\varepsilon^3-1.048\varepsilon^2+0.822\varepsilon$ $\sigma(\varepsilon)_{cyl,max}$=100MPa $\sigma(\varepsilon)_{vert,max}$=173MPa υ=0.45 $\sigma(\varepsilon)_{rad,max}$=100MPa ε_{max}=1.5 $G(\varepsilon)_{max}$=8MPa	nonlinear orthotropic elastic-plastic	G, Shear modulus K, Bulk modulus
Annulus shell	$\sigma(\varepsilon)=5.081\varepsilon^3-1.048\varepsilon^2+0.822\varepsilon$ $\sigma(\varepsilon)_{cyl,max}$=100MPa $\sigma(\varepsilon)_{vert,max}$=173MPa υ=0.45 $G(\varepsilon)_{cyl,max}$=8MPa ε_{max}=1.5 $G(\varepsilon)_{vert,max}$=8MPa E_{rad}=100MPa G_{rad}=8MPa	nonlinear orthotropic elastic	**Subscripts** cyl, cylindrical direction vert, vertical direction rad, radial direction max, maximum value
Nucleus	K=2.5MPa	fluid mechanics	

The main differences of this model compared to the next ones to be presented are,

- Different source for obtaining the annulus characteristics
- Characteristics are the same for tension and compression, with $\sigma(\varepsilon)$ mirrored to the origin of the σ-ε orthogonal coordinate system
- Annulus is represented as an elastic-plastic foam
- Annulus outside shell exists as an orthotropic, elastic material.

For further information about the model please refer to Appendix 6.

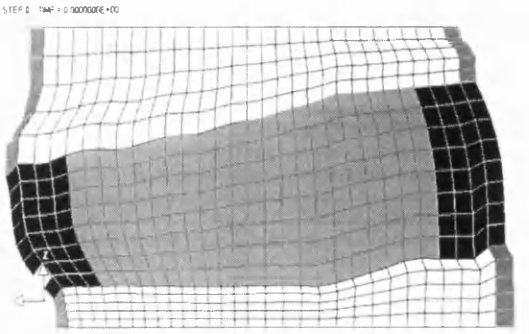

Fig. 30. Cross-section of the model

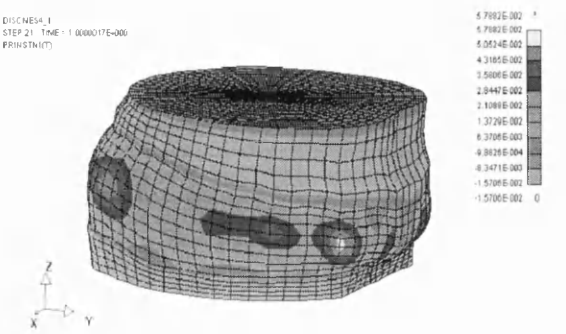

Fig. 31. Principal strains at the annulus surface

In Fig. 31. the overall response of the model can be seen when subjected to compression. A magnified picture of this result is available in Appendix 7. The colours show the principal strain of the outside surface of the annulus fibrosus. The highest strain occurs at the dark areas, which are the most critical points where the disc might fail. This result fits to the medical data perfectly. The disc bulge can be seen nicely too. The y-axis points to the posterior direction, the x to the left lateral and the z to the direction of the head, upwards.

Published results

In the next section mostly the graphs of published results [72] can be found. For further information about the work, please refer to Appendix 6.

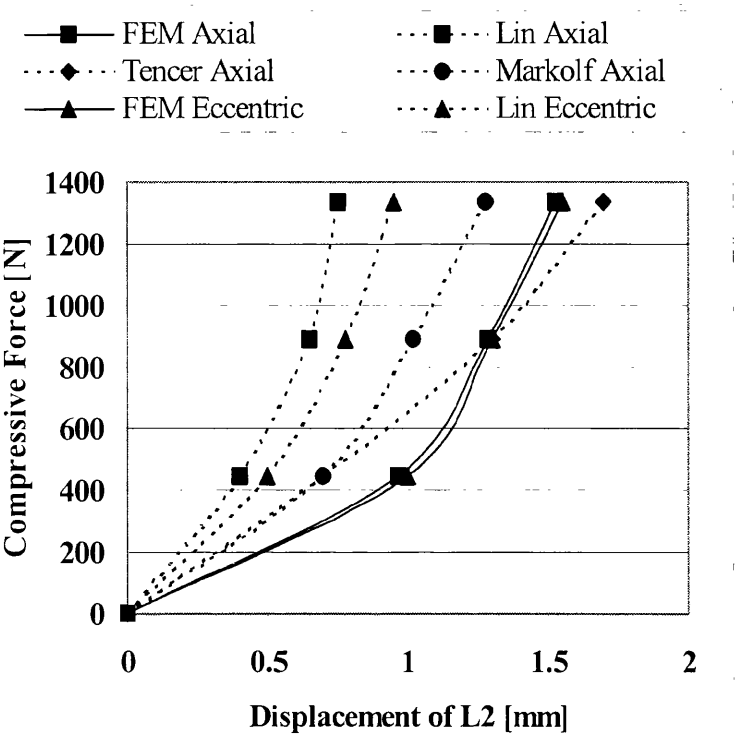

Fig. 32. Vertical displacement for axial and eccentric compression

On Fig. 32. the vertical displacement of the L2 vertebra can be seen for axial and eccentric compression. In this particular case the eccentric compression was flexion. The result is compared to several *in vitro* studies. It can be seen that the simulation follows the overall experimental characteristics, although at low loads the displacement is bigger. Because of the high deviation of the different measurements the model was tested for disc bulge as well.

On Fig. 33. it can be seen that the simulated disc bulge fits the measurements quite accurately in axial compression. The difference in the disc bulge at lateral bending is not significant and is mostly caused by the non-linear geometry. Due to the disc bulge was not measured on the selected sample by Lin et. al. [13], 4 different discs are compared to the FEM results. As it can be seen the literature data gives a wide range of results, therefore direct comparision is not possible. Evaluating the three-dimensional movements of the intervertebral disc model shows a successful approach in terms of disc bulge for lateral bending when the disc is bent sideways on Fig. 34.

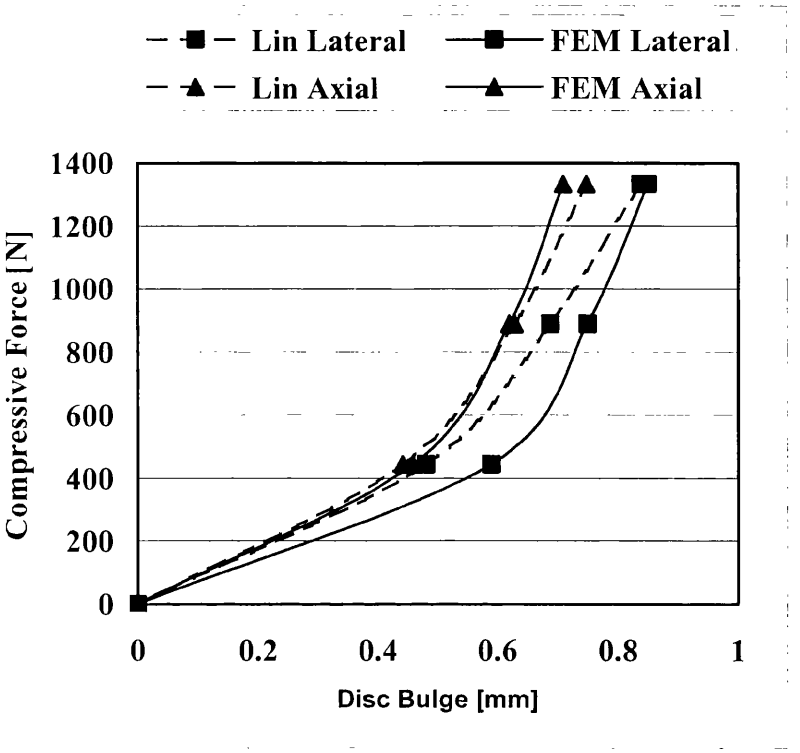

Fig. 33. Disc bulge for axial compression

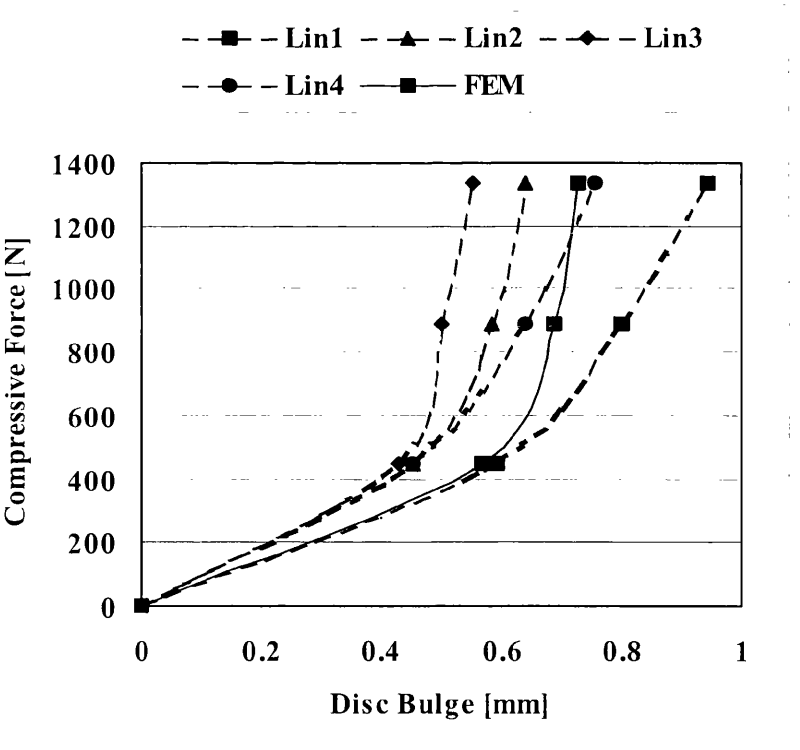

Fig. 34. Disc bulge for lateral bending

The reader might ask the question, how can these values be accepted as good, when sometimes significant differences can be seen. In the field of biomechanics engineers always have to deal with false measurement methods and lack of measured engineering data. The International Society of Biomechanics (ISB) in 1995, [45] initiated standardisation of reporting kinematic data but it has failed to deliver success and received many criticisms from the members. Sometimes the accepted data can have a deviation of 100%. In such conditions predicting a similar characteristics is a promising result. In some cases if the result approaches the expected value within a 10% range, it can be accepted as satisfactory. Currently the aim is to reduce the scatter and discrepancy of the results below 2%. In the future with more developed and standardised measurement techniques and technology researchers will be able to eliminate the uncertainties and increase the accuracy. But until that time biomechanical engineering remains a young, promising era of science where scientists are researching the unknown and unexplored with the methods, tools and technology they currently possess, and working on a new breakthrough in material science and non-linear mechanics.

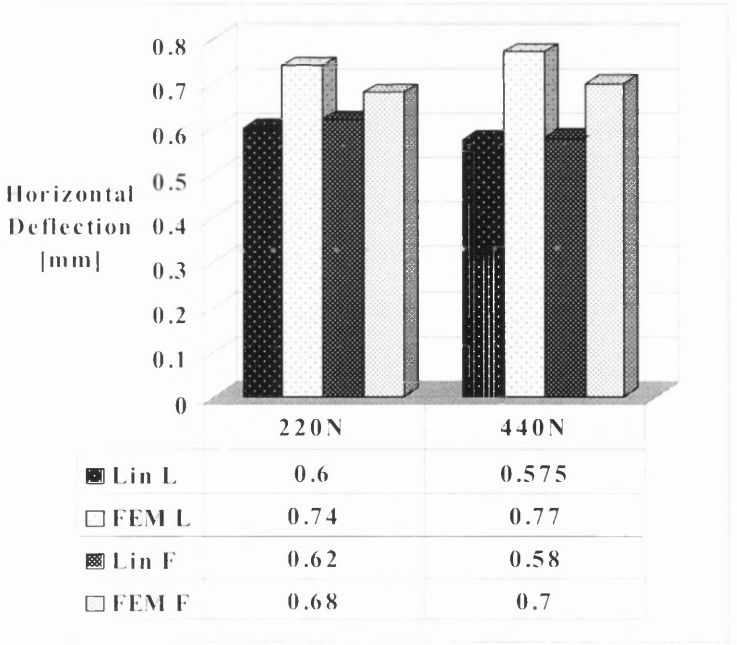

Fig. 35. Combined compression and shear test

On Fig. 35. the result of the combined compression and shear test following *Lin et. al.* [13], Chapter 2. can be seen. The shear response of the model shows a weaker correlation.

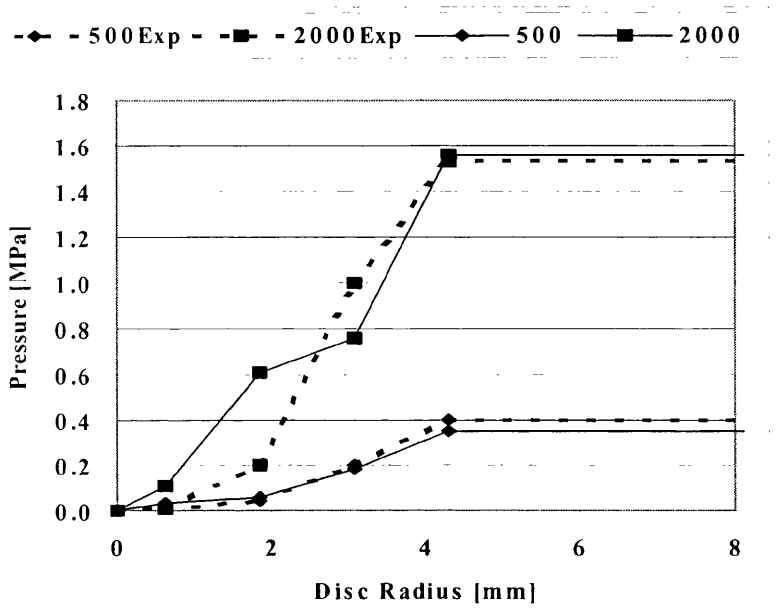

Fig. 36. Intradiscal pressure for axial compression

The final test was to examine the material behaviour of the annulus fibrosus through the pressure developing inside the disc at compression. On Fig. 36. it can be seen that the element data fits the measured values quite well.

Conclusion

A three-dimensional finite element model of the L2-disc-L3 unit was built containing only solids and shells. The fibre-composite properties of the annulus fibrosus were implemented using material orthotropy. All material properties are highly non-linear with a multilinear approach of 8 line segments. Validation of the model by comparison of its response with literature data reflects excellent matching in terms of vertical displacement, disc bulge and intradiscal pressure. The overall validation results of the disc model confirm that this is a promising approach to full computational simulation of human intervertebral discs. However, although the response of the model is reasonably good, there is a need

to reduce the difference between the experimental data and the finite element results, increasing the reliability of the FEM data. Based on this requirement the investigation continued and finally led to Model 3.

8.4 Model 1 and 2 – A Multilinear Approach

Model 1 and 2 are actually two models with the same geometry and mesh as Model 3. The material definition is also identical in Model 1 and 2, but the approach is different. As the results on Model 1 and 2 are directly compared with the results obtained for Model 3, further details of the models can be found in the next section.

8.5 Model 3 – Non-linear, Anisotropic, User-defined Material, a Material Property Sensitivity Study

8.5.1 Introduction

Current mathematical material laws work quite accurately with conventional engineering materials because these materials are linear and isotropic. These laws are much less effective, however, at representing living tissues. Biomechanical engineers therefore often face the problems of modelling material non-linearities, particularly with the soft tissues, muscles and tendons of the human body. The non-linear and often anisotropic structure of these materials makes any mathematical representation very difficult. In particular, the lack of a good general mathematical model of the intervertebral disc has hampered the study of spinal mechanics, as the disc annulus is a non-linear fibrous tissue with highly directional properties. Previous studies have concentrated on the overall behaviour of discs and this has been largely explained but knowledge is still very limited on the effect of the individual disc components. This means that current mathematical models are poor when it comes to describing a prolapsed disc where there has been failure of at least one of the components. This finite element study

described here focuses on the disc annulus properties and their effect on disc behaviour. The novelty of this study lay in the material formulation of the annulus fibrosus, which changes its Young's modulus according to a non-linear curve. The results have led to some important conclusions on the sensitivity of the material property values of the discs.

Nomenclature:

F	force
σ	stress
ε	strain
τ	shear stress
E	Young's modulus
ν	Poisson's ratio
G	shear modulus
γ	shear strain
K	bulk modulus
T	time
r, t, z	radial, tangential, vertical component
β_i, β_0	fibre direction to the horizontal plane, 30°

8.5.2 Finite Element Model Overview

Fig. 37. shows a sagittal section of the 3D solid model of the L2-L3 lumbar vertebra-disc-vertebra complex. The anatomical model is a full-size 3D Pro/Engineer solid model, based on the male data sets supplied by the Visible Human Project. [75] It must be remembered that this data therefore represents only one particular man, even though the fact that he was in the fiftieth percentile by size means that he is typical of most people. Strictly, however, the data do not apply to women, the young, the old and the exceptionally short or tall. The main

geometric factors of the elliptical cross-section model are shown in Table 3, together with the model data.

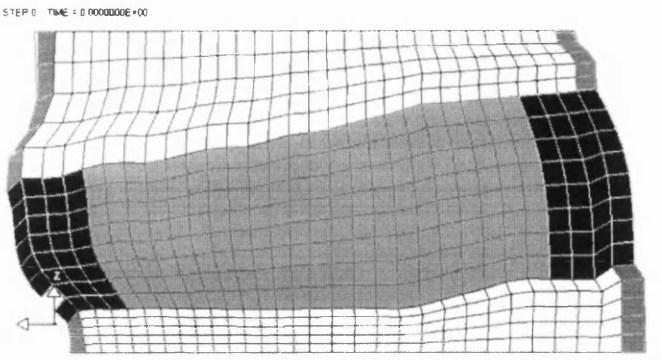

Fig. 37. Sagittal section of the finite element model

Table 3. Main geometric factors

Total number of elements	2860
Total number of nodes	3107
Total number of annulus solids	540
Total number of annulus outside shells where applicable	180
Total number of nucleus solids	560
Total number of cancellous bone solids	1288
Total number of cortical bone solids	252
Disc height [mm]	15.00
Anterior-posterior disc length [mm]	40.30
Lateral disc width [mm]	55.60
Disc cross-sectional area [mm^2]	987.26
Nucleus cross-sectional area [mm^2]	697.98
Top surface area [mm^2]	1436.18
Bottom surface area [mm^2]	1712.54

The model was meshed in Altair Hypermesh® and the FEM code was written [2] in LS-Dyna3D®. Model checks and post processing were performed in the Oasys® environment. During the model generation the main aim was to build an anatomically and mechanically relevant lumbar intervertebral disc model keeping the calculation time as short as possible. The model contains the nucleus

pulposus, the annulus fibrosus, and part of the second and third lumbar vertebrae divided into cancellous bone and cortical shell.

The two biggest obstacles to be overcome in finite element studies of living tissue are the non-linearity and the anisotropy. Both of them play a significant role in the real intervertebral disc to ensure that the necessary stiffness, damping and stability are achieved. It is therefore essential that they should be modelled correctly here. This chapter compares three intervertebral disc models, which are different in the material formulation of the annulus fibrosus.

8.5.3 FEM Representation of the Disc Annulus

In the first two models, referred to as Model 1, and Model 2, the annulus is described as an orthotropic, non-linear material. The problem of non-linearity was approached by using eight straight-line segments to represent and replace the original, continuously varying, experimentally determined stress-strain characteristics satisfactorily. Sectioning the stress-strain curve can be done with different methods, which results in different accuracy. To get a widely comprehensive view on the value of the approach, two types of analogy were chosen. In Model 1, the original tensile-compressive stress-strain curve was divided using a linear division scale on the ε-axis in the $0\text{-}\varepsilon_{max}$ domain. In Model 2 the ε-axis was again divided into eight sections but this time it was done on a quadratic basis. This second method gives a finer resolution at small deformation, where the change is faster in the Young's modulus. The average accuracy is around 2% at the beginning of the curve. However at large deformation the deviation can grow up to 10%, which is a considerable initial error. To show how much importance the accuracy has, Model 2 was tested by approaching the curve both from the top and from the bottom with the line segments. Fig. 38. shows the result.

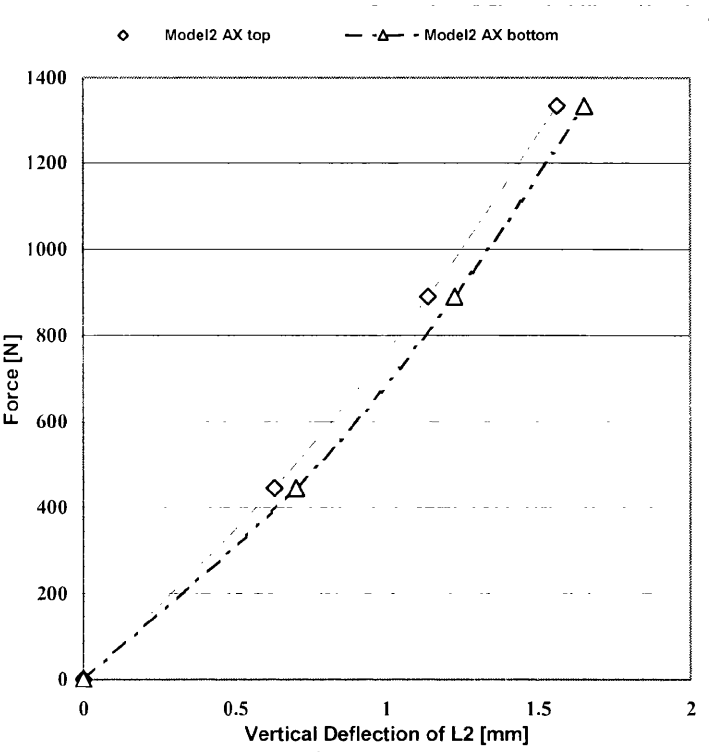

Fig. 38. Different approaches in Model 2 (AX-axial compression)

The main disadvantage of using this method is that the stress-strain function is not continuous in the domain. Furthermore the sectioned stress-strain curve was mirrored about the origin so that it is identical in tension and compression. Compromises therefore had to be made with the accuracy and hence the sectioned curve averages the tensional and compressional properties, although it is estimated that the average inaccuracy introduced is never more than 2%. The drawback to this approach is that the requirement for new input data at every change from one straight section of the stress-strain function to the next leads to an increased model preparation time.

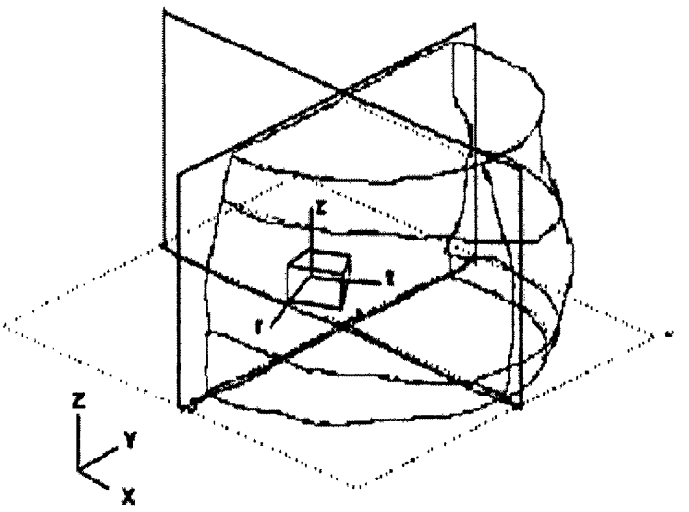

Fig. 39. Coordinate systems

The orthotropy was supplied by giving different directional properties to the annulus solids and furthermore a 2-dimensional non-linear orthotropic shell surrounding the outer disc annulus surface. Details of the coordinate systems used in the models are given in Fig. 39, while the annotations used are given in the Nomenclature section. The x-axis points to the left lateral direction and the y-axis to the posterior direction. The z-axis points upward, towards the head. The r, t, z orthogonal element coordinate system is rotating in a global cylindrical system with z initially vertical and r initially pointing out from the centroid of the disc slice. Please note that at complex geometries such as the intervertebral disc the axes of some elements might not follow the theoretical coordinate directions due to the limitations of the mesh options. Furthermore for different tensile and compressive properties the element axes are sensitive to their orientation. In the presented models the annulus mesh required special care. After the meshing was done, the element coordinate systems were manually rotated into the right direction. Up to 8° difference in the orientation of the element axes will cause less then 1% error in the directional material stiffness, which is considered to be negligible.

In the third model, referred to as Model 3, a very different approach was chosen to describe the annulus fibrosus as a non-linear, orthotropic material. In this approach a new material law was programmed into the User Defined Material Properties (UMAT) [2] of LS-Dyna3D®, which was the software package used for the construction of the finite element model of the overall disc. The code was written in Fortran 77. More information on LS-Dyna UMAT can be found in Appendix 10. The introduced law is highly non-linear and anisotropic represented by the following general strain energy density function. This representation is useful for different FE solvers.

$$W = \frac{1}{2}\left[\left(\frac{AE(1-\nu_{11})}{(1+\nu_{11})(1-2\nu_{11})} + \frac{AE\nu_{21}}{(1+\nu_{21})(1-2\nu_{21})} + \frac{AE\nu_{31}}{(1+\nu_{31})(1-2\nu_{31})}\right)\varepsilon_{11}^2 + \right.$$
$$+\left(\frac{BE\nu_{12}}{(1+\nu_{12})(1-2\nu_{12})} + \frac{BE(1-\nu_{22})}{(1+\nu_{22})(1-2\nu_{22})} + \frac{BE\nu_{32}}{(1+\nu_{32})(1-2\nu_{32})}\right)\varepsilon_{22}^2 +$$
$$+\left(\frac{CE\nu_{13}}{(1+\nu_{13})(1-2\nu_{13})} + \frac{CE\nu_{23}}{(1+\nu_{23})(1-2\nu_{23})} + \frac{CE(1-\nu_{33})}{(1+\nu_{33})(1-2\nu_{33})}\right)\varepsilon_{33}^2 +$$
$$\left. + \frac{DE}{2(1+\nu_{23})}\gamma_{23} + \frac{DE}{2(1+\nu_{31})}\gamma_{31} + \frac{DE}{2(1+\nu_{32})}\gamma_{32}\right]$$

To reduce the number of constants needed to describe the disc annulus, the following simplifications were introduced.

$$\nu_{11} = \nu_{22} = \nu_{33} = \nu_{12} = \nu_{23} = \nu_{31}$$

and

$$\nu_{ij} = \nu_{ji}$$

E is the vertical Young's modulus, ν is the Poisson's ratio of the material, A, B, C are multipliers representing stiffness difference caused by the fibres, D is the multiplier between the shear modulus, G and the Young's modulus, E, ε and γ are the engineering strain and the shear strain respectively. Index *1,2,3* denotes the local *r, t, z* element coordinate directions respectively.

The A, B, C, D constants were obtained on the following basis. At the local element coordinate system A represents the radial, B the tangential and C the vertical stiffness multiplier. The vertical stiffness of the annulus is obtained from

the literature and forms the basis of the initial input curve, with C=1. To obtain the value for B, calculations on the fibre orientation presented later in the section on orthotropy were used.

$$B = \frac{C}{\tan \beta_i}$$

where β_i is the actual fibre direction in degrees to the horizontal plane. The constant A was defined as A=C, as it was impossible to obtain a satisfactory value of the radial annulus stiffness from the literature. Preliminary tests on changes in the value of the annulus radial stiffness showed a low sensitivity on the overall response of the model. However increasing the value of A resulted a bigger disc bulge. Stresses within the annulus did not change significantly. Constant D represents the connection between the Young's modulus, E and the shear modulus, G. In Model 3, D was chosen to be 1, since the strain energy density function already contains the $G = \frac{E}{2(1+\nu)}$ linear relation by default.

For tension and compression the annulus is given a third order, non-linear characteristic in which the failure of the material is neglected, in the sense that it is assumed that the failure point is never reached. It is quite easy to describe this function with a third-order polynomial. Third order polynomial representation was chosen because it is continuously differentiable in any point of the domain of variability. The recommended precision for the polynomial constants is three or more significant digits. For 1% change in the value of the polynomial constants a, b, c, d the estimated sensitivity of $\Delta\sigma/\sigma$ reaches around 1% for the third-order constant a, at large deformations and for the first-order constant c, at small deformations. It is around 0.2% for the second order constant b, and 0.02% for d if $d \rightarrow 0$. LS-Dyna3D® handles the real values in single precision [2]. The number of significant digits for single precision literals is 7. The mathematical description of sensitivity can be seen in Appendix 9.

Let the input data for the FE solver be the four polynomial constants of a non-linear third-order stress-strain curve, a, b, c, d.

$$\sigma = a \cdot \varepsilon^3 + b \cdot \varepsilon^2 + c \cdot \varepsilon + d$$

The Young's modulus of the intervertebral disc at a certain strain ε can be calculated by deriving this function at the current strain, $\varepsilon_{(r,\,t,\,z)}(T)$.

$$E(\varepsilon) = \frac{d\sigma}{d\varepsilon}$$

The software approximates the strain increment from the previous time step, then it calculates $E_{(r,\,t,\,z)}(T)$. With this value of E the software then calculates the stress increment between the current and the previous time step using the following functions obtained by differentiating the strain energy density function W by ε for the r, t, z directions,

$$\sigma_{r_i} = \sigma_{r_{i-1}} + \frac{E_r}{1+\nu}\left[\varepsilon_r + \frac{\nu}{1-2\nu}\left(\varepsilon_r + \varepsilon_t + \varepsilon_z\right)\right]$$

$$\sigma_{t_i} = \sigma_{t_{i-1}} + \frac{E_t}{\tan\beta_i \cdot (1+\nu)}\left[\varepsilon_t + \frac{\nu}{1-2\nu}\left(\varepsilon_r + \varepsilon_t + \varepsilon_z\right)\right]$$

$$\sigma_{z_i} = \sigma_{z_{i-1}} + \frac{E_z}{1+\nu}\left[\varepsilon_z + \frac{\nu}{1-2\nu}\left(\varepsilon_r + \varepsilon_t + \varepsilon_z\right)\right]$$

Where β_i is the actual fibre direction in degrees to the horizontal plane, $\nu = 0.3$ is the Poisson's ratio.

From these stresses the software calculates the expected strain increment at r, t, z for the next time step using Hooke's law. The shear stresses are calculated as usual,

$$G_{r,t,z} = \frac{E_{r,t,z}}{2(1+\nu)}$$

$$\tau = G \cdot \gamma$$

With this method, if the time step is small enough the elements follow the non-linear characteristics accurately in the local coordinate system. To achieve the required anisotropy and orthotropy the vertical stress-strain curve was scaled down to the r, t, z element coordinate directions on a similar way as it was explained at determining constatnt A, B, and C. The effect of stiffening to the tangential and weakening to the vertical directions during tension-compression caused by the changing angle between the annulus fibres was neglected in this model after some preliminary tests on the sensitivity of the overall model

behaviour on the changing fibre direction revealed that at small deformation its effect is negligible, despite of the quite significant changes of the $\frac{E_z}{E_t}$ ratio.

Several measurements had been done on the annulus stiffness. [7, 57] However unfortunately most of them were recording the force-deflection curve only and failed to give enough details on the initial sample length. Therefore the experiments of Tadano *et. al.* [35] were chosen to represent the annulus characteristics in the material model. In this study the overall stiffness of a denucleated Grade 1, non-degenerated intervertebral disc were tested. The vertical stress-strain characteristics of the annulus fibrosus for both tension and compression were recorded immediately by a computer controlled test machine. The effect of inhomogeneity was also tested. The annulus vertical stiffness was downscaled to 10% of the anterior and posterior stiffness towards the lateral side of the disc. The tests evaluated were showing no significant changes in the overall response at different load cases, probably because not the full annulus cross section takes part in the load bearing at once. Based on these results, the annulus inhomogeneity was neglected in the model.

Table 4. Comparison of the material properties

Material Name	Material Parameter			
	Model 1, Model 2		**Model 3**	
Cortical bone	E=12000MPa	υ=0.3	E=12000MPa	υ=0.3
Cancellous bone	E=100MPa	υ=0.2	E=100MPa	υ=0.2
Annulus solid	$\sigma(\varepsilon)_{vert,max}$=100MPa $\sigma(\varepsilon)_{tan,max}$=173MPa $\sigma(\varepsilon)_{rad,max}$=100MPa $G(\varepsilon)_{max}$=8MPa	 υ=0.45 ε_{max}=1.5 $G(\varepsilon)=E(\varepsilon)/2(1+\nu)$	$\sigma(\varepsilon)_{vert}=187.2\varepsilon^3+17.3\varepsilon^2+4.4\varepsilon$ [MPa] $\sigma(\varepsilon)_{tan}=\sigma(\varepsilon)_{vert}/\tan(\beta)$ $\sigma(\varepsilon)_{rad}=\sigma(\varepsilon)_{vert}$ $G(\varepsilon)=E(\varepsilon)/2(1+\nu)$	 υ=0.3
Annulus shell	$\sigma(\varepsilon)_{vert,max}$=100MPa $\sigma(\varepsilon)_{tan,max}$=173MPa $G(\varepsilon)_{vert,max}$=8MPa $G(\varepsilon)_{tan,max}$=8MPa E_{rad}=100MPa G_{rad}=8MPa	 υ=0.45 ε_{max}=1.5 $G(\varepsilon)=E(\varepsilon)/2(1+\nu)$	N/A	
Nucleus	K=2.5MPa	(Bulk modulus)	K=2.5MPa	(Bulk modulus)

8.5.4 Representation of the Nucleus

In both models the nucleus pulposus was taken to be essentially a pure Newtonian fluid and was described by its bulk modulus, K. The properties of the cortical and cancellous bone were taken from previous FE studies. [18] Table 4. shows a summary of the material properties.

8.5.5 Boundary Conditions

The validity of the models and the analysis procedure has been established by comparison with those values that are also available from direct experimental measurements e.g. response of the disc-body unit to axial and eccentric compressive loads in terms of axial displacement, the disc bulge and displacement of various nodes inside the disc.

The disc model and the boundary conditions were built to comply with the measurements of Lin *et. al.* [13] Specimen 10 was chosen as closest to the geometric factors of the computational model. The above specimen was an L2-L3 vertebra-disc-vertebra joint. The level of degeneration was Grade 1 according to Nachemson *et. al.* [15, 16], which means a non-degenerated disc. In the model, as in the experimental measurement, the top and bottom of the two vertebrae were truncated to achieve two flat, horizontal loading surfaces parallel to the middle disc plane. At uniform compression the load was applied in the experiments directly by the crosshead of the testing machine. This resulted in a relatively uniform distribution of load across the ends of the specimen, provided the top and bottom loading surfaces stayed parallel. This technique ensures that there is no need to know the exact location of the centre point. The specimen was loaded first to 445N, then to 899N, and finally to 1334N. The loading rate was less than 12.7mm/s. For the FEA the load was applied as a ramp pattern of uniform pressure to the top surface of the L2 vertebra. The equivalent force to this pressure was consequently 445N, 899N, and 1334N. In all simulations the bottom vertebra was fixed in 6 degrees of freedom. To avoid any tilting of the top vertebra, its top surface was also constrained against x and y translation.

To produce an off-centre compression, first the centre of the disc has to be located. By Lin *et. al.* the centroidal axis of the specimen was defined as the position where the preload caused the minimum vertical deflection. This method is difficult to follow in FEA. Therefore in our analysis we defined the A-P centre point where if the disc is loaded the top surface of the upper vertebra produces the lowest angle of rotation on the x-axis throughout its motion. In this way the resultant bending moment in addition to the compression causing more deformation was avoided. In the experiments the loading was done by a wedge-shaped test rig. Since the computer model is symmetrical, it is satisfactory to load the disc in one point with a nodal force. The same equivalent force was used as before, displaced by 10mm to the lateral or frontal direction following the method used in the experiments. For flexion the top vertebra was constrained against x translation, for lateral bending against y-translation.

There was no additional damping applied to the model. For the investigation into the internal movements in the disc, the loading had to be slow enough to avoid dynamic shocks throughout the disc body and let the nodes creep into their steady state. Therefore a slow displacement of 0.8mm was applied to the top vertebra as a ramp pattern. The end time of the simulation was set to 1s, this gives a displacement velocity of 0.8mm/s. This displacement occurs at an equivalent load of 1500N axial compressive force in a disc with the same anterior-posterior diameter as in the FEM model. Unfortunately the time penalty of the relatively slow loading is enormous, since the creep depending on the shear properties of an oil-like substance is slow.

8.5.6 Non-linearity

Fig. 40. shows the difference between the 8-line segments linearly and quadratically sectioned, and the non-linear approach for axial compression. The problem with the accuracy at small deformation can be clearly seen in the results for Model 1, which generally shows weaker characteristics at low strains. Although it becomes stiffer later, this is not enough to compensate for the fast changes in the Young's modulus.

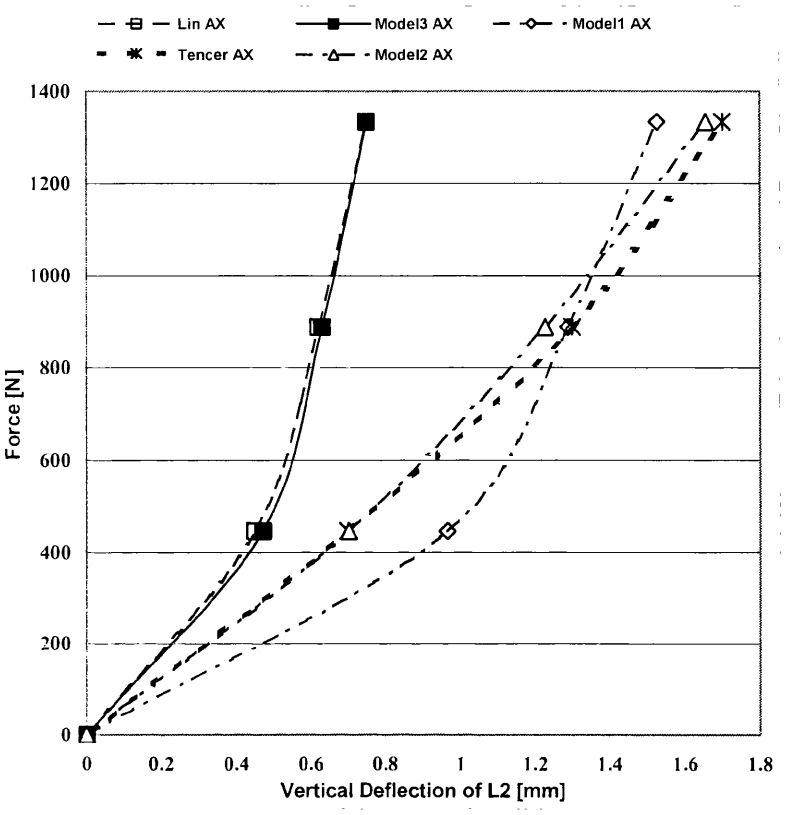

Fig. 40. Response to axial compression

The second approach shows some improvements in the stiffness at small deformation, nevertheless the overall behaviour is more like a weaker intervertebral disc, as Tencer's [70] curve averaging a series of experiments shows. There is a major change in the precision of the movements in Model 3, with better non-linearity. In the first two models, even though the characteristic was satisfactory, the actual results were very far from being acceptable. The response to eccentric loading was not comprehensible since only Model 3 gave acceptable results.

The third model shows tremendous improvement in accuracy. The result is still a bit weaker than the measured data. This depends on the robustness of the error correction of the approach in the model characteristics. It can be improved by calculating up to the second derivative, but this will cause an extra time penalty.

$$f(x+\Delta x) = f(x) + \frac{df(x)}{dx}\Delta x + \frac{1}{2}\frac{d^2 f(x)}{dx^2}\Delta x^2$$

More details can be found in Appendix 8.

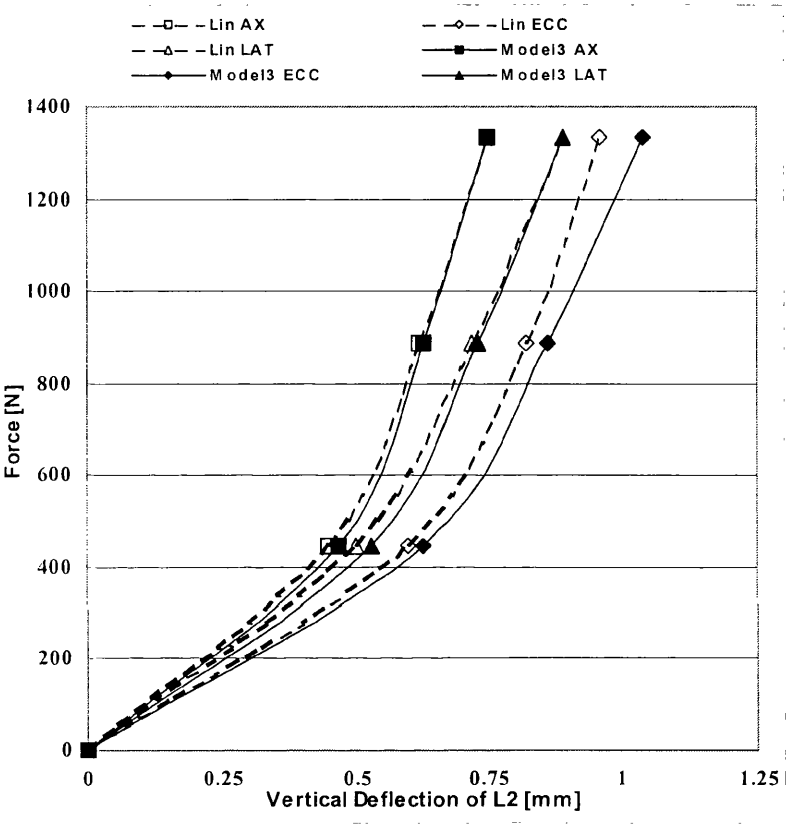

Fig. 41. Response to forward and lateral bending (AX- axial compression; ECC- eccentric compression; LAT- lateral bending)

The usefulness of the third method shows particularly at eccentric loading. In Fig. 41. the displacement of the second vertebra under eccentric forward and lateral bending can be seen. There is a greater error at eccentric loading. This is caused by a very simple practical problem; determination of the exact location of the loading is extremely hard, since it is hardly possible to define the centre point of the disc. The position of the load in the simulation does not fully correspond to the measurement.

8.5.7 Orthotropy

The intervertebral disc annulus has a significant anisotropy generated by the fibre direction. [7, 10, 18, 51, 58] The annulus fibres are oriented at +30 degrees to the horizontal plane at every second layer and to –30 at the remaining. Similar properties can be represented by material orthotropy. In the first two models the material orthotropy was achieved by using an orthotropic elastic shell. The third model simulates the orthotropy based on a simple calculation of the fibre direction. Most of the measurements give the vertical stress-strain curve as a result. The tangential stresses can be calculated easily with trigonometric functions if it is assumed that the material is homogeneous in the *t, z* directions. As can be seen on Fig. 42,

$$F_t = F_z \cdot \frac{1}{\tan \beta_i}$$

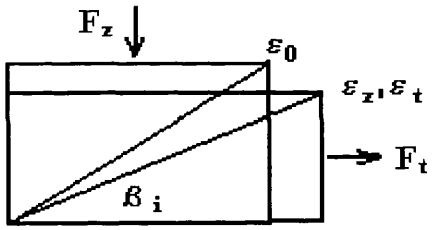

Fig. 42. Change of fibre direction

Furthermore, during compression there is a small change in the fibre direction. In the i-th time step, if the strain is known then the angle in the element is expressed by:

$$\beta_i = \arctan\left[\frac{\left(1+\varepsilon_{z_i}\right)\cdot \tan \beta_0}{\left(1+\varepsilon_{t_i}\right)}\right]$$

Scientists agree that the 30 degrees directional layout of the annulus fibres play a significant role in the mechanics of intervertebral discs. There are several various theorems about the purpose of such a structure. However the question of what exactly they do besides change the stiffness of the annulus into a form of orthotropy remains unanswered. Therefore several tests were launched to find out

what disc properties are governed by the annulus fibre direction. To do this, orthotropy was removed from the models, and the results were compared.

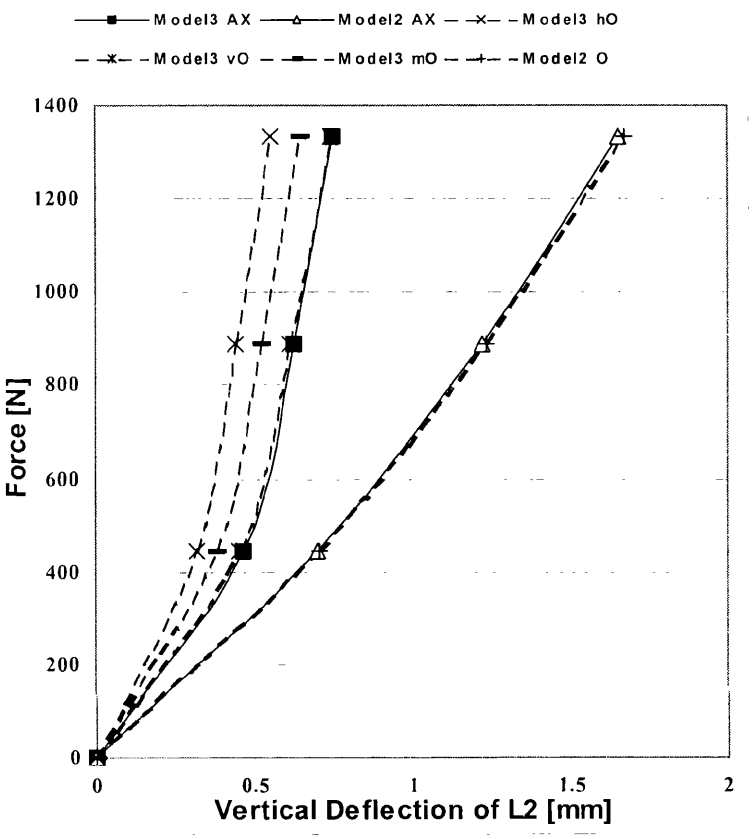

Fig. 43. Effect of removing the orthotropy *(h, v, m denote whether the former horizontal, vertical component of the directional annulus properties or the mean value of these two stress-strain curves were introduced into the model; o denotes that the orthotropy has been removed)*

As can be seen in Fig. 43, the response to axial compression did not change significantly in any of the models. Some values even got closer to the measured curves without introducing orthotropy. The answer to this behaviour lay in the fact that the tangential and radial components of the displacements are significantly smaller then the vertical. Because of this the effect of the fibre direction is negligible in this case. The main disc property governing the motion of the top vertebra in compression is the vertical component of the annulus stiffness and its level of nonlinearity. The fibre direction does not affect directly the pure loading case of the intervertebral disc. It affects the more complex stress

states like the change in the disc bulge, fluid flow shaping the geometry and the torsional properties.

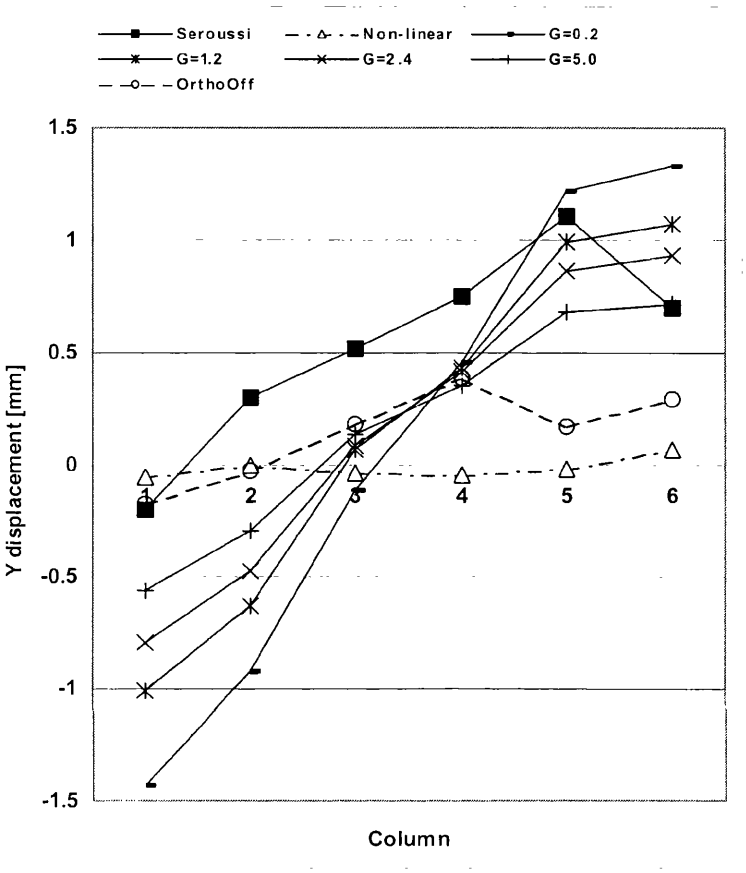

Fig. 44. Migration of inside nodes along the y-axis

8.5.8 Shear Properties

Throughout the investigation so far a non-linear shear function has been used to describe the changes in the shear stress. This function uses the general Hooke's law to determine the shear modulus $G(\varepsilon)$ if the Young's modulus $E(\varepsilon)$ and the Poisson's ratio ν are known. Our model has shown some instability absorbing shockwaves with non-linear shear properties. Therefore a linear shear function was also introduced instead of the non-linear one. There are some data available about the displacement of limited nodes inside the disc, which describe the movements of the material inside. This map on the migration of inside nodes shows the displacements occurring in the disc during compression. Together with

the bulge of the outside boundary it helps in fine-tuning the shear properties of the model.

The displacement of some nodes of the disc in the sagittal plane was investigated. Seroussi *et. al.* [43] described the mid-sagittal intradiscal deformations of *in vitro* intact specimens subjected to compression, flexion and extension. The technique was based on radiographic detection of 0.5 mm metal beads embedded in an array within the disc material. In a finite element model this can be represented with an array of the mid-sagittal nodes.

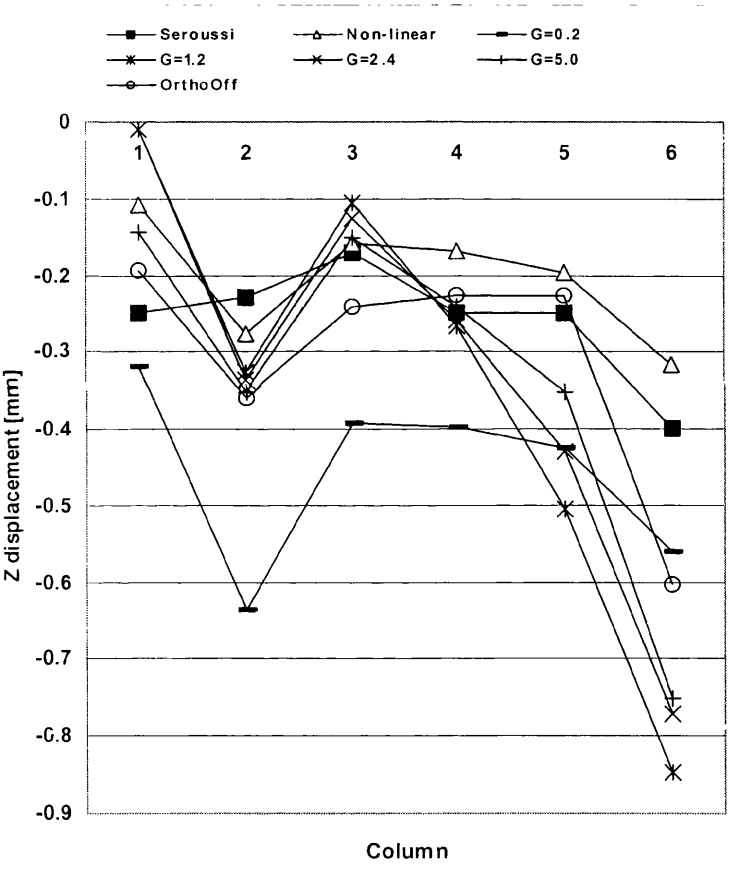

Fig. 45. Migration of inside nodes along the z-axis

Four layers of nodes were picked. Each of the layers contained 6-6 nodes horizontally. The average of the displacement of the 4 nodes in the 6 columns aligned vertically to each other was calculated at every simulation along the vertical z-axis and the horizontal y-axis.

Overall six tests were run; one with non-linear shear characteristics, four with different linear shear values ranging from 0.2 to 5.0 MPa and one calculation was also run with the orthotropy removed. In all tests the model was subjected to pure compression only. Since only the average displacements of ten measurements were published by Seroussi *et. al.* [43] the loading conditions were fitted to the mean values. A displacement of 0.81 mm was applied to the top of the L2 vertebra. The constraints were the same as for uniform compression described earlier in the boundary conditions section.

In Fig. 44, a set of curves can be seen with different linear shear properties. The figure also includes one curve showing the result of the non-linear approach and one with the orthotropy removed for comparison. The results become clearer by comparing this figure against Fig. 45, which shows the movement of the nodes in the vertical direction. However, although the non-linear shear properties give good agreement with the measured values of vertical movement, they give a poor response in terms of horizontal displacement, where shearing is more likely to occur. The result suggests that the shear properties are linear, or nearly linear, in intervertebral discs. At constant shear modulus the curve became smoother and started to show similar characteristics to those available in the literature in both the y and z directions. The end points of the curves have major significance for displacements along the y-axis. They show the expected increase or decrease in the disc bulge. If the shear modulus is higher, the disc bulge becomes smaller. The effect of orthotropy was also checked at this level.

There is a major change in the movements if we remove the orthotropy. The curve becomes more distorted within the annulus. Again, introducing orthotropy does not make much change in the vertical movements but can cause an increase in the disc bulge.

Table 5. Comparison of the annulus fibrosus characterisation

Model	Non-linearity	Orthotropy	Shear properties
1	Approaching the original characteristics with 8 line segments. Distribution of segmentation projected to ε-axis is linear. *Input variables:* 9 breakpoints of the segments of the vertical approach from $0,0\text{-}\varepsilon_{max},\sigma_{max}$	Scaled directional properties to radial, tangential direction based on the vertical stiffness. Orthotropic elastic shell applied to the outer annulus surface.	linear G=constant
2	Approaching the original characteristics with 8 line segments. Distribution of segmentation projected to ε-axis is quadratic. *Input variables:* 9 breakpoints of the segments of the vertical approach from $0,0\text{-}\varepsilon_{max},\sigma_{max}$	Scaled directional properties to radial, tangential direction based on the vertical stiffness. Orthotropic elastic shell applied to the outer annulus surface.	linear G=constant
3	Approaching the original characteristics with third-order non-linear equation. *Input variables:* 4 polynomial constants of the equation of the vertical component of the stress-strain curve	Scaled directional properties to radial, tangential direction based on the vertical third order stress-strain curve.	non-linear $G(t)=E(t)/2(1+\nu)$

8.5.9 Conclusion

Three finite element models of the human intervertebral disc were constructed with different annulus material formulations. Table 5. shows a summary of the properties. All models were based on the same characteristics and evaluated against independent sources. Two models were built using widely known modelling methods while the third one used a new material formulation. Tests have been run investigating the effect on the accuracy of the input data. Significant results were gained, especially showing the effect of non-linearity. The result shows that the new material formulation has higher accuracy in simulating the three-dimensional movements of the intervertebral disc in a wide range of dynamic loading situations. Under complex loading the effectiveness of the approach on the input curve has great significance and results in more accurate prediction of displacements under load. Furthermore the number of input data

required was reduced significantly by the third method. This, together with the more straightforward mathematical description, saves enormous time for the user.

The shear properties of the annulus material were also tested, together with the orthotropy. Throughout the simulations the features of the disc, which are governed by these properties, were of special interest. Increasing shear modulus decreases the change in the disc bulge. This is balanced by the orthotropy, where introducing orthotropy increases the bulge of the disc annulus.

Validation of the model by comparison of its response with literature data shows excellent matching in terms of vertical displacement for both axial and eccentric loading. However, similar comparison of the shear values and the disc bulge shows some differences. Therefore further investigation of the non-linear shear properties of the annulus fibrosus could lead to excellent disc simulation for any loading situation. Using the new material formulation did not increase computation time compared to the built-in material models. Nevertheless a greater accuracy was proven. The validation results of the disc confirm that the presented way of implementing non-linear materials into FEM solvers is a promising approach to full computational simulation of non-linear anisotropic materials such as the annulus of the intervertebral disc. The results were published, more information on some results can be also found in Appendix 11. [74] The main part of the FORTRAN 77 subroutine of Model 3 can be seen in Appendix 12.

CHAPTER 9. – EXPERIMENTAL WORK

9.1 Model 4 - Experimental Project

In parallel with the computational work an experimental project was also carried out. [73] The aim of this experiment was to build a large-scale model [94] of the intervertebral disc. The objective was to investigate which material parameters are important from the engineering point of view. The project was expected to give useful information, which would help to find the answer to the following questions,

- Does the multilayer structure of the annulus fibrosus play an important role in reducing the radial stresses?
- What is the role of the distinctive fibre direction?
- Does the annulus take part directly in the vertical load bearing?
- How does the thickness of the annulus affect the disc stiffness?
- What is the role of the nucleus?
- How does the pressure inside the disc nucleus affect the overall mechanical response, especially the initial pressure?
- What is the effect of the viscosity of the nucleus?
- What is the effect of the fluid loss?
- Which main properties govern the disc bulge directly?

One of the largest and most universal problems in biomechanics is the lack of fully validated and reliable engineering data on the mechanical properties of the soft tissues found in the human body. This is often linked to a poor understanding of the detailed mechanical behaviour of the various components in any complex structure composed of soft tissue. Certainly this is true of the intervertebral disc where the role and contribution of each component is only understood in a general way, not in the quantitative engineering manner that is required for advances in biomechanical analysis or modelling.

The main obstacle to improved understanding is the difficulty, both practical and ethical, is experimenting on living human tissue. The purpose of the work described here is to circumvent this difficulty by constructing and testing a large-scale mechanical model of a typical intervertebral disc in order to show the quantitative contribution of each component under a variety of loads and indicate the precise mode of failure.

Results of stress and strain have been obtained, so far only for axial compression, which show excellent quantitative and qualitative agreement for the model as a whole with the latest data on human discs. More importantly, however, tests on incomplete versions illustrate the contribution of each component and a failure test led to a physiologically accurate herniated disc. Future work will involve bending and extensional loads as well as improved modelling of Sharpey's fibres.

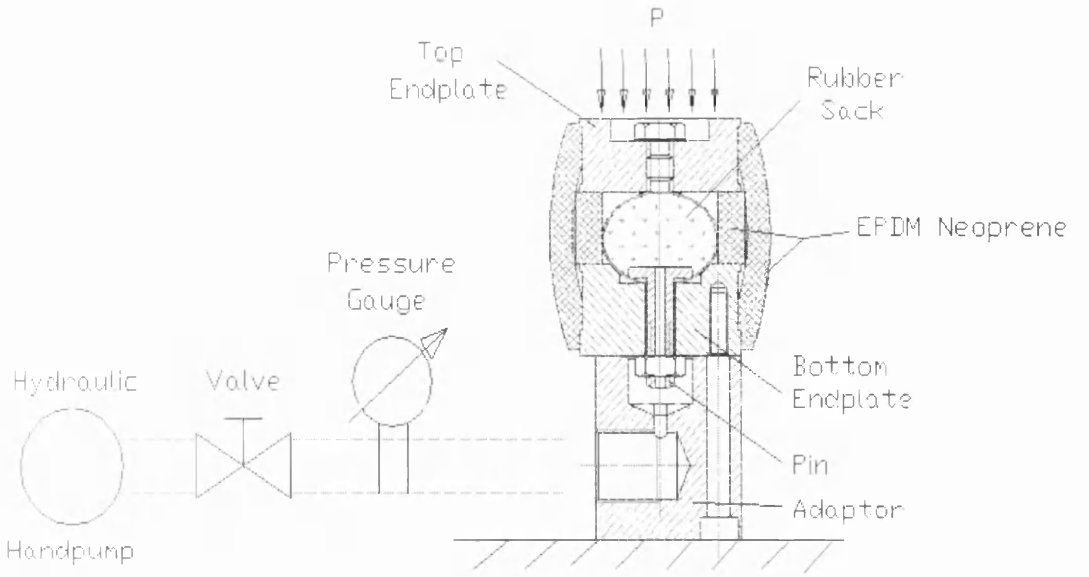

Fig. 46. Schematics of the large-scale experimental assembly

9.1.1 Model and Methods

A large-scale model of a typical lumbar intervertebral disc was built maintaining the 12:40 height-diameter ratio of the human L2-L3 intervertebral disc. The main aim was to include all the individual components of a disc, which are believed to actively affect the overall mechanical response during compression. The detailed design of the model can be found in Appendix 13. As shown in Fig. 46, the model consists of a thin rubber sac containing pressurized fluid as the *nucleus pulposus*, a surrounding ring of layers of closed cell EPDM neoprene rubber from Paulamar Ltd. simulating the *annulus fibrosus*, and an outer wrapping of string to represent Sharpey's fibres. These three components are sealed between two steel end plates that act as the adjacent vertebrae and serve as mounts in a universal testing machine. Neoprene was chosen because its measured characteristics was nearly identical to the vertical stiffness of the annulus fibrosus documented by Tadano *et. al.* [35] The overall diameter is 80 mm and so the scale is approximately 2:1 in comparison to a typical lumbar intervertebral disc. The bottom end plate has pressure tappings to allow variation and measurement of the pressure inside the rubber sac "nucleus". One tapping leads to the side of the end plate, the other upwards, into the sac. The sac is mounted on the bottom end plate with a hollow pin allowing free fluid flow. The pin has a T-shape cross-section, which securely seals the rim of the sack, separating the fluid from the other parts. To the side of the bottom end plate a hydraulic hand pump was connected through a shutter-valve and a pressure gauge. The device then was tested with a universal test machine.

Several tests were performed with different arrangements in order to establish the effect of each component on an Avery (Birmingham) type: 7105 CCN Serial No. E66319, Max. Capacity 15000 lb universal test machine. All tests involved axial and eccentric compression with the load applied by varying the displacement in steps of 0.05 inches ($\approx$ 1.27 mm). At axial compression the parallel heads of the machine were used directly to compress the disc, at eccentric compression a wedge-shape adapter was applied 10mm away from the top-plate centre as it can be seen in Appendix 14. The reaction force, the overall vertical

deflection, the bulge in the disc diameter and the pressure inside the model were recorded for each step. The bulge was measured with an external calliper at the largest diameter. All the measurements were performed three times and results were then averaged.

The vertebrae are represented by metal end plates. The currently purchased annulus material is Closed Cell Expanded (EPDM) Neoprene. On all of the materials used in this experiment a tensile test was done with a Monsanto Tensometer 20, Montech UK, Serial No: st20-095. Tensile tests on the Neoprene were according to *BS2782:320A/ISO527*. Tensile tests were carried out on different strings as well which used to wrap the model. To obtain the most accurate characteristics two different setups were used. Case 1. was a tensile test on a single string, and Case 2. on three, parallel connected wires. The strength was calculated then based on the equations of parallel-connected springs.

where,

$$\sigma = \frac{F}{A} = E\varepsilon$$

at case 1.

$$F = kx$$

at case 2.

$$F = k_1 x + k_2 x + k_3 x$$

k is the spring constant ($k_1=k_2=k_3$), F is the tensile force measured, A is the cross sectional area of the wire, E is the Young's modulus, and ε is the engineering strain measured.

Model 1	no strings around the annulus and air within the nucleus
Model 6	oil-filled, wrapped with 0.5 mm fishing line generating 15° orthotropy
Model 7	same as Model 6 plus initial pressure of 0.2 MPa applied to the nucleus
Model 14	0.1 MPa achieved with tighter wrap around the annulus
Model 15	tighter wrap around the annulus, initial pressure of 0.2 MPa applied to the nucleus

Model 16 0.2 MPa initial pressure fully achieved by the wrap around the annulus

Model 17 same as Model 16 subjected to 15mm off-centre compression

Model 18 same as Model 16 subjected to 10mm off-centre compression

9.1.2 Results & Discussion

Throughout the tests the response of the large-scale model to deformation shown in Fig. 47. was recorded together with the actual disc diameter and the pressure inside the nucleus sac. In Fig 47. the strain values are calculated by dividing the top plate displacement by the initial disc height. The stress values are calculated dividing the loading force by the disc area. The disc area is determined by the mean value of the actual smallest and largest disc diameter. At the first test the rubber sac was filled with air and the outer wrapping was omitted. Next the model was wrapped with different strength strings and filled with oil. Different densities of oil were tried but the results did not change significantly although overall a higher density fluid causes slightly stiffer characteristics. Sacs with different wall thickness and strength were also tested but the overall results showed no difference. Several tests were carried out with different initial pressures in the sac and the effect of releasing some fluid from the sac under load was also investigated. Increase of the amount of fluid in the sac tended to increase the disc height rather than cause the disc to bulge, as recorded in the experiments of Markolf *et. al.* [11] As the test deformation could be applied at different rates it was possible to study hysteresis during loading and unloading. Finally, as the large-scale model was unable to reach the overall stiffness of an intact, healthy intervertebral disc with any of these originally planned arrangements, an extra horizontal layer of string was applied to reduce the bulge and increase the stiffness.

Table 6. shows the effect of changing the model properties. The – sign shows that there were no considerable changes in the overall properties; + shows a small improvement; ++ shows positive changes.

Table 6. Effect of changes

	increase in overall stiffness	decrease of bulge	increase in nucleus pressure
increasing nucleus density	+	-	-
stiffer sack material	-	-	-
increasing nucleus pressure	++	+	++
stiffer strings around the annulus	-	-	-
tighter wrap around annulus	++	++	++

The findings confirm that the intervertebral disc bulge shown in Fig. 48. is surprisingly small even at high loads and the results suggest that the annulus structure is 'designed' to reduce the bulge. Please note that the measured bulge values were divided by 2 as the model was twice as big as the disc of *Lin et. al.* [13] The role of the annulus fibres simulated by the wrapping around the Neoprene in compression is to help to contain the nucleus fluid and at the same time, to reduce the bulge by increasing the overall stiffness of the disc. Vertical load bearing of the annulus occurs only at extremely high loads, where the deformation of the disc is so high that the annulus gets jammed between the two endplates. The radial softness of the annulus absorbs the deformation caused by the pressurized nucleus fluid and, at the same time, the high number of fibre layers acts against the bulge, surrounding the nucleus as a fibre-reinforced tube. Increasing the initial pressure of the nucleus results in generally stiffer characteristics, especially at small deformation. The force-pressure diagram in Fig. 49. shows the effect of fluid loss. Especially at high loads the load-bearing capability of the intervertebral disc reduces dramatically even at a relatively small pressure drop. At the same time the bulge becomes slightly bigger and the disc loses height. It was observed, that changes in the stiffness of the sac material did not cause significant changes in the overall characteristics, until the material itself was easily deformable and elastic. The stiffness of the strings wrapping the nucleus did not change the overall characteristics in compression. Their stiffness plays a more significant role at torsion, where the annulus fibres are subjected to a larger deformation. Several tests were done on fluids filling the nucleus with different viscosity and density. None of the parameters caused major difference in

the quasi-static results. Since the rubber sacs were made of elastomers, use of oil-based lubricants had to be avoided as nucleus fluid.

As can be seen in Fig. 50, off-centre compression tests were also carried out. Here the centre of the top plate was selected as reference point to calculate the strains. Stresses were calculated on the same way described above at axial compression loads. Again, a weaker overall characteristics can be seen, as described earlier in the finite element results. Failure occurred once during testing close to the maximum compressive load of 3000N, accompanied by a loud, popping sound documented earlier in the literature. [11] The rubber sac did not rupture, but bulged out as is seen in a real disc hernia. Pictures of the failed specimen and the setup can be seen in Appendix 14.

Summarising the results, the following answers have been found to the questions raised at the beginning of the chapter.

- The multiplayer structure of the annulus did not prove to have significant effect on the disc behaviour, although changes in the thickness of the annulus do affect the disc response; thicker annulus results in slightly stiffer characteristics.
- Different fibre directions did not have any effect on the disc behaviour in compression. This suggests that the fibre direction may be more important in torsion, where the fibres act directly against the motion.
- The main role of the nucleus is load bearing. Because of its nearly incompressible nature it acts as a hydraulic spring-damper together with the surrounding soft tissues. The structure is very similar to the pneumatic suspension of heavy goods vehicles.
- The changing pressure within the nucleus has a significant effect on the overall stiffness. Higher pressure increases the disc stiffness. The model was especially sensitive to the changes in the initial pressure. The most realistic results were gained by achieving the initial pressure purely by adjusting the disc structure rather than injecting extra amounts of fluid into the nucleus later. Of special importance to medical practice is that injecting fluid into the

nucleus of a prolapsed disc can increase the load bearing capability but it can never fully overcoming the fact that the structure is not intact.

- Changes of the viscosity of the nucleus fluid did not result in any changes in the measured properties.
- Fluid loss in a loaded disc results in a drop in the load bearing capability of the structure, and the disc bulge becomes bigger.
- The disc bulge was reduced by the tighter wrapping around the annulus which acts against the internal nucleus pressure.

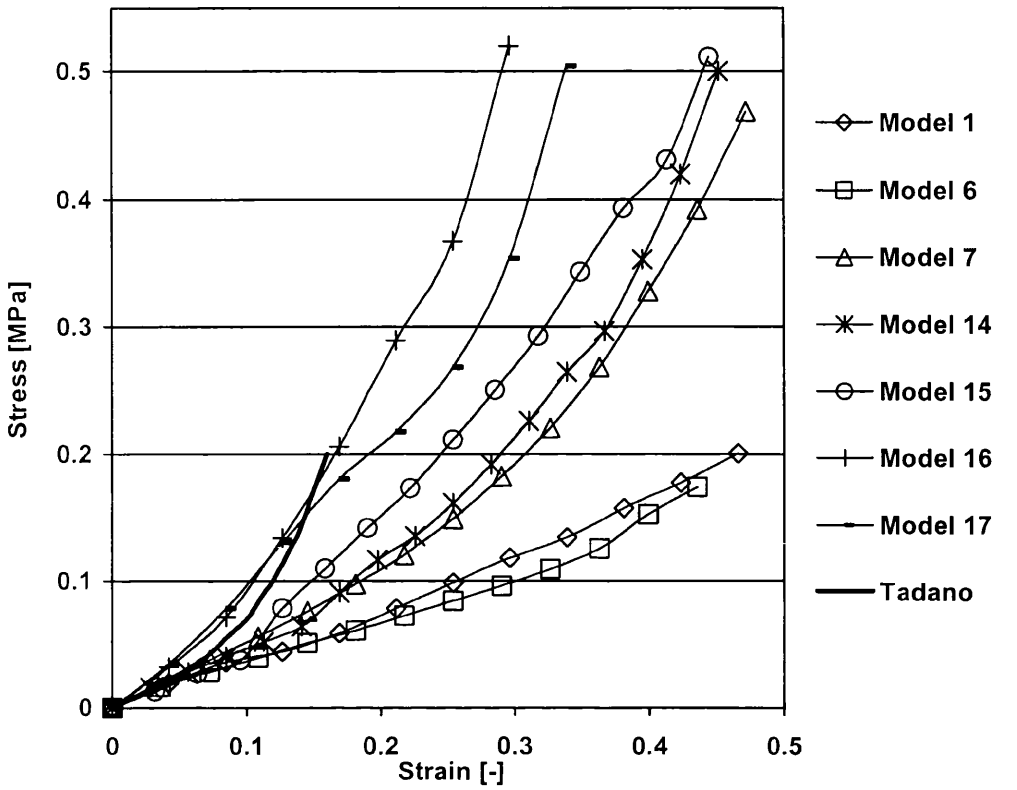

Fig. 47. Response of the large-scale model to compression

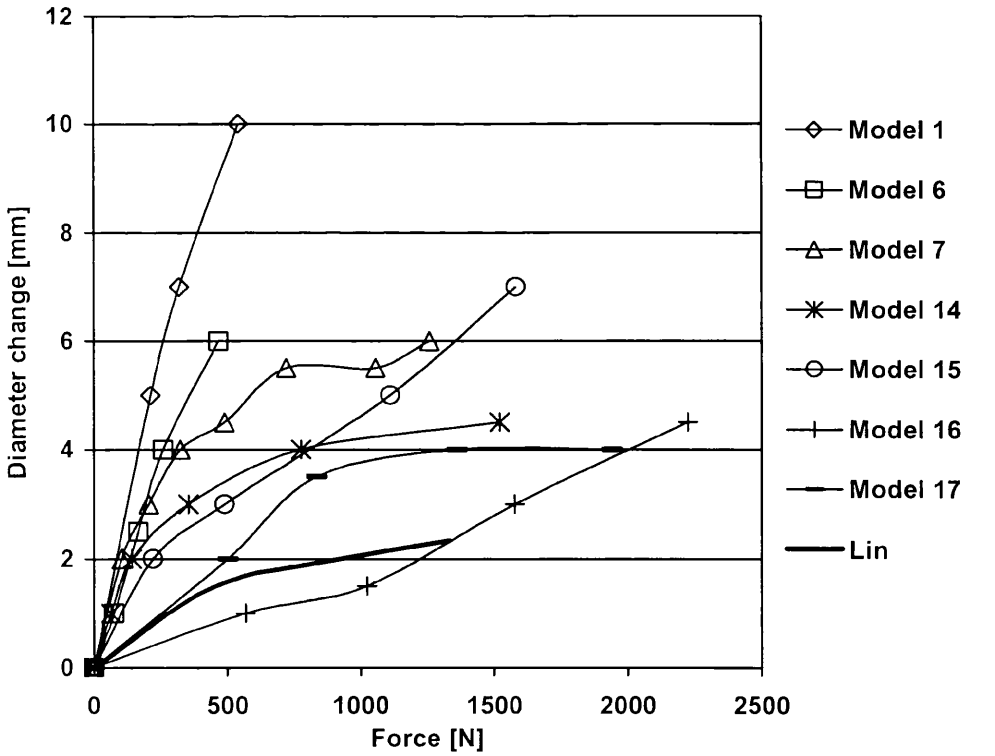

Fig. 48. Diameter change representing the disc bulge

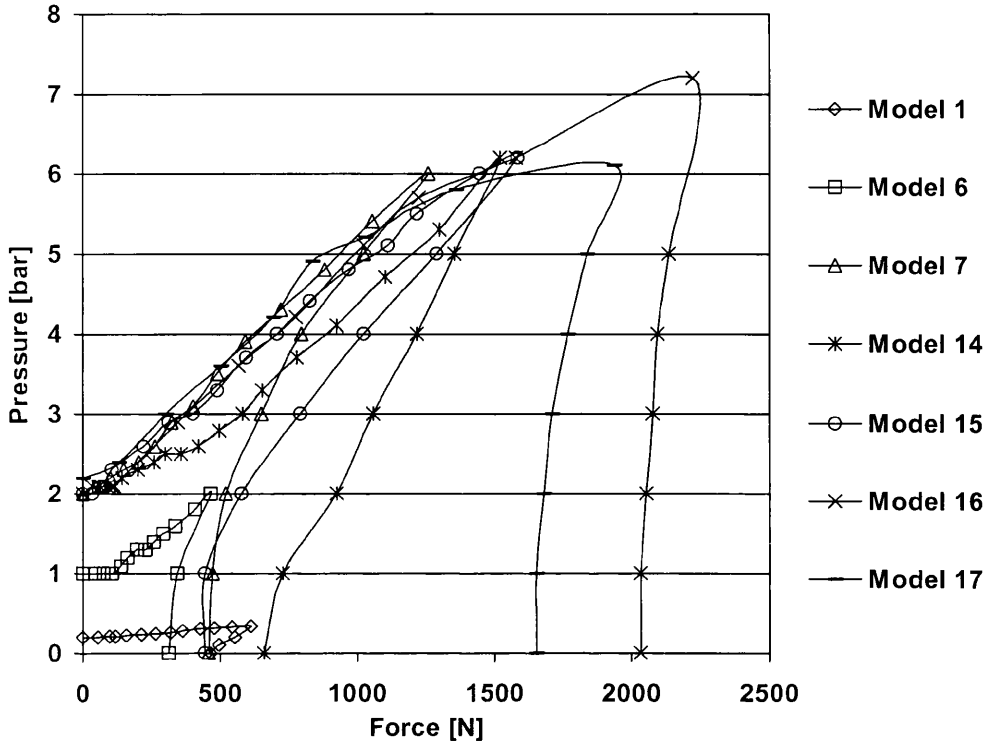

Fig. 49. Effect of fluid loss - pressure change inside the model

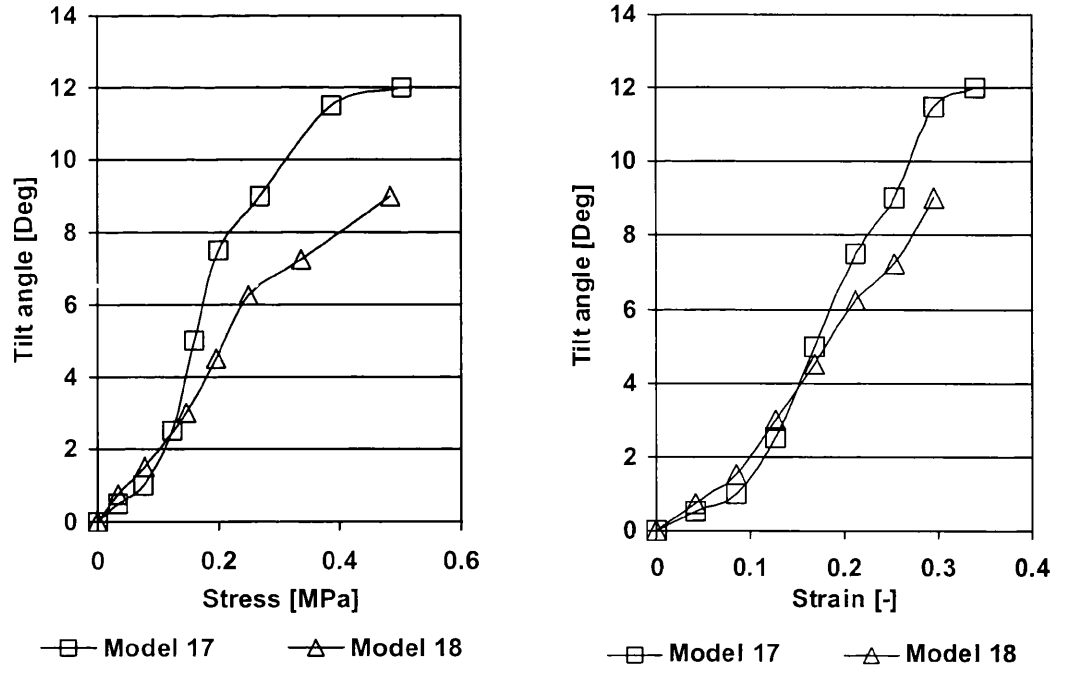

Fig. 50. Top plate rotation at eccentric compression

CHAPTER 10. – MODELLING THE LUMBAR SPINE

10.1 Biomechanically Relevant Anatomy

From a structural point of view the most important element of the body is the spine. It is the equivalent of a chassis in a vehicle, the part to which all the specialised components are attached. It differs from a vehicle chassis, however, by being flexible so that the body can twist and bend forwards and backwards or from side to side. This flexibility is provided by the discs of soft tissue that separate the vertebrae in the regions where the flexibility is required.

Segmental instability exists as a clinical entity although it is poorly understood and imprecisely defined. The normal spine is a relatively stable mechanical structure. Early investigators had assumed the spine to behave as a hinge joint, without translational motion present. As it can be seen on Fig. 51. the spine of the crash test dummies are close to this representation. However the spine is not a perfect hinge joint as it normally allows coupled motion (angular and translational) during flexion and extension.

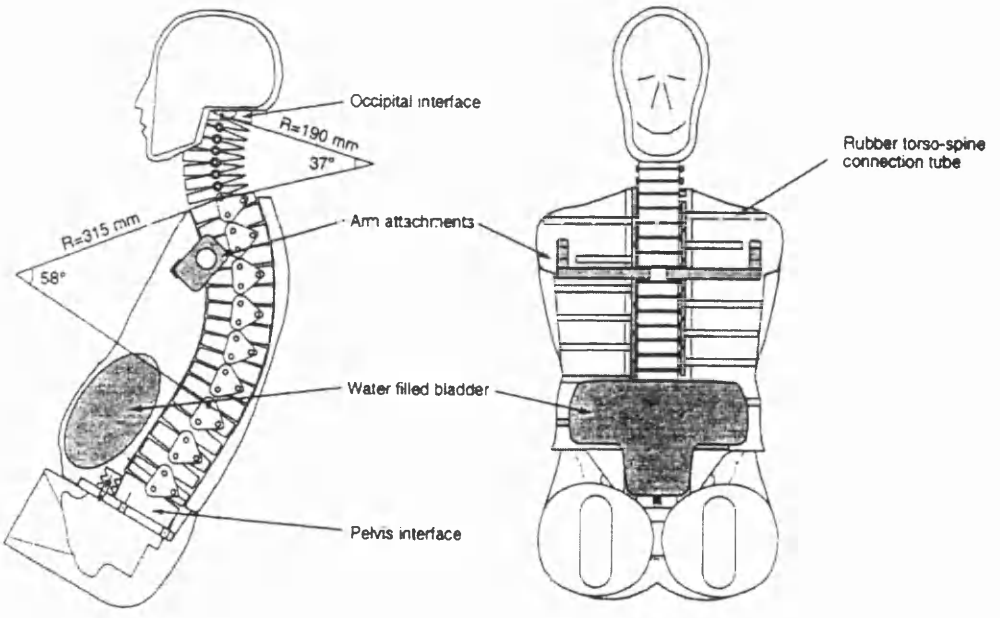

Fig. 51. Spinal column of a rear impact dummy

In this chapter, after a brief overview of the ligaments and muscles of the lumbar spine the process of building an FE model of the full human lumbar ligamentous L1-S1 spine is described in details. The intervertebral discs are modelled following the same analogy described in Chapter 8. The vertebrae here contain the posterior elements as well. This allows the facets to interlock during their movement. The model also contains the ligaments. Some preliminary tests were done on loading the model.

10.1.1 Ligaments of the Lumbar Spine

Ligaments are uniaxial structures; they are most effective in carrying loads along the direction in which the fibres run. In this respect they are much like rubber bands. They readily resist tensile forces but buckle when subjected to compression. Nature has designed the spine in such a way that when the functional spine unit is subjected to different complex force and torque vectors, the individual ligaments provide tensile resistance to external loads by developing tension. The ligaments have many different functions. [51] They must allow adequate physiologic motion and fixed postural attitudes between vertebrae with a minimum expenditure of muscle energy. They also must protect the spinal cord by restricting the motions within well-defined limits. They share with the muscles the role of providing stability to the spine within its physiologic ranges of motion. Finally, they must protect the spinal cord in traumatic situations in which high loads are applied with fast speeds. In these highly dynamic situations, not only is the displacement to be restricted within safe limits, but large amounts of energy that are suddenly applied to the spine must also be absorbed.

Anatomy of the ligaments of the upper cervical region is distinct and quite different [95] from the rest of the spine. This study concentrates on the biomechanically relevant anatomy of the lumbar spine. There are seven ligaments of the spine [50] shown in Fig. 52.

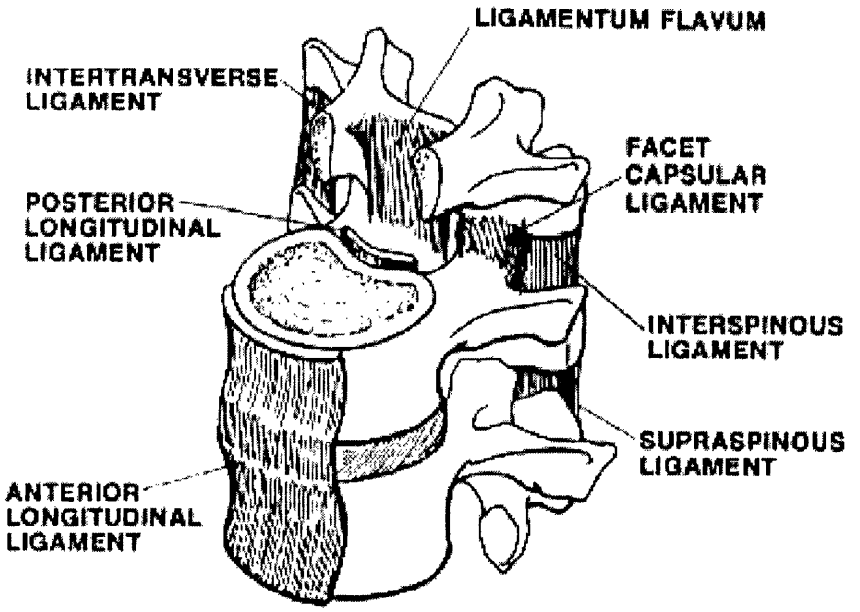

Fig. 52. Ligaments of the lumbar spine

Anterior Longitudinal Ligament

The anterior longitudinal ligament is a strong band, which extends along the anterior surfaces of the vertebral bodies. It is broader below then above, thicker and narrower in the thoracic then in the cervical and lumbar regions, and somewhat thicker and narrower opposite to the bodies of the vertebrae then opposite to the intervertebral discs. It is attached, above, to the basilar part of the occipital bone from which it extends to the anterior tubercle of the atlas, then to the front of the body of the axis and is continued down as far as the upper part of the front of the sacrum. It consists of longitudinal fibres, firmly fixed to the intervertebral discs and to the margins of the vertebral bodies, but loosely attached at the intermediate levels of the bodies. In the latter situation the ligament is thick and fills up the concavities on the anterior surfaces, and makes the profile of the vertebral column flatter. It is composed of several layers of fibres, of which the most superficial are the longest and extend over three or four vertebrae. The intermediate fibres extend between two or three vertebrae, while the deepest reach from one vertebra to the next. At the sides of the bodies the ligament consists of few short fibres, which connect adjacent vertebrae.

Posterior Longitudinal Ligament

The posterior longitudinal ligament is inside the vertebral canal on the posterior surfaces of the bodies of the vertebrae. Above it is attached to the body of the axis, and is continued downwards to the sacrum. Its upper end is continuous with the tectorical membrane. It consists of smooth glistening fibres, attached to intervertebral discs and to the margins of vertebral bodies, but separated between these attachment by emerging basivertebral veins, and by veins, which drain these into the anterior internal vertebral plexuses. At cervical end upper thoracic levels the ligament is broad and nearly uniform in width, but in the lower thoracic and lumbar regions it is denticulated, being narrow over the vertebral bodies and broad over the discs. It consists of superficial layers bridging the interval between three or four vertebrae and deeper layers, which extend between adjacent vertebrae. These deeper layers, sometimes termed as perivertebral ligaments, are in turn close to end, in adult life, fused with the annulus fibrosus of the adjoining intervertebral disc.

Ligamentum Flavum

The ligamentum flavum connects the laminae of adjacent vertebrae and are best seen from the interior of the vertebral canal. Their attachments extend from the articular capsules to the regions where the laminae fuse to form the spine. Their posterior margins come into contact and are to a certain extents united. Small intervals being left for the passage of veins from the internal to the posterior external vertebral venous plexuses. The predominant component of a ligamentum flavum is yellow elastic tissue, the fibres of which, almost perpendicular in direction are attached to the lower part of the anterior surface of the laminae above and the posterior surface and upper margin of the laminae below. The ligaments are thin, but broad and long in the neck. Thicker in the thoracic region, and thickest at lumbar levels. Although they seem to be paired because of a midline cleavage, each is rather like a single structure that extends from the roots of the articular process on one side to the corresponding process on the other. The ligament is composed of a large amount of elastic fibres and represents the most pure elastic tissue in the human body. It has been noted, however, that with aging there is an increase in the relative amount of fibrous tissue.

Interspinous Ligaments

The interspinous ligament is thin and almost membranous, connect adjoining spines, and their attachments extend from the root to the apex of each process. They meet the ligamentum flavum in front and supraspinous ligament behind. They are narrow and elongated in the thoracic region, broader, thicker and quadrilateral in from the lumbar region, and only slightly developed in the neck. The direction of fibres in these ligaments has commonly been described as oblequely dorsocaudal.

Supraspinous Ligaments

The supraspinous ligament is a strong fibrous chord, which connects together the apices of the spine from the seventh cervical vertebra to the sacrum. It is thicker and broader in the lumbar region then in the thoracic, and intimately blended in both situations with the neighbouring fascia. The most superficial fibres of this ligament extend over three or four vertebrae. Those more deeply seated are pass between the two or three vertebrae while the deepest connect the spine of neighbouring vertebra and are continuous with the interspinous ligaments. Between the spine of the seventh cervical vertebra and the external occipital protuberance it is much expended and called the ligamentum nuchae.

Intertransverse Ligament

The intertransverse ligaments are between the transverse processes. In the cervical region they consist of a few, irregular, scattered fibres and are largely replaced by intertransverse muscles. In the thoracic region they are rounded cords intimately connected with the deep muscles of the back. In the lumbar region they are thin and membranous.

Articular Capsules

The capsular ligaments are attached just beyond the margins of the adjacent articular processes. The fibres are generally oriented in a direction perpendicular to the plane of the facet joints. They are shorter and more taut in the thoracic and lumbar regions than in the cervical region.

10.1.2 Physical Properties of Ligaments

In describing the functional role of the ligaments, precise description of their anatomy is necessary. Unfortunately, such information is seldom available from the standard anatomic texts. For each ligament, this should include ligament length, cross-sectional dimensions, three-dimensional coordinates of the attachment points to the vertebra, direction and material properties. Most of these data are presently not available, and the information is very limited.

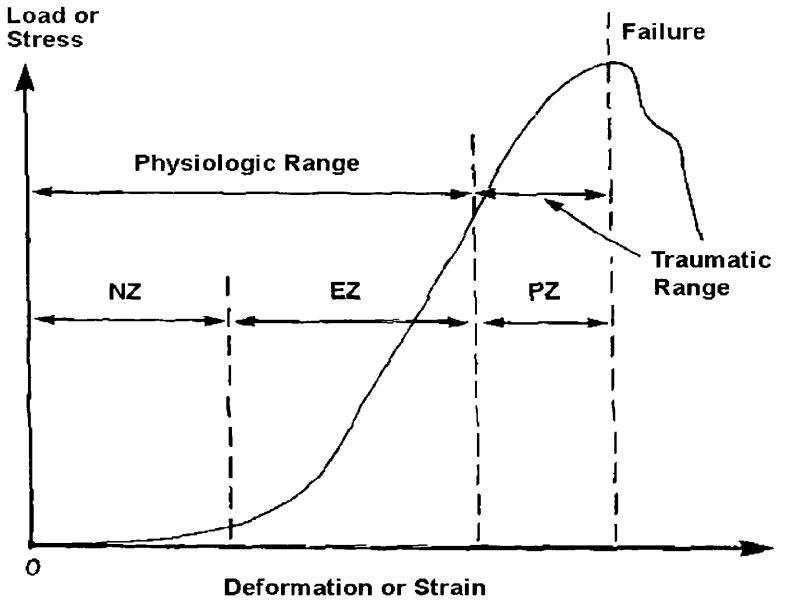

Fig. 53. Non-linear characteristics of ligaments

Besides the strength of a ligament, which is important during spinal trauma, there are other important characteristics that help to provide physiologic functions. One such characteristics is the nonlinearity of the load-displacement curve shown in Fig. 53. The load-displacement curve is usually divided into three regions, the neutral zone (NZ), the elastic zone (EZ), and the plastic zone (PZ). The neutral zone is the displacement beyond the neutral position due to application of a small force. The elastic zone is the displacement beyond the neutral zone up to the physiologic limit. The plastic zone is beyond the elastic zone until failure occurs. The neutral and elastic zones combined together constitute the physiologic range of motion, while the plastic zone is the region of

increasing trauma. Viscoelasticity of ligaments is another important characteristic that is responsible for its shock-absorbing characteristics of spinal ligaments.

10.1.3 Failure Modes

The ligaments transfer tensile loads from bone to bone. When they are subjected to large loads, failure may occur either within the ligaments or in the bone at the point of the attachment.

10.1.4 Muscles of the Lumbar Spine

The spine, with its ligaments intact, but devoid of muscles, is an extremely unstable structure. The lumbar spine has few muscles attached, mostly for stabilizing the structure. Movements of the trunk is achieved mostly with muscles attached to the thoracic level.

Erector spinae

This is more developed in the thoracic region, attaching to the spinous processes in the lumbar region.

Multifidus

This consists of a number of fleshy and tendinous fasciculi, which lie deep in the forgoing muscles and fill the groove at the side of the spines of the vertebrae from the sacrum to the axis. It arises from the back of the sacrum.

Intertransversarii

These are small muscles placed between the transverse processes of the vertebrae. In the lumbar region they consist of two sets of muscles.

The stabilising effect of all of the lumbar muscles can be achieved in the model by strengthening the appropriate ligaments close to the regions where they attach.

10.2 Digitalisation of the Lumbar Spine, Common Problems and its Solutions

Computer Aided Design (CAD) has gone through a major breakthrough in the past twenty years. However, accurate modelling of complex geometries such as the vertebra still remain an almost insurmountable task for engineers. There are several difficulties in data collection, some are technical others are moral. Although current *in vivo* techniques such as X-ray, MRI, CT or Ultrasound data are giving more accurate, high-resolution images of the human skeleton and tissue with less scatter, the interface between these data and CAD software remains undeveloped. Measurement of a human lumbar vertebra *in vitro* is also difficult. Commonly used coordinate measuring machines often require specially customised tips to be able to reach all necessary points. This makes the measurements expensive and time consuming.

Another method used by the Visible Human Project is scanning the dissected body of one male and one female dataset. Here they obtained images of the cross-section of the body, slicing the frozen cadaver carefully into 1- 0.3 mm sections, then photographing them. Probably this method gave the most accurate, true-colour images. However, the resolution in the direction perpendicular to the cutting surface is limited, and some of the samples were also smeared in the direction of the cut. Another problem emerged from the posture of the body. Throughout the measurements the body must stay in one, fixed, preferably neutral posture. Tilting the body in any direction makes the CAD model generation, and especially the work with the model later, very difficult due to the limitation of current geometrical and mathematical tools in describing free surfaces.

10.2.1 CAD Model Generation

Generating the CAD model of a full lumbar spine is not an easy task. Here a detailed description is given about the methods used to generate the full CAD model. The geometry of the lumbar spine is complex. [96] The spinal column has a well-defined recognisable curvature in the mid-sagittal plane. Furthermore, each

vertebra is different in its alignment and posture. The position of the facets and the shape of the arches varies quite distinctively. It is essential to define a unique local coordinate system for each disc and vertebra to follow the curved centre line.

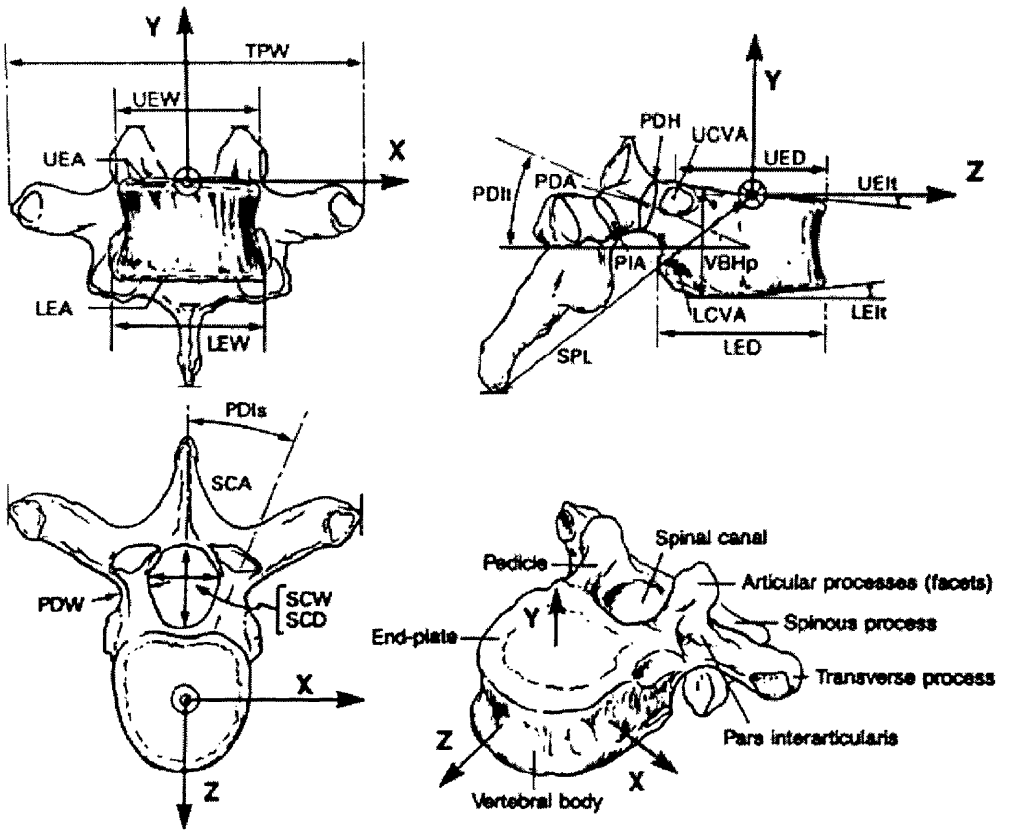

Fig. 54. Recommendation of documenting vertebra dimensions (Each dimension is defined by a mnemonic consisting of three capital letters followed by a single lowercase letter, when needed. The first two letters represent the name of the anatomic part; the third letter represents the dimension. TP=transverse process; UE=upper end plate; LE=lower end plate; PD=pedicle; SP=spinous process; SC=spinal canal; PI=pars interarticularis; VB=vertebral body; W=width; A=area; D=depth; H=height; I=inclination. Suffixes are: t=transverse plane; p=posterior)

The first problem rises actually in determining the exact location of this centre line and, together with it, the origin of the local coordinate system. To fully understand the problem, we have to describe the main dimensions of the vertebra in the global system. Several studies dealt with this problem, and up to a certain complexity, a range of suggestions were made. Fig. 54. shows the recent recommendation of documenting the dimensions of a vertebra [96]. In our model the origin of the local coordinate axes of the individual vertebrae were chosen to be at the point where the midsagittal plane, the bottom plane of the vertebral body

or the disc, and the frontal arch of the spinal chord canal on the back of the nearest vertebral body meet. The x-axis points to the lateral and the y-axis to the posterior direction. The z-axis points upwards towards the head.

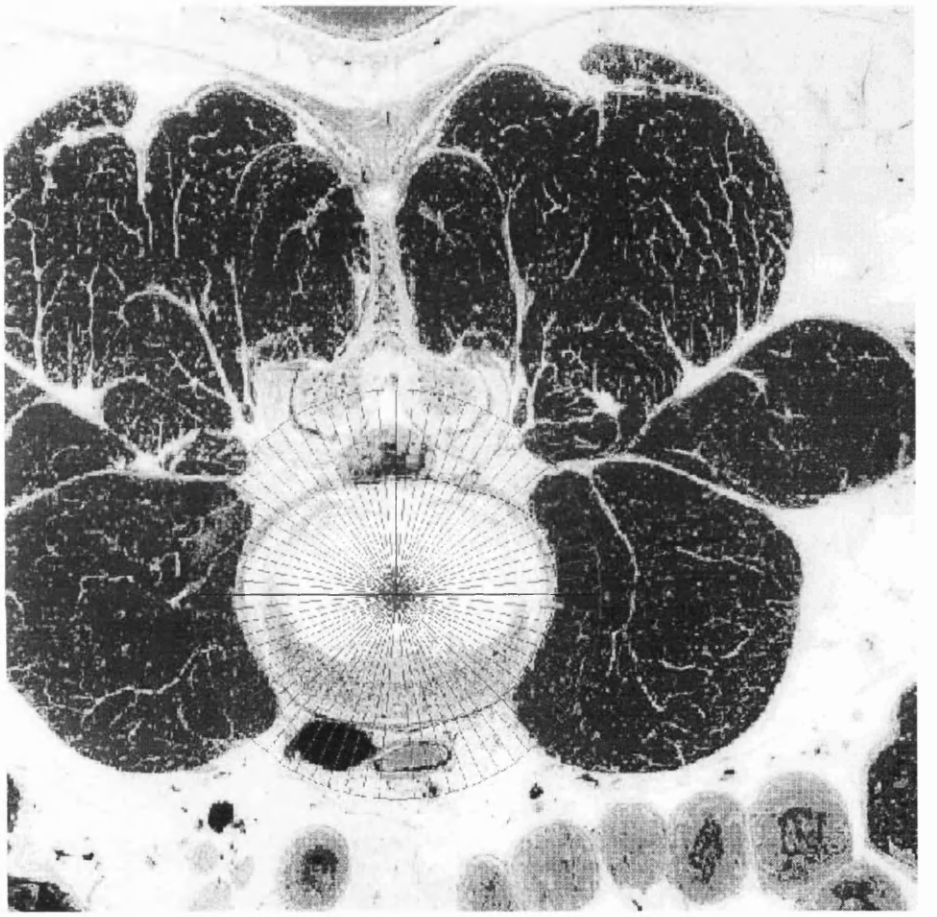

Fig. 55. Visible human project image with reference grid

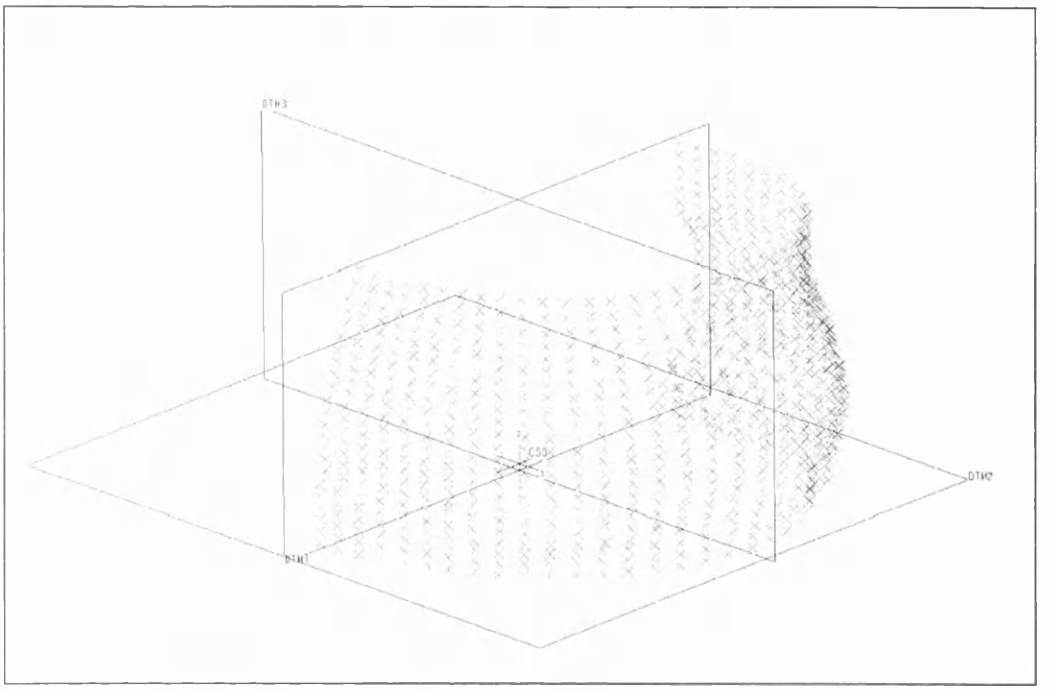

Fig. 56. Nodal dataset

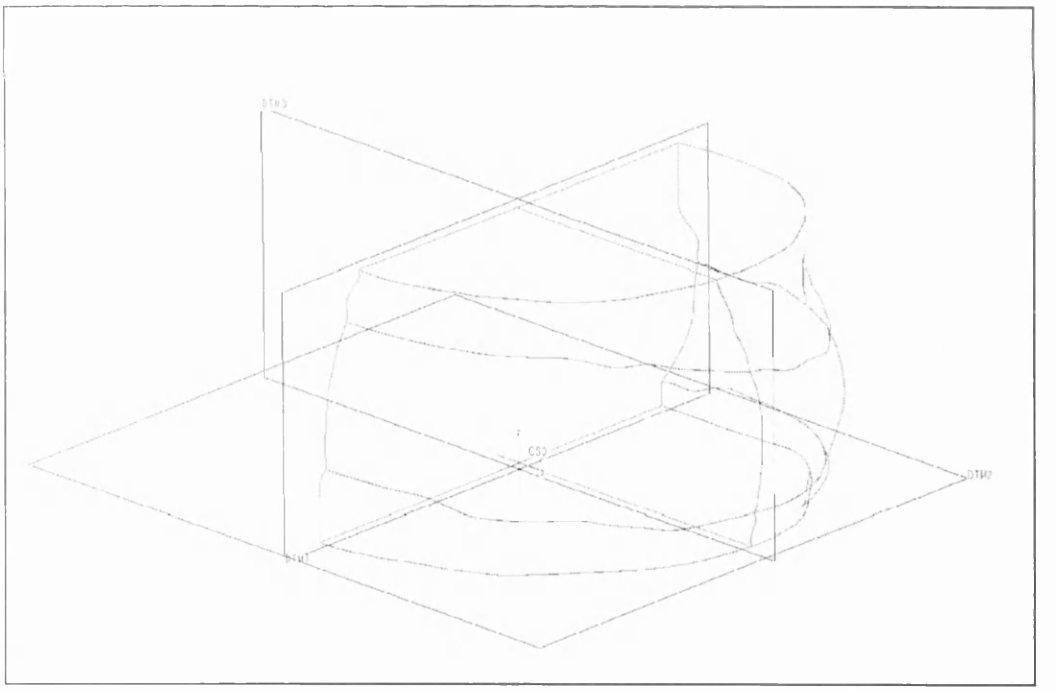

Fig. 57. Wireframe

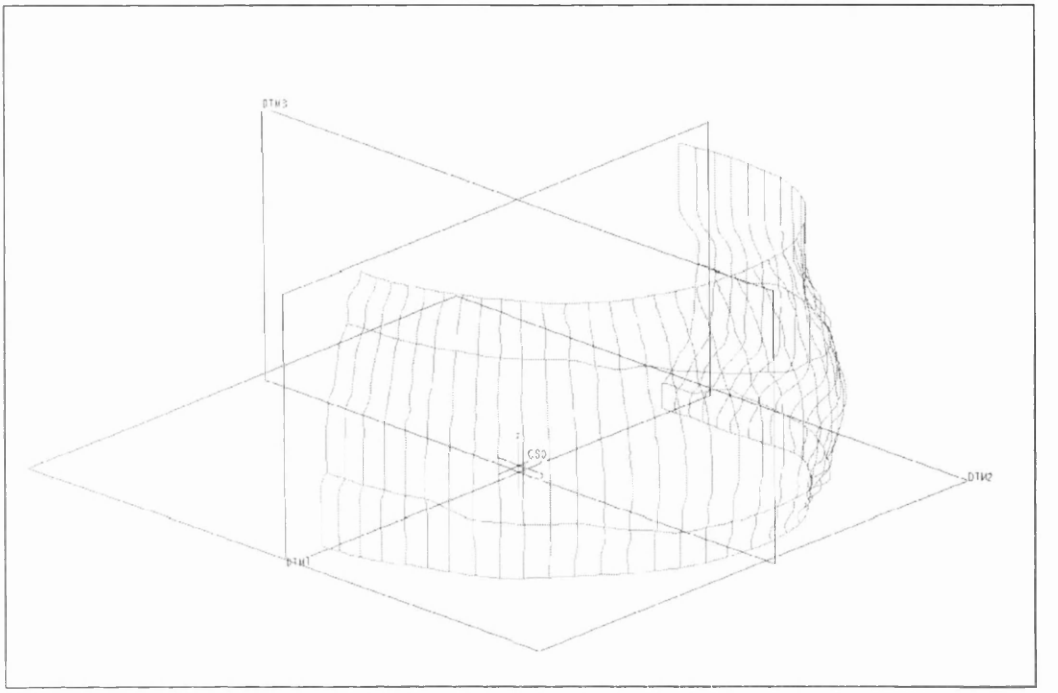

Fig. 58. Surface Model

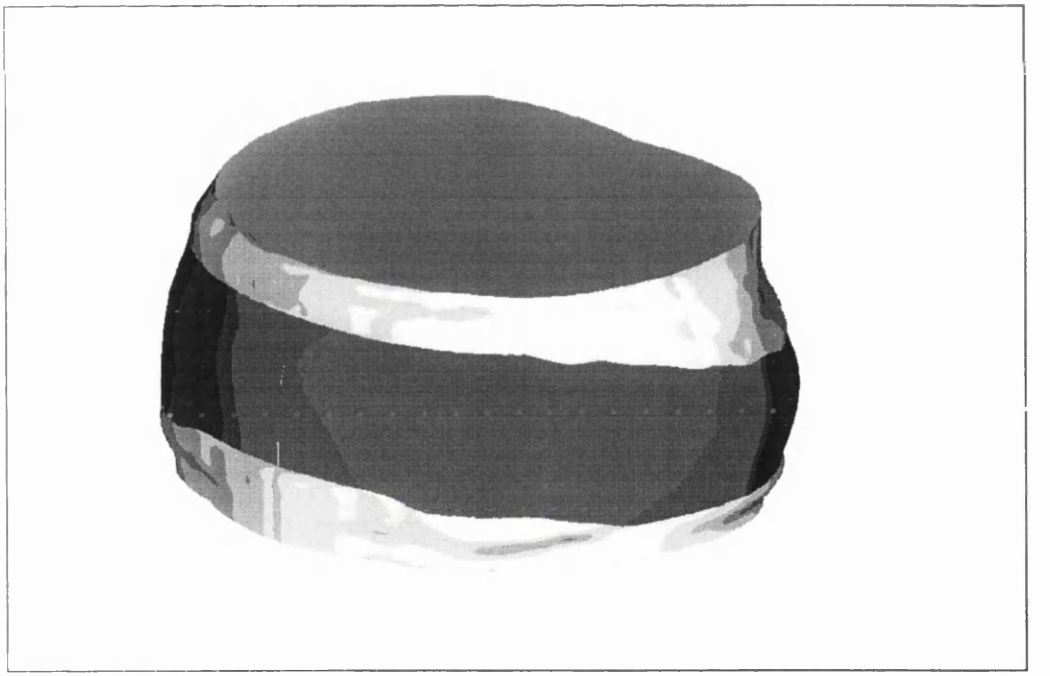

Fig. 59. Solid Model

Altair Hypermesh® and LS-Dyna3D® need a surface model as a geometry input. The surface boundaries have to be closed with no gaps between the

coincident surfaces. Furthermore, Hypermesh can work only with surfaces, which have three or four sides only, eg. defined by three or four lines forming the surface boundary. Throughout the model generation the user has to pay attention to this future requirement. This restriction also applies to volumes defined by surrounding surfaces. Since the non-degenerated healthy spine can be considered to be symmetric in the midsagittal plane, only half of the spine was digitised, then mirrored. To obtain the geometry as accurately as possible, reference nodes were selected on the disc boundary, which were then digitised from the VHP images. The process is shown in Fig. 55-59. The centre of the x-y coordinate system on the VHP images was moved from the top left corner to the centre of the disc or vertebral body at that level on the z-axis. The centre of the disc was defined at the intersection of the midsagittal plane and the line marking the greatest lateral diameter. These coordinates are defined in the global coordinate system. Coordinates of the left side boundary of each disc and vertebra were taken at each level in every 10°. The left side boundary was chosen because here the boundary line is more distinctive then on the right side due to the slicing direction. The distance between the levels, or the vertical resolution of the VHP male dataset, is 1 mm. The body of the VHP male was tilted sideway by 2°, which results in the spinal column following this alignment as shown in Appendix 15. To compensate this, the distance of the midsagittal plane nodes from the imaginary centre plane was calculated, and then all nodes were shifted in the x-direction by that value. The midsagittal plane is given by the connecting lines of the centre points at the front and back arches of the vertebral bodies or the discs. The coordinate nodes obtained were connected to a wireframe and the necessary surfaces were generated. The outline of the model can be seen in Fig. 60. The wireframe of the model is shown in Fig. 61.

Fig. 60. Outline of the solid model

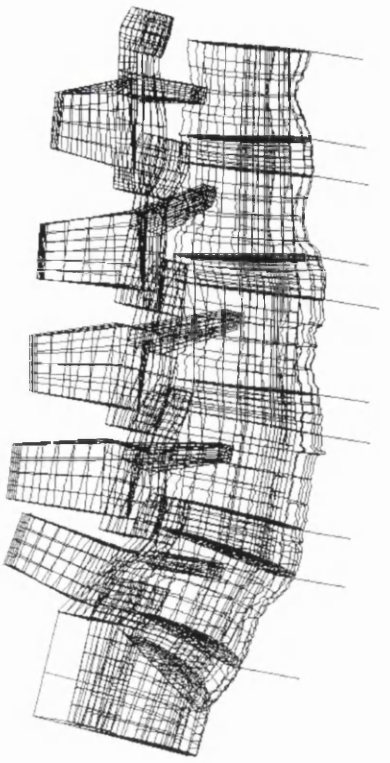

Fig. 61. Model surface wireframe

So far, with the above process, the three-dimensional surface model of all vertebral bodies and discs of the lumbar spine is ready, but the processes are still missing from the model. The most important surfaces of the processes are the facet joint surface. Since interlocking and distribution of loads happens on this joint, it is important to model the shape and alignment of this joint accurately Facet alignment in the model compared to literature data [51] can be seen on Fig. 62. Coordinates of 5 nodes of both facet joint surfaces at each level were taken. The locations of the tips of the spinous and transverse processes were also taken, and their thickness was also measured. The posterior boundary of the neural arch was also digitised. Carefully analysing the disc geometry, a simplified model of the neural arch was generated. Although the model of this region is simplified, it stays very accurate in the biomechanically important regions like the facets and the processes, where ligaments attach. Fig. 63. shows one vertebra with the facets.

After adding the top surface of the sacrum, the result is an accurate model of the whole lumbar spine. The full FE model can be seen in Appendix 16.

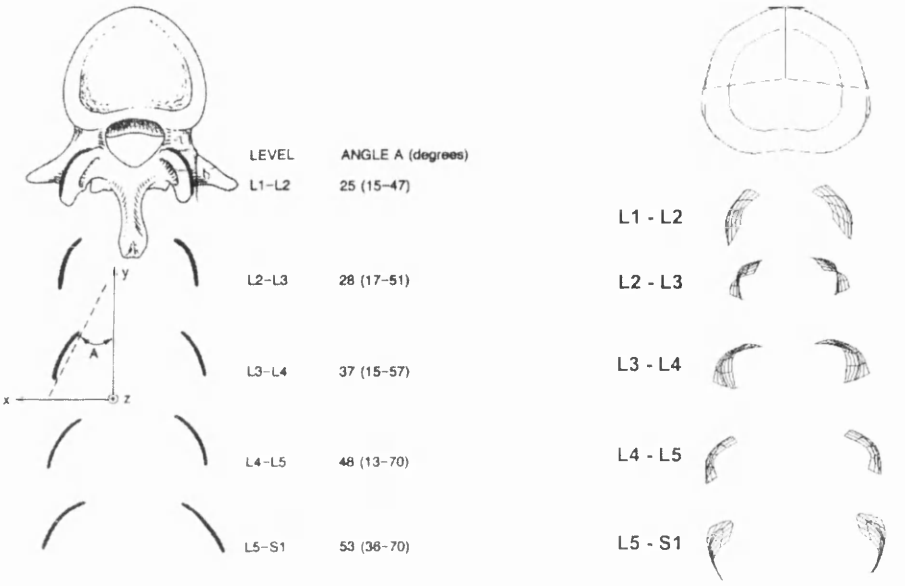

Fig. 62. Alignment of the facets in literature (left) and in the model (right)

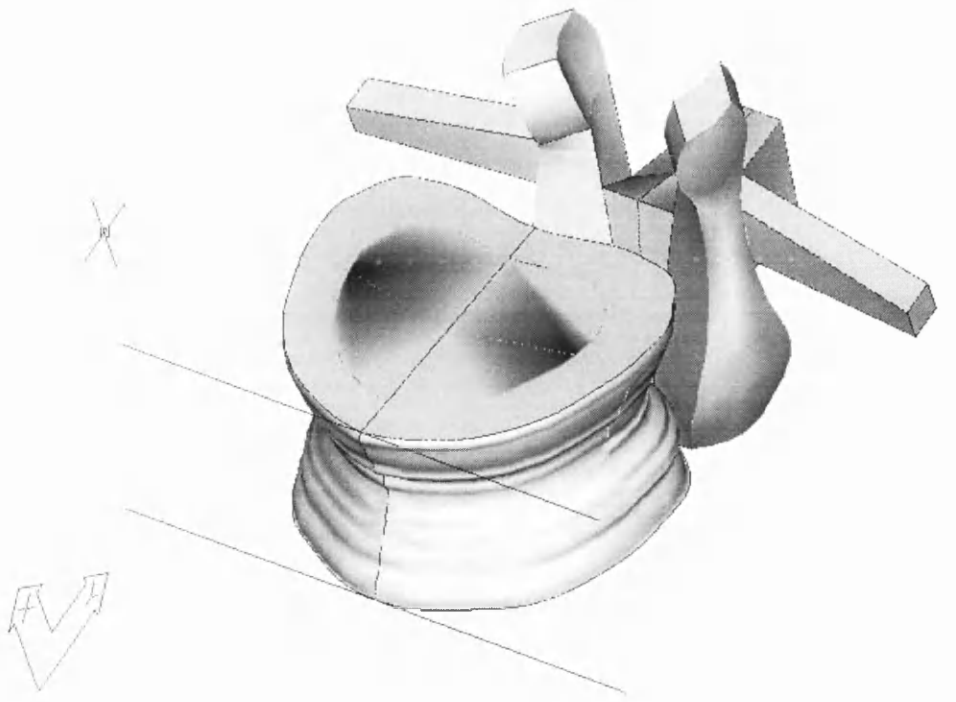

Fig. 63. Render view of one vertebra with its processes and facets

The next step of the FE model generation is the mesh generation. After importing the model as an IGES to Hypermesh, it was meshed with solids. The geometric non-linearities of the spine and the neural arch again make the meshing procedure a very challenging task. The main difficulties rise from the curvature of the spinal column and the non-centralised alignment of the nucleus pulposus. Since the boundary nodes of the individual spine components have to coincide, the existing mesh becomes a parent of the one to be created at the neighbouring regions. There are certain properties to be inherited by the next mesh. Since the lumbar spine consists of 11 segments, the inherited properties might develop a high level of distortion in the mesh at the last few segments. The distortion already became noticeable within 5 segments. This effect can be devastating for meshing the whole spine column. The level of distortion can be reduced using a less fine mesh, or a more simplified geometry. The model can be seen on Fig. 64. at the middle of the mesh generation.

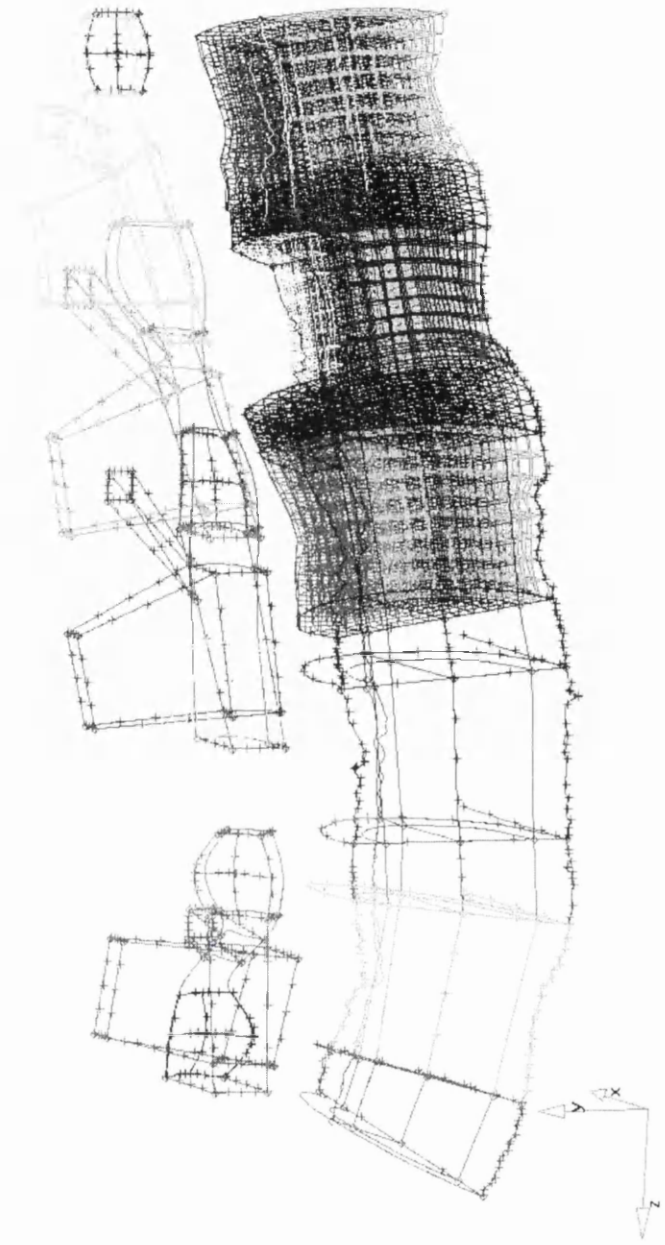

Fig. 64. Mesh generation with the Hypermesh software

After meshing, the model was imported into LS-Dyna, where material properties were allocated to all the individual components. The code for an intervertebral disc can be seen in Appendix 17. For simplicity, and keeping the calculation time low, the ligaments were modelled as linear springs. The stiffness of the ligaments was obtained from the literature. [85] Table 7. shows the model summary.

Table 7. Summary of the lumbar spine model

Total number of elements	28678
Total number of nodes	35137
Total number of beams	384
Total number of quads	224
Total number of hexagons	28070
Total number of master contact segments	350
Total number of slave contact segments	300
Height of L1-S1 between the top vertebra surfaces [mm]	193.00
Height of the full model [mm]	216.80
Ligament data	*E [Mpa]*
Ligamentum Flavuum	10
Anterior Longitudinal Ligament	20
Posterior Longitudinal Ligament	20
Interspinous Ligament	50
Transverse Ligament	50

As there is very few data available in the literature on the behaviour of the full lumbar spine, [21, 97] a simple test was chosen to see the feasibility of the model. The situation simulated is showing the spine aligning from the unloaded posture, directly implicated into the model from the nature of the VHP dataset to the normal standing position of the body, loaded by the weight of the trunk. Similar physical conditions can be found in astronauts returning from zero gravity, or on certain fun-rides, when the body returns from a horizontal position to vertical. The calculation time for such a big model exceeded 6 hours on the DEC Alpha 400 personal workstation. Finding the steady state for certain variables can take several days depending on the loading conditions.

The boundary conditions were defined and loads were added. The sacrum was constrained in all directions, the vertebrae were constrained against x-displacements. A relatively small follower force of 400N was added perpendicular to the centre of the top surface [98] of the L1 vertebra simulating the weight of the trunk. To speed up the simulation, gravity of 9.81m/s was also added. To reduce

shockwaves bouncing back from the constrained sacrum, global damping was also added to the model. Based on the first results, it could be assumed, that the sacrum by its size and geometry acts as a final damper of shockwaves on the spinal column, and significantly reduces the large, traumatic springback effects. With this it is protecting the vertebrae from incredible high load amplitudes, which could arise as a result of signal interference magnifying shockwaves. Similar role of the tail in the animal world is already known.

The vertical and horizontal displacement of the L1 vertebra was recorded. Since there is a lack of literature data, it is hard to evaluate the results obtained. As it was expected, the spinal column has bent backwards. The horizontal displacement of the L1 vertebra was 2mm, the vertical displacement was 0.2mm. These results show how well our spine is distributing the load, minimising the vertical displacement of the vertebrae. Fig. 65. shows the model in the deformed state. As shown by the dark regions, the predicted location of the highest stresses in the intervertebral discs is posterior. The presented model of the full lumbar spine confirms the success of the novel material description interacting with other components on a larger scale. With more powerful processing power computational simulation of the full spine can soon become reality.

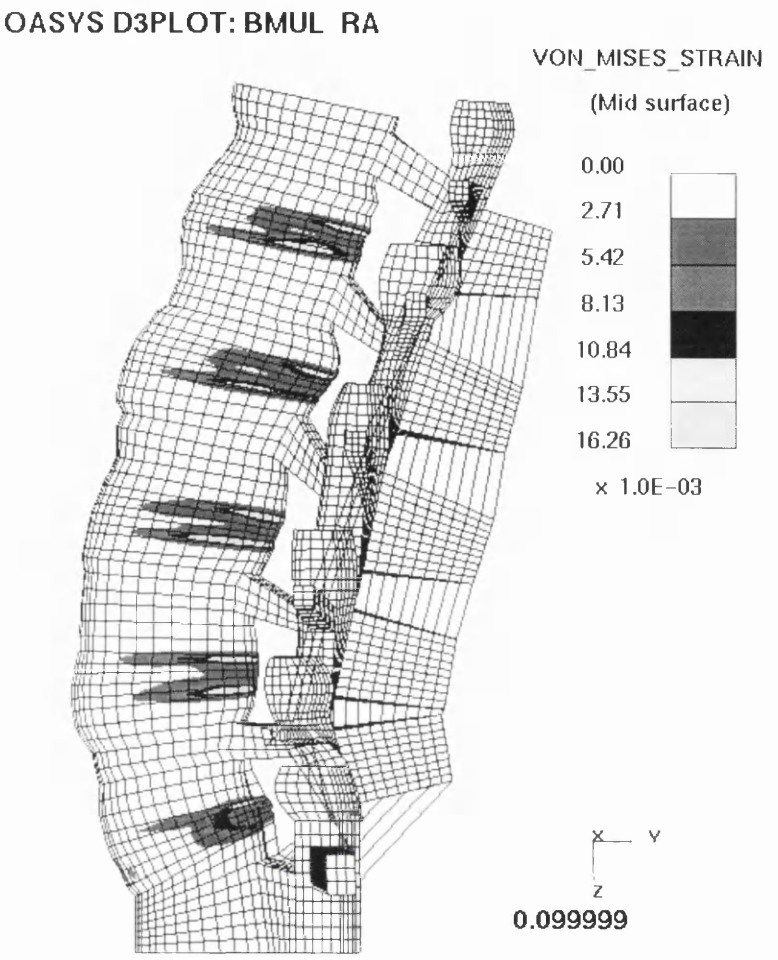

Fig. 65. The lumbar spine after deformation

CHAPTER 11. - CONCLUSION

Throughout the presented PhD study the human lumbar spine and its individual components were investigated. The aim of this study was to formulate a material description for intervertebral discs suitable for finite element solvers. The material had to be validated for three-dimensional movements of the disc. Therefore, special attention was given to the intervertebral discs in all aspects. The structure, behaviour, kinematics, dynamics, and material characteristics of the disc, together with their measurement techniques were studied. The feasibility of implementing the nucleus and annulus properties into finite element solvers was thoroughly investigated. To fully understand the link between the different load cases and the disc response, a wide range of tests were launched.

The human lumbar intervertebral disc has a unique structure, and it can not be substituted with any other samples. As there are great difficulties in obtaining and testing human cadavres, tests on real discs were excluded in this study. The necessary material property data was obtained from the available literature. For validation, the geometry and boundary conditions were obtained from carefully selected, independent measurements. For comparison, where it was possible, key values available for direct measurements were selected from the literature to reduce the secondary errors.

The basis of the study is formed by a novel approach to implementing a fully non-linear, anisotropic material into the LS-Dyna3D dynamic finite element solver, presented in Chapter 8. This was supported by a finite element study on an L2-L3 lumbar spine motion segment validating the material formulation and the material parameters used throughout various tests on the model, presented also in Chapter 8. In the model, the novel material definition simulated the annulus fibrosus. It was capable of simulating the full non-linearity of the material, together with its anisotropic properties. It is also possible to define different tensile and compressive properties for any local coordinate directions within certain limits; the freedom of this option is restricted by the mathematical description of the input curve. An experimental study, presented in Chapter 9, was done on a large-scale model of the L2-L3 motion segment. Here, the interaction between the individual structural components, and their influence on the overall

disc behaviour were investigated. Analytical studies are presented in Chapters 7. and 8. on the disc components and their effects on some disc parameters. Finally, a detailed FE model of the full lumbar L1-S1 spine together with the posterior elements of the vertebrae and the attaching ligaments was built and tested. Only preliminary results were obtained from this study, which are presented in Chapter 10, since running the model needs exceptional computational power.

Throughout the simulations, the features of the disc, which are governed by the individual properties, were of special interest. The material property sensitivity studies resulted in the following conclusions presented below in Table 8.

Table 8. Summary of the results, novel findings, and data reconfirmed. (L-Literature data, F-Finite Element Analysis result, A-Analytical result, E-Experimental result; (√) shows if the same result appears in an independent study, while (•) marks the results of the present study together with the page number)

Results, findings, reconfirmed data	**L**	**F**	**A**	**E**
Small differences in the location of the compressive load on the top vertebra surface result in significant differences in the overall disc response.	√	• 38		• 115
The accuracy of approaching the non-linear material properties of soft-tissues with multi-linear characteristics is low, since there are fast and significant changes in the value of the Young's modulus. Non-linear material description is necessary.		• 99		
The mechanical effect of the cartilaginous end plate as a load-bearing component is negligible.	√	•√ 80		
Modelling bones as rigid bodies generates extremely high resultant stresses in the surrounding material, especially at large compressive loads. The FE simulation showed that the cause of this effect was that the lack of the inward bulging of the end plate generated high nucleus pressure. The bulging end plate in fact generates space for a reasonable volume of nucleus fluid compared to the total disc volume, reducing the pressure within the nucleus, which presses the surrounding components outwards. This process then results in lower stresses in the annulus, and smaller disc bulge.	√	• 81		

Results, findings, reconfirmed data	L	F	A	E
Highest stresses occur at the postero-lateral side of the disc in most of the real-life load cases.	√	•√ 82		
Non-linearity of the annulus fibrosus is one of the key elements in disc FEM.	√	•√ 102		
The radial annulus stiffness is secondary, it mainly affects the disc bulge. Increasing the stiffness increases the bulge.		• 94		• 115
Changes in the fibre direction throughout the deformation of the disc do not affect the disc response to compression or bending significantly, despite changes in the E_z / E_t ratio being significant at very large loads. It is believed that fibre direction has higher importance in torsion.	√	• 96	√	
Changes in tangential stiffness of the annulus affect the disc bulge. Higher stiffness results in a bigger bulge.		• 102		
Inhomogeneity of the annulus does not affect the overall disc response in compression, flexion, extension, or lateral bending.		• 96		
Vertical stiffness of the annulus is the key element in disc FEM for compressive loads. This finding is not valid if shear or torsional loads are introduced.	√	•√ 102		
Shear properties are linear or nearly linear. Increase of the shear modulus results in smaller disc bulge.		• 105		
Increase in nucleus density slightly, but not significantly, increases the overall stiffness of the disc.		• n/a		• 114
Stiffer sac material had no effect on disc response, and the sac remained ideally elastic compared to the surrounding structures.				• 114
Increase in nucleus pressure significantly increased the overall stiffness, and reduced the absolute change in the disc bulge. In an unloaded state, it resulted in an increased disc height, rather than increase in the disc diameter.	√		√	• 114

Results, findings, reconfirmed data	L	F	A	E
Nucleus volume change has little effect on the disc bulge.	√		• 73	• 114
Stiffer strings simulating the annulus fibres around the nucleus resulted in no significant change in the overall stiffness in compression.				• 114
Tighter wrap of strings around the annulus significantly increased the overall stiffness, and decreased the bulge. It also increased the pressure inside the disc. This phenomenon has proved to be the key parameter in building the experimental disc model.				• 114
Vertical load bearing of the annulus occurs only at extremely high loads.		• 96		• 114
Load bearing capability of the disc reduces as the nucleus pressure drops.	√			• 114
Up to a certain compressive force, the outside annulus boundary is under small compressive stresses. Further increasing the load results in the annulus being slightly tensed.	√	• 82	• 73	
Changes in the area of the outer annulus boundary caused by compressive and tensile stresses in the region are negligible. Note, that higher stresses and strains exist within the deeper annulus.	√	• 82	• 73	

With the help of the presented material description for the disc annulus, the mechanical behaviour of a particular intervertebral disc now can be simulated more accurately. The third-order polynomial form of the model input enables the user to implement progressive non-linear characteristics in an easy, user-friendly way, and handles this type of characteristics better than the existing models. Most large deformation material laws are limited to work with regressive characteristics, and become instable if the input characteristics happens to be progressive. One of the best examples is the Mooney-Rivlin material. The material law is fully non-linear and anisotropic. It is compressible, which increases the numerical stability of the subroutine. There is a possibility, within certain limits, to define different characteristics for tension and compression.

Using the above material law modelling the annulus fibrosus in intervertebral discs, the response of the disc to complex loading becomes significantly more accurate, especially if the disc is not only subjected to compression, but bending moments and shear forces are also present. The novel approach enables full, three-dimensional simulation of the disc movements in dynamic situations. Furthermore, this can be extended to modelling of the full human spinal column, which can be extremely profitable at simulating the movements of the human spine in a wide range of dynamic situations. Some examples can be spinal movements in car crash tests, and seat designs, particularly in aerospace modelling of the ejection process or crash landing. The use of the model can be extended generally to any organic soft tissue. Combining it with the already implemented material laws, like poroelasticity, viscoelasticity and viscous damping, plasticity, or failure models, the number of applications are almost infinite. The disadvantage of the model is that it is ideally elastic, so there is no energy loss throughout the cyclic movements of the modelled body. Adding viscous damping to the system is one way to overcome this problem. For nearly incompressible materials, viscous damping also reduces hourglassing.

Tests have been run investigating the effect of the accuracy of the input data. Significant results were gained, especially showing the effect of non-linearity. The result shows that the new material formulation has higher accuracy in simulating the three-dimensional movements of the intervertebral disc in a wide range of dynamic loading situations. Under complex loading the effectiveness of the approach on the input curve has great significance and results in more accurate prediction of displacements under load. Furthermore the number of input data required was reduced significantly by the third method. This, together with the more straightforward mathematical description, saves enormous time for the user.

The shear properties of the annulus material were also tested, together with the orthotropy. Throughout the simulations the features of the disc which are governed by these properties were of special interest. Increasing shear modulus decreases the change in the disc bulge. This is balanced by the orthotropy, where introducing orthotropy increases the bulge of the disc annulus. Therefore further

investigation of the shear characteristics and the changes in the directional properties of the annulus fibrosus would be useful as it could lead to excellent disc simulation on the micro structural level for any loading situation.

In comparison with previous FE models Model 3 represents a considerable advance on accuracy for both axial and eccentric compression. The form of the input for the stress-strain properties is also well advanced compared to the recently used techniques giving an easy-to-use interface to the user. Although the shear properties show differences the results and behaviour does not stay behind compared to previous studies. The mesh represents the newest technology with relatively low number of elements. The disc geometry is equally detailed as it can be seen in the recenty generated models.

Validation of the model by comparison of its response with literature data shows excellent matching in terms of vertical displacement for both axial and eccentric loading. However, similar comparison of the shear values and the disc bulge shows some differences. Therefore further investigation of the non-linear shear properties of the annulus fibrosus could lead to improved simulation. Using the new material formulation did not increase computation time compared to the built-in material models. Nevertheless a greater accuracy was proven. The validation results of the disc confirm that the presented way of implementing non-linear materials into FEM solvers is a promising approach to full computational simulation of non-linear anisotropic materials such as the annulus of the intervertebral disc.

APPENDIX 1. – THE HUMAN SPINE

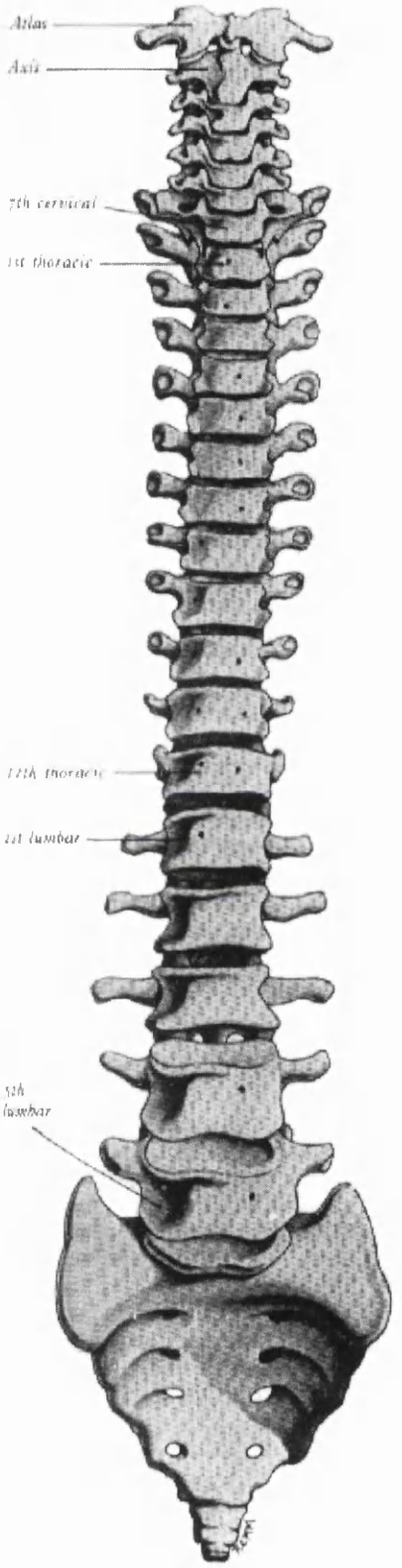
Atlas
Axis
7th cervical
1st thoracic
12th thoracic
1st lumbar
5th lumbar

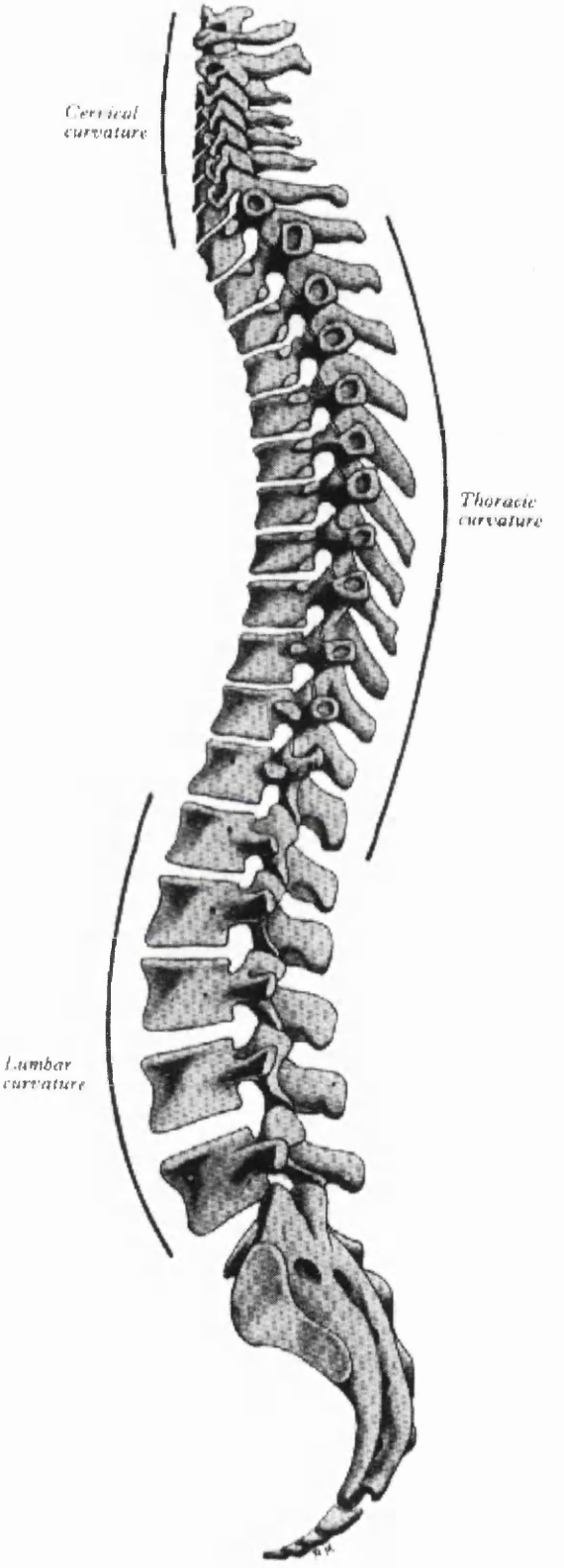
Cervical curvature
Thoracic curvature
Lumbar curvature

APPENDIX 2. – SCHEMATICS OF THE LARGE-SCALE EXPERIMENTAL MODEL

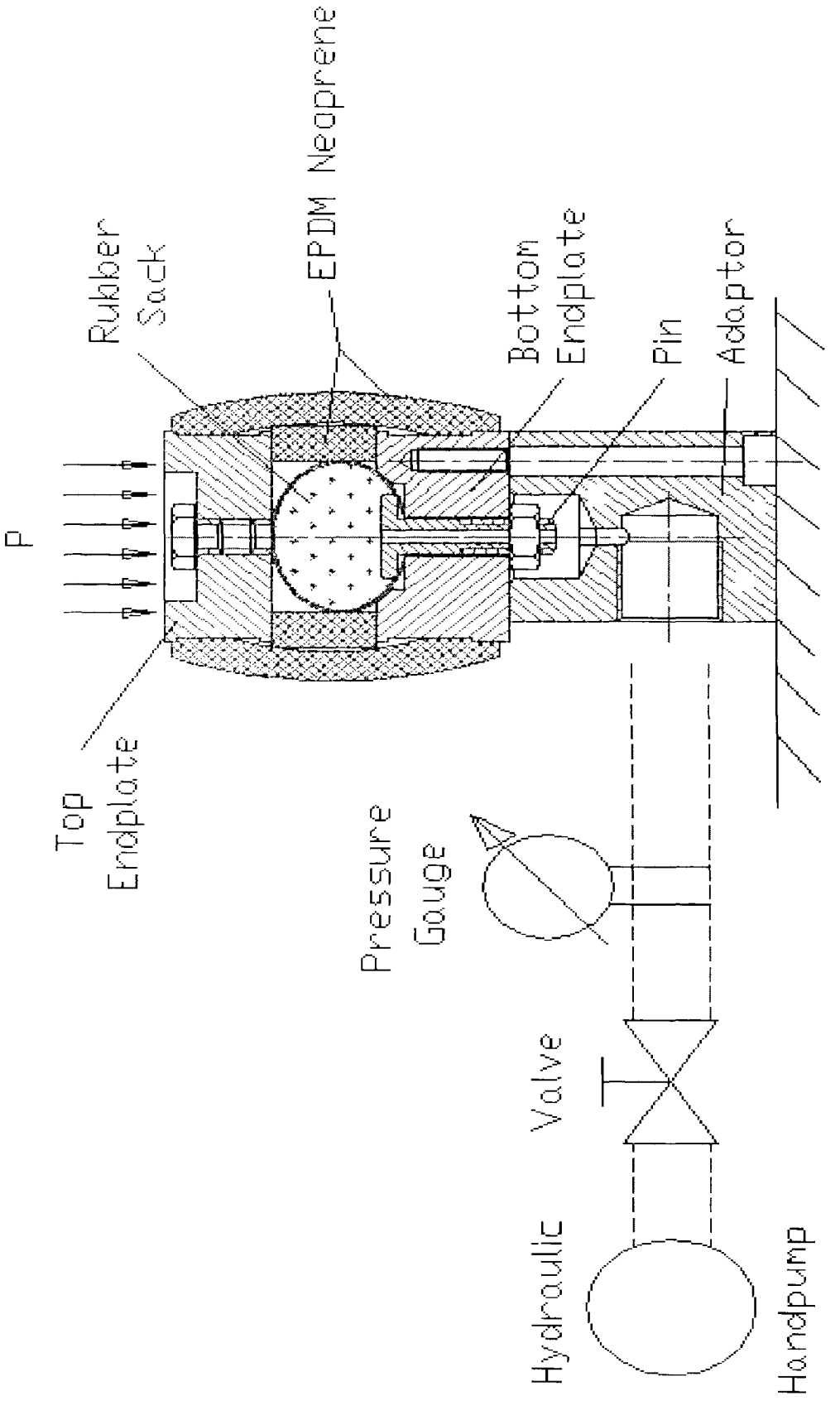
P
Rubber Sack
EPDM Neoprene
Bottom Endplate
Pin
Adaptor
Top Endplate
Pressure Gauge
Hydraulic Valve
Handpump

APPENDIX 3. – MATERIAL DATA

Linear Anisotropic Behaviour

The most general linear relationship between stress and strain can not be expressed in terms of the stress and strain matrices. The general relationship would require a four-dimensional array of stiffnesses or compliances. This can be represented in tensor notation, as will be seen. If the stresses and strains are represented by column vectors, then the relationship can be written in matrix form as

$$\begin{bmatrix} \sigma_{xx} \\ \sigma_{yy} \\ \sigma_{zz} \\ \tau_{yz} \\ \tau_{zx} \\ \tau_{xy} \end{bmatrix} = \begin{bmatrix} c_{11} & c_{12} & c_{13} & c_{14} & c_{15} & c_{16} \\ c_{21} & c_{22} & c_{23} & c_{24} & c_{25} & c_{26} \\ c_{31} & c_{32} & c_{33} & c_{34} & c_{35} & c_{36} \\ c_{41} & c_{42} & c_{43} & c_{44} & c_{45} & c_{46} \\ c_{51} & c_{52} & c_{53} & c_{54} & c_{55} & c_{56} \\ c_{61} & c_{62} & c_{63} & c_{64} & c_{65} & c_{66} \end{bmatrix} \cdot \begin{bmatrix} \varepsilon_{xx} \\ \varepsilon_{yy} \\ \varepsilon_{zz} \\ \gamma_{yz} \\ \gamma_{zx} \\ \gamma_{zy} \end{bmatrix}$$

or

$$\tau = C \cdot \gamma$$

where τ and γ are the above column vectors of stresses and strains respectively and C is the array of stiffnesses c_{ij}. The inverse relationship is given by

$$\gamma = S \cdot \tau$$

where S is an array of compliances.

Work and Energy

During a small change in the deformation of an elastic body, suppose that positive x face of the elementary cuboid moves through a small displacement d_{xx} relative to the negative x face, where

$$d_{xx} = \delta\left(\frac{\partial u_x}{\partial x}\right)dx = \partial\varepsilon_{xx}dx$$

(Here, an incremental change in quantity during deformation is indicated by the symbol δ preceding it.) The only work done on the cuboid is by the stress σ_{xx} and is given by

$$\delta W_{xx} = \sigma_{xx}dydzd_{xx} = \sigma_{xx}\delta\varepsilon_{xx}dxdydz$$

If the positive y face moves through a small displacement d_{yz} relative to the negative y face, then

$$d_{yz} = \delta\left(\frac{\partial u_z}{\partial y}\right)dy$$

In this case, the only net work done is by the stress τ_{yz} and is given by

$$\delta W_{yz} = \tau_{yz} dxdzd_{yz} = \tau_{yz}\delta\left(\frac{\partial u_z}{\partial y}\right)dxdydz$$

Similarly, the work done during a small displacement of the positive z face in the y direction relative to the negative z face is

$$\delta W_{zy} = \tau_{zy}\delta\left(\frac{\partial u_y}{\partial z}\right)dxdydz$$

Because τ_{yz} and τ_{zy} are equal, the sum of these two increments of work is

$$\delta W_{yz} + \delta W_{zy} = \tau_{zy}\delta\left(\frac{\partial u_z}{\partial y} + \frac{\partial u_y}{\partial z}\right)dxdydz = \tau_{yz}\delta\gamma_{yz}dxdydz$$

The total work done by all such increments is

$$\delta W = \left(\sigma_{xx}\delta\varepsilon_{xx} + \sigma_{yy}\delta\varepsilon_{yy} + \sigma_{zz}\delta\varepsilon_{zz} + \tau_{yz}\delta\gamma_{yz} + \tau_{zx}\delta\gamma_{zx} + \tau_{xy}\delta\gamma_{xy}\right)dxdydz = (\delta\gamma)^T\tau dV$$

where dV is the volume of the cuboid.

If the stress σ_{xx} and the strain ε_{xx} are increased in proportion to one another up to their final values, then the work done per unit volume is given by the area W_{xx} and is equal to $\frac{1}{2}\sigma_{xx}\varepsilon_{xx}$. For a linearly elastic body, all the stresses and strains can be increased in proportion to one another and then the total work done per unit volume is

$$W_v = \tfrac{1}{2}\gamma^T\tau = \tfrac{1}{2}\tau^T\gamma$$

Ignoring thermal effects, the energy stored in an elastic body is equal to the work done and is entirely a function of the final state of stress and strain. If additional stresses τ' induce additional strains γ', then the total work done per unit volume is

$$W_v' = \tfrac{1}{2}\sigma_{xx}\varepsilon_{xx} + \sigma_{xx}\varepsilon'_{xx} + \tfrac{1}{2}\sigma'_{xx}\varepsilon'_{xx} + \ldots = \tfrac{1}{2}\gamma^T\tau + \gamma'^T\tau + \tfrac{1}{2}\gamma'^T\tau'$$

Because the response is linear, the stress increments τ' will induce the strain increments γ' if applied in the absence of initial stress and strain, so that the work done per unit volume by applying the stresses in reverse order is

$$W_v' = \tfrac{1}{2}\gamma'^T\tau' + \gamma^T\tau' + \tfrac{1}{2}\gamma^T\tau$$

Because the body is elastic, the work is the same as that given by W_v', so that

$$\gamma^T \tau' = \gamma'^T \tau = \tau^T \gamma'$$

which is a form of Betti's theorem for stresses and strains.

From

$$\tau' = C\gamma'$$

$$\gamma^T C\gamma' = \gamma'^T C\gamma = \gamma^T C^T \gamma'$$

$$\gamma^T \left(C - C^T\right)\gamma' = 0$$

for any γ^T and γ'.

It follows that

$$C = C^T$$

or c_{ij} is equal to c_{ji}. Therefore in the 6x6 array of stiffnesses or compliances there are no more than 21 independent coefficients.

Linear Isotropic Behaviour

Let $c_{ij} \equiv T_{\varepsilon\sigma}$ and $s_{ij} \equiv T_{\sigma\varepsilon}$

The material matrix is more simple at linear isotropic elastic material properties.

$$T_{\varepsilon\sigma} = \frac{1}{E} \cdot \begin{bmatrix} 1 & -\nu & -\nu & 0 & 0 & 0 \\ -\nu & 1 & -\nu & 0 & 0 & 0 \\ -\nu & -\nu & 1 & 0 & 0 & 0 \\ 0 & 0 & 0 & 2(1+\nu) & 0 & 0 \\ 0 & 0 & 0 & 0 & 2(1+\nu) & 0 \\ 0 & 0 & 0 & 0 & 0 & 2(1+\nu) \end{bmatrix}$$

From this the Hooke's law

$$\{\varepsilon\} = [T_{\varepsilon\sigma}] \cdot \{\sigma\} + \{\varepsilon_0\}$$

where

ν Poisson's ratio

$\{\ \}$ Column vector

and

$$\{\varepsilon\} = \{\varepsilon_0\} + \{\varepsilon_e\}$$

$$\{\varepsilon_e\} = \{\varepsilon\} - \{\varepsilon_0\}$$

$$\{\varepsilon_e\} = [T_{\varepsilon\sigma}] \cdot \{\sigma\}$$

$$\{\sigma\} = [T_{\sigma\varepsilon}] \cdot \{\varepsilon_e\}$$

where the inverse matrix is

$$[T_{\sigma\varepsilon}] = [T_{\varepsilon\sigma}]^{-1}$$

$$T_{\sigma\varepsilon} = \frac{E}{(1+\nu)(1-2\nu)} \cdot \begin{bmatrix} (1-\nu) & \nu & \nu & 0 & 0 & 0 \\ \nu & (1-\nu) & \nu & 0 & 0 & 0 \\ \nu & \nu & (1-\nu) & 0 & 0 & 0 \\ 0 & 0 & 0 & \frac{(1-2\nu)}{2} & 0 & 0 \\ 0 & 0 & 0 & 0 & \frac{(1-2\nu)}{2} & 0 \\ 0 & 0 & 0 & 0 & 0 & \frac{(1-2\nu)}{2} \end{bmatrix}$$

APPENDIX 4. – ANNULUS INHOMOGENITY

The following mathcad source is calculating the values of $E_{i,j}$ in every 10 degrees of the cylindrical coordinate system. Since Mathcad is unable to display cylindrical coordinates, all results first has to be transformed to the orthogonal system. This is done by transforming the matrix of the points. Values of r and A are theoretical, the aim is only to show the pattern of the annulus strength. Due to the large matrices only part of the matrix is displayed.

$A := 0.1$

$i := 0..36$

$j := 0..36$

$r_i := 0.01 \cdot \frac{0.02 \cdot i}{72}$

$y_j := \frac{360 \cdot j}{36}$

$E_{i,j} := \frac{0.3 \cdot A \cdot \cos(y_j \cdot deg)}{1 - 0.7 \cdot \frac{r_i}{0.02}}$

r =

	0
0	0.01
1	0.01
2	0.011
3	0.011
4	0.011
5	0.011
6	0.012
7	0.012
8	0.012
9	0.013
10	0.013
11	0.013
12	0.013
13	0.014
14	0.014

y =

	0
0	0
1	10
2	20
3	30
4	40
5	50
6	60
7	70
8	80
9	90
10	100
11	110
12	120
13	130
14	140

E =

	0	1	2	3	4	5	6	7
0	0.046	0.045	0.043	0.04	0.035	0.03	0.023	0.016
1	0.047	0.046	0.044	0.041	0.036	0.03	0.023	0.016
2	0.048	0.047	0.045	0.041	0.036	0.031	0.024	0.016
3	0.048	0.048	0.045	0.042	0.037	0.031	0.024	0.017
4	0.049	0.048	0.046	0.043	0.038	0.032	0.025	0.017
5	0.05	0.049	0.047	0.043	0.038	0.032	0.025	0.017
6	0.051	0.05	0.048	0.044	0.039	0.033	0.025	0.017
7	0.052	0.051	0.048	0.045	0.039	0.033	0.026	0.018
8	0.052	0.052	0.049	0.045	0.04	0.034	0.026	0.018
9	0.053	0.053	0.05	0.046	0.041	0.034	0.027	0.018

$X_{i,j} := r_i \cdot \cos(y_j \cdot deg)$

$Y_{i,j} := r_i \cdot \sin(y_j \cdot deg)$

$Z_{i,j} := E_{i,j}$

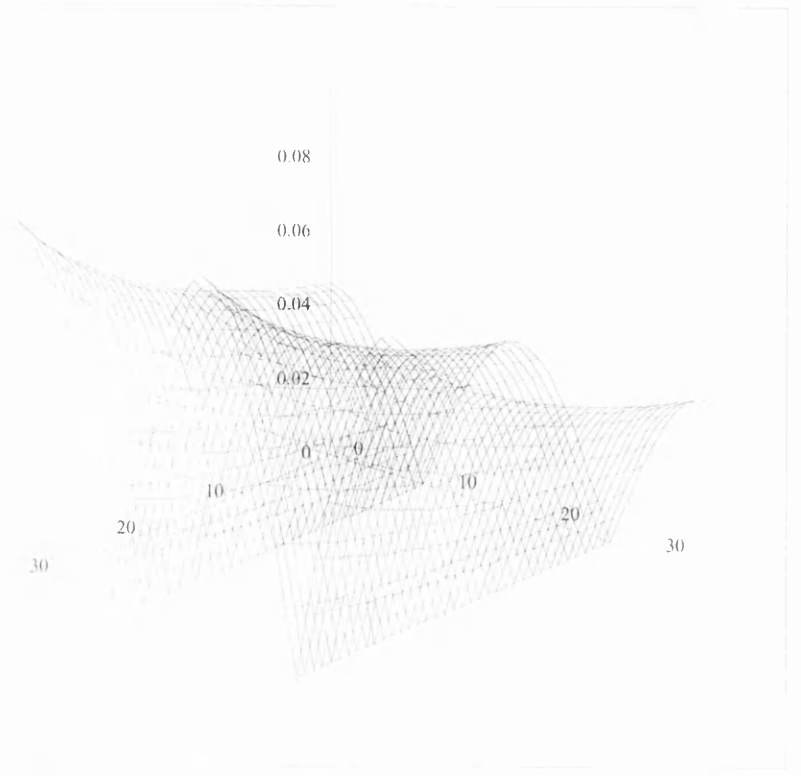

E

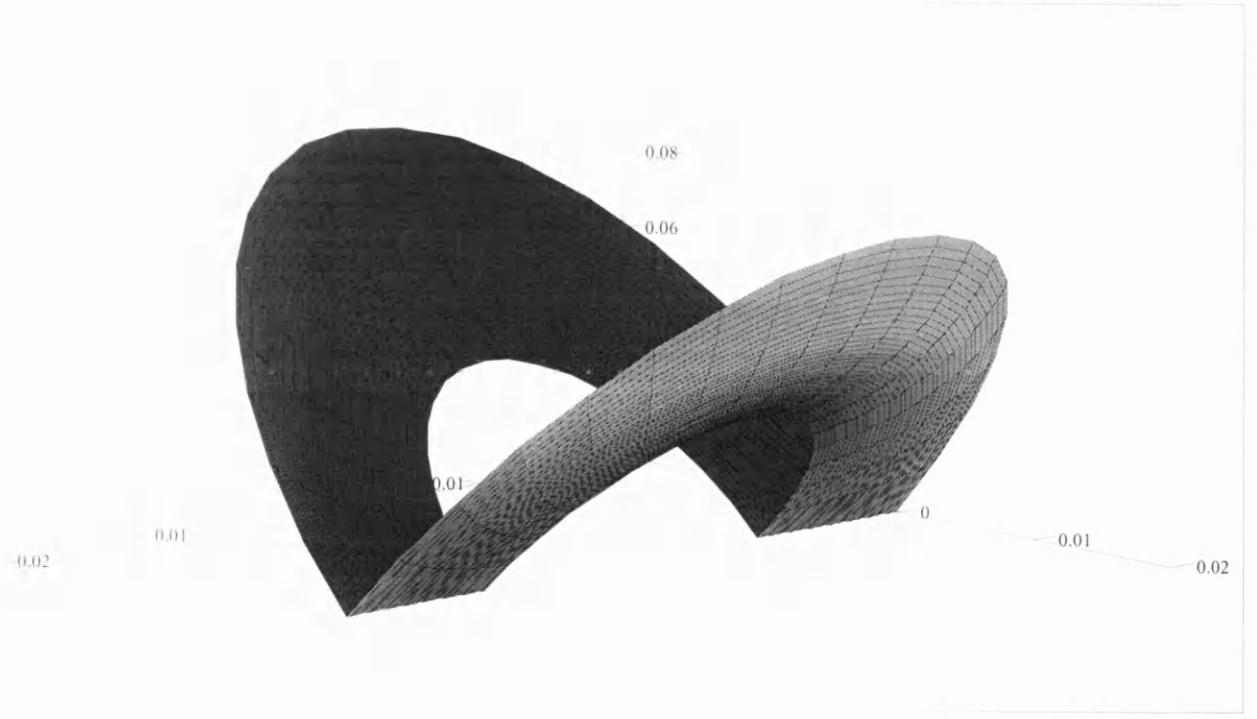

X, Y, Z

APPENDIX 5. – THIRD-ORDER POLYNOMIAL APPROACH OF THE ANNULUS CHARACTERISTICS

	E	e
	0	0
	8.6667	0.1
	18.0180	0.185
	27.7778	0.24
A	37.0370	0.27
	45.1977	0.295
	52.9101	0.315
	59.7015	0.335
	64.2254	0.355

Degree of polynomial fit

$k := 3$

Number of data points

$n := 9$

$X := A^{\langle 1 \rangle}$ $Y := A^{\langle 0 \rangle}$

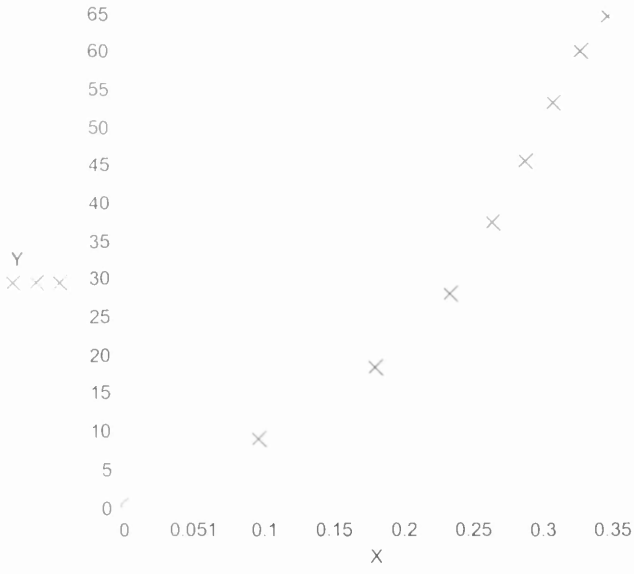

$z := regress(X, Y, k)$

Polynomial fitting function:

$fit(x) := interp(z, X, Y, x)$

Coefficients:

$coeffs := submatrix(z, 3, length(z) - 1, 0, 0)$

$coeffs^T = \begin{pmatrix} 0.3 & 55.626 & 88.665 & 783.846 \end{pmatrix}$

$$R^2 := \frac{\sum (fit(X) - mean(Y))^2}{\sum (Y - mean(Y))^2} = 0.996$$

Degrees of freedom: $n - k - 1 = 5$

Plots $y(x) := 0.3 - 55.626 \cdot x + 88.665 \cdot x^2 - 783.846 \cdot x^3$

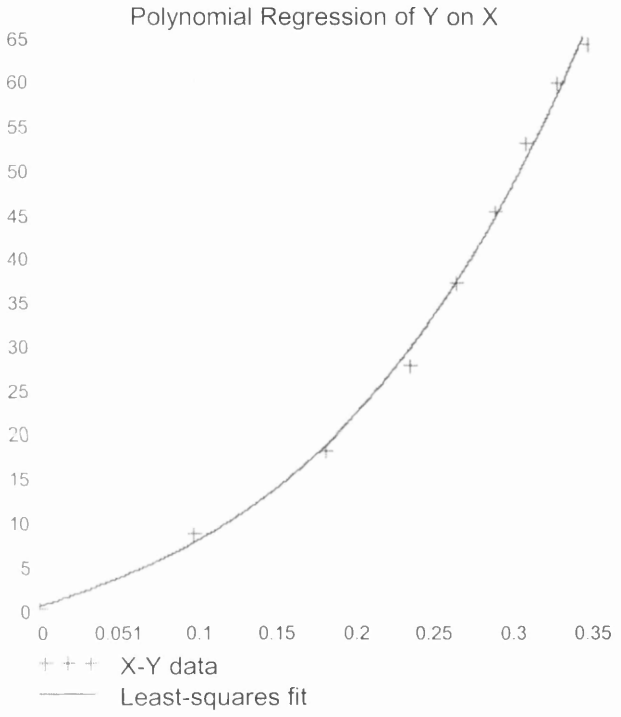

$scale := \max(fit(X) - Y) \cdot 1.1$

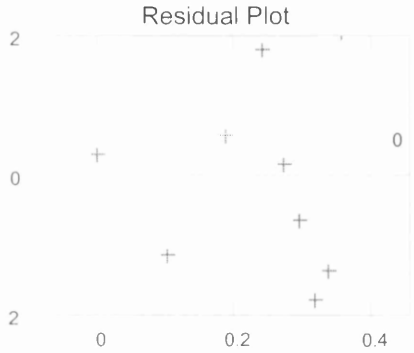

APPENDIX 6. – ANALYSIS OF THE HUMAN LUMBAR INTERVERTEBRAL DISC BASED ON A THREE-DIMENSIONAL NON-LINEAR FINITE ELEMENT MODEL

Az emberi ágyéki csigolya porckorongjának analízise háromdimenziós nemlineáris „véges elem" modellel[1]

Analysis of the human lumbar intervertebral disc based on a three-dimensional non-linear finite element model

Géza T. Nagy[2], Waldemar Z. Golinski[2], Richard Gentle[2]

Absztrakt

Az ismertetésre kerülő munka az L2-L3 emberi ágyéki csigolya porckorongjának háromdimenziós, nemlineáris, dinamikus „véges elem" analízise (FE). Az FE modell magában foglalja a porckorong biomechanikailag releváns egyedi összetevői anizotropikus anyagi tulajdonságainak a jellemzését. Az újdonság a porckorong mikrostruktúrájának merev elemekkel, és nem egydimenziós rugókkal való modellezésében áll. Ennélfogva az elemek egymással kölcsönhatásba léphetnek, valamint bemutathatják a nyírásra, csavarásra és hajlításra adott válaszukat. Az eredmény egy olyan modell, amely a porc anizotrópia valamennyi vonatkozásainak sokban javított ábrázolását adja, és ezért lehetővé teszi a csigolya-porckorong egyszerű, tengelyirányú terhelésen túli, excentrikus terhelésre adandó mechanikai válaszának a pontos leírását.

Kulcsszavak: csigolya-porckorong, lumbáris gerinc szakasz, deréktáji fájdalom, FEM (véges elem modellezés), nemlineáris

1. Bevezetés

A gerincrészek részletes mechanikai viselkedése jó megismerésének a hiánya számottevő gát az emberek biztonságának és egészségének javításában, a legkülönfélébb helyzetekben, kezdve az egyszerű emeléssel egészen a személyautóban elszenvedett balesetig. Ez sehol sem kézzelfoghatóbb, mint a csigolya-porckorongoknál, mivel ezek döntő fontosságúak a nagy terhelések átvitelében és elosztásában, valamint a hajlékonyság biztosításában. Ezeknek a bonyolult struktúrájuk egyben megnehezíti az analízisüket is. Mindazonáltal lényeges, hogy elkészüljön a gerinc valamennyi porckorongjának egy olyan számítógépes modellezése, amely lehetővé teszi a dinamikus traumahelyzetek teljes biomechanikai analízisét abból a célból, hogy előre megmondható legyen a sérülés módja; ami ennek az ismertetésre kerülő munkának a célja.

Abstract

The work described is a three-dimensional non-linear dynamic finite element (FE) analysis of the L2-L3 human lumbar intervertebral disc. The FE-model includes characterisation of anisotropic material properties of the biomechanically relevant individual components of the disc. The novelty lies in modelling the disc microstructure with solid elements rather than as one-dimensional springs. Hence the components can interact with each other as well as exhibit responses to shear, torsion and bending. The result is a model, which gives a much-improved representation of all aspects of disc anisotropy and therefore allows an accurate depiction of the mechanical response of an intervertebral disc under eccentric loading in addition to the simpler axial loading.

Keywords: *intervertebral disc, lumbar spine, low back pain, FEM, non-linear*

1. Introduction

The lack of a good understanding of the detailed mechanical behaviour of all the parts of the spine is a major obstacle to improving the safety and health of people in a wide variety of situations, ranging from simple lifting operations to passenger vehicle crashes. Nowhere is this more apparent than in the intervertebral discs since they are crucial in the transmission and distribution of large loads, and in providing flexibility, but have such a complex structure that they are difficult to analyse. Nevertheless it is essential that computational models of all the discs in the spine are developed so that full biomechanical analysis may be carried out of dynamic trauma situations in order to predict the mode of injury; that is the aim of the work reported here.

The most important component of the intervertebral disc, from a structural perspective, is the annulus fibrosus since it bears most of the loads. As well as simple weight bearing, it also

1. A BUDAMED '99 Konferencián elhangzott előadás szerkesztett változata

2. Department of Mechanical and Manufacturing Engineering, Biomechanics Research Group, The Nottingham Trent University, Burton St., Nottingham, NG1 4BU, GB
geza.nagy@ntu.ac.uk

Strukturális szempontból a csigolya-porckorong legfontosabb eleme az annulus fibrosus, mert erre jut a teher legnagyobb része. Miként az egyszerű nyomócsapágynál, a gerinc mozgása során keletkezett differenciális nyomó-, húzó- és nyíróerő következményeképpen ez is deformálódik. Ennek összetétele proteoglycanokból és más proteinekből álló vizes gélbe beágyazott fibrosus collagén mátrix. Az annulus erősen irányított és rétegelt struktúrája arra enged következtetni, hogy ennek az anyagi viselkedése számottevően nemlineáris és anizotropikus lesz. Ezen komplex anyag meghibásodásának a megértése elvezethet a porckorong mechanikus degenerációjának, és más szimptomatikus porckorong rendellenességeknek a megmagyarázásához, valamint a gerinc egészének a jobb megértéséhez.

A lágyrészeknek nemlineáris rugókénti régebbi számítógépes modellezéseivel értek el bizonyos sikereket, különösen olyan esetekben, amikor a szalagok csak axiálisan deformálódtak; a Notingham Trent Egyetem cervicalis gerinc modellje (*1. ábra*) erősen támaszkodik erre az ábrázolásra.

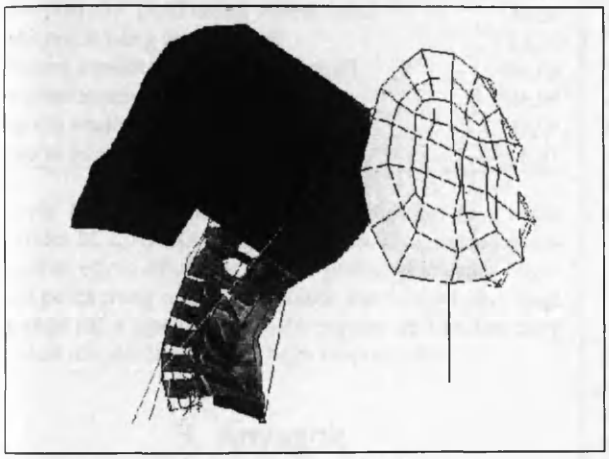

Ábra/*Figure* 1. Ostorcsapás szimulációja FEM-mel
Simulation of Whiplash by FEM

A porckorongok hasonló módon történő vizsgálatánál azonban számos hiányosság derült ki. Noha a porckorongok általános sztatikus terhelés–elhajlás tulajdonságait pontosan lehet reprodukálni, a nyomás részletekben történő reprezentációja, az egyes összetevőkben levő nyírás és csavarás nem találkozik a meglevő *in vitro* adatokkal. Ezért kell megkísérelni az annulus fibrosus anyagi tulajdonságainak a komplett jellemzését, még ha ez, a hiányzó műszaki adatok miatt, majdnem leküzdhetetlen feladat. A hiányzó anyagi állandók meghatározása valamelyest könnyebbé tehető az ortotropia feltételezésével, de további kompromisszumok lehetőségét is vizsgálják.

2. A modell

Az ebben az írásban közölt tanulmány céljai: az ágyéki csigolya porckorong-csigolya egység lumbális véges elemből álló modelljének a kifejlesztése, a modell validációja a porckorong jellemzőinek rendelkezésre álló kísérletileg összegyűjtött irodalmi adataival, (pl. átfogó felelet a porckorong-test egységnek az axiális és excentrikus nyomó terhelésre, porckorongon belüli nyomás, porckorong kidomborodás, függőleges elhajlás) és a különböző elemekben, különféle terhelési viszonyok melletti feszültségek és deformációk analízise. A modell kidolgozásakor az an-

deforms in response to the differential compressive, tensile and shear forces generated during spinal movement. Its composition is that of a fibrous collagen matrix embedded within an aqueous gel of proteoglycans and other proteins. The highly oriented and layered structure of the annulus suggests that its material behaviour will be significantly non-linear and anisotropic. Understanding the failure of this complex material should lead to a better explanation of mechanical disc degeneration and other symptomatic disc disorders, as well as increased understanding of the spine as a whole.

Early computational modelling of soft tissues as non-linear springs had some success, particularly with ligaments in situations where they only deform axially; the Nottingham Trent University cervical spine model shown in Fig. 1 *relies heavily on this representation.*

Similar treatment of the discs, however, was recognised as having many shortcomings. Although the overall static load-deflection properties of the disc could be reproduced accurately, a detailed representation of the pressure, shear and torsion in the individual components did not fit available in vitro *data. It is therefore necessary to attempt a complete characterisation of the material properties of the annulus fibrosus, even though this is an almost insurmountable task due to lack of engineering data. The determination of the required material constants is made somewhat easier by assuming orthotropy but further compromises are currently being evaluated.*

2. Model

The objectives of the study reported in this paper are development of a finite element model of the lumbar intervertebral disc-vertebra unit, validation of the model by comparison with available experimentally acquired literature data of the disc characteristics, (e.g. the overall response of the disc-body unit to axial and eccentric compressive loading, intradiscal pressure, disc bulge, vertical deflection) and analysis of the stresses and deformations occurring in the various elements in different loading situations. When building the model, the anterior-posterior geometry differences, the material and geometry non-linearities, the annulus-nucleus-cartilaginous end plate microstructure around the embedded collagenous fibre structure and the topology in the proteoglycan matrix were taken into consideration.

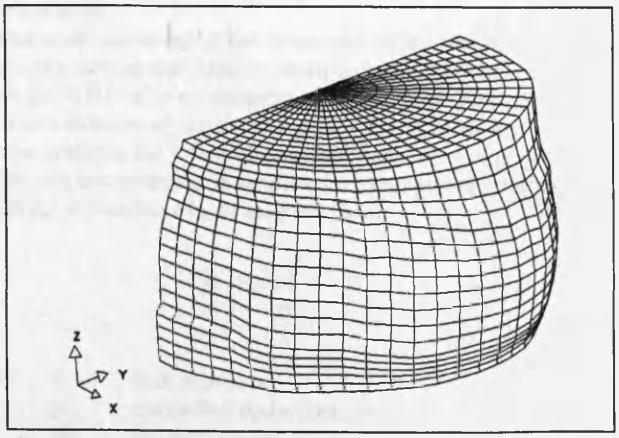

Ábra/*Figure* 2. A 3D FEM modell anterior-laterális nézete
The 3D FEM Model Anterior-lateral View

rior-posterior geometriai különbözőségeket, az anyag és a geo-etria nemlinearitásait, az annulus-nucleus-porcos véglemeznek beágyazott kollagénes rostos szerkezet körüli mikrostruktúráját s a proteoglycan mátrix topológiáját vették figyelembe.

A *2. ábrán* látható a Notingham Trent Egyetem Biomecha-ikai Kutató Csoportja által készített 3D térbeli modellje az L2-3 ágyéki csigolya-porckorong-csigolya komplexusnak. Az ana-ómiai modell egy életnagyságú, 3D Pro/Engineer térelemekből solidokból) álló modell, mely a Visible Human Project adatso-zin alapszik [16]. Első analízisként az átlagos férfi adatsort vá-asztottuk, mint amelyik a leggyakoribb férfi gépkocsi utas. A érfiak statisztikailag is sokkal gyakrabban kerülnek súlyok emelése miatt porcsérüléses állapotba. A modell fő geometriai méreteit az *1. táblázat* mutatja.

1. **táblázat. A modellnél használt geometriai méretek**

Porckorong magasság [mm]	15,00
Anterior-posterior porckorong átmérő [mm]	40,30
Laterális porckorong átmérő [mm]	55,60
Porckorong keresztmetszet területe [mm²]	493,63
Nucleus keresztmetszet területe [mm²]	348,99
L2 csigolya tetejének területe [mm²]	718,09
L3 csigolya tetejének területe [mm²]	856,27

A modellt Altair Hypermesh 3D-vel hálóztuk be, és a véges elem kódot PC LS-DYNA3D-vel generáltuk [6]. A modell gene-rálása során egy anatómiailag és mechanikailag releváns csigo-vaközti porckorong modell elkészítése volt a fő cél úgy, hogy a számolási idő a lehető legrövidebb legyen. Az annulust négy belső solid rétegre és egy külső héjra bontottuk fel.

3. Anyagok

A modell 8 csomópontú térelemekkel (solidokkal) került beháozásra. A háló sűrűségét konvergencia elemzés alapján válasz-ottuk meg, és legalább annyira finomra választottuk, mint más korábbi porckorong modellekét. A teljes modell tartalmazza a nucleus pulposust, az annulus fibrosust és részlegesen a máso-dik, valamint harmadik lumbaris csigolyát. A kerület mentén harminc osztással lett behálózva, sugárirányban tizenöt, függőle-gesen pedig tizennyolc rétegben. Maga a porckorong magassági irányban nyolc rétegbe rendezett térelemekből áll, és a maradék tíz réteg az L2 és L3 csigolyák között azonos arányban oszlik meg. Radiális irányban a nucleus pulposus tizenegy rétegű, a külső négy alkotja a nucleust körülvevő annulus fibrosus gyűrűt. Az annulus négy belső rétegben elrendezett solidokra osztott és egy külső kétdimenziós héjjal rendelkezik. A csontok szivacsos magra, és az azt borító kortikális héjra lettek felosztva.

A csigolyaközi porkorong geometriájának következtében a függőleges tengelyhez közeli elemeknek nem téglaszerű az alakjuk, ezért ezen elemek kimeneti adatait nem használtuk fel. Ez a nucleusnak csak néhány elemét érinti, és a numerikus szá-molásoknál nem okoz számottevő hibákat.

A nucleus pulposust, a gyakorlatban megszokott módon, mint folyadékot modellezzük, és a Poisson-féle tényezőjével jel-lemezzük:

$$K = \frac{p}{\Delta v / v}$$

Fig. 2 *shows the 3D solid model of the L2-L3 lumbar vertebra-disc-vertebra complex built by the Biomechanics Research Group of the Nottingham Trent University. The anatomical model is a full-size 3D Pro/Engineer solid model, based on the data sets of the Visible Human Project [16]. For first analysis the average male dataset was chosen as the most common vehicle occupant. Males are statistically also more often involved in disc trauma caused by lifting weights. The main geometric features of the model are shown in* Table 1.

Table 1. Geometric factors used for the model

Disc height [mm]	*15.00*
Anterior-posterior disc diameter [mm]	*40.30*
Lateral disc diameter [mm]	*55.60*
Disc cross-sectional area [mm²]	*493.63*
Nucleus cross-sectional area [mm²]	*348.99*
L2 vertebra top surface area [mm²]	*718.09*
L3 vertebra bottom surface area [mm²]	*856.27*

The model was meshed in Altair Hypermesh 3D and the finite element code was generated with PC LS-DYNA3D [6]. During the model generation the main aim was to build an anatomically and mechanically relevant intervertebral disc model keeping the calculation time as short as possible. The annulus is divided into four inside layers of solids and an outside shell.

3. Materials

The model was meshed with 8-node solids. The density of the mesh was selected based on a convergence study and was at least as fine as other previous models of the disc. The overall model contains the nucleus pulposus, the annulus fibrosus and part of the second and third lumbar vertebrae. It was meshed by thirty divisions circumferentially, fifteen layers of elements radially and eighteen layers vertically. The height of the disc itself consists of eight layers of bricks and the remaining ten layers are shared by part of the L2 and L3 vertebras equally. In the radial direction the nucleus pulposus contains eleven layers, the outside four forming the ring of the annulus fibrosus surrounding the nucleus. The annulus is divided into four inside layers of solids and it has an outside two-dimensional shell. The bones are divided into a cancellous core covered by a cortical shell.

Due to the geometry of the intervertebral disc the elements close to the vertical axis have an invalid shape as bricks and so the output data of these elements were not used. This affects only some elements of the nucleus and does not cause any significant errors in the numerical calculation.

The nucleus pulposus is modelled, as is common practice, as a fluid. It is defined by its bulk modulus:

$$K = \frac{p}{\Delta v / v}$$

where K *bulk modulus*
p *equivalent hydrostatic pressure*
Δv *volume change*
v *initial volume*

ahol K Poisson-féle tényező
p ekvivalens hidrosztatikai nyomás
Δv térfogat változás
v kiinduló térfogat

A természet által használt természetes anyagok ismerete nélkül biomechanikai mozgás numerikus analízisét lehetetlen elvégezni. Egy kifejlett porckorongnál az annulus ellenáll a csigolya véglemezekre merőlegesen ható igénybevételeknek, és vízszintes nyomásgradienst mutat amikor a csigolya összetett hajlító és összenyomó hatásoknak van kitéve. [11]. Az annulus fibrosusnak, mint az alapanyagokból képzett mátrixba beágyazott kollagén rostok keverékének, anizotróp anyagi tulajdonságai okozzák ennek a struktúrának az inhomogén természetét. Ezért a csigolyaközi porckorong modellezésének a legfontosabb része az annulus tulajdonságok legpontosabb elérése. Azonban mind a mai napig nagyon nehéz a biológiai anyagok szilárdságáról pontos adatokat kapni. Az adatgyűjtésnek számos nehézsége akad, némelyek technikai, mások morális jellegűek. Az új modellben a 8 csomópontú solidokkal modellezett legbelső négy réteg annulus anyaga orthotropic nemlineáris plasztikus-elasztikus hab anyag. A külső, vékony 3D héj 2Ds nemlinearitással rendelkező, nemlineáris elasztikus tulajdonságú.

A számítógép-idő extrém megnövekedése miatt az annulus fibrosus radiális nonlinearitását elhanyagoltuk [13]. A szivacsos és corticalis csont anyagi tulajdonságait az előző analitikus és kísérletes vizsgálatok alapján választottuk meg [12]. A 2. táblázatban találhatók a modell anyagi tulajdonságai. Minden értéket, mint globális koordinátát adtunk meg, kivéve az annulus anyagi jellemzőit, [1], [2], [3], [4], [7], [12], [14] amelyek egy hengeres globális koordináta-rendszerben forgó helyi koordináta-elemekben adottak.

It is impossible to perform a numerical analysis of biomechanical motions without a the knowledge of natural materials used by nature. The annulus in a mature disc resists compressive stresses perpendicular to the vertebral end plates and exhibits horizontal stress gradients when the disc is subjected to combined bending and compression [11]. The anisotropic material properties of the annulus fibrosus as a composite of collagenous fibres embedded in a matrix of ground substance give rise to the nonhomogenous nature of this structure. Therefore the most important part of modelling the intervertebral disc is to achieve accurate annulus properties. However up to the present date it remains very difficult to obtain accurate data describing the strength of biological materials. There are several difficulties of data collection, some are technical and others are moral. In the recent model the annulus material in the inner four layers modelled by 8 node solids is orthotropic non-linear elastic-plastic foam. The outside thin 3D shell has non-linear elastic properties with 2D nonlinearity.

Because of the extreme growth of the computation time the radial nonlinearity of the annulus fibrosus was neglected [13]. The material properties of the cancellous and cortical bone were selected based on previous analytical and experimental studies [12]. Table 2. shows the material properties of the model. All values are given as global coordinates, except the material properties of the annulus [1], [2], [3], [4], [7], [12], [14] which are defined in the local element coordinate system rotating in a cylindrical global system.

4. Boundary conditions

The validity of the model and the analysis procedure has been established by comparison of those values that are also available for direct experimental measurements e.g. response of the

Anyag *Material*	**Rugalmassági együttható** *Elastic coefficients*		**Konstitutív sajátosságok** *Constitutive relation*	**Nómenklatúra** *Nomenclature*
Carticalis csont *Cortical bone*	$E = 12$ MPa	$\upsilon=0.3$	elasztikus/*elastic*	E, Young-modulus *Young's modulus* υ, Poisson-hányados *Poisson's ratio* σ, feszítés/*Stress* ε, nyúlás/ *Strain* G, nyírás modulus/ *Shear modulus* K, Poisson-féle tényező/ *Bulk modulus*
Szivacsos csont *Cancellous bone*	$E = 100$ MPa	$\upsilon=0.2$	elasztikus/*elastic*	
Szilárd annulus *Annulus solid*	$\sigma(\varepsilon) = 5.081\varepsilon^3 - 1.048\varepsilon^2 + 0.822\varepsilon$ $\sigma(\varepsilon)_{cyl,max} = 100$MPa $\sigma(\varepsilon)_{vert,max} = 173$ MPa $\sigma(\varepsilon)_{rad,max} = 100$ MPa $G(\varepsilon)_{max} = 8$ MPa	$\upsilon=0.45$ $\varepsilon_{max}=1.5$ $G(\varepsilon)=\sigma(\varepsilon)$	nemlineáris/*nonlinear* orthotropic/*orthotropic* rugalmas-plasztikus/*elastic-plastic*	
Annulus héj *Annulus shell*	$\sigma(\varepsilon) = 5.081\varepsilon^3 - 1.048\varepsilon^2 + 0.822\varepsilon$ $\sigma(\varepsilon)_{cyl,max} = 100$ MPa $\sigma(\varepsilon)_{vert,max} = 173$ MPa $G(\varepsilon)_{cyl,max} = 8$ MPa $G(\varepsilon)_{vert,max} = 8$ MPa $E_{rad} = 100$ MPa $G_{rad} = 8$ MPa	$\upsilon = 0.45$ $\varepsilon_{max} = 1.5$ $G(\varepsilon) = \sigma(\varepsilon)$	nemlineáris/*nonlinear* orthotropic/*orthotropic* rugalmas/*elastic*	**Alsóindex/*Subscripts*** cyl, hengeres irány/ *cylindrical direction* vert, függőleges irány *vertical direction* rad, radiális irány *radial direction* max, maximális érték *maximum value*
Nucleus	$K = 2.5$ MPa		folyadék mechanika/*fluid mechanics*	

2. táblázat/*Table 2.* A modellezésnél használt anyagok jellemzői / *Material properties used for the model*

4. Peremfeltételek

modell validálását és az analizálási eljárást a közvetlen kísérleti mérések céljára is rendelkezésre álló értékekkel történő összehasonlítással végeztük el. Ilyenek például: a porckorongot egységnek az axiális és excentrikus nyomó terhelésre adott válasza az axiális elmozdulás és a kitüremlés szempontjából; nyíróerők a vízszintes elmozdulás függvényében. Minden szimulációnál az L3 csigolya alsó felszíne minden szabadsági fok tekintetében rögzített volt. Minden terhelést lépcsős függvény formájában alkalmaztunk. Tiszta összenyomásnál tengelyirányú nyomást alkalmaztunk. Az ekvivalens összenyomó erő 445 N, 889 N és 1334 N volt. Ugyanekkora erőt alkalmaztunk a vízszintes síkban, és szagittális vagy frontális irányokban is. A kombinált összenyomási- és nyírási vizsgálatot 223 N és 445 N ekvivalens összenyomó erővel végeztük, és az L2-es csigolya felső síkjának a közepére133 N nyíróerőt alkalmaztunk.

5. Eredmények

létrehozott modell tesztelésére és ellenőrzésére Lin méréseit alkalmaztuk [5]. Ezek a mérések ugyanazon az L2-L3 mintán számos vizsgálatot foglalnak magukban; axiális és excentrikus, valamint kombinált összenyomás-nyírás vizsgálatokat. A mért értékek között az L2 vertikális és horizontális elmozdulásai, és az elülső valamint oldalsó kitüremlések is megtalálhatók. Az L2 tengelyirányú nyomás hatására történő vertikális elmozdulásait összehasonlítottuk más munkákkal [7], [15].

Ennek a tanulmánynak a gyengesége, hogy a kísérleti vizsgálatok terhelési viszonyai számos bizonytalanságot tartalmaznak. A kísérleti- és a numerikus modell adatai közti különbségeket a méréskori terhelési feltételek nem kielégítő szimulációja okozhatja, ami az információ-hiány következménye lehet. A porckorong modellünk valódi életkörülmények között keletkezett, szalagokkal és lágy szövetekkel körülvéve és támogatva. Az *in vitro* tanulmányoknál a gerinc helyzetét meg lehetett változtatni, ami befolyásolná az eredményekhez tartozó kezdeti feltételeket. Azonban, különösen kisebb terhelések mellett, a modell eltérése nagyobb, ami valószínűleg a fentebb leírt hibából adódik. (*3. ábra*)

disc-body unit to axial and eccentric compressive loads in terms of axial displacement and disc bulge; shear forces as a function of horizontal displacement. In all simulations the bottom surface of the L3 vertebra was fixed to all degrees of freedom. All loads were applied as step functions. At pure compression an axial pressure was applied. The equivalent compressive forces were 445N, 889N and 1334N. The same pressure was used with a moment in the horizontal plane and in the sagittal or frontal direction. The combined compression and shear test was done by applying 223N and 445N equivalent compressive force as pressure, and 133N shear force at the centre of the top of the L2 vertebra.

5. Results

To test and evaluate the created model, Lin's measurements were chosen [5]. These measurements include several tests on the same L2-L3 sample with axial and eccentric compression and combined compression-shear tests. Among the measured values the vertical and horizontal displacement of L2 and the anterior and lateral bulge can be found. The vertical displacement of L2 under axial compression was also compared to some other works [7], [15]. The intradiscal pressure of the annulus fibrosus was evaluated based on the work of McNally and Wilke [9], [17].

The weakness of this study is that the loading conditions of the experimental tests contain many uncertainties. Differences between the experimental data and the numerical model could be caused by improper simulation of the measurement loading conditions due to lack of information. Our disc model is generated in the real life position, surrounded and supported by the ligaments and soft tissues. In the in vitro *studies the position of the vertebrae might have been changed, which would affect the initial conditions of the results. As seen in* Fig. 3, *the vertical displacement of the L2 vertebra for axial and eccentric compression follows the overall characteristic. However especially at low loads the deflection of the model is bigger which is most likely caused by the effect described above.*

Because of the high deviation of the different measurements the model can not be evaluated based only on these values.

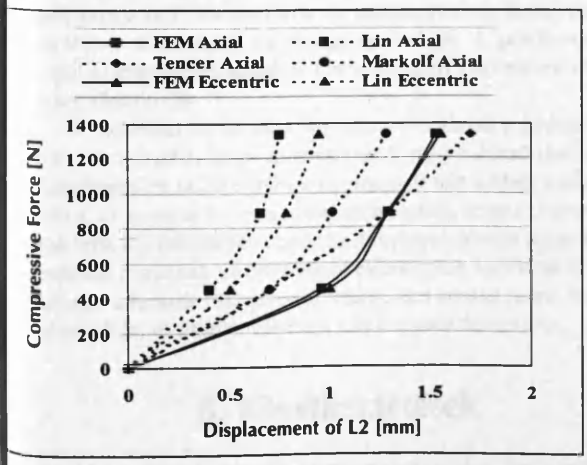

3. ábra. Függőleges elmozdulás tengelyirányú és excentrikus nyomás hatására

Figure 3. Vertical Displacement for Axial and Eccentric Conpression

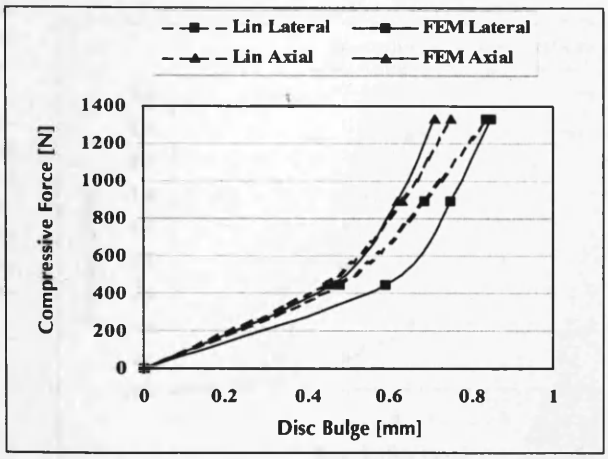

4. ábra. Porckorong kitüremlés tengelyirányú összenyomás hatására

Figure 4. Disc Bulge for Axial Compression

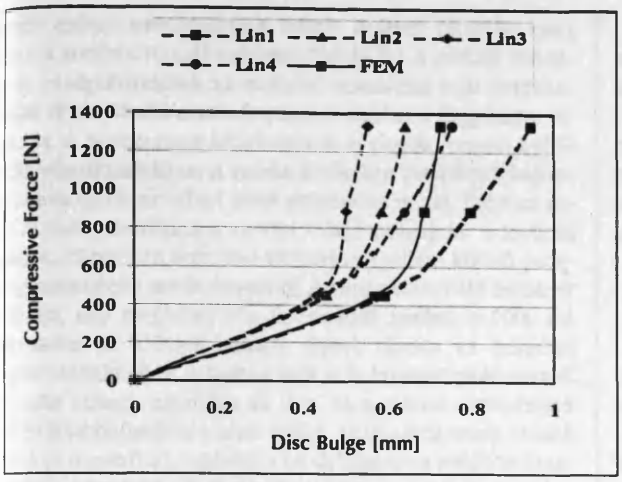

5. ábra. Porckorong kitüremlés oldalirányú hajlásra
Figure 5. Disc Bulge for Lateral Bending

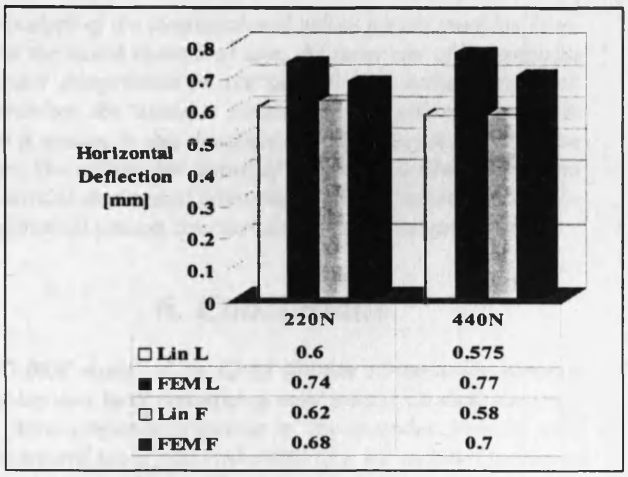

6. ábra. Kombinált kompressiós és nyíró vizsgálat
Figure 6. Combined Compression and Shear Test

A különböző mérések közti nagy eltérések miatt, a modellt nem lehet csak ezeknek az értékeknek az alapján értékelni. Ezért a második lépésben az összehasonlítás céljára mérési értékeinkhez az elülső és az oldalsó porckorong kitüremlést választottuk, mivel ezek az értékek közvetlenül mérhetők. A *4. ábrán* látható a porckorong kitüremlése tengelyirányú összenyomás hatására. A FEM modell elülső irányú porckorong kitüremlése 0,98-as varianciával követi a mérési görbét. Az eltérés az oldalirányú porckorong kitüremlésnél nem jelentős, és zömmel geometriai különbségekből adódó. Az *5. ábrán* látható, hogy a porckorong excentrikus terhelések esetében is a mérési határon belül van, és hasonló jellemzőket mutat. A következő kiértékelési lépés a porckorongnak nyírás hatására adódó válasza volt. A megfelelő nyíró terhelésnek és az annulus fibrosus funkciójának a meghatározása nehéz volt, mivel hiányoztak a nyírási tulajdonságok időbeni változására vonatkozó irodalmi adatok. A modellben a G(ε)-re és a σ(ε) ugyanazt a görbét használtuk. A nyírási válasz gyengébb karakterisztikát mutat a *6. ábrán*.

Az utolsó mérés az annulus fibrosus anyag porc közötti nyomás hatására történő viselkedésének a vizsgálata volt. A *7. ábra* a porckorongon belüli nyomást mutatja 500 N és 2000 N tengelyirányú terhelés hatására. A karakterisztikát összevetettük McMillan méréseinek az eredményeivel [8]. A porckorongon belül az elemekben kialakult nyomás a mért értékekhez tökéletesen illeszkedik.

A modellen az annulus fibrosusra vonatkozó számított adatok azt mutatják, hogy az annulusnak még a külső pereme is függőleges és radiális irányú nyomásnak van kitéve. Mindazonáltal, az annulus kerületi adatai azt mutatják, hogy az összenyomó erők következtében ebben az irányban is létezik nyomás. Az annulus rostjainak az orthotropic elrendezése szétosztja a vertikális és a radiális összenyomó erőket, ami kerület menti feszültséget okoz, és az ellensúlyozza a kitüremlési folyamatot.

6. Következtetések

Az L2-L3 ágyéki csigolya-porckorong-csigolya komplexumra készült egy 3D FEM modell, amely csak szilárd és héj elemekből áll. Az annulus fibrosus rost-összetételi tulajdonságait orthotropikus anyag használatával valósítottuk meg. Valamennyi anyag

Therefore for the second stage comparison the anterior and lateral disc bulge was chosen as a value can be measured directly. On Fig. 4 *the disc bulge can be seen during axial compression. The anterior disc bulge of the FEM model follows the measured curve within 0.98 of variance. The difference in the lateral disc bulge is not significant, and is mostly caused by the geometry differences. It can be seen in* Fig. 5 *that the disc bulge at eccentric loading is also inside the measured limits and shows similar characteristics. The next evaluation stage was checking the overall response of the disc to shearing. Defining the proper shear moduli and function of the annulus fibrosus was difficult due to the lack of a time-history for the shear properties in the literature. In the model a similar curve was used for G(ε) as for s(ε). The shear-response shows a weaker characteristic on* Fig. 6.

The final test was to examine the material behaviour of the annulus fibrosus through the intradiscal pressure. Fig. 7 *shows the pressure inside the disc for axial compression at 500N and 2000N. The characteristic was compared to McMillan's results [8]. The intradiscal pressure developing in the elements completely fits the measured values.*

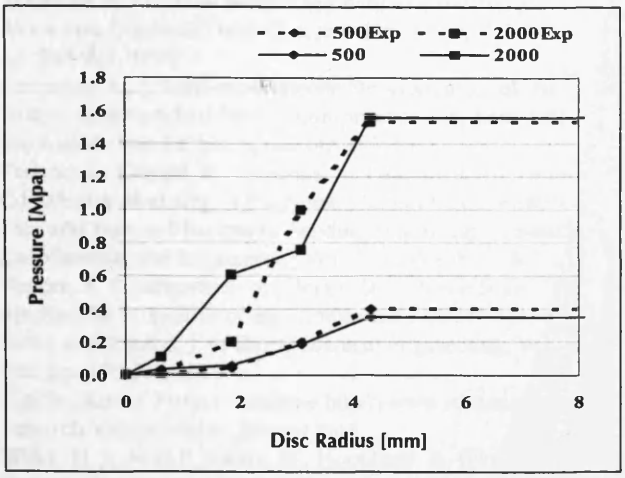

7. ábra. Porckorongon belüli nyomás axiális terhelés hatására.
Figure 7. Intradiscal Pressure for Axial Compression.

emzői erősen nemlineárisak voltak. A jelen vizsgálat ezen dsait a korábbi vizsgálatok nem ölelték fel. A modell validá- az eredményeknek az irodalmi adatokkal való összeha- lítása révén kiváló eredményeket szolgáltat a függőleges el- dulás, a porckorong kitüremlés és a porckorongon belüli más vonatkozásában. A nyírási értékekre vonatkozó hason- összehasonlítás azonban némi eltéréseket mutat. Ezért az an- us fibrosus nemlineáris nyírási tulajdonságainak a további gálata, bármilyen terhelési viszonyok melletti kitűnő porc- rong szimulációt eredményezhet. A véges-elem háló összetett ktúrája, egy meglehetősen finom háló mellett is 9000 alá kkentette az elemek számát. Ezzel, dacára az összetett gtörvényeknek, a számítási időt is le lehetett csökkenteni. ha még számos szóródás áll fent, és a mérési eredmények zött különbözőségeket lehet találni, az új porckorong modell idációja megerősíti, hogy ez a modell ígéretes megközelítése emberi csigolyák közti porckorongok számítógépes teljes mulációjának. ■

Analysis of the computational values for the annulus fibrosus in the model shows that even the outer rim of the annulus is under compression in the vertical and radial directions. Nevertheless the annulus circumferential values show, that there is tension in this direction after applying the compressive forces. The orthotropic layout of the annulus fibres distributes the vertical and radial compressive forces, resulting in a circumferential tension counterbalancing the bulging process.

6. Conclusions

A 3D FEM model of the L2-L3 lumbar vertebra-disc-vertebra complex was built containing only solid and shell elements. The fibre-composite properties of the annulus fibrosus were implemented using material orthotropy. All material properties were highly non-linear. These features of the present analysis have not been incorporated previously. Validation of the model by comparison of its response with literature data reflects excellent matching in terms of vertical displacement, disc bulge and intradiscal pressure. However, similar comparison of shear values shows some differences. Therefore further investigation of the non-linear shear properties of the annulus fibrosus could lead to excellent disc simulation for any loading situation. The overall structure of the finite element mesh reduced the number of elements below 9000 at a rather fine mesh. With this the calculation time was reduced as well despite the sophisticated material laws. Although there are a lot of scatter and discrepancies can be found in the experimental results the overall validation of the new disc model confirms that this is a promising approach to full computational simulation of human intervertebral discs. ■

Irodalomjegyzék / *References*

Adams, M. A., Green T. P., Tensile Properties of the Annulus Fibrosus I-II., Eur. Spine J., Vol. 2, pp. 203-213, 1993.

Belytschko, T., Kulak, R. F., Schultz, A. B., Galante, J. O., Finite Element Stress Analysis of an Intervertebral Disc, J. Biomechanics, Vol. 7, pp. 277-285, 1974.

Berkson, M. H., Nachemson, A., Schultz, A. B., Mechanical Properties of Humn Lumbar Spine Motion Segments, Part I-II., J. of Biomechanical Engineering, Vol. 101, pp. 46-56, 1979.

Galante, J. O., Tensile Properties of the Human Lumbar Annulus Fibrosus, Acta Orthopedica Scandinavica, Supplementum No. 100, Munksgaard Copenhagen, 1967.

Lin, H. S., Liu, Y. K., Adams, K. H., Mechanical Response of the Lumbar Intervertebral Joint Under Physiological Complex Loading, J. of Bone and Joint Surgery, Vol. 60a, No. 1, pp. 41-55, 1978.

LS-DYNA3D Users Manual, Livermore Software Technology Corporation, 1997.

Markolf, K. L., Morris, J. M., The Structural Components of the Intervertebral Disc, J. of Bone and Joint Surgery, Vol. 56a, No. 4, pp. 675-687, 1974.

McMillan, D. W., McNally, D. S., Garbutt, G., Adams, M. A., Stress Distributions Inside Intervertebral Discs: The Validity of Experimental Stress Profilometry, Proc. I. Mech. E., Vol. 210, pp. 81-87, 1996.

McNally, D. S., Adams, M. A., Internal Intervertebral Disc Mechanics as Revealed by Stress Profilometry, Spine, Vol. 17, No. 1, pp. 66-73, 1992.

[10] Seyed, A., Shirazi, A., Suresh, C. S., Abdul M. A., Stress Analysis of the Lumbar Disc-Body Unit in Compression, Spine, Vol. 9, No. 2, pp. 120-133, 1984.

[11] Shirazi, A., On the Fibre Composite Material Models of Disc Annulus – Comparison of Predicted Stresses, J. Biomechanics, Vol. 22, No. 4, pp. 357-365, 1989.

[12] Shirazi, A., Abdul M. A., Suresh, C. S., Mechanical Response of a Lumbar Motion Segment in Axial Torque Alone and Combined with Compression, Spine, Vol. 11, pp. 914-927, 1986.

[13] Sonnerup, L., A Semi-experimental Stress Analysis of the Human Intervertebral Disc in Compression, Experimental Mechanics, Vol. 12, No. 3, pp. 142-147, 1972.

[14] Tadano, S., Katagiri, K., Umehara, S., Ukai, T., A Constitutive Modeling of the Human Lumbar Intervertebral Disc and Forward-Backward Bending Simulation, Bio-medical Materials and Engineering, Vol. 7, pp.179-191, 1997.

[15] Tencer, A. F., Ahmed, A. M., Burke, D. L., Some Static Mechanical Properties of the Lumbar Intervertebral Joint, Intact and Injured, J. of Biomechanical Engineering, Vol. 104, pp. 193-201, 1982.

[16] Visible Human Project Database http://www.nlm.nih.gov/research/visible/visible_human.html

[17] Wilke, H. J., Neef P., Caimi, M., Hoogland, T., Claes, L. E., New in Vivo Measurements of Pressures in the Intervertebral Disc in Daily Life, Spine, Vol. 24, No. 8, pp. 755-762, 1999.

APPENDIX 7. – PRINCIPAL STRAINS AT THE ANNULUS SURFACE

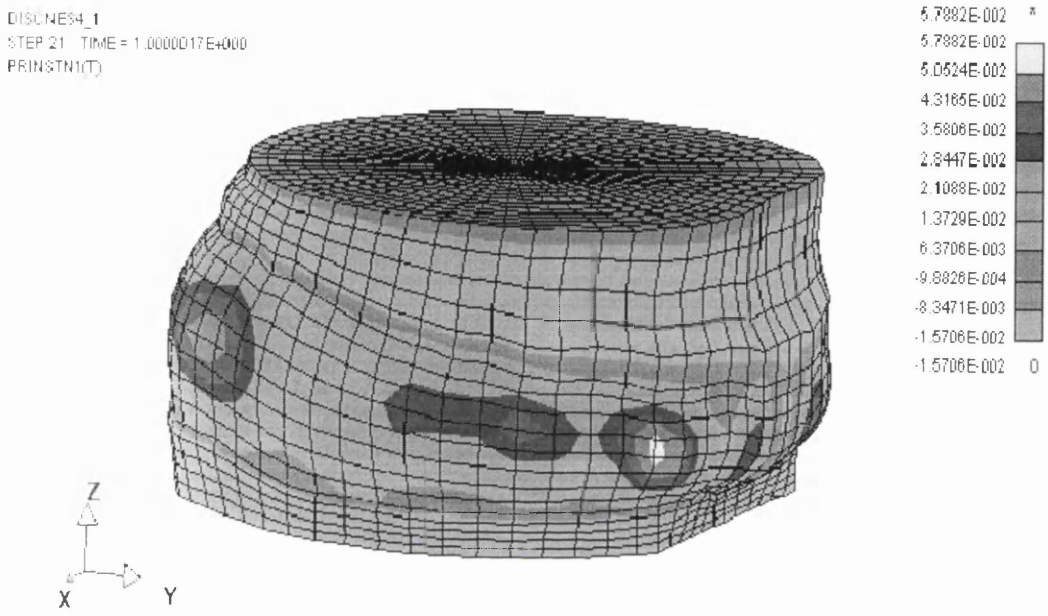
DISCNES4_1
STEP 21 TIME = 1.0000017E+000
PRINSTN1(T)
5.7882E-002
5.7882E-002
5.0524E-002
4.3165E-002
3.5806E-002
2.8447E-002
2.1088E-002
1.3729E-002
6.3706E-003
-9.8826E-004
-8.3471E-003
-1.5706E-002
-1.5706E-002
0
Z
X
Y

APPENDIX 8. – APPROACHING CONTINOUS FUNCTIONS WITH THEIR TAYLOR SERIES

If the f(x) function is k times (k→ ∞) differentiable at the point (a), it can be approached by its Taylor polynomial [99], T(x).

$$f(x) \to T(x) = \sum_{k=0}^{\infty} f^{(k)}(a)\frac{(x-a)^k}{k!}$$

introducing x=a+ξ,

$$T(a+\xi) = \sum_{k=0}^{\infty} f^{(k)}(a)\frac{(\xi)^k}{k!}$$

changing a=x and ξ=Δx,

$$f(x+\Delta x) \to T(x+\Delta x) = \sum_{k=0}^{\infty} f^{(k)}(x)\frac{(\Delta x)^k}{k!}$$

$$f(x+\Delta x) \approx \sum_{k=0}^{n} f^{(k)}(x)\frac{(\Delta x)^k}{k!} = T_n(x+\Delta x)$$

therefore the function can be approached by,

$$f(x+\Delta x) \approx f(x)$$

$$f(x+\Delta x) \approx f(x) + f'(x)\cdot\Delta x \qquad \text{as it is used in UMAT}$$

$$f(x+\Delta x) \approx f(x) + f'(x)\cdot\Delta x + \frac{1}{2}f''(x)\cdot\Delta x$$

$$f(x+\Delta x) \approx f(x) + f'(x)\cdot\Delta x + \frac{1}{2}f''(x)\cdot\Delta x + \frac{1}{6}f'''(x)\cdot\Delta x$$

.

.

.

The difference between the function and its Taylor polynomial approach can be estimated with the Lagrange remainder,

$$r_n(x+\Delta x) = f(x+\Delta x) - T_n(x+\Delta x)$$

$$r_n(x+\Delta x) = f^{(n+1)}(\eta)\frac{\Delta x^{n+1}}{(n+1)!}$$

where η is a value between x and x+Δx.

Let M be the maximum of the absolute value of the differential $f^{(n+1)}(\eta)$, than the error H is,

$$H \le M\frac{|\Delta x|^{n+1}}{(n+1)!}$$

If the Taylor series approach is taken into consideration only to the first derivative,

$$\max H_2 = M_2 \frac{(\Delta x)^2}{2}$$

and

$$\lim_{n\to\infty} H = 0$$

from

$$\lim_{n\to\infty} \frac{|\Delta x|^{n+1}}{(n+1)!} = 0$$

the Taylor series is convergent.

APPENDIX 9. – SENSITIVITY

Sensitivity of the Material Constants

Basic Equations

$$y = f(x)$$

$$\Delta y = f'(x) \cdot \Delta x$$

$$\frac{\Delta y}{y} = \frac{x \cdot f'(x)}{f(x)} \cdot \frac{\Delta x}{x}$$

Sensitivity of the polynomial constants

$$\sigma(\varepsilon, a, b, c, d) = a\varepsilon^3 + b\varepsilon^2 + c\varepsilon + d$$

Sensitivity to a, b, c, d is respectively,

$$\left.\frac{\Delta\sigma(\varepsilon)}{\sigma(\varepsilon)}\right|_a = \frac{a\varepsilon^3}{a\varepsilon^3 + b\varepsilon^2 + c\varepsilon + d} \cdot \frac{\Delta a}{a}$$

$$\left.\frac{\Delta\sigma(\varepsilon)}{\sigma(\varepsilon)}\right|_b = \frac{b\varepsilon^2}{a\varepsilon^3 + b\varepsilon^2 + c\varepsilon + d} \cdot \frac{\Delta b}{b}$$

$$\left.\frac{\Delta\sigma(\varepsilon)}{\sigma(\varepsilon)}\right|_c = \frac{c\varepsilon}{a\varepsilon^3 + b\varepsilon^2 + c\varepsilon + d} \cdot \frac{\Delta c}{c}$$

$$\left.\frac{\Delta\sigma(\varepsilon)}{\sigma(\varepsilon)}\right|_a = \frac{d}{a\varepsilon^3 + b\varepsilon^2 + c\varepsilon + d} \cdot \frac{\Delta d}{d}$$

At a given ε, the change in σ can be obtained if the change in any of the four constants is known. The result will be %.

The overall change will be,

$$\left.\frac{\Delta\sigma(\varepsilon)}{\sigma(\varepsilon)}\right|_{a,b,c,d} = \frac{1}{\sigma(\varepsilon)}\left[a\varepsilon^3\frac{\Delta a}{a} + b\varepsilon^2\frac{\Delta b}{b} + c\varepsilon\frac{\Delta c}{c} + d\frac{\Delta d}{d}\right]$$

APPENDIX 10. – IMPLEMENTING THE HOOKE'S LAW IN LS-DYNA UMAT

User Defined Material Properties

The DEC LS-DYNA3D software package lets the user to define its own material properties. (This option is not supported by the PC version). However this can be done with lots of care and plenty of restrictions. Defining User Defined Material (UMAT) to LS-DYNA is not straightforward and requires special attention from the user. The following section describes the opportunities and the work done on this field.

Firstly the open code of LS-DYNA3D was obtained from Livermore Software Technology Corporation (LSTC) by contacting *support@lstc.com*. A set of object files and a MAKEFILE are supplied in a tarred, gzipped file. The directory list of these files can be found in Appendix 5. Note that user defined materials (UMAT) are not supported by the PC version of LS-DYNA. Therefore the UNIX version has to be used.

Next, the user defined material code in FORTRAN77 programming language has to be written. The new code has to be implemented into the file DYN21.F. Writing a user defined material code is no trivial task. Proficiency is needed in both mechanics and computer programming. Modifying the UMAT code might lead to system crash or instability as the process includes the full recompilation of the LS-DYNA executable. LSTC does not give any technical support to UMAT and encourages only experienced users to use the time consuming process to write their own code. Developer's package and debugger as such is not existing. The user has to write the FORTRAN 77 subroutine fully "by hand".

How to Compile

Finally if the code is ready, it has to be compiled into the LS-DYNA3D executable. To do this, a FORTRAN77 and a C++ compiler are needed running on the machine. The MAKEFILE that comes with the object code of DYNA3D has to be edited to introduce a reference to the user's code. The original

MAKEFILE source can be seen in Appendix 6. Here DYNxx.O and the other necessary modifications are not included yet. (xx stands for a number between 41 and 50 inclusive). First of all, a new DYN??.O file has to be generated. It can be made by temporarily rename DYN21.F to DYNxx.F and replace the DYN21.O section to DYNxx.O in the MAKEFILE. Then if MAKEFILE is ran, it will generate the new file called DYNxx.O. If something goes wrong an error message can be seen saying "Don't know how to make DYNxx.O". After setting everything back, the MAKEFILE has to be edited again. UMATxx.O must be included just before DYN21.O. Also the section "SOUBROUTINE UMAT xx" has to be commented out from the file DYN21.F. The file DYN21.F is provided by LSTC with the object code of LS-DYNA.

To compile and link the code the modified MAKEFILE has to be run. Verify that the subroutine in UMATxx.O is used rather than the corresponding subroutine in DYN21.O. This can be confirmed from the screen output during the make operation. This will generate a new LS-DYNA3D executable under the name LS-DYNA_9402_DEC_40_USERDEF at version 940_2a. This file has to be copied into the LS-DYNA3D program directory, which is by default the directory, /USR/OASYS71/EXECUTABLES. Here, the LS-DYNA executable has to be relinked to the new executable file including the new, user defined material in the hidden file .OA_PREF. This can be done by putting the name of the new executable file into the line SHELL*DYNA_VERSION.

Model Definition

To use the freshly implemented new material, from the current .KEY (PC version .DYN) model file, the new material has to be referred by the *MAT_USER_DEFINED_MATERIAL_MODELS material card. This card will point to the appropriate user subroutine. In this material card the following options have to be defined.

```
$---+----1----+----2----+----3----+----4----+----5----+----6----+----7----+----8
$                    (6) DEFINE PARTS CARDS
$---+----1----+----2----+----3----+----4----+----5----+----6----+----7----+----8
*PART
$HEADING
 PART PID =         1 PART NAME :MESH
$       PID       SID       MID     EOSID      HGID      GRAV    ADPOPT      TMID
          1         1         1
$---+----1----+----2----+----3----+----4----+----5----+----6----+----7----+----8
$                    (7) MATERIAL CARDS
$---+----1----+----2----+----3----+----4----+----5----+----6----+----7----+----8
*MAT_USER_DEFINED_MATERIAL_MODELS
$MATERIAL NAME:MESH
$       MID        RO        MT       LMC       NHV    IORTHO     IBULK        IG
         1 2.300E+03        41         8        10         0         3         4
$     IVECT     IFAIL
          0         0
$        P1        P2        P3        P4        P5        P6        P7        P8
 2.600E+02 2.500E+00 3.100E+00 2.600E+01 0.000E+00 0.000E+00 0.000E+00 0.000E+00
$---+----1----+----2----+----3----+----4----+----5----+----6----+----7----+----8
$                    (7.1) SECTION CARDS
$---+----1----+----2----+----3----+----4----+----5----+----6----+----7----+----8
*SECTION_SOLID
$PROPERTY NAME:MESH
$       SID    ELFORM
          1         1
$---+----1----+----2----+----3----+----4----+----5----+----6----+----7----+----8
```

MID	Material identification number. A unique number has to be chosen.
RO	Mass density.
MT	User material subroutine number. It has to be between 41 and 50 inclusive.
LMC	Length of material constants array, which is equal to the number of material constants to be input.
NHV	Number of history variables to be stored.
IORTHO	Set to 1 if the material is orthotropic.
IBULK	Address of the bulk modulus in material constants array.
IG	Address of the shear modulus in material constants array.
IVECT	Vectorisation flag.
IFAIL	Failure criterion flag.
P1...PN	Material parameters in material constants array.

The number of history variables is arbitrary and can be any number greater than or equal to 0. Here note, that from the structure of the object code, it seems that the maximum number of history variables can be only 80 without major modification in the main programme. History variables are stored in HSV(n). These are for each element or gauss point. They can be used for storage of intermediate integrations, flags, accumulated plastic strains or anything we put here. Basically it is an array of numbers that is stored between time steps, so upon next re-entry to the routine this information can be retrieved. Anything stored in HISV(1) becomes available to LS-TAURUS as the equivalent plastic strain. By using a flag in the input data (say cm(48)) and a case statement inside the UMAT, it can be controlled what TAURUS displays later. The coordinate system definition is optional but is probably necessary if the model involves material that have directional properties such as composites and anisotropic plasticity models. When the coordinate system option is used, then all data passed to the constitutive model is in the local system.

A bulk modulus and the shear modulus are required for transmitting boundaries, contact interfaces, rigid body constraints and time step size calculations. Up to ten subroutines can be currently implemented simultaneously to update stresses in solids, shells, thick shells and beam elements.

Write the UMAT in single precision if it is possible. A double precision version may add up to 40% extra time since these routines are called a lot.

The language of the LS-DYNA object code is FORTRAN77, this will be compiled through C++ to machine code. There is no existing documentation of the variable structure of LS-DYNA. The programmer have to rely on himself and the LSTC helpdesk. Since the fluctuation is rather high among the LSTC programmers asking the helpdesk takes some weeks if the problem is deeper and they often can not find adequate solution.

The user material subroutine functions has to refer to the local element coordinate system. Furthermore it has to fit to the software's own local to global coordinate system transformation matrix. Modifying these transformation matrices is very risky and time consuming. The UDM code has to contain the stress update in a form of

$$\sigma_{i+1} = \sigma_i + \delta\sigma_i$$

SIG(i) is passed to UMAT and UMAT passes than back. These are accumulated stresses. So they are essentially stress at time t. Then, stress at time t+dt and increment SIG(i) can be calculated before return.

EPS(i) are passed to UMAT and these are incremental strains, i.e. linear strain added since the previous step.

Test results with UMAT

Since there were many obstacles to obtaining the DEC FORTRAN and C++ compilers the work implementing UDM code to LS-DYNA have been delayed for more than 2 month. Finally a solution was found, so the work could proceed.

First, the Hooke's law, as a commonly used and easily controllable material law was implemented to ensure that all the aspects of UMAT coding were understood. The Hooke's law is included as default in LS-DYNA3D under the name MAT_ELASTIC. The two properties were tested against each other. The graph below shows one example that the two results are perfectly matching.

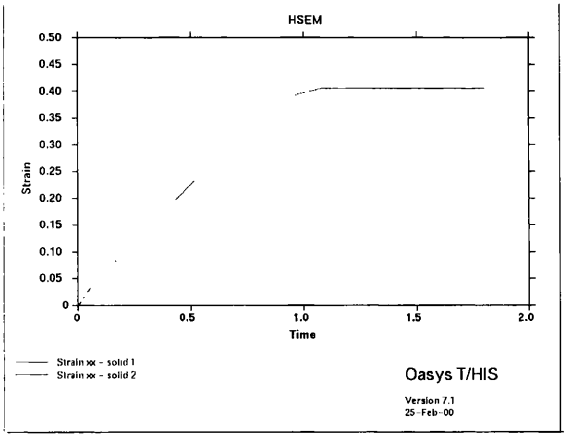

LS-DYNA3D, as it was mentioned before needs the stresses as a function of their own increment. The $\{\varepsilon\}=[T_{\varepsilon\sigma}]\cdot\{\sigma\}+\{\varepsilon_0\}$ form of the Hooke's law is well known and widely used. The inverse form of the function is not so common. It can be obtained from the previous form by solving the system of the following three equations.

$$\varepsilon_x-\varepsilon_{0x}=\frac{1}{E}\left[\sigma_x-\nu(\sigma_y+\sigma_z)\right]$$

$$\varepsilon_y-\varepsilon_{0y}=\frac{1}{E}\left[\sigma_y-\nu(\sigma_x+\sigma_z)\right]$$

$$\varepsilon_z-\varepsilon_{0z}=\frac{1}{E}\left[\sigma_z-\nu(\sigma_y+\sigma_x)\right]$$

The solution of the problem is using the Cramer's rule

$$\sigma_x=\sigma_{x0}+\frac{E}{(1+\nu)(1-2\nu)}\left[(1-\nu)\varepsilon_x+\nu(\varepsilon_y+\varepsilon_z)\right]$$

$$\sigma_y=\sigma_{y0}+\frac{E}{(1+\nu)(1-2\nu)}\left[(1-\nu)\varepsilon_y+\nu(\varepsilon_x+\varepsilon_z)\right]$$

$$\sigma_z=\sigma_{z0}+\frac{E}{(1+\nu)(1-2\nu)}\left[(1-\nu)\varepsilon_z+\nu(\varepsilon_x+\varepsilon_y)\right]$$

These functions were implemented into the LS-DYNA3D UMAT section in the file DYN21.F.

APPENDIX 11. – SIGNIFICANCE OF THE ANNULUS PROPERTIES TO FINITE ELEMENT MODELING OF INTERVERTEBRAL DISCS

Journal of Musculoskeletal Research, Vol. 5, No. 3 (2001) 159–171

ORIGINAL ARTICLES

SIGNIFICANCE OF THE ANNULUS PROPERTIES TO FINITE ELEMENT MODELING OF INTERVERTEBRAL DISCS

G. T. Nagy and C. R. Gentle

Department of Mechanical and Manufacturing Engineering
Biomechanics Research Group, The Nottingham Trent University, Nottingham, UK

Received May 10, 2001; Accepted May 25, 2001

ABSTRACT

Current mathematical material laws work quite accurately with conventional engineering materials because they are linear and isotropic. These laws are much less effective, however, at representing living tissues. Biomechanical engineers therefore often face the problems of modelling material non-linearities, particularly with the soft tissues, muscles and tendons of the human body. The non-linear and often anisotropic structure of these materials makes any mathematical representation very difficult. In particular, the lack of a good general mathematical model of the intervertebral disc has hampered the study of spinal mechanics, as the disc annulus is a nonlinear fibrous tissue with highly directional properties. Previous studies have concentrated on the overall behavior of discs and this has been largely explained but knowledge is still very limited on the effect of the individual disc components. This means that current mathematical models are poor when it comes to describing a prolapsed disc, where there has been failure of at least one of the components. This finite element study described here focuses on the disc annulus properties and their effect on disc behavior. The novelty of this study lies in the material formulation of the annulus fibrosus, which changes its Young's modulus according to a non-linear curve.

Keywords: Intervertebral disc, Lumbar spine, Low back pain, FEM, Nonlinear

INTRODUCTION

From a structural point of view the most important element of the body is the spine. It is the equivalent of a chassis in a vehicle, the part to which all the specialized components are attached. It differs from a vehicle chassis, however, by being flexible so that the body can twist and bend forwards and backwards or from side to side. This flexibility is provided by the discs of soft tissue that separate the vertebrae in the regions where the flexibility is required.

These are the intervertebral discs and these, in turn, are made up of three components. The bulk of the disc, as indicated in Fig. 1, is the annulus

Correspondence to: Prof. Geza T. Nagy, Department of Mechanical and Manufacturing Engineering, Biomechanics Research Group, The Nottingham, NG1 4BU, UK.

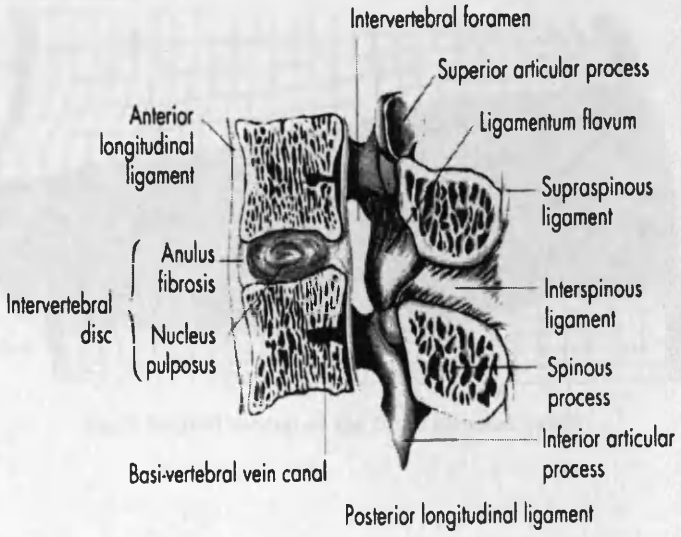

Fig. 1 Longitudinal section of lumbar vertebral segment.

fibrosus, which is a hollow ring of cartilaginous tissue. The hollow core is filled by the nucleus pulposus, which is a gel, composed essentially of water. Wrapped around the outside of the annulus fibrosus are the anterior and posterior longitudinal ligaments which behave like an elastic support stocking to contain the bulging of the disc under load.

Nomenclature:

F	force
σ	stress
ε	strain
τ	shear stress
E	Young's modulus
ν	Poisson's ratio
G	shear modulus
γ	shear strain
K	bulk modulus
T	time
r, t, z	radial, tangential, vertical component
β_i, β_0	fiber direction to the horizontal plane, 15°.

The most important component of the intervertebral disc, again from a structural perspective, is the annulus fibrosus since it bears most of the loads.[1] As well as simple weight bearing, it also offers most of the resistance to relative movement between adjacent vertebrae by deforming in response to the differential compressive, tensile and shear forces generated during the movement.[2] Its composition is that of a fibrous collagen matrix embedded within an aqueous gel of proteoglycans and other proteins.[3] The highly oriented and layered structure of the annulus suggests that its material behavior will be significantly nonlinear and anisotropic.[4] Understanding the failure of this complex material should lead to a better explanation of mechanical disc degeneration[5] and other symptomatic disc disorders, as well as an increased understanding of the spine as a whole.

The purpose of this study, therefore, is to produce a finite element model of the annulus fibrosus, which incorporates a realistic mathematical model of the material properties. The overall aim is to build this into a full and general simulation of the intervertebral disc that can be used in a complete biomechanical analysis of the various forms of spinal trauma.

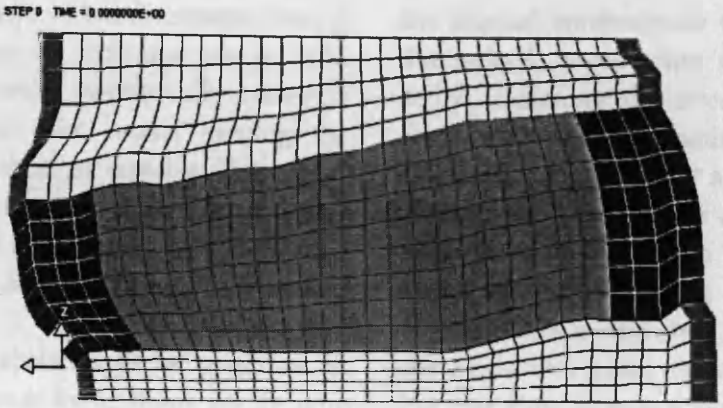

Fig. 2 Sagittal section of the finite element model.

1. Finite Element Model

Figure 2 shows a sagittal section of the 3D solid model of the L2–L3 lumbar vertebra-disc-vertebra complex built by the Biomechanics Research Group of the Nottingham Trent University. The anatomical model is a full-size 3D Pro/Engineer solid model, based on the male data sets supplied by the Visible Human Project.[6]

It must be remembered that this data therefore represents only one particular man, even though the fact that he was in the fiftieth percentile by size means that he is typical of most people. Strictly, however, the data do not apply to women, the young, the old and the exceptionally short or tall. The main geometric factors of the elliptical cross-section model are shown in Table 1, together with the model data.

The model was meshed in Altair Hypermesh 3D® and the FEM code[7] was written in LS-DYNA 3D®. Model checks and post processing were

Table 1 Main Geometric Factors.

Total number of elements	2860
Total number of nodes	3107
Annulus solids	540
Annulus outside shells where applicable	180
Nucleus solids	560
Cancellous bone solids	1288
Cortical bone solids	252
Disc height [mm]	15.00
Anterior-posterior disc length [mm]	40.30
Lateral disc width [mm]	55.60
Disc cross-sectional area [mm^2]	987.26
Nucleus cross-sectional area [mm^2]	697.98
Top surface area [mm^2]	1436.18
Bottom surface area [mm^2]	1712.54

performed under Oasys v7.1 environment. During the model generation, the main aim was to build an anatomically and mechanically relevant lumbar intervertebral disc model keeping the calculation time as short as possible. The model contains the nucleus pulposus, the annulus fibrosus, and part of the second and third lumbar vertebrae divided into cancellous bone and cortical shell.

The two biggest obstacles to be overcome in finite element studies of living tissue are the nonlinearity and the anisotropy. Both of them play a significant role in the real intervertebral disc to ensure that the necessary stiffness, damping and stability are achieved. It is therefore essential that they should be modelled correctly here. This paper compares three intervertebral disc models,[8] which are different in the material formulation of the annulus fibrosus.[9]

2. Annulus Models

In the first two models, referred to as Model 1 and Model 2, the annulus is described as an orthotrophic, nonlinear material. The problem of nonlinearity was approached by using eight straight-line segments to represent and replace the original, continuously varying, experimentally determined stress-strain characteristics satisfactorily. Sectioning the stress-strain curve can be done with different methods, which results in different accuracy. To get a widely comprehensive view on the value of the approach, two types of analogy were chosen. In Model 1, the original curve was divided using a linear division scale on the ε-axis in the $0\text{-}\varepsilon_{max}$ domain. In Model 2, the ε-axis was again divided into eight sections but this time it was done on a quadratic basis. This second method gives a finer resolution at small deformation, where the change is faster in the Young's modulus. The average accuracy is around 2% at the beginning of the curve. However, at large deformation the deviation can grow up to 10%, which is a considerable initial error. To show how much importance the accuracy has, Model 2 was tested both approaching the curve from the top and from the bottom with the line segments. Figure 4 shows the result.

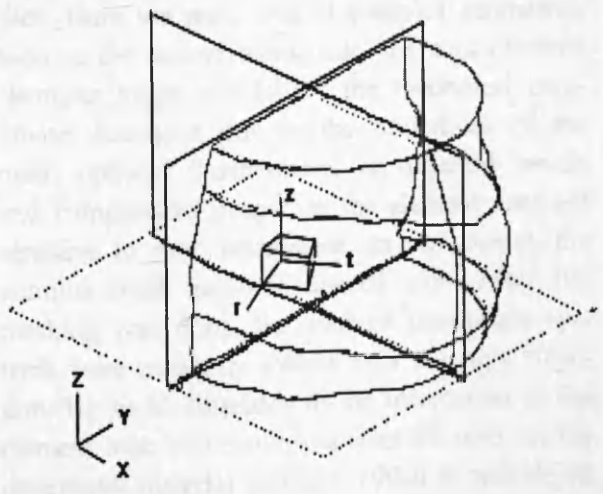

Fig. 3 Coordinate systems.

The main disadvantage of using this method is that the new stress-strain function is not continuous in the domain. Furthermore, the sectioned stress-strain curve was mirrored about the origin so that it is identical in tension and compression. Compromises therefore had to be made with the accuracy and hence the sectioned curve averages the tensional and compressional properties, although it is estimated that the average inaccuracy introduced is never more than 2%. The drawback to this approach is that the requirement for new input data at every change from one straight section of the stress-strain function to the next leads to an increased computational time.

The orthotropy was supplied by giving different directional properties to the annulus solids and furthermore a 2-dimensional nonlinear orthotropic shell surrounding the outer disc annulus surface. Details of the coordinate systems used in the

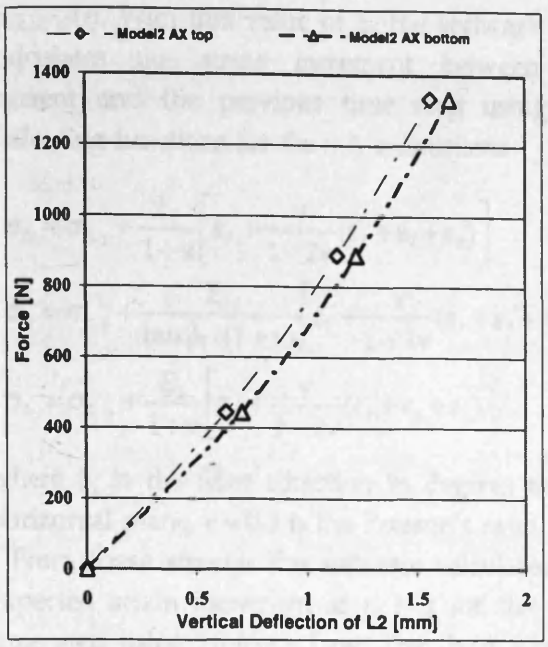

Fig. 4 Different approaches in Model 2.

models are given in Fig. 3, while the annotations used are given in the Nomenclature Section. The x-axis points to the left lateral direction and the y-axis to the posterior direction. The z-axis points upward, towards the head. The r, t, z orthogonal element coordinate system is rotating in a global cylindrical system with z initially vertical and r initially pointing out from the centroid of the disc slice. Here we note, that at complex geometries such as the intervertebral disc, the axes of some elements might not follow the theoretical coordinate directions due to the limitations of the mesh options. Furthermore, at different tensile and compressive properties the element axes are sensitive to their orientation. In our model, the annulus mesh required special care. After the meshing was done, the element coordinate systems were manually rotated into the right direction. Up to 8° difference in the orientation of the element axes will cause less then 1% error in the directional material stiffness, which is considered to be neglectable.

In the third model, referred to as Model 3, a very different approach was chosen to describe the annulus fibrosus as a nonlinear, orthotropic material. In this approach, a new material law was programmed into the User Defined Material Properties of LS-DYNA®, which was the software package used for the construction of the finite element model of the overall disk. The code was written in Fortran 77. For tension and compression the annulus is given a third-order, nonlinear characteristic in which the failure of the material is neglected, in the sense that it is assumed that the failure point is never reached. It is quite easy to describe this function with a third-order polynomial. Third-order polynomial representation was chosen because it is continuously differentiable in any point of the domain of variability. Recommended precision for the polynomial constants is three or more significant digits. For 1% change in the value of the polynomial constants a, b, c, d the estimated sensitivity of $\Delta\sigma/\sigma$ reaches around 1% for the third-order constant a, at large deformations and for the first-order constant c, at small deformations. It is around 0.2% for the second-order constant b, and 0.02% for d if $d \to 0$. LS-DYNA® handles the real values in single precision. The number of significant digits for single precision literals is 7.

Let the input data be the four polynomial constants of a nonlinear third-order stress-strain curve, a, b, c, d.

$$\sigma = a \cdot \varepsilon^3 + b \cdot \varepsilon^2 + c \cdot \varepsilon + d$$

The Young's modulus of the intervertebral disc at a certain time can be calculated by deriving this function at the current strain, $\varepsilon_{(r,\,t,\,z)}(t)$.

$$E(\varepsilon) = \frac{d\sigma}{d\varepsilon}$$

The software approximates the strain increment from the previous time step, then it calculates

$E_{(r,\,t,\,z)}(t)$. With this value of E, the software then calculates the stress increment between the current and the previous time step using the following functions for the r, t, z directions.

$$\sigma_{r_i} = \sigma_{r_{i-1}} + \frac{E_r}{1+\nu}\left[\varepsilon_r + \frac{\nu}{1-2\nu}(\varepsilon_r + \varepsilon_t + \varepsilon_z)\right]$$

$$\sigma_{t_i} = \sigma_{t_{i-1}} + \frac{E_t}{\tan\beta_i \cdot (1+\nu)}\left[\varepsilon_t + \frac{\nu}{1-2\nu}(\varepsilon_r + \varepsilon_t + \varepsilon_z)\right]$$

$$\sigma_{z_i} = \sigma_{z_{i-1}} + \frac{E_z}{1+\nu}\left[\varepsilon_z + \frac{\nu}{1-2\nu}(\varepsilon_r + \varepsilon_t + \varepsilon_z)\right]$$

where β_i is the fiber direction in degrees to the horizontal plane, $\nu = 0.3$ is the Poisson's ratio.

From these stresses the software calculates the expected strain increment at r, t, z for the next time step using Hooke's Law. The shear stresses are calculated as usual,

$$G_{r,t,z} = \frac{E_{r,t,z}}{2(1+\nu)}$$

$$\tau = G \cdot \gamma$$

With this method, if the time step is small enough the elements follow the nonlinear characteristics accurately in the local coordinate system. To achieve the required anisotropy and orthotropy the vertical stress-strain curve was scaled down to the r, t, z element coordinate directions differently. The effect of stiffening to the tangential and weakening to the vertical directions during tension-compression caused by the changing angle between the annulus fibers was neglected in this model.

Several measurements have been done on the annulus stiffness. Unfortunately, most of them were recording the force-deflection curve only and failed to give enough details on the initial sample length. Therefore the experiments of Tadano *et al.*[17] were chosen to represent the annulus characteristics in the material model. In this study the overall stiffness of a denucleated Grade 1, non-degenerated intervertebral disc was tested. The vertical stress-strain characteristics of the annulus fibrosus for both tension and compression was recorded immediately by a computer controlled test machine.

3. Nucleus

In both models, the nucleus pulposus was taken to be essentially a pure Newtonian fluid and was

Table 2 Comparison of the Material Properties.

Material Name	Material Parameter			
	Model 1, Model 2		Model 3	
Cortical bone	$E = 12000$ MPa	$\nu = 0.3$	$E = 12000$ MPa	$\nu = 0.3$
Cancellous bone	$E = 100$ MPa	$\nu = 0.2$	$E = 100$ MPa	$\nu = 0.2$
Annulus solid	$\sigma(\varepsilon)_{vert,max} = 100$ MPa		$\sigma(\varepsilon)_{vert} = 187.2\varepsilon^3 + 17.3\varepsilon^2 + 4.4\varepsilon$ [MPa]	
	$\sigma(\varepsilon)_{tan,max} = 173$ MPa	$\nu = 0.45$	$\sigma(\varepsilon)_{tan} = \sigma(e)_{vert}/\tan(\beta)$	
	$\sigma(\varepsilon)_{rad,max} = 100$ MPa	$\varepsilon_{max} = 1.5$	$\sigma(\varepsilon)_{rad} = \sigma(\varepsilon)_{vert}$	
	$G(\varepsilon)_{max} = 8$ MPa	$G(\varepsilon) = E(\varepsilon)/2(1+\nu)$	$G(\varepsilon) = E(\varepsilon)/2(1+\nu)$	$\nu = 0.3$
Annulus shell	$\sigma(\varepsilon)_{vert,max} = 100$ MPa			
	$\sigma(\varepsilon)_{tan,max} = 173$ MPa	$\nu = 0.45$		
	$G(\varepsilon)_{vert,max} = 8$ MPa	$\varepsilon_{max} = 1.5$		
	$G(\varepsilon)_{tan,max} = 8$ MPa	$G(\varepsilon) = E(\varepsilon)/2(1+\nu)$		
	$E_{rad} = 100$ MPa			
	$G_{rad} = 8$ MPa			
Nucleus	K = 2.5 MPa	(Bulk modulus)	K = 2.5 MPa	(Bulk modulus)

described by its bulk modulus, K. The properties of the cortical and cancellous bone were taken from previous FE studies.[10,11] Table 2 shows a summary of the material properties.

4. Boundary Conditions

The validity of the models and the analysis procedure has been established by comparison with those values that are also available for direct experimental measurements,[12] e.g. response of the disc-body unit to axial and eccentric compressive loads in terms of axial displacement, the disc bulge and displacement of various nodes inside the disc.

The disc model and the boundary conditions was built to comply with the measurements of Lin *et al.* Specimen 10 was chosen as closest to the geometric factors of the computational model. The above specimen was an L2–L3 vertebra-disc-vertebra joint. The level of degeneration was Grade 1 according to Galante, which means a non-degenerated disc. In our model, so as in the measurement, the top and bottom of the two vertebras were truncated to achieve two flat, horizontal loading surfaces parallel to the middle disc plane. At uniform compression, the load was applied in the experiments directly by the crosshead of the machine. This resulted in a relatively uniform distribution of load across the ends of the specimen, provided the top and bottom loading surfaces stay parallel. This technique ensures that there is no need to know where the exact location of the center point is. The specimen was loaded first to 445 N, then to 899 N, and finally to 1334 N. The loading rate was less than 1.27 cm/sec. At FEA, the load was applied as ramp pattern of uniform pressure to the top surface of the L2 vertebra. The equivalent force to this pressure was consequently 445 N, 899 N, and 1334 N, respectively. In all simulation, the bottom vertebra was fixed in 6 degrees of freedom. To avoid the tilting of the top vertebra, its top surface was also constrained against x- and y-translation.

To produce an off-center compression, first the center of the disc has to be located. By Lin *et al.*, the centroidal axis of the specimen was defined at the position where the preload caused the minimum vertical deflection. This method is difficult to follow in FEA. Therefore in our analysis we defined the A-P center point where, if the disc is loaded, the top surface of the upper vertebra produces the lowest angle of rotation on the x-axis throughout its motion. In this way, the resultant bending moment in addition to the compression causing more deformation was avoided. In the experiments, the loading was done by a wedge-shaped test rig. Since the computer model is symmetrical, it is satisfactory to load the disc in one point with a nodal force. The same equivalent force was used as before, displaced by 10 mm to the lateral or frontal direction, following the method used in the experiments. For flexion, the top vertebra was constrained against x-translation; for lateral bending against y-translation.

There was no additional damping applied to the model. For the investigation into the internal movements in the disc, the loading had to be slow enough to avoid dynamic shocks throughout the disc body and to let the nodes creep into their steady state. Therefore, a slow displacement of 0.8 mm was applied to the top vertebra as a ramp pattern. This displacement occurs at an equivalent load of 1500 N axial compressive force in a disc with the same anterior-posterior diameter such as in the FEM model. Unfortunately, the time penalty of the relatively slow loading is enormous, since the creep depending on the shear properties of an oil-like substance is slow.

5. Nonlinearity

Figure 5 shows the difference between the 8-line segments linearly and quadratically sectioned, and the nonlinear approach for axial compression. The problem with the accuracy at low deformation can be clearly seen in the results for Model 1, which generally shows weaker characteristics at low strains. Although it becomes stiffer later, this is not enough to compensate for the fast changes in the Young's modulus.

The second approach shows some improvements in the stiffness at low deformation; nevertheless, the overall behavior is more like a slightly damaged intervertebral disc, as Tencer's curve[13] shows. There is a major change in the precision of the movements in Model 3, with better nonlinearity. In the first two models, even though the characteristic was satisfactory, the actual results were very far from being acceptable. The response to eccentric loading was not comprehensible.

The third model shows tremendous improvement in accuracy. Here we note that the result is still a bit weaker than the measured data. This depends on the robustness of the error correction in the model. It can be improved by calculating up to the second derivative, but this will cause an extra time penalty,

$$f(x+\Delta x)=f(x)+\frac{df(x)}{dx}\Delta x+\frac{1}{2}\frac{d^2f(x)}{dx^2}\Delta x^2.$$

The usefulness of the third method lies particularly in eccentric loading. Figure 6 shows the displacement of the second vertebra under eccentric forward and lateral bending. A greater error can be seen at eccentric loading. This is caused by a very simple practical problem; determination of the exact location of the loading is extremely hard, since it is hardly possible to define the center point of the disc. The position of the load in the simulation does not fully correspond to the measurement.

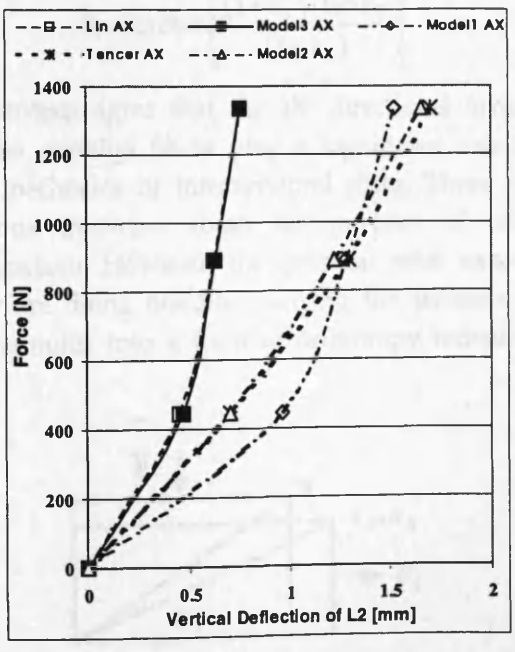

Fig. 5 Response to axial compression.

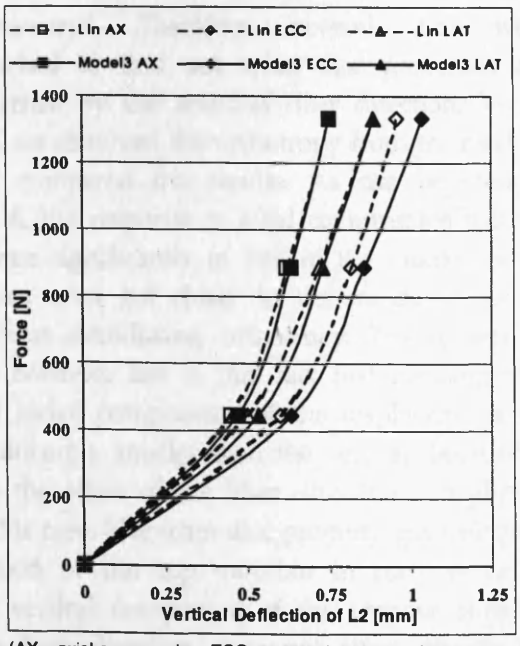

(AX – axial compression; ECC – eccentric compression; LAT – lateral bending)

Fig. 6 Response to forward and lateral bending.

6. Orthotropy

The intervertebral disc annulus has a significant anisotropy generated by the fiber direction.[14] The annulus fibers are oriented at +15 degrees to the horizontal at every second layer and to –15 degrees at the remaining.[15] Similar properties can be represented by material orthotropy.[16] In the first two models, the material orthotropy was achieved by using an orthotropic elastic shell. The third model simulates the orthotropy based on a simple calculation of the fiber direction. Most of the measurements give the vertical stress-strain curve as a result. The tangential stresses can be calculated easily with trigonometric functions if it is assumed that the material is homogeneous in the *t*, *z* directions (Fig. 7),

$$F_t = F_z \cdot \frac{1}{\tan\beta_i}.$$

Furthermore, during compression there is a small change in the fiber direction. In the *i*th time step, if the strain is known, then the angle in the element is expressed by:

$$\beta_i = \arctan\left[\frac{(1+\varepsilon_{z_i})\cdot\tan\beta_0}{(1+\varepsilon_{t_i})}\right]$$

Scientists agree that the 15° directional layout of the annulus fibers play a significant role in the mechanics of intervertebral discs. There are various theorems about the purpose of such a structure. However, the question what exactly they are doing besides changing the stiffness of the annulus into a form of orthotropy remained

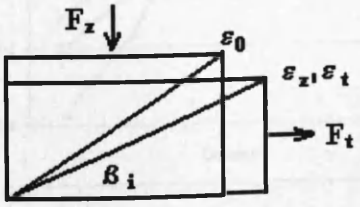

Fig. 7 Change of fiber direction.

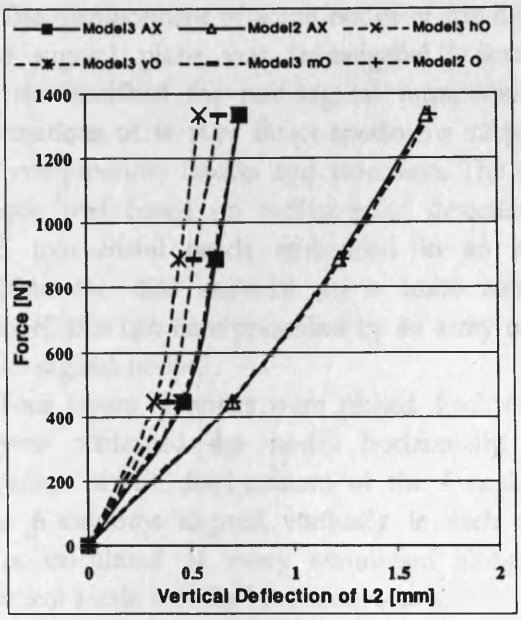

Fig. 8 Effect of removing the orthotropy. (h, v, m denote whether the former horizontal, vertical component of the directional annulus properties or the mean value of these two stress-strain curves were introduced into the model; o denotes that the orthotropy has been removed)

unanswered. Therefore, several tests were launched to find out what disc properties are governed by the annulus fiber direction. To do this, we removed the orthotropy from the models, and compared the results. As can be seen in Fig. 8, the response to axial compression did not change significantly in any of the models. Some values even got closer to the measured curves without introducing orthotropy. The answer to this behavior lies in that fact that the tangential and radial components of the displacements are significantly smaller than the vertical. Because of this the effect of the fiber direction is negligible in this case. The main disc property governing the motion of the top vertebra in compression is the vertical component of the annulus stiffness. The fiber direction does not affect directly the pure loading case of the intervertebral disc. It affects the more complex stress states like the

change in the disc bulge, fluid flow shaping the geometry and the torsional properties.

7. Shear Properties

Throughout the investigation so far, a nonlinear shear function was used to describe the changes in the shear stress. This function uses the general Hooke's law to determine the shear modulus $G(t)$ if the Young's modulus $E(t)$ and the Poisson's ratio ν are known. Our model has shown some instability absorbing shockwaves with nonlinear shear properties. Therefore, a linear shear function was also introduced instead of the nonlinear one. There are some data available about the displacement of limited nodes inside the disc, which describe the movements of the material inside. This map on the migration of the inside nodes shows the displacements occurring in the disc during compression. Together with the bulge of the outside boundary, it helps in fine-tuning the shear properties of the model.[18]

The displacement of some nodes of the disc in the sagittal plane was investigated.[19] Seroussi *et al.* described the mid-sagittal intradiscal deformations of *in vitro* intact specimens subjected to compression, flexion and extension. The technique was based on radiographic detection of 0.5 mm metal beads embedded in an array within the disc material. In a finite element model, this can be represented by an array of the mid-sagittal nodes.

Four layers of nodes were picked. Each of the layers contained 6-6 nodes horizontally. The average of the displacement of the 4 nodes in the 6 columns aligned vertically to each other was calculated at every simulation along the vertical z-axis and the horizontal y-axis.

Overall, six tests were run; one with nonlinear shear characteristics, four with different linear shear values ranging from 0.2 to 5.0 MPa and one calculation was also run with the orthotropy removed. In all the tests, the model was subjected to pure compression only. Since only the average

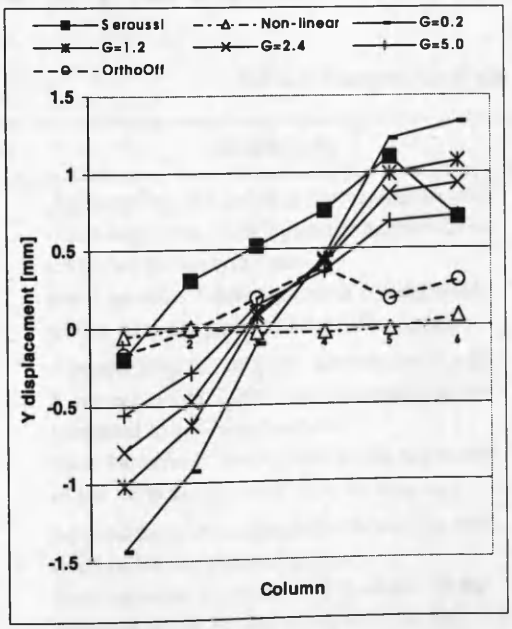

Fig. 9 Migration of inside nodes along the y-axis.

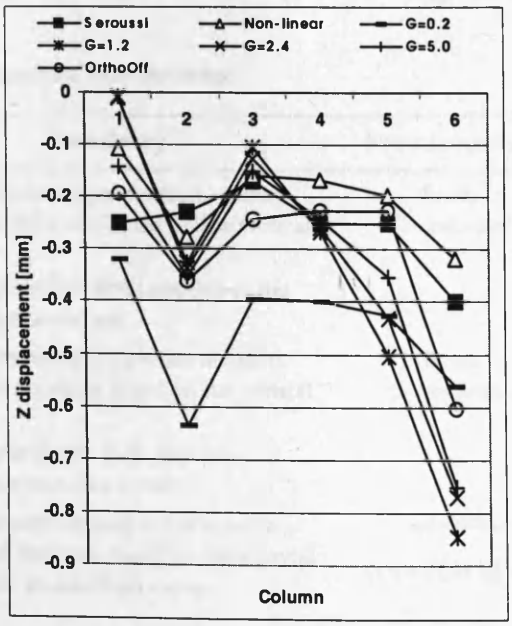

Fig. 10 Migration of inside nodes along the z-axis.

displacements of ten measurements were published by Seroussi *et al.*, the loading conditions were fitted to the mean values. A displacement of 0.81 mm was applied to the top of the L2 vertebra. The constraints were the same as at uniform compression described earlier in the boundary conditions section.

In Fig. 9, a set of curves can be seen with different linear shear properties. The figure also includes one curve showing the result of the nonlinear approach and one with the orthotropy removed for comparison. The results become clearer by comparing this figure with Fig. 10, which shows the movement of the nodes in the vertical direction. However, although the nonlinear shear properties give good agreement with the measured values of vertical movement, they give a poor response in terms of horizontal displacement, where shearing is more likely to occur. The result suggests that the shear properties are linear or nearly linear in intervertebral discs. At constant shear modulus, the curve became smoother and started to show similar characteristics to those available in the literature in both the *y*- and *z*-directions. The end points of the curves have major significance at displacements along the *y*-axis. They show the expected increase or decrease in the disc bulge. If the shear modulus is higher, the disc bulge becomes smaller. The effect of orthotropy was also checked at this level.

There is a major change in the movements if we remove the orthotropy. The curve becomes more distorted within the annulus. Again, introducing orthotropy does not make much change in the vertical movements but can cause an increase in the disc bulge.

CONCLUSION

Three finite element models of the human intervertebral disc were constructed with different annulus material formulations. Table 3 shows a summary of the properties. All models were based on the same characteristics and evaluated against independent sources. Two models were built using widely known modeling methods while the third one used a new material formulation. Tests have been run investigating the effect of the accuracy of the input data. Significant

Table 3 Comparison of the Annulus Fibrosus Characterization.

Model	Nonlinearity	Orthotropy	Shear Properties
1	Approaching the original characteristics with 8 line segments. Distribution of segmentation projected to ε-axis is linear. *Input variables:* 9 breakpoints of the segments of the vertical approach from 0,0-ε_{max},σ_{max}	Scaled directional properties to radial, tangential direction based on the vertical stiffness. Orthotropic elastic shell applied to the outer annulus surface.	linear G = constant
2	Approaching the original characteristics with 8 line segments. Distribution of segmentation projected to ε-axis is quadratic. *Input variables:* 9 breakpoints of the segments of the vertical approach from 0,0-ε_{max},σ_{max}	Scaled directional properties to radial, tangential direction based on the vertical stiffness. Orthotropic elastic shell applied to the outer annulus surface.	linear G = constant
3	Approaching the original characteristics with third-order non-linear equation. *Input variables:* 4 polynomial constants of the equation of the vertical component of the strain curve.	Scaled directional properties to radial, tangential direction based on the vertical third order stress-strain curve.	non-linear $G(t) = E(t)/2(1 + \nu)$

results were gained, especially showing the effect of non-linearity. The result shows that the new material formulation has higher accuracy in simulating the three-dimensional movements of the intervertebral disc in a wide range of dynamic loading situations. Under complex loading, the effectiveness of the approach on the input curve has great significance and results in more accurate prediction of displacements under load. Furthermore, the quantity of input data required was reduced significantly by the third method. This, together with the more straightforward mathematical description, saves enormous time for the user.

The shear properties of the annulus material were also tested, together with the orthotropy. Throughout the simulations, the features of the disc, which are governed by these properties, were of special interest. Increasing shear modulus decreases the change in the disc bulge. This is balanced by the orthotropy, where introducing orthotropy increases the bulge of the disc annulus. Therefore, further investigation of the shear characteristics and the changes in the directional properties of the annulus fibrosus would be useful as it could lead to excellent disc simulation on the micro structural level for any loading situation.

Validation of the model by comparison of its response with literature data shows excellent matching in terms of vertical displacement for both axial and eccentric loading. However, similar comparison of the shear values and the disc bulge shows some differences. Therefore, further investigation of the nonlinear shear properties of the annulus fibrosus could lead to excellent disc simulation for any loading situation. Using the new material formulation did not increase computation time compared to the built-in material models. Nevertheless, a greater accuracy was proven. The validation results of the disc confirm that the presented way of implementing nonlinear materials into FEM solvers is a promising approach to full computational simulation of nonlinear anisotropic materials such as the annulus of the intervertebral disc.

APPENDIX — FORTRAN CODE

The main part of the FORTRAN 77 subroutine of Model 3 is shown below.

```
subroutine umat44 (cm,eps,sig,hisv,dt1,capa,etype,time)
c    cm(1)= constant
c    cm(2)= first order constant
c    cm(3)= second order constant
c    cm(4)= third order constant
c    cm(5)= Poisson's ratio
     if (etype.eq.'brick') then
c     incrementing eps=eps+delta eps
      cm(11)=cm(11)+eps(1)
      cm(12)=cm(12)+eps(2)
      cm(13)=cm(13)+eps(3)
c     differentiating sig(eps) >>> E(t)
      n=4.0
      p1=cm(n)
      p2=cm(n)
      p3=cm(n)
      dp1=0.0
      dp2=0.0
      dp3=0.0
      do j=n-1,1,-1
        dp1=dp1*cm(11)+p1
        dp2=dp2*cm(12)+p2
        dp3=dp3*cm(13)+p3
        p1=p1*cm(11)+cm(j)
        p2=p2*cm(12)+cm(j)
        p3=p3*cm(13)+cm(j)
      enddo
c     calculation of stress state
      x1=dp1/(1.+cm(5))
      x2=3.732*dp2/(1.+cm(5))
      x3=dp3/(1.+cm(5))
      y=cm(5)/(1.-2.*cm(5))
      z=eps(1)+eps(2)+eps(3)
c     incrementing sig(1,2,3) and tau(4,5,6)
      sig(1)=sig(1)+x1*(eps(1)+y*z)
      sig(2)=sig(2)+x2*(eps(2)+y*z)
      sig(3)=sig(3)+x3*(eps(3)+y*z)
      sig(4)=sig(4)+.5*x1*eps(4)
      sig(5)=sig(5)+.5*x2*eps(5)
      sig(6)=sig(5)+.5*x3*eps(6)
     endif
      return
      end
```

References

1. Markolf, KL, Morris JM. The structural components of the intervertebral disc. *J Bone Joint Surg* **56A**(4):675–687, 1974.
2. Berkson MH, Nachemson A, Schultz AB. Mechanical properties of human lumbar spine motion segments, Part I–II. *J Biomech Eng* **101**:46–56, 1979.
3. Inoue H. Three-dimensional architecture of lumbar intervertebral discs. *Spine* **6**(2):139–145, 1981.
4. Sonnerup L. A semi-experimental stress analysis of the human intervertebral disc in compression. *Exp Mech* **12**(3):142–147, 1972.
5. Galante JO. Tensile properties of the human lumbar annulus fibrosus. *Acta Orthop Scand* (Suppl. 100), Munksgaard, Copenhagen, 1967.
6. Visible Human Project Database, http://www.nlm.nih.gov/research/visible/visible_human.html
7. LS-DYNA3D Users Manual, Livermore Software Technology Corporation, http://www.lstc.com, 1997.
8. Nagy GT, Golinski WZ, Gentle CR. Analysis of the human lumbar intervertebral disc based on a three-dimensional non-linear finite element model. *Hospital Med Eng* **38**(1):5–11, 2000.
9. Nagy GT, Gentle CR. Soft tissue modelling in intervertebral discs, *Proc 10th Int Conf BioMed Eng*, Singapore, 6–9 December 2000.
10. Brown T, Hansen RJ, Yorra AJ. Some mechanical tests on the lumbosacral spine with particular reference to the intervertebral disc. *J Bone Joint Surg* **39A**(5):1135–1164, 1957.
11. Seyed A, Shirazi A, Suresh CS, Abdul MA. Stress analysis of the lumbar disc-body unit in compression. *Spine* **9**(2): 120–133, 1984.
12. Lin HS, Liu YK, Adams KH. Mechanical response of the lumbar intervertebral joint under physiological complex loading. *J Bone Joint Surg* **60A**(1):41–55, 1978.
13. Tencer AF, Ahmed AM, Burke DL. Some static mechanical properties of the lumbar intervertebral joint, intact and injured. *J Biomech Eng* **104**:193–201, 1982.
14. Shirazi A. On the fibre composite material models of disc annulus — Comparison of predicted stresses. *J Biomech* **22**(4):357–365, 1989.
15. Adams MA, Green TP. Tensile properties of the annulus fibrosus I–II. *Eur Spine J* **2**:203–213, 1993.
16. Belytschko T, Kulak RF, Schultz AB, Galante JO. Finite element stress analysis of an intervertebral disc. *J Biomech* **7**:277–285, 1974.
17. Tadano S, Katagiri K, Umehara S, Ukai T. A constitutive modelling of the human lumbar intervertebral disc and forward-backward bending simulation. *Biomed Mat Eng* **7**:179–191, 1997.
18. Shirazi A, Abdul MA, Suresh CS. Mechanical response of a lumbar motion segment in axial torque alone and combined with compression. *Spine* **11**:914–927, 1986.
19. Seroussi RE, Krag MH, Muller DL, Pope MH. Internal deformations of intact and denucleated human lumbar disc subjected to compression, flexion and extension loads. *J Orthop Res* **7**(1):122–131, 1989.

APPENDIX 12. – UMAT FORTRAN 77 SUBROUTINE

The Fortran77 Code

```
subroutine umat44 (cm,eps,sig,hisv,dt1,capa,etype,time)
c     cm(1)= constant
c     cm(2)= first order constant
c     cm(3)= second order constant
c     cm(4)= third order constant
c     cm(5)= poisson's ratio
    if (etype.eq.'brick') then
c      incrementing eps=eps+delta eps
      cm(11)=cm(11)+eps(1)
      cm(12)=cm(12)+eps(2)
      cm(13)=cm(13)+eps(3)
c     differentiating sig(eps) >>> E(t)
      n=4.0
      p1=cm(n)
      p2=cm(n)
      p3=cm(n)
      dp1=0.0
      dp2=0.0
      dp3=0.0
      do j=n-1,1,-1
        dp1=dp1*cm(11)+p1
        dp2=dp2*cm(12)+p2
        dp3=dp3*cm(13)+p3
        p1=p1*cm(11)+cm(j)
        p2=p2*cm(12)+cm(j)
        p3=p3*cm(13)+cm(j)
      enddo
c     calculation of stress state
      x1=dp1/(1.+cm(5))
      x2=3.732*dp2/(1.+cm(5))
      x3=dp3/(1.+cm(5))
      y=cm(5)/(1.-2.*cm(5))
      z=eps(1)+eps(2)+eps(3)
c     incrementing sig(1,2,3) and tau(4,5,6)
      sig(1)=sig(1)+x1*(eps(1)+y*z)
      sig(2)=sig(2)+x2*(eps(2)+y*z)
      sig(3)=sig(3)+x3*(eps(3)+y*z)
      sig(4)=sig(4)+.5*x1*eps(4)
      sig(5)=sig(5)+.5*x2*eps(5)
      sig(6)=sig(5)+.5*x3*eps(6)
    endif
      return
      end
```

APPENDIX 13. – EXPERIMENTAL MODEL DESIGN AND ASSEMBLY

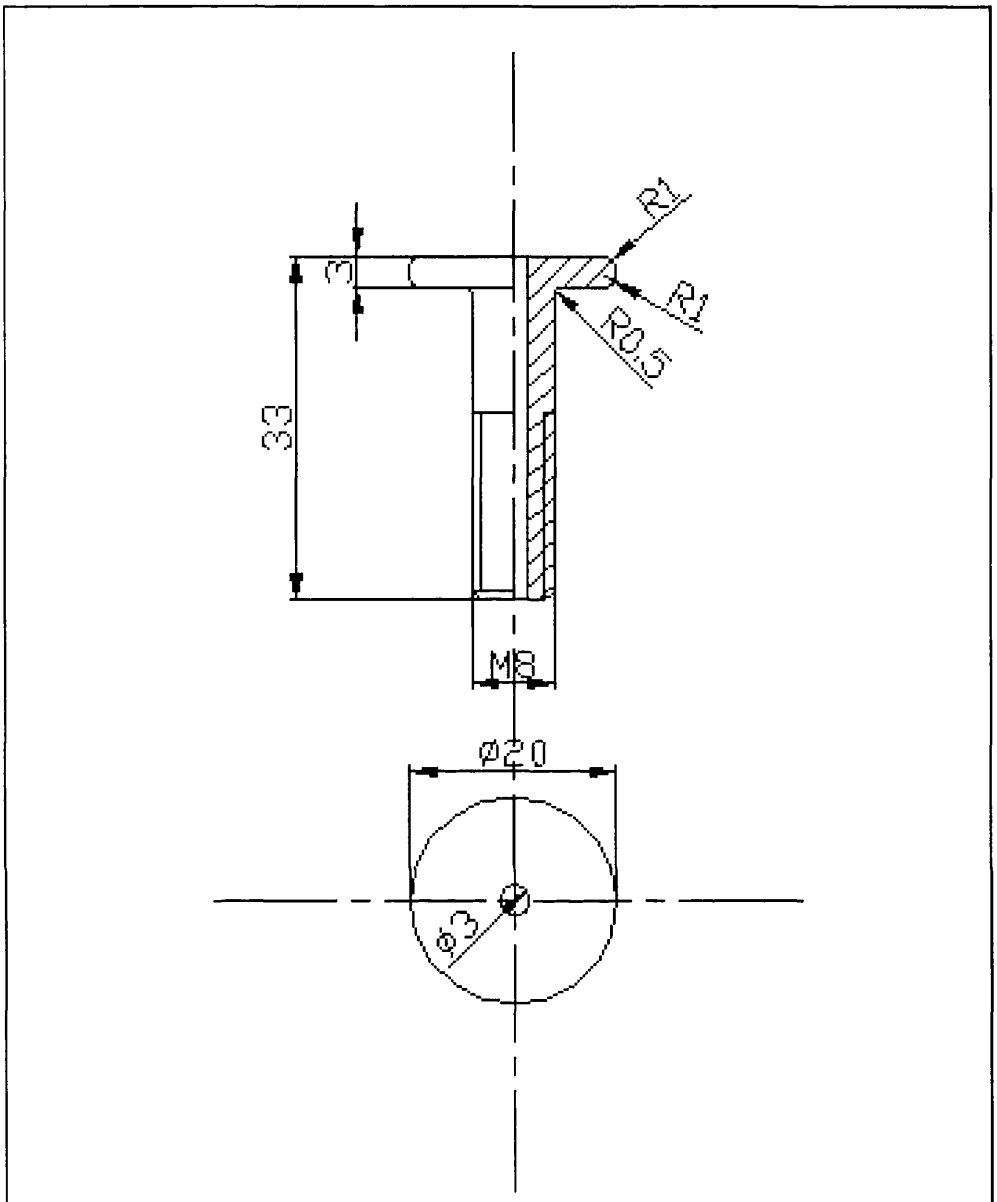

Geza Nagy ext: 4728	M 1:1

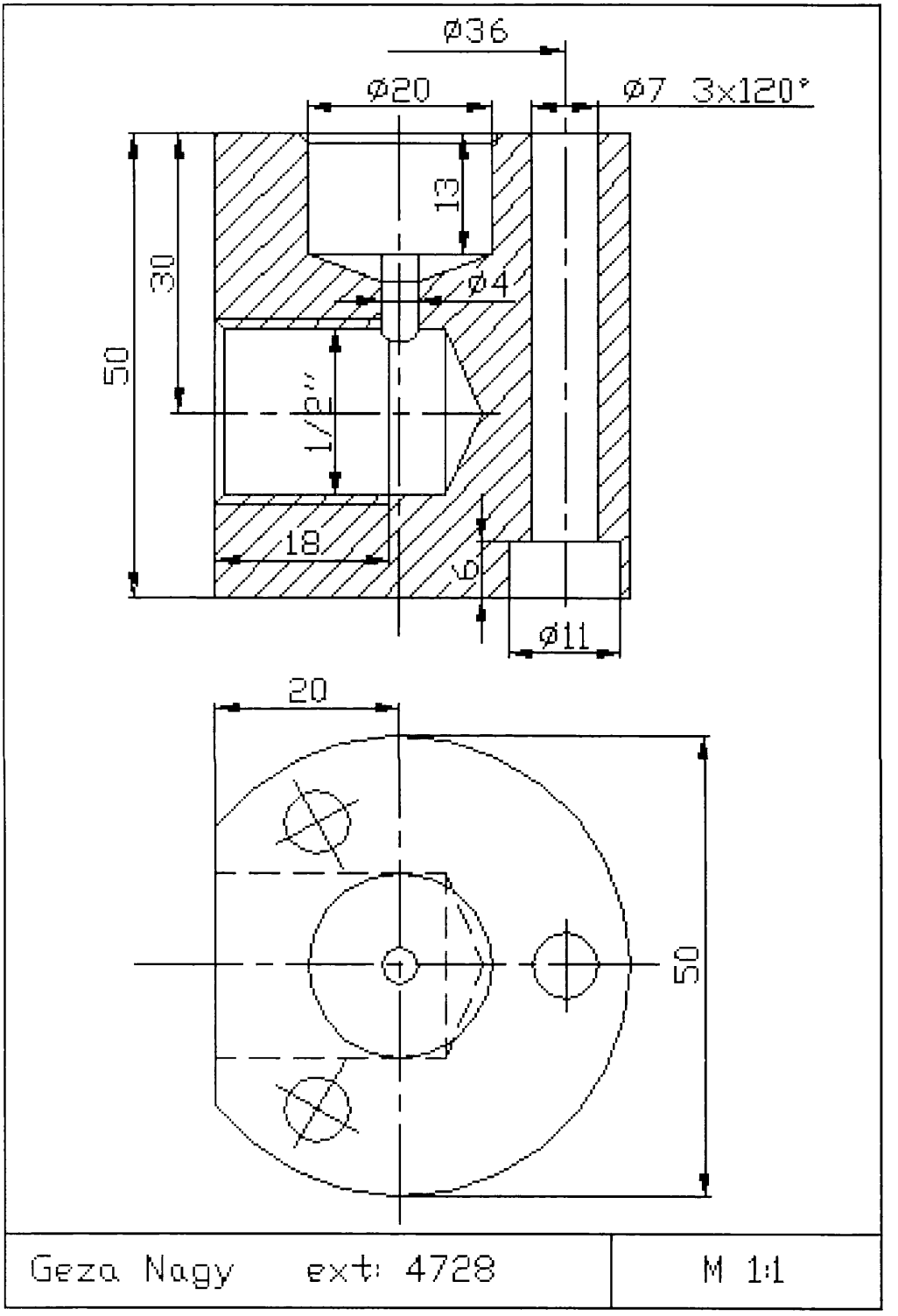
ø36
ø20
ø7 3x120°
13
30
50
ø4
1/2''
18
6
ø11
20
50
Geza Nagy ext: 4728
M 1:1

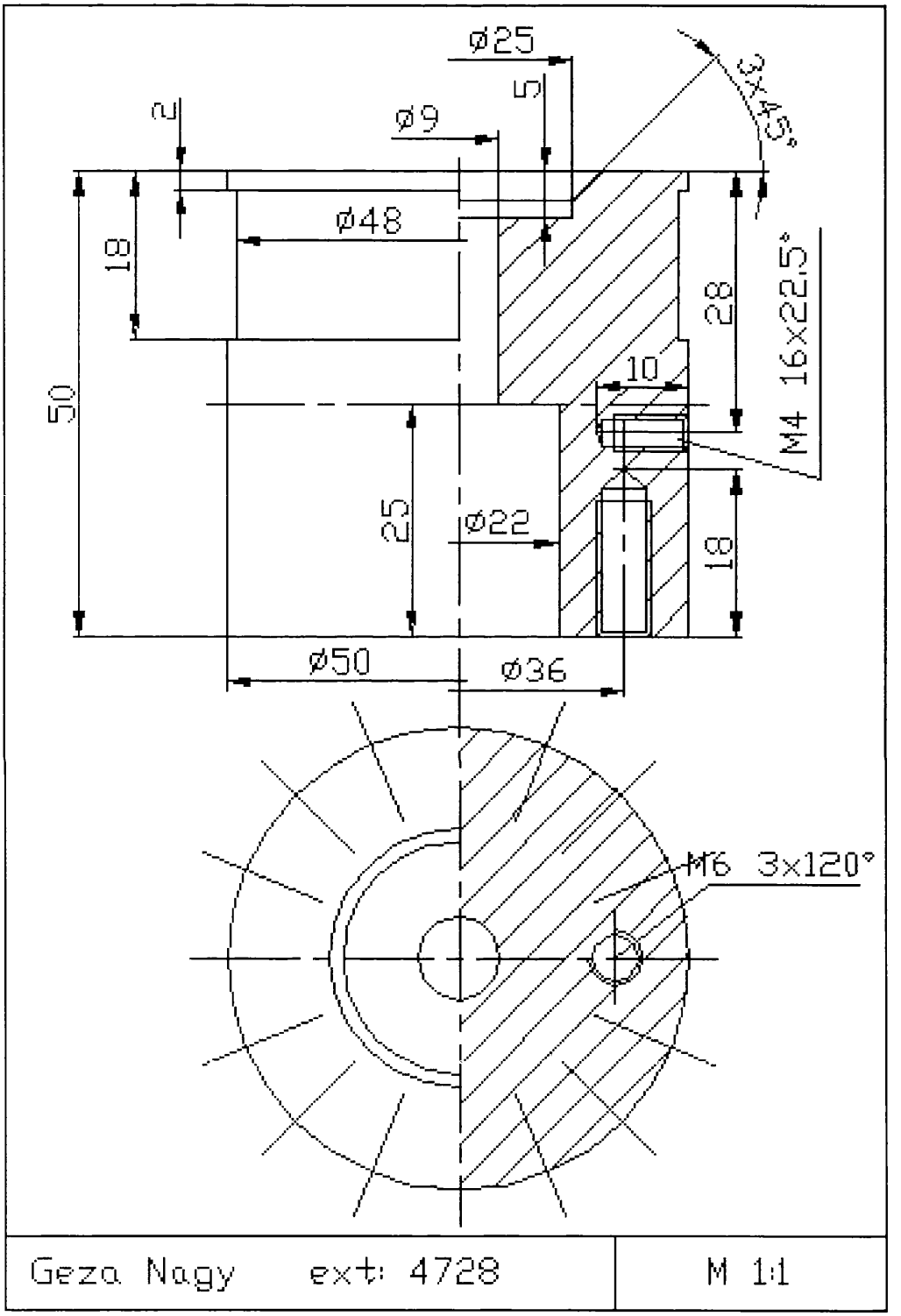
ø25
5
3x45°
2
ø9
ø48
18
28
M4 16x22,5°
10
50
25
ø22
18
ø50
ø36
M6 3x120°
Geza Nagy ext: 4728
M 1:1

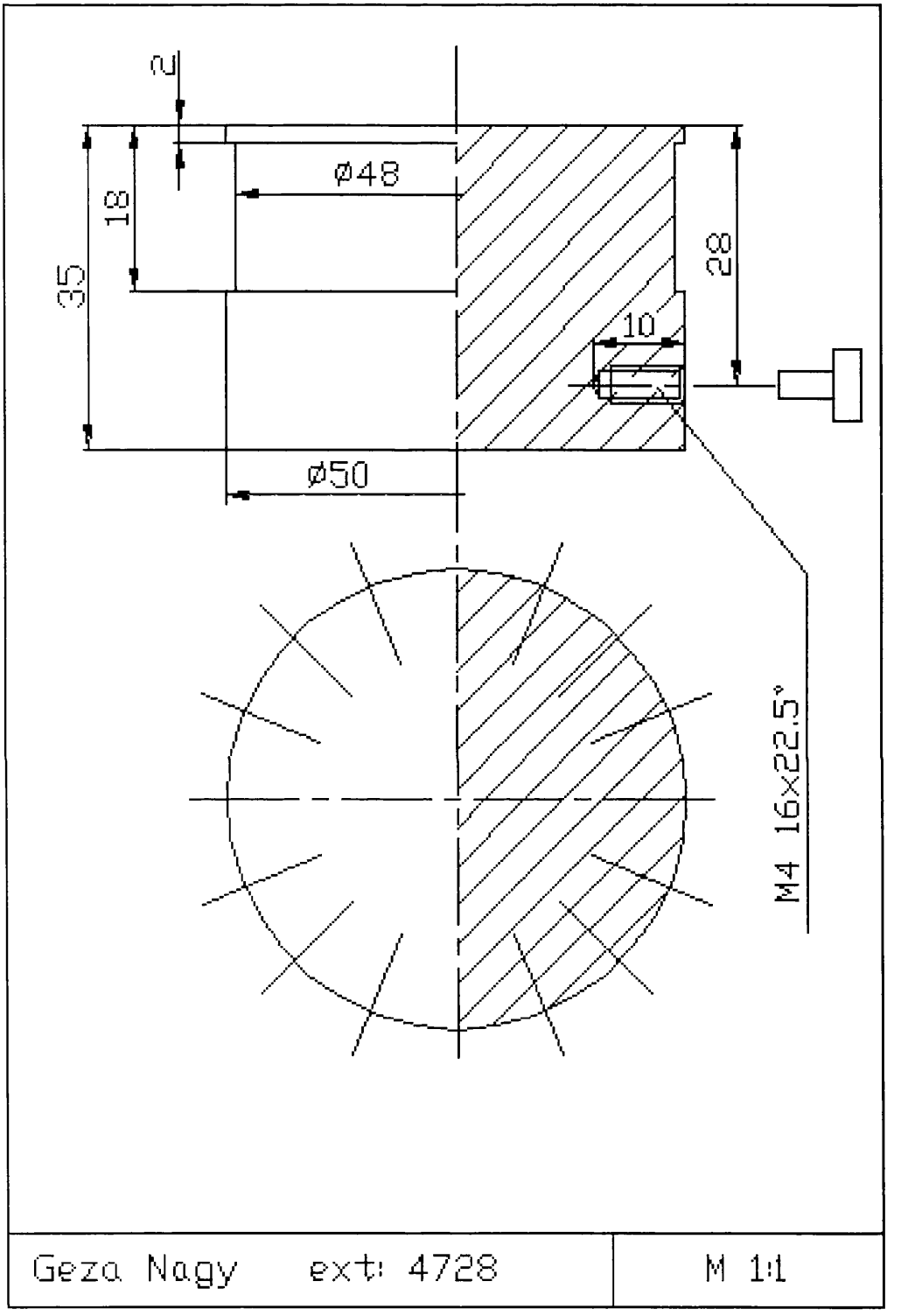
2
18
35
ø48
28
10
ø50
M4 16x22.5°
Geza Nagy ext: 4728
M 1:1

APPENDIX 14. – EXPERIMENTAL MODEL SETUP AND TESTS

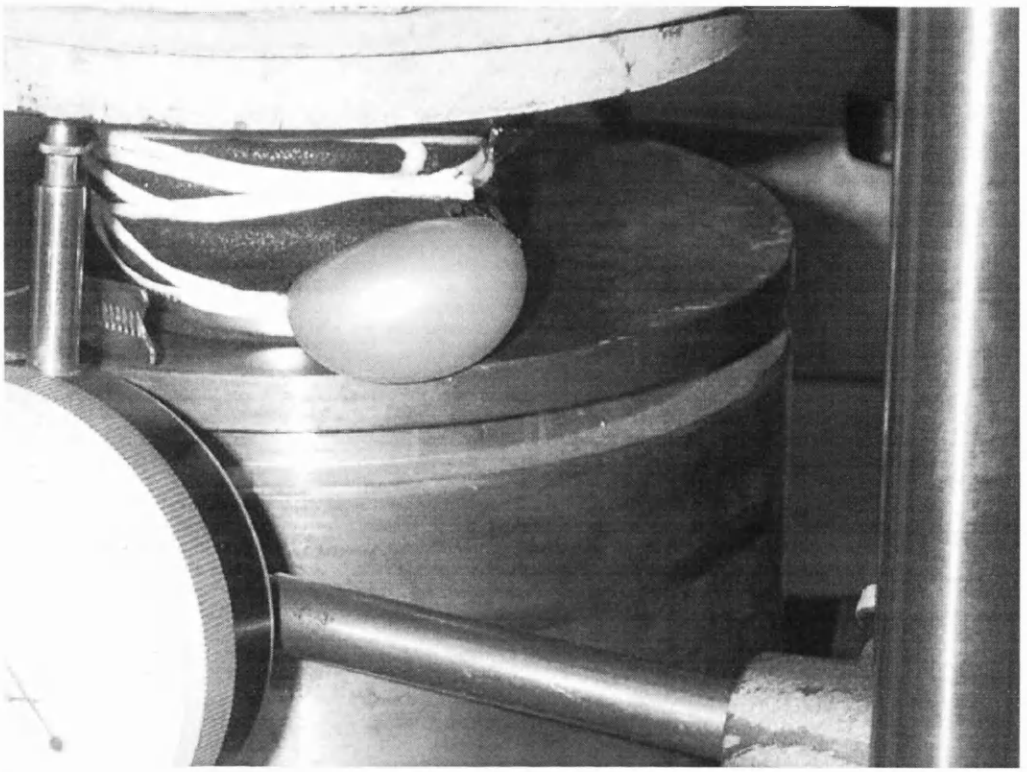

Failure

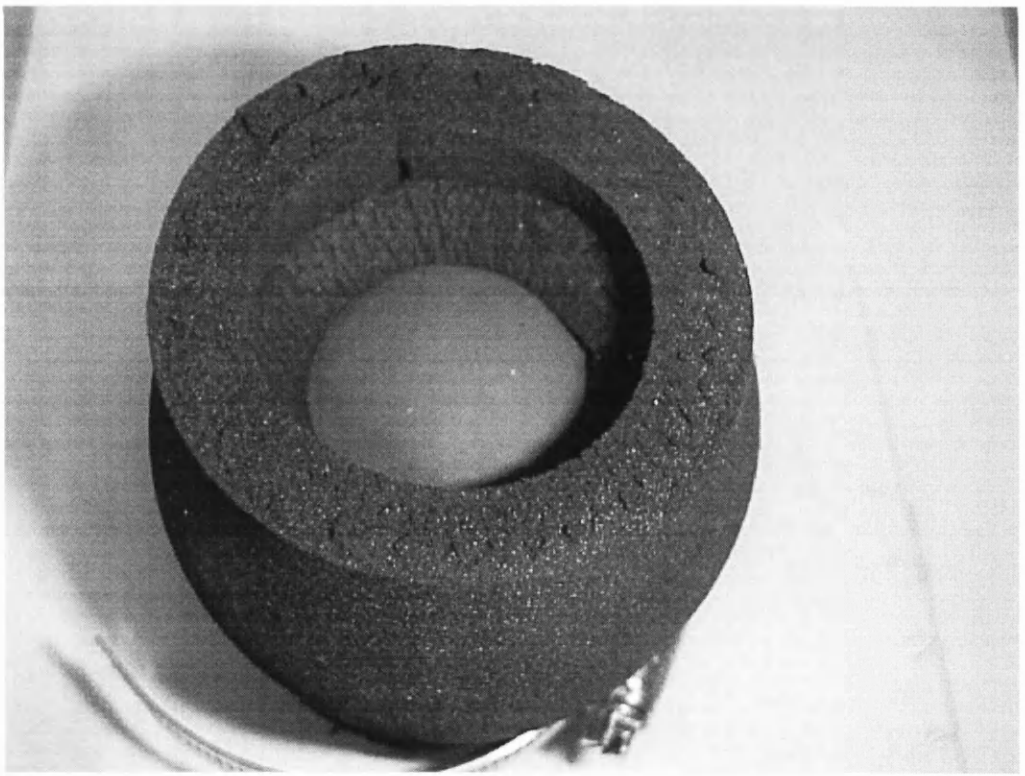

Structure

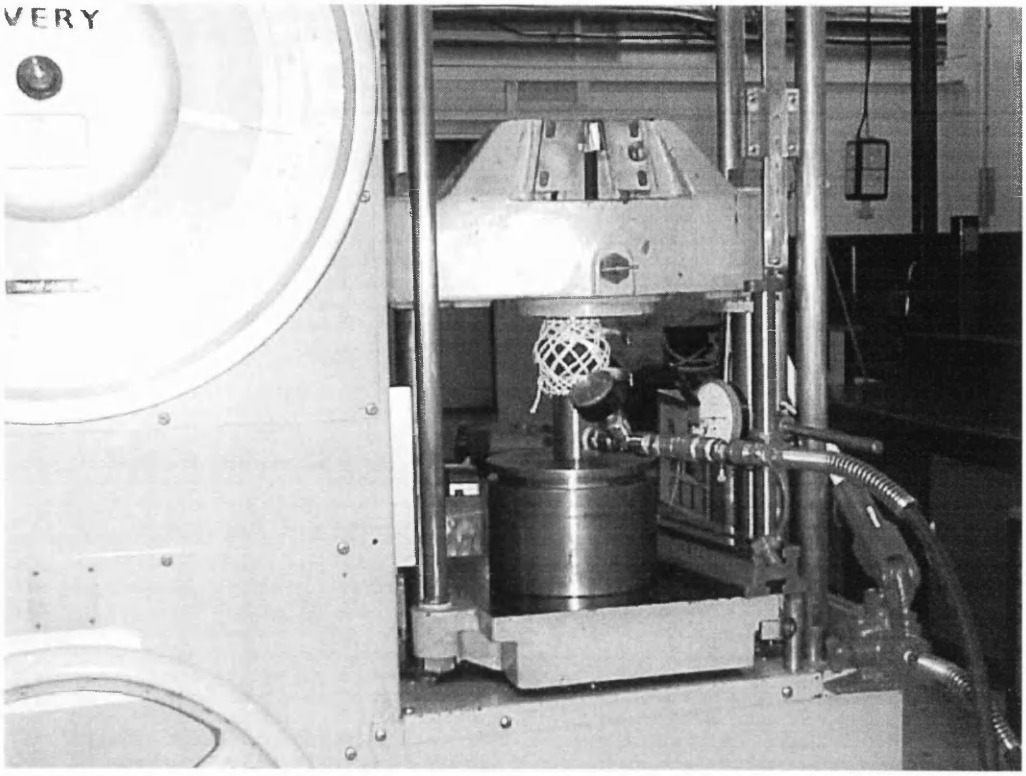

Setup

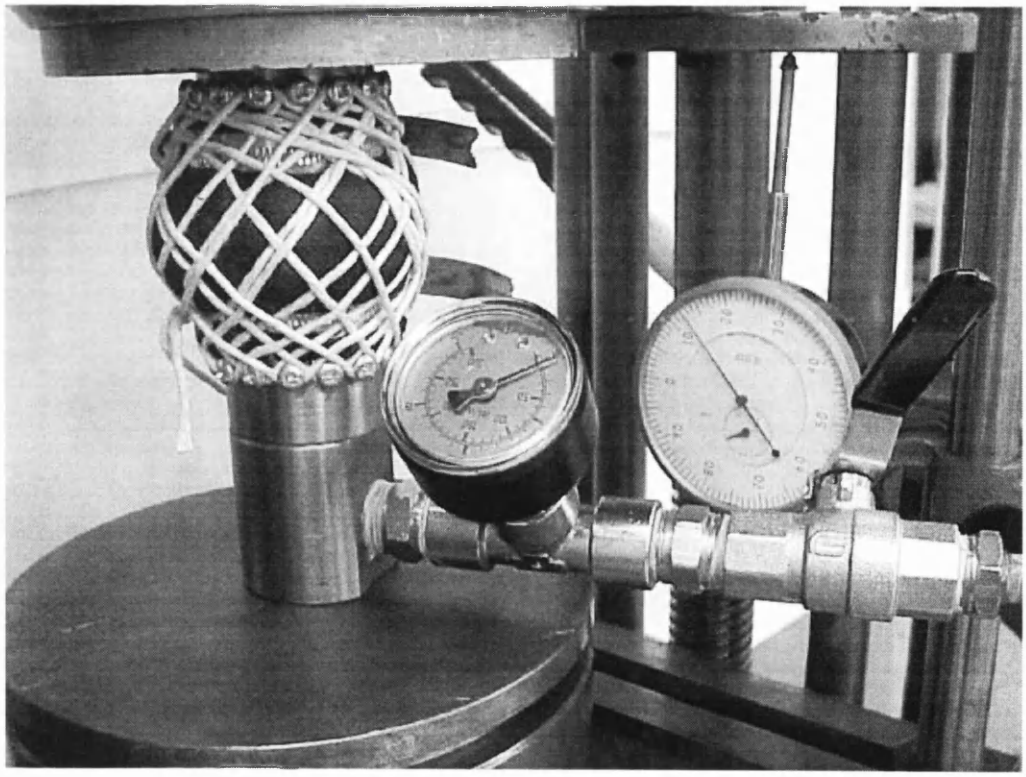

Unloaded

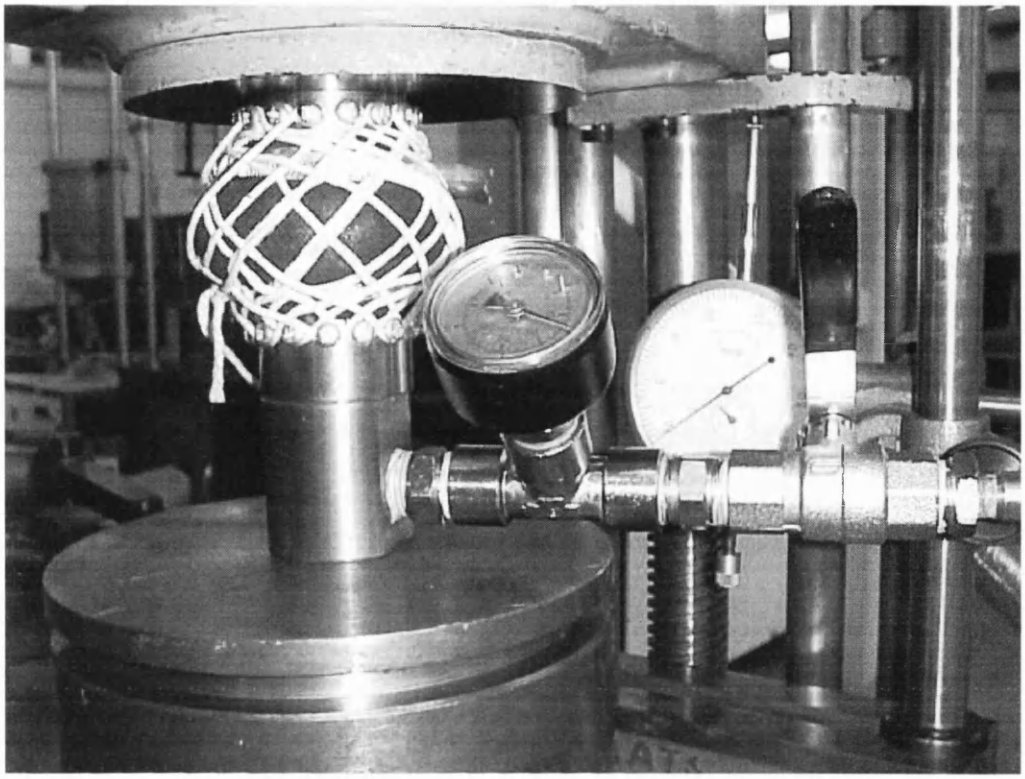

Axial Compression

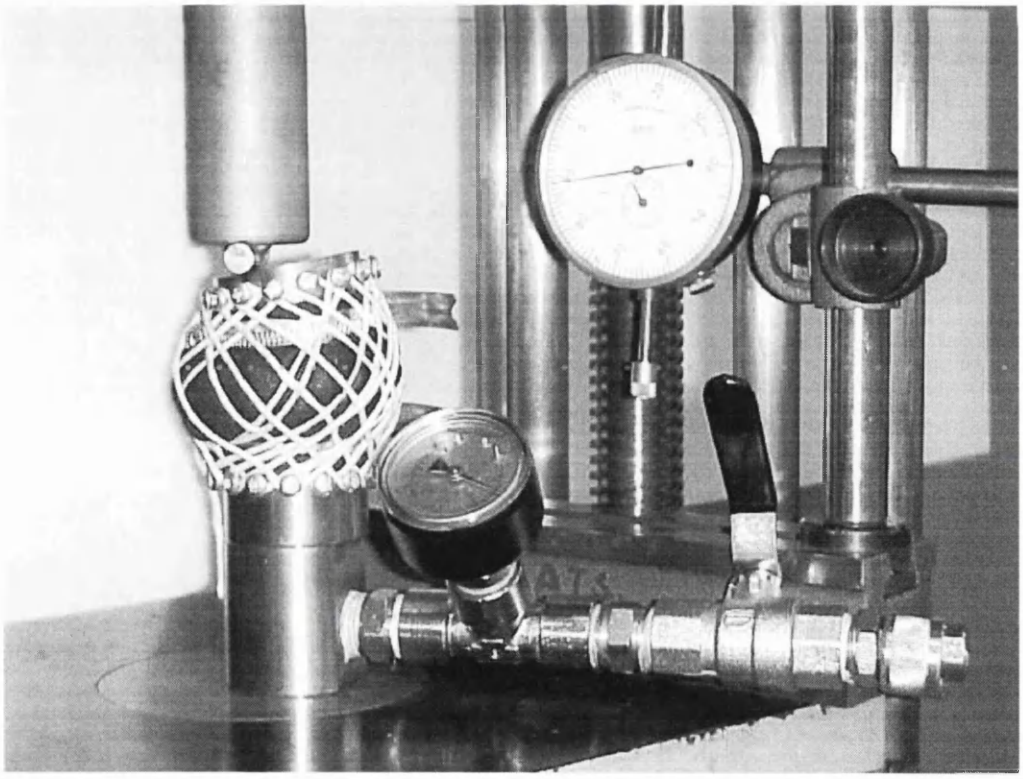

Eccentric Compression

APPENDIX 15. – SPINAL COLUMN CURVATURE OF VHP MALE

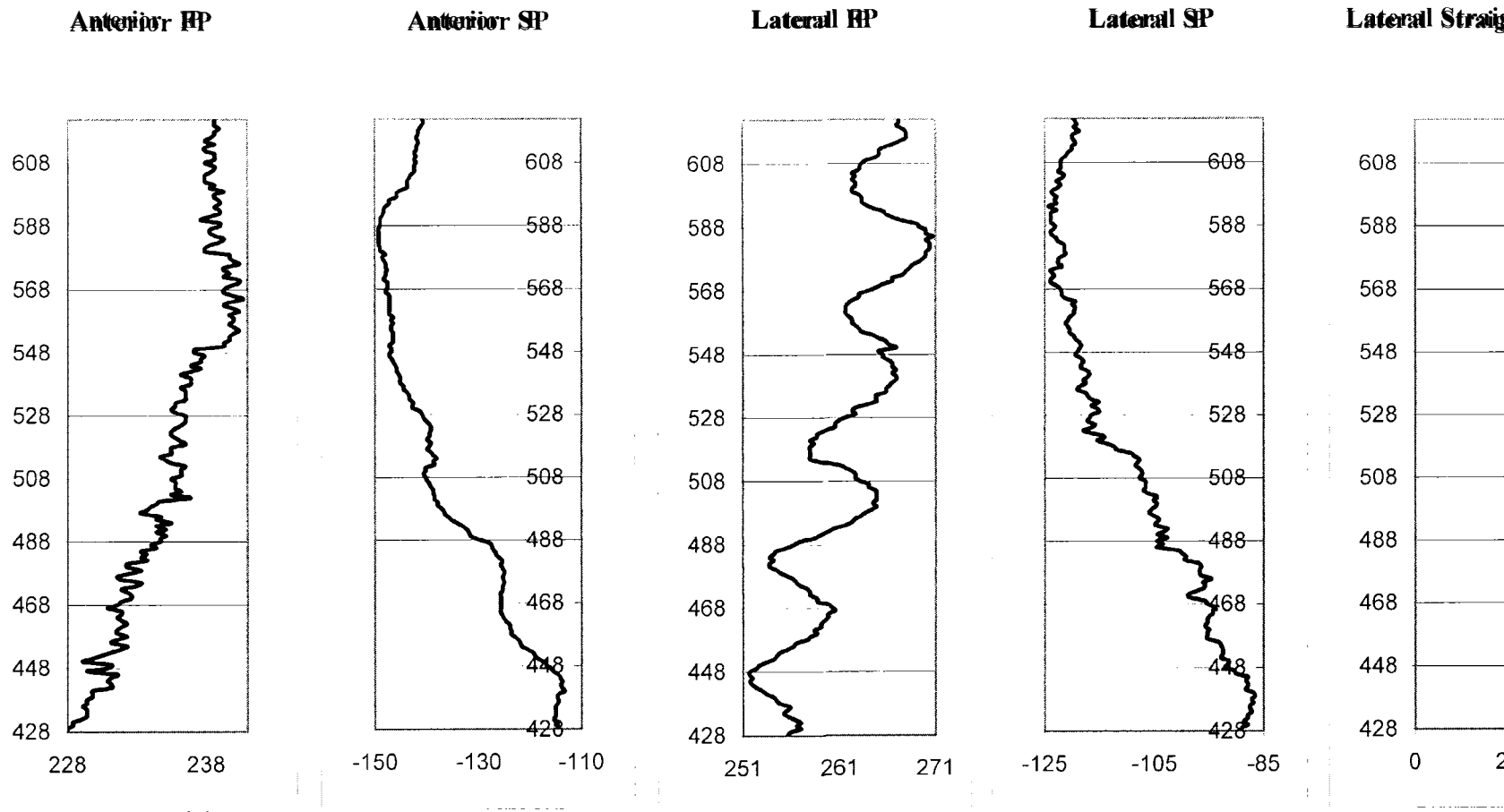

(Units are in mm, FP-frontal plane, SP-sagittal plane, nodes are on the vertebral body or on the connecting interertebral discs, note that the spinal column is upside-d so at 448mm-L1, at 488mm-L2, at 515mm-L3, at 560mm-L4, 600mm-L5.)

APPENDIX 16. – FE MODEL OF THE L1-S1 LUMBAR SPINE

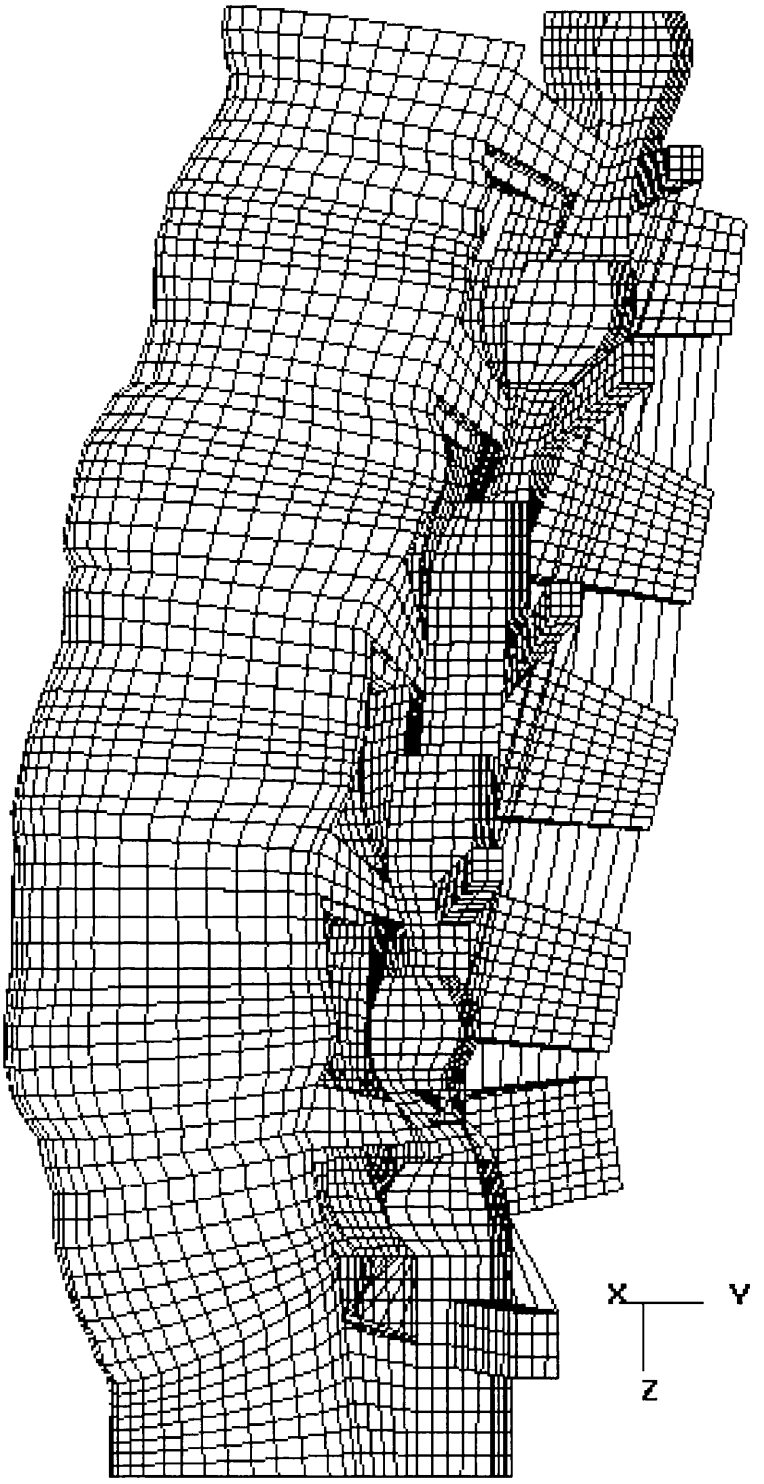
X
Y
Z

APPENDIX 16

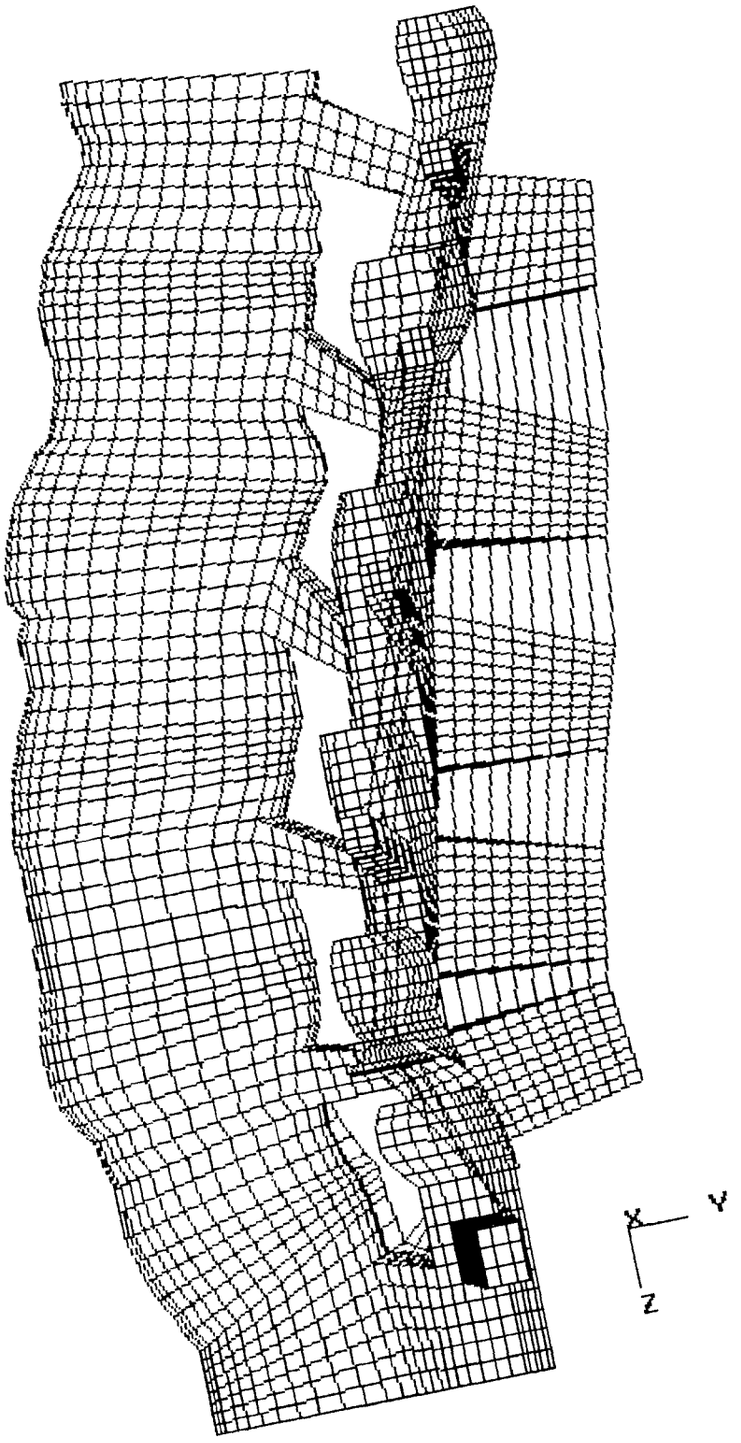

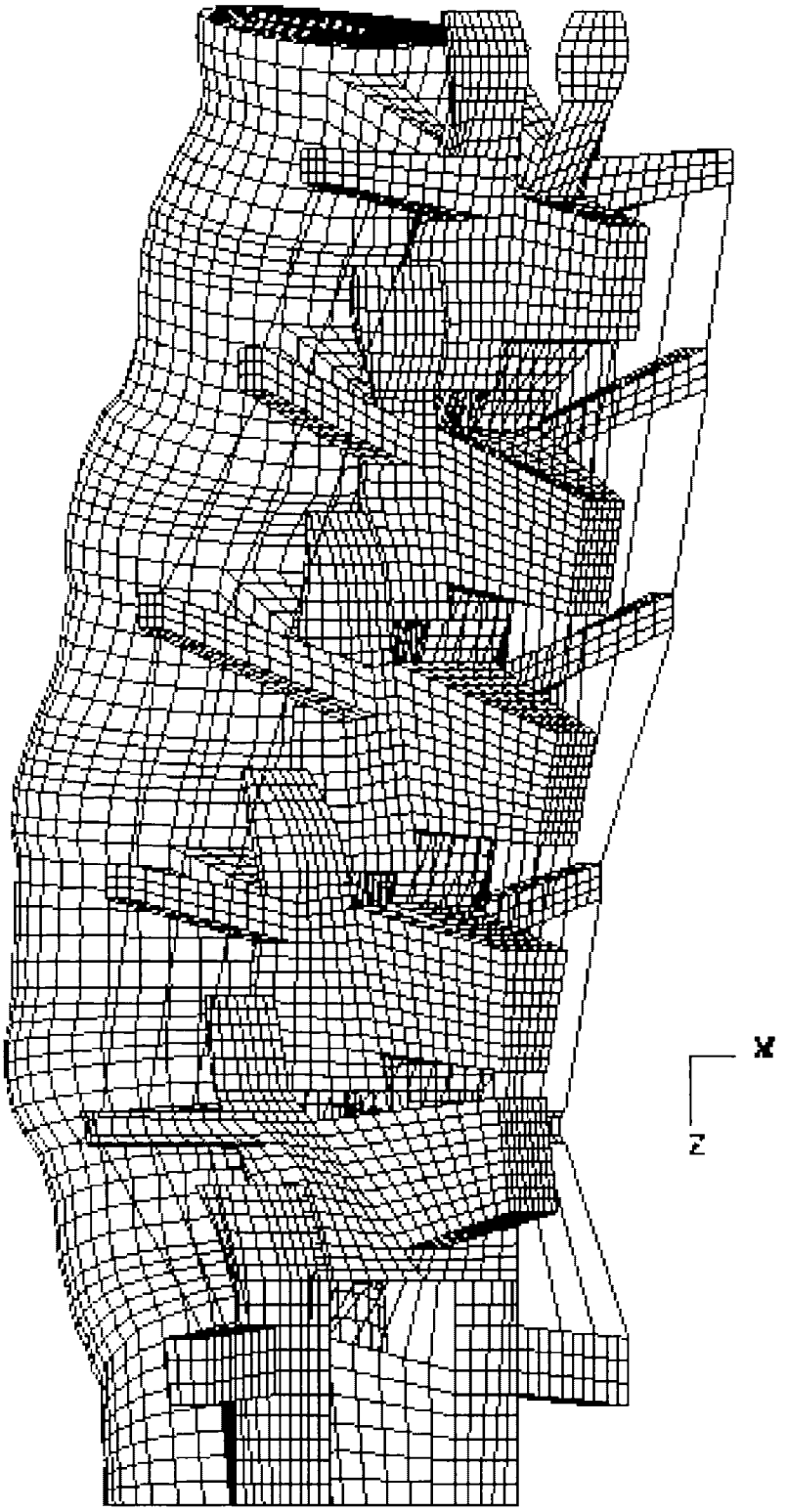
X
Z

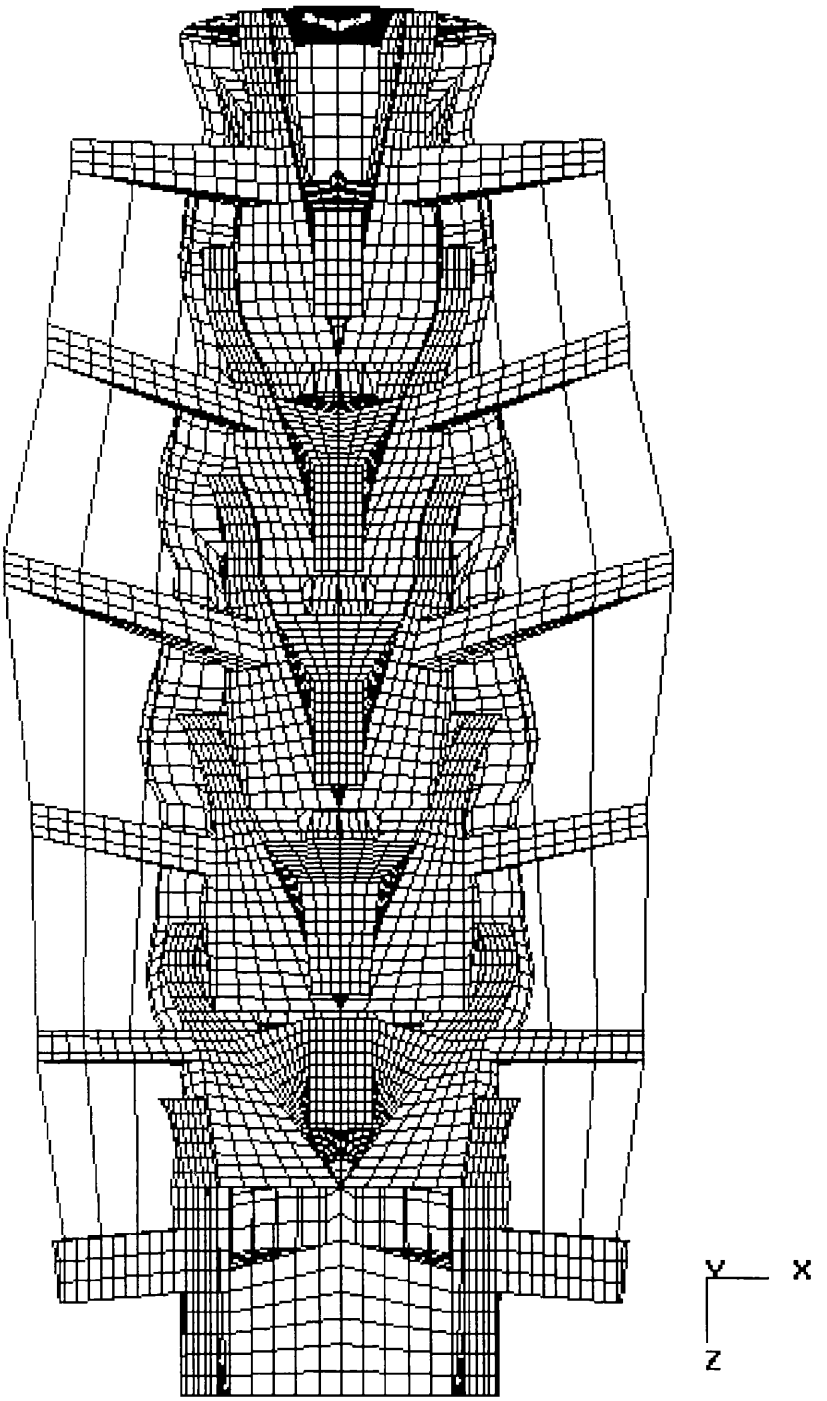
Y
X
Z

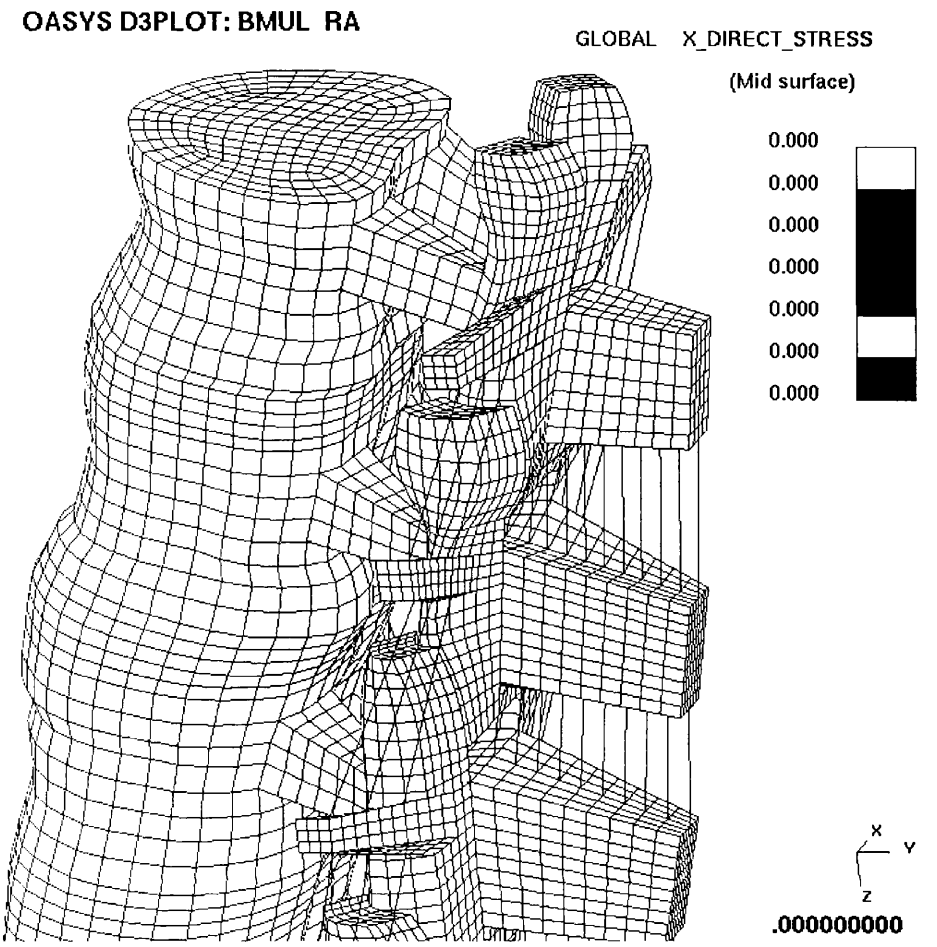
OASYS D3PLOT: BMUL RA
GLOBAL X_DIRECT_STRESS
(Mid surface)
0.000
0.000
0.000
0.000
0.000
0.000
0.000
X
Y
Z
.000000000

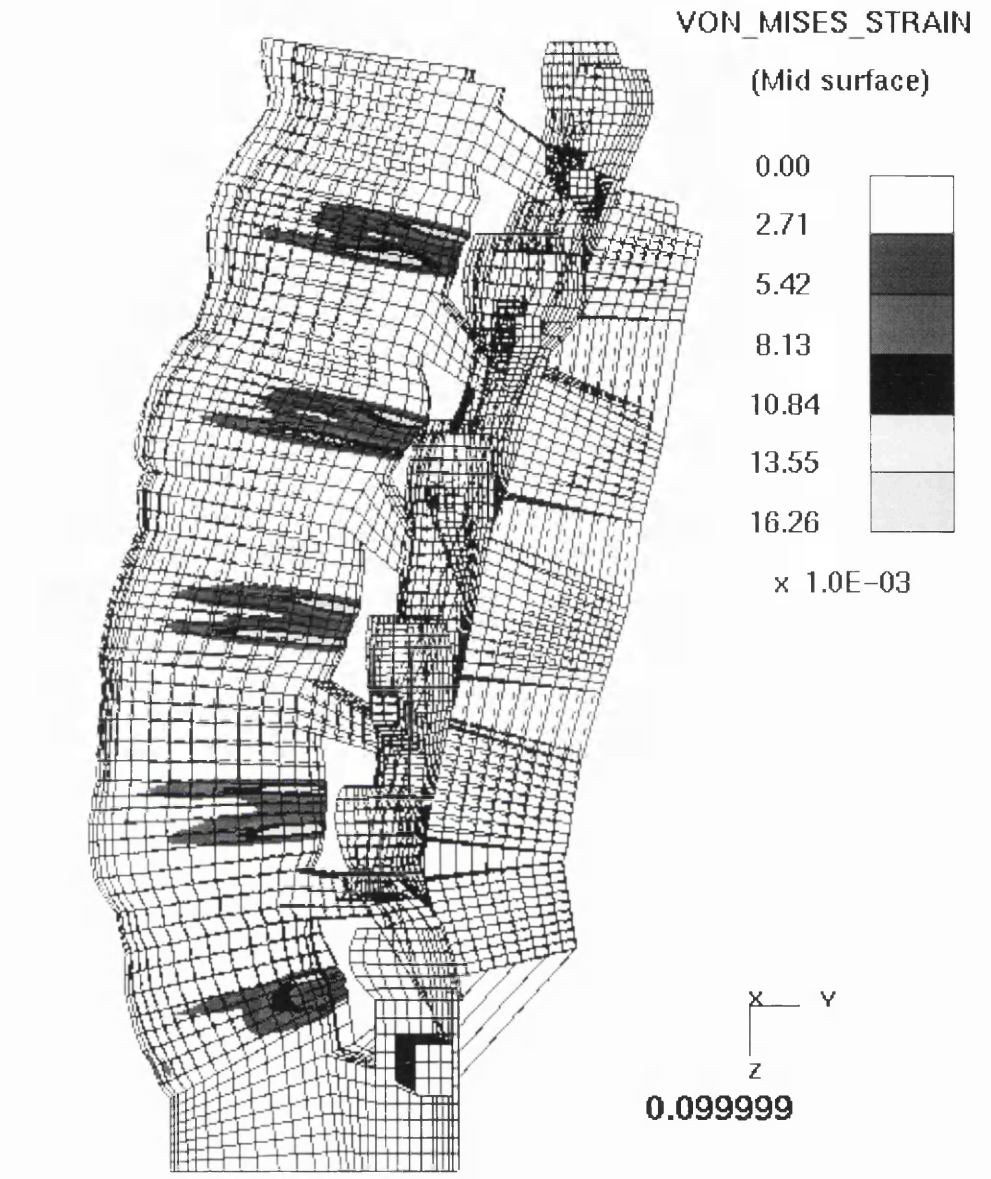
OASYS D3PLOT: BMUL RA
VON_MISES_STRAIN
(Mid surface)
0.00
2.71
5.42
8.13
10.84
13.55
16.26
x 1.0E-03
X
Y
Z
0.099999

APPENDIX 17. – LS-DYNA .KEY OF A DISC

```
*KEYWORD
$---+----1----+----2----+----3----+----4----+----5----+----6----+----7----+----8
$
$ DYNA3D(936) DECK WAS WRITTEN BY: ETA/FEMB VERSION 26
$ DATE  : Aug 30, 2000 at 18:06:18
$
$---+----1----+----2----+----3----+----4----+----5----+----6----+----7----+----8
$                    (1) TITLE CARD.
$---+----1----+----2----+----3----+----4----+----5----+----6----+----7----+----8
*TITLE
DISC
$---+----1----+----2----+----3----+----4----+----5----+----6----+----7----+----8
$                    (2) CONTROL CARDS.
$---+----1----+----2----+----3----+----4----+----5----+----6----+----7----+----8
*CONTROL_TERMINATION
$    ENDTIM    ENDCYC     DTMIN    ENDNEG    ENDMAS
  .210E-01         0      .000      .000      .000
*CONTROL_TIMESTEP
$    DTINIT      SCFT      ISDO    TSLIMT      DTMS      LCTM     ERODE     MS1ST
  .100E-06      .900         0
*CONTROL_HOURGLASS
$       IHQ        QH
         1      .100
*CONTROL_BULK_VISCOSITY
$        Q2        Q1
     1.500      .060
*CONTROL_SHELL
$    WRPANG     ITRIST     IRNXX    ISTUPD    THEORY       BWC     MITER
    20.000          2        -1         0         2         2         1
*CONTROL_CONTACT
$    SLSFAC    RWPNAL    ISLCHK    SHLTHK    PENOPT    THKCHG     ORIEN
      .100
$    USRSTR    USRFAC     NSBCS    INTERM     XPENE
         0         0        10         0     4.000
*CONTROL_ENERGY
$      HGEN      RWEN    SLNTEN     RYLEN
         1         2         1         1
*CONTROL_DAMPING
$    NRCYCK      DRTOL    DRFCTR    DRTERM    TSSFDR    IRELAL     EDTTL    IDRFLG
       250       .001      .995
*CONTROL_OUTPUT
$     NPOPT    NEECHO    NREFUP    IACCOP     OPIFS    IPNINT    IKEDIT
         0         0         0         0      .000         0       100
$---+----1----+----2----+----3----+----4----+----5----+----6----+----7----+----8
$                    (3) DATABASE CONTROL CARDS - ASCII HISTORY FILE
$---+----1----+----2----+----3----+----4----+----5----+----6----+----7----+----8
*DATABASE_HISTORY_NODE_SET
$       ID1       ID2       ID3       ID4       ID5       ID6       ID7       ID8
         1
*DATABASE_HISTORY_NODE_SET
$       ID1       ID2       ID3       ID4       ID5       ID6       ID7       ID8
         2
*DATABASE_HISTORY_SOLID_SET
$       ID1       ID2       ID3       ID4       ID5       ID6       ID7       ID8
         3
*DATABASE_HISTORY_SOLID_SET
$       ID1       ID2       ID3       ID4       ID5       ID6       ID7       ID8
         4
*DATABASE_HISTORY_SOLID_SET
$       ID1       ID2       ID3       ID4       ID5       ID6       ID7       ID8
         5
$OPTION : BEAM    BEAM_SET   NODE   NODE_SET
$         SHELL   SHELL_SET  SOLID  SOLID_SET
$         TSHELL  TSHELL_SET
$---+----1----+----2----+----3----+----4----+----5----+----6----+----7----+----8
$                    (4) DATABASE CONTROL CARDS FOR ASCII FILE
$---+----1----+----2----+----3----+----4----+----5----+----6----+----7----+----8
$---+----1----+----2----+----3----+----4----+----5----+----6----+----7----+----8
*DATABASE_ELOUT
  .100E-02
*DATABASE_GLSTAT
  .100E-02
*DATABASE_RBDOUT
  .100E-02
*DATABASE_NODOUT
```

```
  .100E-02
$OPTION : SECFORC RWFORC NODOUT ELOUT  GLSTAT
$         DEFORC  MATSUM NCFORC RCFORC DEFGEO
$         SPCFORC SWFORC ABSTAT NODFOR BNDOUT
$         RBDOUT  GCEOUT SLEOUT MPGS   SBTOUT
$         JNTFORC AVSFLT MOVIE
$---+----1----+----2----+----3----+----4----+----5----+----6----+----7----+----8
$                    (5) DATABASE CONTROL CARDS FOR BINARY FILE
$---+----1----+----2----+----3----+----4----+----5----+----6----+----7----+----8
*DATABASE_BINARY_D3PLOT
$  DT/CYCL      LCDT    NOBEAM
  .100E-02
*DATABASE_BINARY_D3THDT
$  DT/CYCL      LCDT    NOBEAM
  .100E-02
$*DATABASE_BINARY_OPTION
$  DT/CYCL      LCDT    NOBEAM
$
$OPTION : D3DRFL D3DUMP RUNRSF INTFOR
$---+----1----+----2----+----3----+----4----+----5----+----6----+----7----+----8
*DATABASE_EXTENT_BINARY
         0         0         3         1         1         1         1         1
         0         0         0         0         0         0
$---+----1----+----2----+----3----+----4----+----5----+----6----+----7----+----8
$                    (6) DEFINE PARTS CARDS
$---+----1----+----2----+----3----+----4----+----5----+----6----+----7----+----8
*PART
$HEADING
 PART PID =         1 PART NAME :NUCLEUS
$       PID       SID       MID      EOSID      HGID      GRAV    ADPOPT      TMID
         1         1         1
*PART
$HEADING
 PART PID =         2 PART NAME :ANNULUS
$       PID       SID       MID      EOSID      HGID      GRAV    ADPOPT      TMID
         2         2         2
*PART
$HEADING
 PART PID =         3 PART NAME :BCORTICA
$       PID       SID       MID      EOSID      HGID      GRAV    ADPOPT      TMID
         3         3         3
*PART
$HEADING
 PART PID =         4 PART NAME :BCANCELL
$       PID       SID       MID      EOSID      HGID      GRAV    ADPOPT      TMID
         4         4         4
*PART
$HEADING
 PART PID =         5 PART NAME :TCORTICA
$       PID       SID       MID      EOSID      HGID      GRAV    ADPOPT      TMID
         5         5         5
*PART
$HEADING
 PART PID =         6 PART NAME :TCANCELL
$       PID       SID       MID      EOSID      HGID      GRAV    ADPOPT      TMID
         6         6         6
*PART
$HEADING
 PART PID =         7 PART NAME :TOP
$       PID       SID       MID      EOSID      HGID      GRAV    ADPOPT      TMID
         7         7         7
$---+----1----+----2----+----3----+----4----+----5----+----6----+----7----+----8
$                    (7) MATERIAL CARDS
*MAT_ELASTIC_FLUID
$MATERIAL NAME:NUCLEUS
$       MID        RO         E        PR        DA        DB         K
         1 7.850E+03 0.000E+00 0.000E+00 0.000E+00 0.000E+00 1.400E+07
$        VC        CP
         .3   1.0E+20
$
*MAT_USER_DEFINED_MATERIAL_MODELS
$MATERIAL NAME:ANNULUS
$       MID        RO        MT       LMC       NHV    IORTHO     IBULK        IG
         2 7.850E+03        45         8        30         0         7         8
$    IVECT     IFAIL
```

```
         0         0
$       P1        P2        P3        P4        P5        P6        P7        P8
 0.000E+00 4.472E+06 1.733E+07 1.872E+08 2.500E-01 0.000E+00 1.400E+07 1.000E+10
$
*MAT_ELASTIC
$MATERIAL NAME:BCORTICA
$       MID        RO         E        PR        DA        DB         K
         3 7.850E+03 1.200E+13 3.000E-01 0.000E+00 0.000E+00 0.000E+00
$
*MAT_ELASTIC
$MATERIAL NAME:BCANCELL
$       MID        RO         E        PR        DA        DB         K
         4 7.850E+03 1.000E+11 3.000E-01 0.000E+00 0.000E+00 0.000E+00
$
*MAT_ELASTIC
$MATERIAL NAME:TCORTICA
$       MID        RO         E        PR        DA        DB         K
         5 7.850E+03 1.200E+13 3.000E-01 0.000E+00 0.000E+00 0.000E+00
$
*MAT_ELASTIC
$MATERIAL NAME:TCANCELL
$       MID        RO         E        PR        DA        DB         K
         6 7.850E+03 1.000E+11 3.000E-01 0.000E+00 0.000E+00 0.000E+00
$
*MAT_ELASTIC
$MATERIAL NAME:TOP
$       MID        RO         E        PR        DA        DB         K
         7 7.850E+03 1.000E+17 3.000E-01 0.000E+00 0.000E+00 0.000E+00
$---+----1----+----2----+----3----+----4----+----5----+----6----+----7----+----8
$                    (7.1) SECTION CARDS
$---+----1----+----2----+----3----+----4----+----5----+----6----+----7----+----8
*SECTION_SOLID
$PROPERTY NAME:NUCLEUS
$       SID    ELFORM
         1         1
*SECTION_SOLID
$PROPERTY NAME:ANNULUS
$       SID    ELFORM
         2         1
*SECTION_SOLID
$PROPERTY NAME:BCORTICA
$       SID    ELFORM
         3         1
*SECTION_SOLID
$PROPERTY NAME:BCANCELL
$       SID    ELFORM
         4         1
*SECTION_SOLID
$PROPERTY NAME:TCORTICA
$       SID    ELFORM
         5         1
*SECTION_SOLID
$PROPERTY NAME:TCANCELL
$       SID    ELFORM
         6         1
*SECTION_SHELL
$PROPERTY NAME:TOP
$       SID    ELFORM      SHRF       NIP      PROPT   QR/IRID     ICOMP
         7         2  .100E+01       2.0        1.0        .0
$        T1        T2        T3        T4      NLOC
 0.300E+00 0.300E+00 0.300E+00 0.300E+00
$---+----1----+----2----+----3----+----4----+----5----+----6----+----7----+----8
$                    (8) NODAL POINT CARDS
$---+----1----+----2----+----3----+----4----+----5----+----6----+----7----+----8
*NODE
$   NODE               X               Y               Z      TC      RC
    1000  .123176100E+02 -.862291000E+01  .180952700E+02
    1001  .100485100E+02 -.981761100E+01  .181302800E+02
    1002  .109599700E+02 -.112813200E+02  .179860000E+02
    1003  .131712800E+02 -.945059900E+01  .180014000E+02
    1004  .769558300E+01 -.106354700E+02  .181427200E+02
.
.
.
```

REFERENCES

[1] Glaskin, M., A pain in the neck, Automotive Engineering, Vol. 2, pp. 46-47, 2000.

[2] Livermore Software Technology Corporation, LS-Dyna User's Manual, http://www.lstc.com, 1997.

[3] Murphy, P. L., Volinn, E., Is occupational low back pain on the rise, Spine, Vol. 24, No. 7, pp 691-697, 1999.

[4] Hirsch, C., The reaction of intervertebral discs to compression forces, J. of Bone and Joint Surgery, Vol. 37a, No. 6, pp. 1188-1196, 1955.

[5] Brown, T., Hansen, R. J., Yorra, A. J., Some mechanical tests on the lumbosacral spine with particular reference to the intervertebral discs, J. of Bone and Joint Surgery, Vol. 39a, No. 5, pp. 1135-1164, 1957.

[6] Horton, W. G., Further observations on the elastic mechanism of the intervertebral disc, J. of Bone and Joint Surgery, Vol. 40b, No. 3, pp. 552-557, 1958.

[7] Galante, J. O., Tensile properties of the human lumbar annulus fibrosus, Acta Orthopaedica Scandinavica, No. 100, Copenhagen, 1967.

[8] Sonnerup, L., A semi-experimental stress analysis of the human intervertebral disk in compression, Experimental Mechanics, Vol. 12, No. 3, pp 142-147, 1972.

[9] Belytschko, T., Kulak, R. F., A finite element method for a solid enclosing an inviscid, incompressible fluid, J. of Applied Mechanics, Vol. 40, pp. 609-610, 1973.

[10] Belytschko, T., Kulak, R. F., Schultz A. B., Finite element stress analysis of an intervertebral disc, J. Biomechanics, Vol. 7, pp. 277-285, 1974.

[11] Markolf, K. L., Morris, J., M., The structural components of the intervertebral disc, J. of Bone and Joint Surgery, Vol. 56a, No. 4, pp. 675-687, 1974.

[12] Wu, H. C., Yao, R. F., Mechanical behavior of the human annulus fibrosus, J. Biomechanics, Vol. 9, pp. 1-7, 1976.

[13] Lin, H. S., Liu, Y. K., Adams, K. H., Mechanical response of the lumbar intervertebral joint under physiological complex loading, J. of Bone and Joint Surgery, Vol. 60a, No. 1, pp. 41-55, 1978.

[14] Lin, H. S., Liu, Y. K., Ray G., Nikravesh, P., Systems identification for material properties of the intervertebral joint, J Biomechanics, Vol. 11, pp. 1-14, 1978.

[15] Schultz, A. B., Warwick, D. N., Berkson, M. H., Nachemson, A. L., Mechanical properties of human lumbar spine motion segments – part I, J. of Biomechanical Engineering, Vol. 101, pp. 46-52. 1979.

[16] Berkson, M. H., Nachemson, A., Schultz, A. B., Mechanical properties of human lumbar spine motion segments – part II, J. of Biomechanical Engineering, Vol. 101, pp. 53-57. 1979.

[17] Inoue, H., Three-dimensional architecture of lumbar intervertebral discs, Spine, Vol. 6, No. 2, pp. 139-146, 1981.

[18] Shirazi, A., Ahmed, A. M., Shrivastava, S. C., Finite element study of a lumbar motion segment subjected to pure sagittal plane moments, J. Biomechanics, Vol. 19, No. 4, pp. 331-350, 1986.

[19] Shirazi, A., Drouin, G., Load bearing role of facets in a lumbar segment under sagittal plane loadings, J. Biomechanics, Vol. 20, No. 6, pp. 601-613, 1987.

[20] Shirazi, A., On the fibre composite material models of disc annulus – comparision to predicted stresses, J. Biomechanics, Vol. 22, No. 4, pp. 357-365, 1989.

[21] Shirazi, A., Parnianpour, M., Nonlinear response analysis of the human ligamentous lumbar spine in compression, Spine, Vol. 18, No. 1, pp. 147-158, 1993.

[22] Wang, J. L., Engin, A. E., Shirazi, A., Parnianpour, M., Viscoelastic behavior of disc annulus fibrosus: the response of a quasi-linear viscoelastic model to external loads, Engineering Systems Design and Analysis, Vol. 64, No. 4, pp. 177-182, 1994.

[23] Shirazi, A., Parnianpour, M., Effect of changes in lordosis on mechanics of the lumbar spine lumbar curvature in lifting, J. of Spinal Disorders, Vol. 12, No. 5, pp. 436-447, 1999.

[24] Goel, V. K., Seenivasan, G., Applying bone adaptive remodelling theory to ligamentous spine, IEEE Engineering in Medicine and Biology, Vol. 13, pp. 508-516, 1994.

[25] Goel, V. K., Park, H., Kong, W., Investigation of vibration characteristics of the ligamentous lumbar spine using the finite element approach, J. of Biomechanical Engineering, Vol. 116, pp. 377-383, 1994.

[26] Goel, V. K., Ramirez, S. A., Kong, W., Gilbertson, L. G., Cancellous bone Young's modulus variation within the vertebral body of a ligamentous lumbar spine – application of bone adaptive remodelling concepts, J. of Biomechanical Engineering, Vol. 117, pp. 266-271, 1995.

[27] Goel, V. K., Monroe, B. T., Gilbertson, L. G., Brinckmann, P., Nat, R., Interlaminar shear stresses and laminae separation in a disc, Spine, Vol. 20, No. 6, pp. 689-698, 1995.

[28] Tencer, A. F., Ahmed, A. M., The role of secondary variables in the measurement of the mechanical properties of the lumbar intervertebral joint, J. of Biomechanical Engineering, Vol. 103, pp. 129-137, 1981.

[29] Adams, M. A., Hutton, W. C., The effect of posture on the lumbar spine, J. of Bone and Joint Surgery, Vol. 67b, No. 4, pp. 625-629, 1985.

[30] Adams, M. A., Hutton, W. C., Has the lumbar spine a margin of safety in forward bending, Clinical Biomechanics, Vol. 1, No. 1, pp. 3-6, 1986.

[31] Adams, M. A., Dolan, P., Hutton, W. C., Diurnal variations in the stresses on the lumbar spine, Spine, Vol. 12, No. 2, pp. 130-137, 1987.

[32] McNally, D. S., Adams, M. A., Internal intervertebral disc mechanics as revealed by stress profilometry, Spine, Vol. 17, No. 1, pp. 66-73, 1992.

[33] McMillan, D. W., McNally, D, S., Garbutt, G., Adams, M. A., Stress distributions inside intervertebral discs: the validity of experimental stress profilometry, J. of Engineering in Medicine, Vol. 210, pp. 81-87, 1996.

[34] Adams, M. A., McNally, D. S., Chinn, H., Dolan, P., Posture and the compressive strength of the lumbar spine, Clinical Biomechanics, Vol. 9, No. 1, pp. 5-14, 1994.

[35] Tadano, S., Katagiri, K., Umehara, S., Ukai, T., A constitutive modelling of the human lumbar intervertebral disc and forward-backward bending simulation, Bio-Medical Materials and Engineering, Vol. 7, No. 3, pp.

179-191, 1997.

[36] Lin, R. M., Chang, G. L., Chang L. T., Biomechanical properties of muscle-tendon unit under high-speed passive stretch, Clinical Biomechanics, Vol. 14, pp. 412-417, 1999.

[37] Zheng, Y. P., Mak, A. F. T., Extraction of quasi-linear viscoelastic parameters for lower limb soft tissues from manual identation experiment, J. of Biomechanical Engineering, Vol. 121, pp. 330-339, 1999.

[38] Ophir, J., Alam, S. K., Garra, B., Kallel, F., Konofagou, E., Krouskop, T., Varghese, T., Elastography: ultrasonic estimation and imaging of the elastic properties of tissues, Proc. Instn. Mech. Engrs, Vol. 213, No. H, pp. 203-233, 1999.

[39] Gatton, M. L., Pearcy, M. J., Kinematics and movement sequencing during flexion of the lumbar spine, Clinical Biomechanics, Vol. 14, pp. 376-383, 1999.

[40] Green, T. P., Allvey, J. C., Adams, M. A., Spondylosis, Spine, Vol. 19, No. 23, pp. 2683-2691, 1994.

[41] Dolan, P., Earley, M., Adams, M. A., Bending and compressive stresses acting on the lumbar spine during lifting activities, J. Biomechanics, Vol. 27, No. 10, pp. 1237-1248, 1994.

[42] Dolan, P., Kingma, I., Dieen, J., Looze, M. P., Toussaint, H. M., Baten, C. T. M., Adams, M. A., Dynamic forces acting on the lumbar spine during manual handling, Spine, Vol. 24, No. 7, pp. 698-703, 1999.

[43] Seroussi, R. E., Krag, M. H., Muller, D. L., Pope, M. H., Internal deformations of intact and denucleated human lumbar discs subjected to compression, flexion, and extension loads, J. of Orthopaedic Research, Vol. 7, pp. 122-131, 1989.

[44] Chiu, E. J., Lotz, J. C., Majumdar, S., High resolution magnetic resonance imaging of the human intervertebral disc with compression, 41st Annual Meeting, Orthopaedic Research Society, February 13-16, Orlando, Florida, 1995.

[45] Sheehan, F. T., Mitiguy, P., In regards to the ISB recommendations for standardization in the reporting of kinematic data, J. Biomechanics, Vol. 32, pp. 1135-1136, 1999.

[46] Kovach, I. S., Molecular theory of cartilage viscoelasticity, Biophysical Chemistry, Vol. 59, pp. 61-73, 1996.

[47] Klisch, S. M., Lotz, J. C., Application of a fiber reinforced continuum theory to multiple deformations of the annulus fibrosus, J. Biomechanics, Vol. 32, pp. 1027-1036, 1999.

[48] Harusampath, D., Hodges, D, H., Asymptotic analysis of the non-linear behavior of long anisotropic tubes, Int. J. of Non-Linear Mechanics, Vol. 34, pp 1003-1018, 1999.

[49] Wilke, H. J., Neef, P., Caimi, M., Hoogland, T., Claes, L. E., New in vivo measurements of pressures in the intervrtebral disc in daily life, Spine, Vol. 24, No. 8, pp. 755-762, 1999.

[50] Williams, P. L., Warwick, R., Gray's anatomy, Churchill Livingstone, 36th edition, 1980.

[51] White, A. A., Panjabi, M. M., Clinical Biomechanics of the spine, J. B. Lippincott, 2nd edition, 1990.

[52] Malko, J. A., Hutton, W. C., Fajman, W. A., An in vivo magnetic resonance imaging study of changes in the volume and fluid content of the lumbar intervertebral disc during a simulated diurnal load cycle, Spine, Vol. 24, No. 10, pp. 1015-1022, 1999.

[53] Maganaris, C. N., Paul, J. P., Hysteresis measurements in intact human tendon, J Biomechanics, Vol. 33, pp. 1723-1727, 2000.

[54] Shirazi, A., Drouin, G., Nonlinear gross response analysis of a lumbar motion segment in combined sagittal loadings, J. of Biomechanical Engineering, Vol. 110, pp. 216-222, 1988.

[55] Fennell, A. J., Jones, A. P., Hukins, W. L., Migration of the nucleus pulposus within the intervertebral disc during flexion and extension of the spine, Spine, Vol. 21, No. 23, pp. 2753-2757.

[56] Adams, M. A., Dolan, P., Recent advances in lumbar spinal mechanics and their clinical significance, Clinical Biomechanics, Vol. 10, No. 1, pp. 3-19, 1995.

[57] Adams, M. A., Green, T. P., Tensile properties of the annulus fibrosus – part I, Eur. Spine, Vol 2, pp. 203-208, 1993.

[58] Green, T. P., Adams, M. A., Dolan, P., Tensile properties of the annulus

fibrosus – part II, Eur. Spine, Vol 2, pp. 209-214, 1993.

[59] Lotz, J. C., Colliou, O. K., Chin, J. R., Duncan, N. A., Liebenberg, E., Compression induced degeneration of the intervertebral disc: an in vivo mouse model and finite element study, Spine, Vol. 23, No. 23, pp. 2493-2506, 1998.

[60] Adams, M. A., Green, T. P., Dolan, P., The strength in anterior bending of lumbar intervertebral discs, Spine, Vol. 19, No. 19, pp. 2197-2203, 1994.

[61] Meakin, J. R., Hukins, D. W. L., Effect of removing the nucleus pulposus on the deformation of the annulus fibrosus during compression of the intervertebral disc, J. Biomechanics, Vol. 33, pp. 575-580, 2000.

[62] Adams, M. A., Dolan, P., Hutton, W. C., The lumbar spine in backward bending, Spine, Vol. 13, No. 9, pp. 1019-1026, 1988.

[63] Shirazi, A., Ahmed, A. M., Shrivastava, S. C., Mechanical response of a lumbar motion segment in axial torque alone and combined with compression, Spine, Vol. 11, No. 9, pp. 914-927, 1986.

[64] Krismer, M., Haid, C., Rabi, W., The contribution of anulus fibers to torque resistance, Spine, Vol. 21, No. 22, pp. 2551-2557, 1996.

[65] Iartridis, J. C., Setton, L. A., Foster, R. J., Rawlins, B. A., Weidenbaum, M., Mow, V. C., Degeneration affects the anisotropic and nonlinear behaviors of human anulus fibrosus in compression, J. Biomechanics, Vol. 31, pp. 535-544, 1998.

[66] Kaigle, A., Ekstrom, L., Holm, S., Rostedt, M., Hansson, T., In vivo dynamic stiffness of the porcine lumbar spine exposed to cyclic loading: influence of load and degeneration, J. of Spinal Disorders, Vol. 11, No. 1, pp. 65-70, 1998.

[67] Lu, Y. M., Hutton, W. C., Gharpuray, V. M., The effect of fluid loss on the viscoelastic behavior of the lumbar intervertebral disc in compression, J. of Biomechanical Engineering, Vol. 120, pp. 48-54, 1998.

[68] Ohshima, H., Tsuji, H., Hirano, N., Ishihara, H., Katoh, Y., Yamada, H., Water diffusion pathway, swelling pressure, and biomechanical properties of the intervertebral disc during compression load, Spine, Vol. 14, No. 11, pp. 1234-1244, 1989.

[69] Li, L. P., Soulhat, J., Buschmann, M. D., Shirazi, A., Nonlinear analysis of

cartilage in unconfined ramp compression using a fibril reinforced poroelastic model, Clinical Biomechanics, Vol. 14, pp. 673-682, 1999.

[70] Tencer, A. F., Ahmed, A. M., Burke, D. L., Some static mechanical properties of the lumbar intervertebral joint, intact and injured, J. of Biomechanical Engineering, Vol. 104, pp. 193-201, 1982.

[71] Holmes, A. D., Hukins, D. W. L., Freemont, A. J., End-plate displacement during compression of lumbar vertebra-disc-vertebra segments and the mechanism of failure, Spine, Vol. 18, No. 1, pp. 128-135, 1993.

[72] Nagy, G. T., Golinski, W. Z., Gentle, C.R., Analysis of the Human Lumbar Intervertebral Disc Based on a Three-dimensional Non-linear Finite Element Model, Hospital and Medical Engineering, Vol. 38, No. 1, pp. 5-11, 2000.

[73] Nagy, G. T., Gentle, C. R., Experimental Stress Analysis of Intervertebral Discs Based on a Large Scale Model, International Society of Biomechanics XVIIIth Congress, Zurich, Switzerland, July 8-13, 2001.

[74] Nagy, G. T., Gentle, C. R., Significance of the Material Nonlinearity at Finite Element Modelling of the Disc Annulus, J. of Musculoskeletar Research, 5(3) , 2001.

[75] Visible Human Project Database, http://www.nlm.nih.gov/ research/visible/visible_human.html

[76] Dvorak, J., Panjabi, M. M., Chang, D. G., Theiler, R., Grob, D., Functional radiographic diagnosis of the lumbar spine, Spine, Vol. 16, No. 5, pp. 562-571, 1991.

[77] Chen, Y. L., Geometric measurements of the lumbar spine in chinese men during trunk flexion, Spine, Vol. 24, No. 7, pp. 666-669, 1999.

[78] Hayes, M. A., Howard, T. C., Gruel, C. R., Kopta, J. A., Roentgenographic evaluation of lumbar spine flexion-extension in asymptomatic individuals, Spine, Vol. 14, No. 3, pp. 327-331, 1989.

[79] Stephens, G. C., Yoo, J. U., Wilbur, G., Comparision of lumbar sagittal alignment produced by different operative positions, Spine, Vol. 21, No. 15, pp. 1802-1807, 1996.

[80] Stagnara, P., Mauroy, J. C., Dran, G., Gonon, G. P., Constanzo, G., Dimnet, J., Pasquet, A., Reciprocal angulation of vertebral bodies in a

sagittal plane: approach to references for the evaluation of kyphosis and lordosis, Spine, Vol. 7, No. 4, pp. 335-342, 1982.

[81] Kriz, R. D., Microstructure lectures, http://www.jwave.vt.edu/crcd/kriz/lectures/

[82] Constitutive laws, http://www.engin.brown.edu/courses/en224/contitutive.html

[83] Non-linear materials, http://www.engineering.sdsu.edu/~kmn/topic5/

[84] The neture of fluids, http://www.physics.uq.edu.au/ph128/3b.html

[85] Myklebust, J. B., Pintar, F., Yoganandan, N., Cusick, J. F., Maiman, D., Myers, T. J., Sances, A., Tensile strength of spinal ligaments, Spine, Vol. 13, No. 5, pp. 526-531, 1988.

[86] Pioletti, D. P., Rakotomanana, L. R., On the independence of time and strain effects in the stress relaxation of ligaments and tendons, J. Biomechanics, Vol. 33, pp. 1729-1732, 2000.

[87] Hirokawa, S., Tsuruno, R., Three-dimensional deformation and stress distribution in an analytical/computational model of the anterior cruciate ligament, J. Biomechanics, Vol. 33, pp. 1069-1077, 2000.

[88] Hukins D. W. L., A simple model for the function of proteoglycans and collagen in the response to compression of the intervertebral disc, Proc. of the Royal Soc. of London, Vol. B249, pp.281-285, 1992.

[89] Brinckman, P., Grootenboer, H., Change of disc height, radial disc bulge, and intradiscal pressure from discsectomy, Spine, Vol. 16, No. 6, pp. 641-646, 1991.

[90] Sokolnikoff, I. S., Sokolnikoff, E. S., Higher matematics for engineers and physicists, McGraw-Hill, 2nd edition, 1941.

[91] Thomas, G. B., Finney, R. L., Calculus and analytic geometry, Addison-Wesley, 6th edition, 1984.

[92] Goodman, A. W., Analytic geometry and the calculus, Collier Macmillan, 4th edition, 1980.

[93] Shirazi, S. A., Shrivastava, S. C., Ahmed, A. M., Stress analysis of the lumbar disc-body unit in compression, Spine, Vol. 9, No. 2, pp. 120-134, 1984.

[94] Martinez, J. B., Oloyede, A., Broom, N. D., Biomechanics of load-

bearingof the intervertebral disc: an experimental and finite element model, Medical Engineering & Physics, Vol. 19, pp. 145-156, 1997.

[95] Mercer, S., Bogduk, N., The ligaments and anulus fibrosus of the human adult cervical intervertebral disc, Spine, Vol. 24, No. 7, pp. 619-628, 1999.

[96] Panjabi, M. M., Goel, V., Oxland, T., Takata, K., Duranceau, J., Krag, M., Price, M., Human lumbar vertebrae, quantitative three-dimensional anatomy, Spine, Vol. 17, No. 3, pp. 299-306, 1992.

[97] Schultz, A. B., Biomechanics of the human spine and trunk, Handbook of Bioengineering, 1982.

[98] Patwardhan, A. G., Havey, R. M., Meade, K. P., Lee, B., Dunlap, B., A follower load increases the load-carrying capacity of the lumbar spine in compression, Spine, Vol. 24, No. 10, pp. 1003-1009, 1999.

[99] http://scienceworld.wolfram.com